Doctoral Dissertation

Defect interaction between dislocations and grain boundaries in fcc metals

Li Li

April 2022

Graduate School of Engineering
Osaka University

博士学位論文

面心立方格子材料の転位と粒界の相互作用に関する研究

李 力

2022 年 4 月

大阪大学大学院工学研究科

Abstract

It is well established that the defect interaction between dislocations and grain boundaries (GBs) has a substantial impact on the mechanical properties of crystalline materials as the conventional Hall-Petch law. At sub-micron and nano scales, GBs and dislocations are the primary defects of the crystal. Therefore, the mechanical behavior of the nanostructure, such as strength and ductility, is directly determined by their interactions. Even for the polycrystalline materials, it is also dominant to affect the plastic deformation response. Despite the fact that many experiments have been implemented, it is almost impossible to directly observe the details of the defect interactions due to the complexity of the GB structure and the limitation of experimental conditions and resolutions. In light of this constraint, this thesis mainly focused on the interaction between dislocation and GB by molecular dynamics (MD) simulation and nudged elastic band method (NEB) based on the transition state theory (TST) to carry out the following works.

(1) The GB energy maps for <110>/<111>/<100>/<112>-axis tilt symmetric GBs were obtained by MD simulations for typical face-centered cubic (fcc) metals. The generalized stacking fault energy maps were also obtained for the subsequent researches.

(2) The interactions between edge dislocations and <112>-axis tilt symmetric GBs were investigated by MD and NEB in Cu. Fundamental dislocation behaviors of absorption in GB, transmission across GB, and pile-up in front of GB were observed dependent to kinds of GBs. For most cases of absorptions, the leading partial dislocation would be spontaneously absorbed by the GBs and the trailing partial dislocation was absorbed if the further load was applied. Different slip plane affects the interaction mechanisms and the critical interaction shear stress (CISS). Generally, the CISS

decreases if the GB energy increases when we just consider the weakest point along the GB plane. The activation volumes and strain rate sensitivities (SRS) were estimated by TST and they agreed well with the real experimental data.

(3) Then, the interactions between screw dislocations and <110>-axis coherent twin boundaries (CTBs) were investigated in Al, Cu, Ni, Ag, Au, and Pd. It was found that screw dislocation was spontaneously absorbed by the CTB in Al and Pd_Hale, where Pd_Hale implies that the Pd was simulated by using the potential proposed Hale et al. However, dislocation transmitted through the CTB in other cases. The CISS has a strong linear relationship with the reciprocal of the difference between unstable stacking fault energy and stable stacking fault energy. The energy barriers under certain stress states have the same trend. This part directly linked the CISS and interaction mechanisms with the inherent property of the materials. Furthermore, the activation volumes and SRS were all consistent with the experiments.

(4) Finally, abnormal reversible plasticity was observed and reported. The reversible plasticity was caused by the reversible defect interactions between the negative edge dislocation and <110>-axis CTB/<110>-axis $\Sigma 11(\bar{1}13)$ GB and <112>-axis $\Sigma 11(\bar{1}3\bar{1})$ GB in Al, Cu, Ni, and Ag. The positive dislocation, on the other hand, did not support this reversibility. Despite the lack of a direct experiment to verify the findings, this new discovery was compared to other references and demonstrated the plausibility and rationality of its existence.

Keywords: defect interaction; dislocation; grain boundary; transition state theory; nudged elastic band method; molecular dynamics simulations

Content

1. Introduction....1
1.1. Research background of defect interactions....1
1.2. Influencing factors of defect interactions....5
1.3. Research methods of defect interactions....9
1.4. Objective and scope of the research....13
References....15
2. Fundamental theories and methods....27
2.1. Molecular dynamics method....27
2.1.1. Fundamental....28
2.1.2. Integration algorithms....29
2.1.3. Interatomic potentials....30
2.1.4. Ensemble, temperature and pressure control....32
2.1.5. Time step and boundary condition....37
2.2. Transition state theory and NEB method....37
2.2.1. Transition state theory....38
2.2.2. NEB method....39
2.2.3. Activation volume and strain rate sensitivity....43
2.3. Crystal defect analysis method....45
References....47
3. GB energy and stacking fault energy....51
3.1. GB and GB energy....51
3.1.1. Fundamental concept of GB....51
3.1.2. Model of GB and Bi-crystal structure....53
3.1.3. GB energy map....56
3.2. Stacking fault energy and generalized stacking fault curve....61

3.3. Summary.....67
References.....68
4. Interactions between edge dislocations and <112>-axis symmetric tilt grain boundaries in Cu.....70
4.1. Atomic model and calculation condition.....73
4.2. Edge dislocation-GB interactions.....77
4.2.1. Case of absorption.....80
4.2.2. Case of pile-up.....82
4.2.3. Case of transmission.....83
4.2.4. Relationship between critical stress and GB energy.....85
4.3. Transition state theory parameters of interactions.....87
4.3.1. Activation barriers in various strain or stress states.....87
4.3.2. Cases of absorptions.....88
4.3.3. Case of the transmission.....91
4.3.4. Activation volume and strain-rate sensitivity.....93
4.4. Summary.....98
References.....100
5. Interaction between screw dislocations and coherent twin boundaries in FCC metals 106
5.1. Atomic models and simulation condition.....108
5.2. Screw dislocation-CTB interactions.....110
5.2.1. Energy of CTBs and the generalized stacking fault curves.....110
5.2.2. Interactions between CTB and screw dislocation.....113
5.2.3. Relationship between CISS and stacking fault energy.....120
5.3. Analysis of interactions based on the transition state theory.....124
5.3.1. Energy barriers, activation volumes and strain rate sensitivities...124
5.3.2. Relationship between energy barriers and stacking fault energy..129

5.4. Summary 130
References 132
6. Reversible plasticity by reversible defect interactions 137
6.1. Research background 137
6.1.1. Reversible plasticity induced by reversal movement of dislocation 137
6.1.2. Reversible plasticity induced by twinning and detwinning 141
6.1.3. Reversible plasticity induced by twin boundary 144
6.2. Atomic models and simulation condition 146
6.3. Edge dislocation-CTB interactions 147
6.3.1. Material: Aluminum (Al) 147
6.3.2. Material: Copper (Cu) 154
6.3.3. Material: Nickle (Ni) 160
6.3.4. Material: Silver (Ag) 166
6.4. Edge dislocation-<110>-axis-$\Sigma 11(\bar{1}13)$ GB interaction 169
6.4.1. Material: Aluminum (Al) 170
6.4.2. Material: Copper (Cu) 174
6.4.3. Material: Nickle (Ni) 178
6.4.4. Material: Silver (Ag) 182
6.5. Edge dislocation-<112>-axis-$\Sigma 11(\bar{1}3\bar{1})$ GB interaction 184
6.6. Discussion 186
6.7. Summary 190
References 192
7. Conclusion remarks 195
Appendix 199
List of contributions 206
Acknowledgments 207

1. Introduction

1.1. Research background of defect interactions

Metal materials have been widely used in numerous areas of human life from daily pots and pans to aerospace jets. Following the second industrial revolution, the vigorous development of steel, alloy metallurgy, and the other technologies has brought earth-shaking changes to human lives. Until now, metal materials have played a very important role in scientific and technological productions [1–3]. With the rapid developments of micro/nano electromechanical systems (MEMS/NEMS) and the other microelectronic device systems, more and more sub-micron structures are increasingly adopted to enrich people's lives and work. Micro and nano crystalline materials, as well as cutting-edge micro-mechanical manufacturing technologies, aid in the realization of such advanced applications [4–10]. Simultaneously, the related mechanical properties also need to be investigated urgently.

Generally, strength and ductility are the most essential but trade-off measures of polycrystalline metals which are crucial in engineering projects. With the assistance of substantial experimental advancement to synthesize the bulk nanostructured materials, such as the nanocrystals and nano-twinned materials [11–16], the flow stress were remarkably higher than that of the conventional materials. The trend can be described by Hall-Petch power law,

$$\sigma_{critical}(d) = \sigma_0 + kd^{-\alpha} \tag{1-1}$$

Where, d is the average length of the grain size, σ_0 is a materials constant for the starting stress for dislocation movement (or the resistance of the lattice to dislocation motion), k and α are the size-independent parameters. One reasonable interpretation is that, when the grain size decreases to micro or sub-micro scale, the density of grain

boundaries (GBs) rises, obstructing the dislocations and preventing the slip from easily transmitting into the other grain. In this way, the strength should be increased. In Fig. 1-1, however, if the grain sizes decrease to or below 20 nm, an inverse Hall-Petch power low will take over the relationship between the strength and grain size [17,18]. Because there are fewer dislocations in the intragranular region as grain size reduces below 20nm, deformation mechanisms switch from dislocation-GB interactions to GB migration or grain rotation, thereby lowering yielding thresholds.

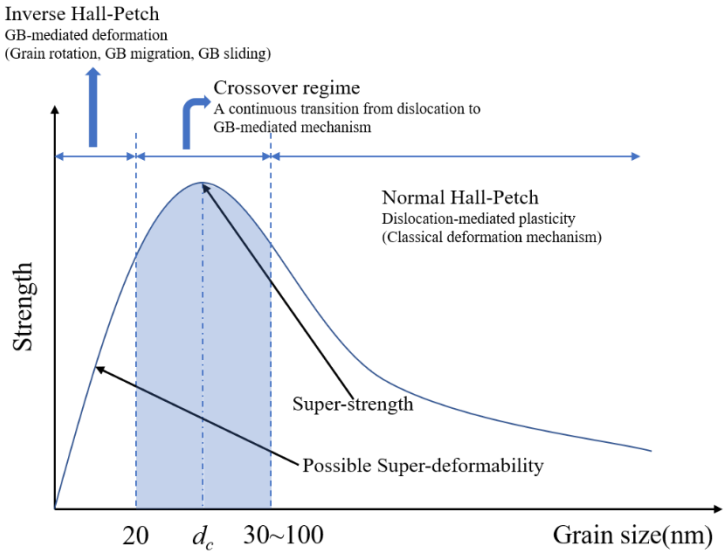

Fig. 1-1 Strength of polycrystalline materials as a function of grain size: Hall–Petch relation and transition to “inverse” Hall–Petch.

The influence of diverse mechanisms on strength and ductility during stress-induced deformations is reflected by the normal and inverse Hall-Petch power laws. Obviously, the maximum strength is the competed results between dislocation-GB interaction and GB self-alone related mechanisms, such as the GB diffusion and GB migration. Because most functional materials created by modern technology adhere with the normal Hall-Petch rule, interactions between dislocations and GBs are particularly essential in contemporary engineering projects.

As the most prevalent and important defects in the polycrystalline materials, vacancies, dislocations and GBs considerably influence the plastic deformation behaviors of metals. Although the interaction between dislocations (the main carrier of crystalline material plasticity) and GBs (two-dimensional defects) is of great interest in the past several decades, many unique aspects of these mysterious interaction processes are still not completely unraveled [19–26]. Several representative scenarios can be categorized as following when incident dislocations impinge the GB [27], as shown in Fig. 1-2: a) dislocation can pile up at the GB, allowing the system's strength to be increased; b) the GB acts as the dislocation source and emit dislocations into the adjacent grain B or on the GB plane because dislocation pile-up increase the local stress concentration; c) the incident dislocation may be absorbed and dissociated into the GBs without triggering dislocation emission into the grain B. d) after absorption in Fig. 1-2 (c), the dislocation may be reemitted into the grain B; e) a transfer of a dislocation from the pile-up in grain A to grain B is depicted in Fig. 1-2 (e), leaving a residual dislocation in the grain boundary behind due to the required continuity of the Burgers vector; f) for an ideal situation, the incident dislocation can entirely transmit through the GB without leaving any residual dislocations on the GB plane and the incoming and outcoming slip planes are identical; g) meanwhile, dislocation may be activated in both side and move towards the GB and incorporated into one geometrically necessary dislocations (GND); h) what is not common but may also occur is the incident dislocation being reflected back to the parent grain A [28].

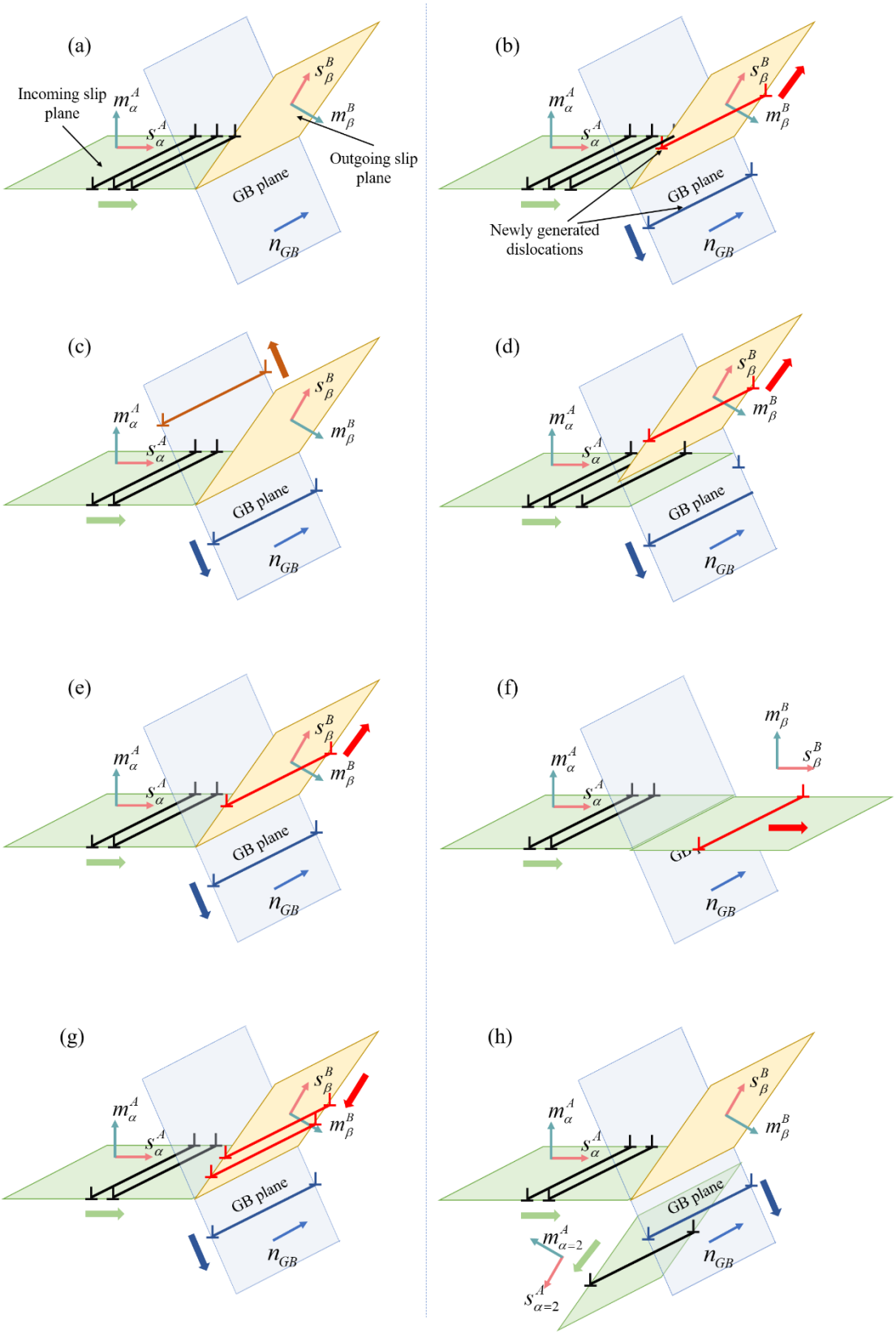

Fig. 1-2 Slip transfer and dislocation interaction mechanisms in adjacent grain A, B,

separated by grain boundary with normal n_{GB}. m is the slip plane normal and s is the slip direction. α and β represent the slip system in grain A and grain B [28].

1.2. Influencing factors of defect interactions

Although plenty of alternatives are possible for the interaction, the results are still affected by many factors. And hence, it still leaves a lot of space for researchers to expand their ideas and talents. Many unique aspects of these mysterious interaction processes are still not completely unraveled [19–23,25,26,29]. Conventionally, the interaction results can be determined by the type of the involved dislocation [28,30,31], the local microstructural attributes of the GBs categorized by the coincidence site lattice (CSL) method [32,33], and the type of chemical elements [25,26]. For example, the material can have a significant impact on the interaction and fundamentally alter the mechanism as well as the critical interaction shear stress (CISS). An early and comprehensive study of dislocation-grain boundary interaction was implemented by Jin et al. [26], wherein the single screw dislocation was introduced to impinge the quasi-two dimensional coherent twin boundary (CTB) in Al, Cu and Ni using atomistic simulation and the results revealed the significance of the chemical element type to the reaction mechanism. Screw dislocation was spontaneously absorbed by the CTB and consequently two partial dislocations were generated on the CTB plane. Additional load simply caused the two partial dislocations to drift apart and slip along the CTB plane. In contrast, the screw dislocation transmitted through the CTB and penetrated into the twinned grain. Further loading drove the penetrated dislocation to move out of the bi-crystal structure from the free surface. Chassagne confirmed similar scenarios, stating that it is natural for the CTB in Al to absorb the screw dislocation without resistance [34]. To confirm this tendency, the other potential files were used. It is clear from these findings that the elements have a substantial impact on the interaction process.

Another factor which is deserved to discussed and investigated is the type of the dislocation. According to the relationship between the line direction and the slip direction, the dislocation can be categorized as screw, edge, or mixed dislocation. In terms of crystal morphology, screw dislocations simply distort the local atomic arrangement. The nucleation of an edge dislocation is equivalent to deleting or inserting a row of atomic layers [35]. The difference between the atomic arrangement drastically altered the interaction mechanisms. When a screw dislocation impinged the CTB in Al, it was absorbed and two partial dislocations were consequently generated as described above. However, when one edge dislocation impinged on the CTB, one partial dislocation was generated and slipped on the CTB. Additionally, one immobile Frank partial dislocation would be formed at the impacting point [22]. In the realistic materials, however, dislocations mainly have the mixture property and will make the interaction very complicated. Pile up, absorption, transmission and reflection may occur at the same time [23].

Another factor, maybe the most prevalent and crucial factor, should be the misorientation angle between the grains, namely, the type of the GBs. Morphologically, nine parameters or degrees of freedoms (DoFs) were used to define the GB structure [36]. The interface motion, which connects two adjacent crystals, is defined by six parameters, while the interface plane is defined by three. The coincidence site lattice (CSL), which is commonly used to described the GB morphology, is therefore defined as the intersection of translation subsets of the two crystal lattices. The coincidence is characterized by a coincidence index Σ which is equal to the ratio of the volume of the coincidence unit cell to the volume of the primitive unit cell of the crystal. The value of Σ varies according to the misorientation θ between the two grains. The screw dislocation, for example, will be absorbed or dissociated by $\Sigma 3$, $\Sigma 9$, and $\Sigma 11$ GB, but it will penetrate through the $\Sigma 57$ and $\Sigma 451$ in Ni [37]. More precisely, this degree of coincidence only reflects one aspect of the influence of the GB structure on the interaction. Because, even for the same

Σ, several potential slip planes exist when considering the periodic arrangement of the GB. 3 independent slip planes exist for Σ9 GB, and two of which yield dissociation results and one of which gives the transmission result. Obviously, the local GB structure significantly affects the interaction outcomes. The Σ only reflects part of the local property and more information is needed to quantitatively estimate the effects of GB structures. Not only the interaction mechanisms but also the global stress response can be dramatically different if the GB is changed. Kuhr et.al estimated the strain-stress behaviors of the room temperature relaxed (RTR) grain boundary sample and the rapidly solidified (RS) boundary sample [38]. They found that a more chaotic GB was formed in the RS sample so that lower global stress was needed to sustain the dislocation-GB interactions.

Depart from the foregoing factors, the doping of hydrogen also has a significant effect on the interaction. In high pressure H gas, H atoms can ingress into metals and impair the mechanical properties of a range of structural materials such as pipelines and pressure vessels, and may cause catastrophic failure [39–47]. The hydrogen atoms will be trapped in the vicinity of the GB region and hence absorb the dislocation. This process facilitates hydrogen embrittlement and reduces the strength of the material [48–54]. The temperature also plays an important role in the determination of interactions. Xu and Hayakawa declared that, in Ni and Ni-based equiatomic alloys, the screw dislocation was inclined to be absorbed at elevated temperature to sustain the high strength but was more likely to penetrate the CTB to furnish the ductility at lower temperature (77 K) [55]. Similar phenomena have been confirmed by the experiments that a significantly higher elongation to fracture of these alloys at 77 K than that at 293 K: ~39%, ~47%, and ~50% at 77 K in comparison with ~28%, ~37%, and ~40% at 293 K for pure Ni, FeNi, and FeNiCoCr, respectively [56–60].

Obviously, it is difficult to get an absolute inference to estimate the proportion of these factors in determining the interaction mechanism. Any of them may directly or indirectly

participate in the interactions. However, some hints can still be concluded from the experimental or statistical aspects for the transmission cases [61].

Several criteria, from the geometric and energetic perspectives, have been proposed to forecast the possible transmitted slip system and critical interaction conditions. As for the criteria that account for the slip system orientations, namely, the misorientation between the two grains, Livingston and Chalmers Criterion may be the first estimation that employed the so-called N-parameter to anticipate the activated slip system in adjacent grain [62], as shown in Fig. 1-3,

$$N_{\alpha\beta} = (m_\alpha^A \cdot m_\beta^B)(s_\alpha^A \cdot s_\beta^B) + (m_\alpha^A \cdot s_\beta^B)(s_\alpha^A \cdot m_\beta^B) \tag{1-2}$$

where, s_α^A, s_β^B are the orientations of slip direction and m_α^A, m_β^B are the slip plane normal. Good agreements were found between this N-parameter criterion and experiments [62–65]. Hereafter, N-modified parameter [66], M-parameter [67], M-modified parameter [68] and L-parameter [69,70] were proposed to furnish the geometrical effect on the transmission.

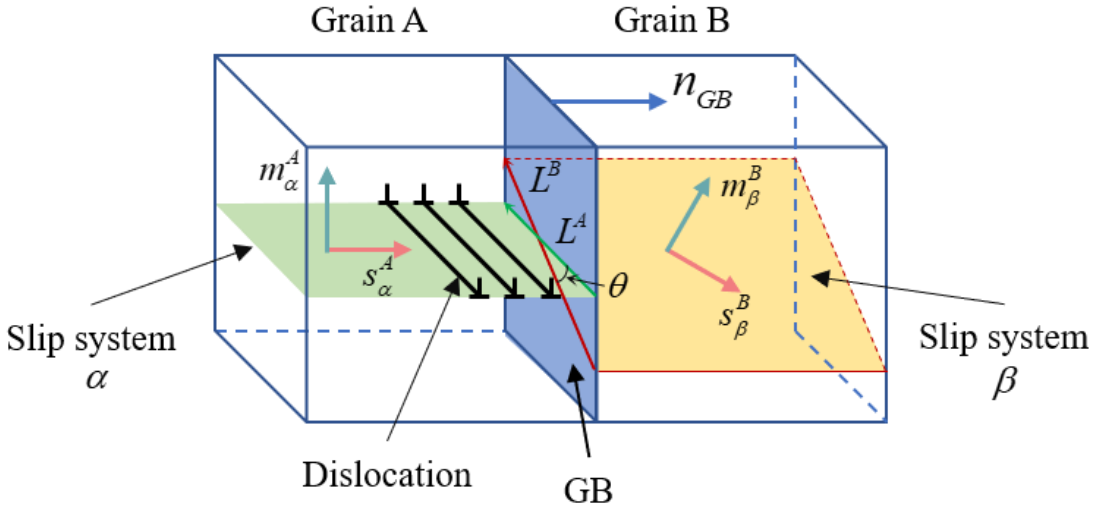

Fig. 1-3 Nomenclature for slip systems α, β in adjacent grains A, B, separated by grain boundary n_{GB}. L^A and L^B are normalized vectors of the lines of intersection.

The geometrical criteria are frequently used in conjunction with the other supplemental criteria. First, the magnitude of the geometrical criterion should be the maximum for the candidate outcoming slip system. Second, the Schmid factor (SF) of the outcoming slip plane should be the maximum so that the resolved shear stress (RSS) is the largest one on the possible slip plane to trigger the penetration [71,72]. Third, the magnitude of residual Burgers vector left on the GB plane after the interaction should be minimized. This is actually a energetical criterion because it is linked to the rising of the strain energy density [73–75]. Bachurin also pointed out that the sign of the incident dislocation can promote or inhibit penetration, because the dislocation will change the local structure of the grain boundary [76].

All in all, the interaction between the GBs and dislocations can be affected by many factors and none of them have an overwhelming advantage to determine the progress of the interaction or the corresponding mechanism. The mechanisms of the interaction, as well as the factors that influence it, are far from being fully understood. Therefore, the interaction between the GBs and dislocations is still a research hotspot in current scientific research.

1.3. Research methods of defect interactions

With the advancement of modern experimental equipment and the expansion of computing capabilities, a growing number of methods are becoming available and being used to analyze defect interactions. This subsection reviews experimental observation methods, computational methods, and some experimental phenomena and computational results observed using these advanced approaches.

Experimentally, examples of *in situ* techniques include synchrotron X-ray diffraction to explore strain transfer across internal interfaces in bulk specimens [77,78], digital image correlation (DIC) in conjunction with scanning electron microscopy (SEM) to explore accumulation of strain as well as slip transfer across interfaces intersecting the

free surface [79–81], electron backscattered diffraction (EBSD) to measure strain accumulation at interfaces and twinning activity during loading in the scanning electron microscope SEM observations of slip traces on free surfaces and transmission electron microscopy (TEM) using a conventional loading stage, nano-indentation, or modified sample forms to explore interactions across interfaces at the nanoscale [82–86]. These technologies have their own advantages and disadvantages in terms of spatial and temporal resolution, sample geometry and thickness constraints, applied stress state, and the number of grain boundaries that can be inspected.

Using TEM and DIC, Lu et al. revealed the effect of the CTBs as shown in Fig. 1-4. In polycrystalline copper containing different volume fractions of nano-sized twins [87], the strain rate sensitivities (SRS) of the ultra-fined crystalline Cu with a high density of CTB is extremely higher than that of the same sample without CTB. The hardness and SRS decrease when the density of CTB decreases. This demonstrated that CTB can act as a barrier to hinder the slip of the dislocation, leading to a result of increasing the strength, and also CTB can be penetrated under certain condition to furnish the ductility. The CTBs with a high density of defects and displaced CTBs also appear to serve as dislocation sources, very much like conventional GBs [14,87,88]. One amazing phenomenon observed by TEM is that under specific condition, the interaction between the dislocation and GBs are reversible which represents a reversible plasticity or pseudo-elasticity [89–91].

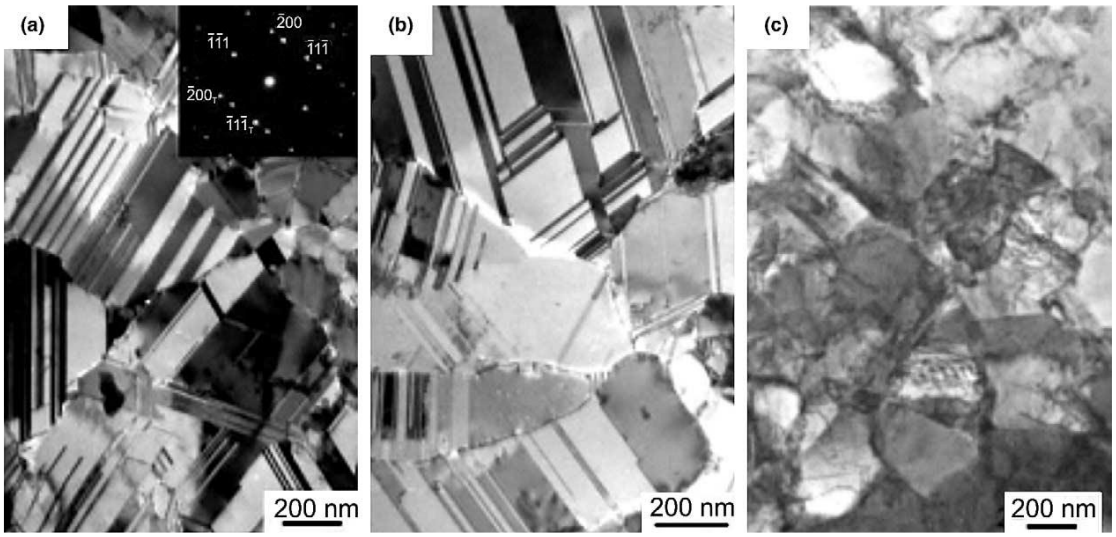

Fig. 1-4 TEM images of the as-processed microstructure of (a) Cu with a higher twin density, (b) Cu with a lower twin density, and (c) control ultra-fined crystalline Cu essentially without twins [87].

In numerical simulations, researchers have developed multi-scale simulation methods ranging from macroscopic finite element method (FEM), and mesoscopic 3d discrete dislocation dynamics (3d-DDD) to microscopic molecular dynamics (MD), molecular statics (MS). Lim et al. developed a so-called SuperDislocation (SD) model to simulate the Hall-Petch effect in polycrystals using FEM techniques [92]. Kuroda et al. also proposed a strain gradient to account for the interface effect for a bi-crystal FEM model [93]. Both of them introduced the GB resistance by calculating the transmissivity factor as mentioned above in the geometric criteria for slip transmission. Nonetheless the traditional bi-crystal model simply and arbitrarily treated the GB as either completely penetrable or completely impenetrable [94–96]. 3d-DDD model likewise demonstrated that the Hall-Petch relationship was dependent on the transmission capability of dislocations [97–99]. Zhang et al. also employed 3d DDD to show that the strain hardening rate and flow stress of nanopillars with a rigid GB were much higher than those of penetrable GB nanopillars [100].

With the continuous abundance of computing resources, atomic-scale numerical simulations, such as the molecular dynamics (MD) technique, were increasingly favored to unmask these interaction processes. Through the MD simulations, the intragranular and intergranular atomistic information and energetic measures can be directly estimated which may figure out the contents that cannot be directly observed in the experiments. As an illustration, an early and comprehensive study of dislocation-grain boundary interaction was implemented by Jin et al. [26], where the single screw dislocation was introduced to impinge the quasi-two dimensional coherent twin boundary in Al, Cu and Ni using atomistic simulation. The results emphasized the significance of chemical element type in the reaction mechanism. A linear relationship between the critical resolved shear stress (CRSS) and a non-dimensional parameter, associated with partial Burgers vector and static stacking fault energy, was stated for the dislocation-CTB interaction of typical face-centered-cubic (FCC) metal [25,34]. Moreover, a mobile partial dislocation slipping on the CTB plane and a sessile residual Frank dislocation retaining at the impinging point are generated when the edge dislocation reacts with CTB [22]. In addition to the dislocation-CTB interaction, the nucleation and lateral motion of GB disconnections, as well as direct transmission, were found in the interaction process of single screw dislocations and more broadly morphological GB structures [37]. Nanoindentation experiments [101,102] and corresponding MD simulation [103] also depicted some seductive slip-GB reaction phenomenon, although the consequent multi-dislocations mainly get the mixture property and sinuous topological shapes which may cause more complex reaction mechanisms and quantitative analysis difficulty.

The approaches above only provided the qualitative analysis of reaction phenomena and the CRSS at extremely low temperature (<10 K) or finite temperature with a very high strain rate through MD or at 0 K through MS simulations. Rare of them consider the energy evolution or the energy barrier for the interaction process. Sangid et al. [104] established the control box method to capture the inversely proportional relationship

between the energy barrier and the statics <110> axis GB boundary energy. Following this way, Chen et al. [105] investigated the matrix dislocation interacting with the twin boundary for hexagonal close packed metal Mg. But this method is sensitive to the choice of the box, no matter the size or the location may also introduce the artificial effects. Nevertheless, the dislocation-GB interaction usually is identified as a thermally activated process [20,106]. This process can be precisely and energetically described by the transition state theory (TST) [107], by which the consequently calculated energy barriers and activation volumes are of the capability to illustrate the rate and thermal effects on the interaction process and link the MD simulation to the rate-dependent bulk material mechanical experiments. Plenty of investigations have been probed with the help of this approach, such as the dislocation-precipitate interaction process [108], cross-slip mechanism of the screw dislocation which is hindered by the stacking fault tetrahedra [109], dislocation nucleation process [110,111].

1.4. Objective and scope of the research

The foregoing researches only qualitatively focus on the interaction processes between dislocations and one or two specific GBs. Some of them generated the dislocations through the void or notch which may nucleate curved and multiple dislocations and further increase the difficulty to quantitively investigate the interaction process. Although the GB structures influence the interaction mechanisms and critical stresses, the general tendency has not been resolved because only limited GB structures were generated and adopted to interact with the dislocation in the preceding researches. A system investigation of the interaction between dislocations and numerous GBs is urgent. On the other hand, some questions come naturally while implementing atomic simulations. How can these atomic-scale interactions be quantitatively reflected in the macroscopic bulk material, especially in the plastic behaviors, and how will the MD results be linked to the experiments?

To overcome the drawbacks of the previous researches and address the question stated above, the objective of this dissertation is expected to reveal the intrinsic mechanisms of the interactions between the single dislocation and GBs. The bi-crystal model which contains one single dislocation and one GB will be our main target because multiple dislocations may make further TST analysis difficult. The main task of this dissertation are 1) to investigate the influence of GB energy on the CISS and to measure the SRS and activation volumes that can be directly compared to the experimental data; 2) to investigate the material dependence on the interaction mechanisms and CISS by considering Al, Cu, Ni, Ag, Au, and Pd; 3) to investigate the interesting but abnormal phenomenon-reversible plasticity appeared in the interaction between edge dislocation and low energy GB.

The present dissertation is composed of 7 chapters. First, Chapter 1 gives the general introduction on the interaction between dislocations and GBs. The theoretical foundation is laid down in Chapter 2, which includes the molecular dynamics approach, transition state theory, and NEB methodologies. In Chapter 3, the GB energy maps and generalized stacking fault energy curves are obtained using MD and NEB. In Chapter 4, defect interaction summary between edge Dislocations and <112>-axis symmetric tilt grain boundaries in Cu on activation barriers and critical stresses are discussed. The GB energy effects will be investigated. In Chapter 5, we focus on the interaction between the screw dislocation and coherent twin boundary in Al, Cu, Ni, Ag, Au and Pd. The material dependence to the present defect interactions will be discussed. Chapter 6 will focus on the reversible plasticity that appeared in Σ11/CTB-Edge dislocation interactions for Al, Cu, Ni, Ag, and Au. The simulations will be compared to the experiments. Finally, the dissertation is summarized in Chapter 7.

References

[1] T. Zhu, J. Li, Ultra-strength materials, Progress in Materials Science. 55 (2010) 710–757.

[2] S. Suresh, J. Li, Materials science: Deformation of the ultra-strong, Nature. 456 (2008) 716–717.

[3] F. Liu, P. Ming, J. Li, Ab initio calculation of ideal strength and phonon instability of graphene under tension, Physical Review B - Condensed Matter and Materials Physics. 76 (2007) 1–7.

[4] A. Rochefort, P. Avouris, F. Lesage, D.R. Salahub, Electrical and mechanical properties of distorted carbon nanotubes, Physical Review B - Condensed Matter and Materials Physics. 60 (1999) 13824–13830.

[5] Y. Kato, R.C. Myers, A.C. Gossard, D.D. Awschalom, Coherent spin manipulation without magnetic fields in strained semiconductors, Nature. 427 (2004) 50–53.

[6] T. Koga, X. Sun, S.B. Cronin, M.S. Dresselhaus, Carrier pocket engineering applied to “strained” Si/Ge superlattices to design useful thermoelectric materials, Applied Physics Letters. 75 (1999) 2438–2440.

[7] A.R. Abramson, C.L. Tien, A. Majumdar, Interface and strain effects on the thermal conductivity of heterostructures: A molecular dynamics study, Journal of Heat Transfer. 124 (2002) 963–970.

[8] O. Stier, M. Grundmann, D. Bimberg, Electronic and optical properties of strained quantum dots modeled by 8-band k·p theory, Physical Review B - Condensed Matter and Materials Physics. 59 (1999) 5688–5701.

[9] T. Kropp, M. Mavrikakis, Effect of strain on the reactivity of graphene films, Journal of Catalysis. 390 (2020) 67–71.

[10] Z. Wu, R.E. Cohen, Pressure-induced anomalous phase transitions and colossal enhancement of piezoelectricity in PbTiO3, Physical Review Letters. 95 (2005) 1–4.

[11] K.S. Kumar, H. Van Swygenhoven, S. Suresh, Mechanical behavior of nanocrystalline metals and alloys, Acta Materialia. 51 (2003) 5743–5774.

[12] M.A. Meyers, A. Mishra, D.J. Benson, Mechanical properties of nanocrystalline materials, Progress in Materials Science. 51 (2006) 427–556.

[13] M. Dao, L. Lu, R.J. Asaro, J.T.M. De Hosson, E. Ma, Toward a quantitative understanding of mechanical behavior of nanocrystalline metals, Acta Materialia. 55 (2007) 4041–4065.

[14] L. Lu, X. Chen, X. Huang, K. Lu, Revealing the maximum strength in nanotwinned copper, Science. 323 (2009) 607–610.

[15] K. Lu, L. Lu, S. Suresh, Strengthening materials by engineering coherent internal boundaries at the nanoscale, Science. 324 (2009) 349–352.

[16] X. Li, Y. Wei, L. Lu, K. Lu, H. Gao, Dislocation nucleation governed softening and maximum strength in nano-twinned metals, Nature. 464 (2010) 877–880.

[17] J.R. Greer, J.T.M. De Hosson, Plasticity in small-sized metallic systems: Intrinsic versus extrinsic size effect, Progress in Materials Science. 56 (2011) 654–724.

[18] C. Carlton, P.J. Ferreira, What is behind the inverse Hall-Petch behavior in nanocrystalline materials?, Materials Research Society Symposium Proceedings. 976 (2006) 19–24.

[19] T. Zhu, J. Li, A. Samanta, H.G. Kim, S. Suresh, Interfacial plasticity governs strain rate sensitivity and ductility in nanostructured metals, Proceedings of the National Academy of Sciences of the United States of America. 104 (2007) 3031–3036.

[20] T. Zhu, J. Li, S. Yip, Atomistic Reaction Pathway Sampling: The Nudged Elastic Band Method and Nanomechanics Applications, in: Nano Cell Mech., John Wiley & Sons, Ltd, Chichester, UK, 2012: pp. 311–338.

[21] D. Chen, S. Xu, Y. Kulkarni, Atomistic mechanism for vacancy-enhanced grain boundary migration, Physical Review Materials. 4 (2020) 1–9.

[22] T. Tsuru, Y. Shibutani, Y. Kaji, Fundamental interaction process between pure

edge dislocation and energetically stable grain boundary, Physical Review B - Condensed Matter and Materials Physics. 79 (2009) 1–4.

[23] D.W. Adams, D.T. Fullwood, R.H. Wagoner, E.R. Homer, Atomistic survey of grain boundary-dislocation interactions in FCC nickel, Computational Materials Science. 164 (2019) 171–185.

[24] T.R. Bieler, P. Eisenlohr, C. Zhang, H.J. Phukan, M.A. Crimp, Grain boundaries and interfaces in slip transfer, Current Opinion in Solid State and Materials Science. 18 (2014) 212–226.

[25] Z.H. Jin, P. Gumbsch, K. Albe, E. Ma, K. Lu, H. Gleiter, H. Hahn, Interactions between non-screw lattice dislocations and coherent twin boundaries in face-centered cubic metals, Acta Materialia. 56 (2008) 1126–1135.

[26] Z.H. Jin, P. Gumbsch, E. Ma, K. Albe, K. Lu, H. Hahn, H. Gleiter, The interaction mechanism of screw dislocations with coherent twin boundaries in different face-centred cubic metals, Scripta Materialia. 54 (2006) 1163–1168.

[27] E. Bayerschen, A.T. McBride, B.D. Reddy, T. Böhlke, Review on slip transmission criteria in experiments and crystal plasticity models, Journal of Materials Science. 51 (2016) 2243–2258.

[28] W. Yu, Z. Wang, Interactions between edge lattice dislocations and Σ11 symmetrical tilt grain boundaries in copper: A quasi-continuum method study, Acta Materialia. 60 (2012) 5010–5021.

[29] T.R. Bieler, P. Eisenlohr, C. Zhang, H.J. Phukan, M.A. Crimp, Grain boundaries and interfaces in slip transfer, Current Opinion in Solid State and Materials Science. 18 (2014) 212–226.

[30] S. Zghal, A. Coujou, A. Couret, Transmission of the deformation through γ-γ interfaces in a polysynthetically twinned TiAl alloy I. Ordered domain interfaces (120° rotational), Philosophical Magazine A: Physics of Condensed Matter, Structure, Defects and Mechanical Properties. 81 (2001) 345–364.

[31] S. Zghal, A. Couret, Transmission of the deformation through γ-γ interfaces in a polysynthetically twinned TiAl alloy II. Twin interfaces (180° rotational), Philosophical Magazine A: Physics of Condensed Matter, Structure, Defects and Mechanical Properties. 81 (2001) 365–382.

[32] T. Shimokawa, T. Kinari, S. Shintaku, Interaction mechanism between edge dislocations and asymmetrical tilt grain boundaries investigated via quasicontinuum simulations, Physical Review B - Condensed Matter and Materials Physics. 75 (2007) 1–11.

[33] W. Yu, Z. Wang, Interactions between edge lattice dislocations and Σ11 symmetrical tilt grain boundary: Comparisons among several FCC metals and interatomic potentials, Philosophical Magazine. 94 (2014) 2224–2246.

[34] M. Chassagne, M. Legros, D. Rodney, Atomic-scale simulation of screw dislocation/coherent twin boundary interaction in Al, Au, Cu and Ni, Acta Materialia. 59 (2011) 1456–1463.

[35] J.P. Hirth, J. Lothe, Theory of dislocation, Krieger Pub. Co, New York, 1982.

[36] L. Priester, Grain Boundaries and Crystalline Plasticity, ISTE Ltd and John Wiley & Sons, Inc, Hoboken,USA, 2011.

[37] J. Li, C. Lu, L. Pei, C. Zhang, R. Wang, Hydrogen-modified interaction between lattice dislocations and grain boundaries by atomistic modelling, International Journal of Hydrogen Energy. 45 (2020) 9174–9187.

[38] B. Kuhr, D. Farkas, I.M. Robertson, D. Johnson, G. Was, Stress Localization Resulting from Grain Boundary Dislocation Interactions in Relaxed and Defective Grain Boundaries, Metallurgical and Materials Transactions A: Physical Metallurgy and Materials Science. 51 (2020) 667–683.

[39] L. Zhang, Z. Li, J. Zheng, Y. Zhao, P. Xu, C. Zhou, C. Zhou, X. Chen, Dependence of hydrogen embrittlement on hydrogen in the surface layer in type 304 stainless steel, International Journal of Hydrogen Energy. 39 (2014) 20578–20584.

[40] H. Barthélémy, Hydrogen storage - Industrial prospectives, International Journal of Hydrogen Energy. 37 (2012) 17364–17372.

[41] H. Barthélémy, Effects of pressure and purity on the hydrogen embrittlement of steels, International Journal of Hydrogen Energy. 36 (2011) 2750–2758.

[42] I.M. Robertson, P. Sofronis, A. Nagao, M.L. Martin, S. Wang, D.W. Gross, K.E. Nygren, Hydrogen Embrittlement Understood, Metallurgical and Materials Transactions B: Process Metallurgy and Materials Processing Science. 46 (2015) 1085–1103.

[43] I.M. Robertson, The effect of hydrogen on dislocation dynamics, Engineering Fracture Mechanics. 68 (2001) 671–692.

[44] B.R.S. Da Silva, F. Salvio, D.S. Dos Santos, Hydrogen induced stress cracking in UNS S32750 super duplex stainless steel tube weld joint, International Journal of Hydrogen Energy. 40 (2015) 17091–17101.

[45] S.P. Lynch, Interpreting hydrogen-induced fracture surfaces in terms of deformation processes: A new approach, Scripta Materialia. 65 (2011) 851–854.

[46] J. Song, W.A. Curtin, Atomic mechanism and prediction of hydrogen embrittlement in iron, Nature Materials. 12 (2013) 145–151.

[47] J. Song, W.A. Curtin, A nanoscale mechanism of hydrogen embrittlement in metals, Acta Materialia. 59 (2011) 1557–1569.

[48] M.. Louthan, G.. Caskey, J.. Donovan, D.. Rawl, Hydrogen embrittlement of metals, Materials Science and Engineering. 10 (1972) 357–368.

[49] A. Nagao, C.D. Smith, M. Dadfarnia, P. Sofronis, I.M. Robertson, The role of hydrogen in hydrogen embrittlement fracture of lath martensitic steel, Acta Materialia. 60 (2012) 5182–5189.

[50] H.K. Birnbaum, P. Sofronis, Hydrogen-enhanced localized plasticity-a mechanism for hydrogen-related fracture, Materials Science and Engineering A. 176 (1994) 191–202.

[51] D.G. Xie, Z.J. Wang, J. Sun, J. Li, E. Ma, Z.W. Shan, In situ study of the initiation of hydrogen bubbles at the aluminium metal/oxide interface, Nature Materials. 14 (2015) 899–903.

[52] M. Li, D.G. Xie, E. Ma, J. Li, X.X. Zhang, Z.W. Shan, Effect of hydrogen on the integrity of aluminium-oxide interface at elevated temperatures, Nature Communications. 8 (2017) 1–7.

[53] G. Lu, E. Kaxiras, Hydrogen embrittlement of aluminum: The crucial role of vacancies, Physical Review Letters. 94 (2005) 1–4.

[54] S. Huang, D. Chen, J. Song, D.L. McDowell, T. Zhu, Hydrogen embrittlement of grain boundaries in nickel: An atomistic study, Npj Computational Materials. 3 (2017) 1–7.

[55] S. Hayakawa, H. Xu, Temperature-dependent mechanisms of dislocation–twin boundary interactions in Ni-based equiatomic alloys, Acta Materialia. 211 (2021) 116886.

[56] Z. Wu, H. Bei, G.M. Pharr, E.P. George, Temperature dependence of the mechanical properties of equiatomic solid solution alloys with face-centered cubic crystal structures, Acta Materialia. 81 (2014) 428–441.

[57] A. Gali, E.P. George, Tensile properties of high- and medium-entropy alloys, Intermetallics. 39 (2013) 74–78.

[58] F. Otto, A. Dlouhý, C. Somsen, H. Bei, G. Eggeler, E.P. George, The influences of temperature and microstructure on the tensile properties of a CoCrFeMnNi high-entropy alloy, Acta Materialia. 61 (2013) 5743–5755.

[59] L. Rémy, A. Pineau, Twinning and strain-induced f.c.c. → h.c.p. transformation on the mechanical properties of Co-Ni-Cr-Mo alloys, Materials Science and Engineering. 26 (1976) 123–132.

[60] H. Beladi, I.B. Timokhina, Y. Estrin, J. Kim, B.C. De Cooman, S.K. Kim, Orientation dependence of twinning and strain hardening behaviour of a high

manganese twinning induced plasticity steel with polycrystalline structure, Acta Materialia. 59 (2011) 7787–7799.

[61] J. Kacher, B.P. Eftink, B. Cui, I.M. Robertson, Dislocation interactions with grain boundaries, Current Opinion in Solid State and Materials Science. 18 (2014) 227–243.

[62] J.D. Livingston, B. Chalmers, Multiple slip in bicrystal deformation, Acta Metallurgica. 5 (1957) 322–327.

[63] D. Gottschalk, A. McBride, B.D. Reddy, A. Javili, P. Wriggers, C.B. Hirschberger, Computational and theoretical aspects of a grain-boundary model that accounts for grain misorientation and grain-boundary orientation, Computational Materials Science. 111 (2016) 443–459.

[64] P.C. Wo, A.H.W. Ngan, Investigation of slip transmission behavior across grain boundaries in polycrystalline Ni3Al using nanoindentation, Journal of Materials Research. 19 (2004) 189–201.

[65] Y. Guo, T.B. Britton, A.J. Wilkinson, Slip band-grain boundary interactions in commercial-purity titanium, Acta Materialia. 76 (2014) 1–12.

[66] J. Luster, M.A. Morris, Compatibility of deformation in two-phase Ti-Al alloys: Dependence on microstructure and orientation relationships, Metallurgical and Materials Transactions A. 26 (1995) 1745–1756.

[67] Z. Shen, R.. Wagoner, W.A.T. Clark, Dislocation pile-up and grain boundary interactions in 304 stainless steel, Scripta Metallurgica. 20 (1986) 921–926.

[68] T.C. Lee, I.M. Robertson, H.K. Birnbaum, Prediction of slip transfer mechanisms across grain boundaries, Scripta Metallurgica. 23 (1989) 799–803.

[69] Y. Shibutani, T. Hirouchi, T. Tsuru, Transfer and Incorporation of Dislocations to Σ3 Tilt Grain Boundaries under Uniaxial Compression, Journal of Solid Mechanics and Materials Engineering. 7 (2013) 571–584.

[70] T. Tsuru, Y. Shibutani, T. Hirouchi, A predictive model for transferability of

plastic deformation through grain boundaries, AIP Advances. 6 (2016) 0–9.

[71] E.A. West, G.S. Was, Strain incompatibilities and their role in intergranular cracking of irradiated 316L stainless steel, Journal of Nuclear Materials. 441 (2013) 623–632.

[72] J.R. Seal, M.A. Crimp, T.R. Bieler, C.J. Boehlert, Analysis of slip transfer and deformation behavior across the α/β interface in Ti-5Al-2.5Sn (wt.%) with an equiaxed microstructure, Materials Science and Engineering A. 552 (2012) 61–68.

[73] T.C. Lee, I.M. Robertson, H.K. Birnbaum, TEM in situ deformation study of the interaction of lattice dislocations with grain boundaries in metals, Philosophical Magazine A: Physics of Condensed Matter, Structure, Defects and Mechanical Properties. 62 (1990) 131–153.

[74] T.C. Lee, I.M. Robertson, H.K. Birnbaum, An HVEM In situ deformation study of nickel doped with sulfur, Acta Metallurgica. 37 (1989) 407–415.

[75] W.A.T. Clark, R.H. Wagoner, Z.Y. Shen, T.C. Lee, I.M. Robertson, H.K. Birnbaum, On the criteria for slip transmission across interfaces in polycrystals, Scripta Metallurgica et Materiala. 26 (1992) 203–206.

[76] D. V. Bachurin, D. Weygand, P. Gumbsch, Dislocation-grain boundary interaction in ⟨1 1 1⟩ textured thin metal films, Acta Materialia. 58 (2010) 5232–5241.

[77] S. Van Petegem, L. Li, P.M. Anderson, H. Van Swygenhoven, Deformation mechanisms in nanocrystalline metals: Insights from in-situ diffraction and crystal plasticity modelling, Thin Solid Films. 530 (2013) 20–24.

[78] H. Van Swygenhoven, S. Van Petegem, In-situ mechanical testing during X-ray diffraction, Materials Characterization. 78 (2013) 47–59.

[79] L. Patriarca, W. Abuzaid, H. Sehitoglu, H.J. Maier, Slip transmission in bcc FeCr polycrystal, Materials Science and Engineering A. 588 (2013) 308–317.

[80] M.D. McMurtrey, G.S. Was, B. Cui, I. Robertson, L. Smith, D. Farkas, Strain localization at dislocation channel-grain boundary intersections in irradiated

stainless steel, International Journal of Plasticity. 56 (2014) 219–231.

[81] W.Z. Abuzaid, M.D. Sangid, J.D. Carroll, H. Sehitoglu, J. Lambros, Slip transfer and plastic strain accumulation across grain boundaries in Hastelloy X, Journal of the Mechanics and Physics of Solids. 60 (2012) 1201–1220.

[82] C. Zambaldi, D. Raabe, Plastic anisotropy of c -TiAl revealed by axisymmetric indentation, Acta Materialia. 58 (2010) 3516–3530.

[83] J. Kacher, I.M. Robertson, Quasi-four-dimensional analysis of dislocation interactions with grain boundaries in 304 stainless steel, Acta Materialia. 60 (2012) 6657–6672.

[84] J.B. Singh, G. Molénat, M. Sundararaman, S. Banerjee, G. Saada, P. Veyssière, A. Couret, In situ straining investigation of slip transfer across α 2 lamellae at room temperature in a lamellar TiAl alloy, Philosophical Magazine Letters. 86 (2006) 47–60.

[85] M. Jin, A.M. Minor, D. Ge, J.W. Morris, Study of Deformation Behavior of Ultrafine-grained Materials Through in Situ Nanoindentation in a Transmission Electron Microscope, Journal of Materials Research. 20 (2005) 1735–1740.

[86] L. Wang, Y. Yang, P. Eisenlohr, T.R. Bieler, M.A. Crimp, D.E. Mason, Twin nucleation by slip transfer across grain boundaries in commercial purity titanium, Metallurgical and Materials Transactions A: Physical Metallurgy and Materials Science. 41 (2010) 421–430.

[87] L. Lu, R. Schwaiger, Z.W. Shan, M. Dao, K. Lu, S. Suresh, Nano-sized twins induce high rate sensitivity of flow stress in pure copper, Acta Materialia. 53 (2005) 2169–2179.

[88] X. Zhou, X. Li, K. Lu, Size Dependence of Grain Boundary Migration in Metals under Mechanical Loading, Physical Review Letters. 122 (2019) 1–6.

[89] Q. Qin, S. Yin, G. Cheng, X. Li, T.H. Chang, G. Richter, Y. Zhu, H. Gao, Recoverable plasticity in penta-twinned metallic nanowires governed by

dislocation nucleation and retraction, Nature Communications. 6 (2015).

[90] S. Yin, G. Cheng, T.H. Chang, G. Richter, Y. Zhu, H. Gao, Hydrogen embrittlement in metallic nanowires, Nature Communications. 10 (2019) 1–9.

[91] M.W. Barsoum, T. Zhen, S.R. Kalidindi, M. Radovic, A. Murugaiah, Fully reversible, dislocation-based compressive deformation of Ti 3SiC2 to 1 GPa, Nature Materials. 2 (2003) 107–111.

[92] H. Lim, M.G. Lee, J.H. Kim, B.L. Adams, R.H. Wagoner, Simulation of polycrystal deformation with grain and grain boundary effects, International Journal of Plasticity. 27 (2011) 1328–1354.

[93] M. Kuroda, Interfacial microscopic boundary conditions associated with backstress-based higher-order gradient crystal plasticity theory, Journal of Mechanics of Materials and Structures. 12 (2017) 193–218.

[94] M.E. Gurtin, A gradient theory of single-crystal viscoplasticity that accounts for geometrically necessary dislocations, Journal of the Mechanics and Physics of Solids. 50 (2002) 5–32.

[95] S. Wulfinghoff, E. Bayerschen, T. Böhlke, A gradient plasticity grain boundary yield theory, International Journal of Plasticity. 51 (2013) 33–46.

[96] E. Bayerschen, M. Stricker, S. Wulfinghoff, D. Weygand, T. Böhlke, Equivalent plastic strain gradient plasticity with grain boundary hardening and comparison to discrete dislocation dynamics, Proceedings of the Royal Society A: Mathematical, Physical and Engineering Sciences. 471 (2015) 20150388.

[97] D. Weygand, L.H. Friedman, E. Van der Giessen, A. Needleman, Aspects of boundary-value problem solutions with three-dimensional dislocation dynamics, Modelling and Simulation in Materials Science and Engineering. 10 (2002) 306.

[98] L. Zhang, Y. Xiang, Journal of the Mechanics and Physics of Solids Motion of grain boundaries incorporating dislocation structure, Journal of the Mechanics and Physics of Solids. 117 (2018) 157–178.

[99] Z. Li, C. Hou, M. Huang, C. Ouyang, Strengthening mechanism in micro-polycrystals with penetrable grain boundaries by discrete dislocation dynamics simulation and Hall – Petch effect, Computational Materials Science. 46 (2009) 1124–1134.

[100] X. Zhang, S. Lu, B. Zhang, X. Tian, Q. Kan, G. Kang, Dislocation–grain boundary interaction-based discrete dislocation dynamics modeling and its application to bicrystals with different misorientations, Acta Materialia. 202 (2021) 88–98.

[101] T.B. Britton, D. Randman, A.J. Wilkinson, Nanoindentation study of slip transfer phenomenon at grain boundaries, Journal of Materials Research. 24 (2009) 607–615.

[102] K.E. Aifantis, A.H.W. Ngan, Modeling dislocation-grain boundary interactions through gradient plasticity and nanoindentation, Materials Science and Engineering A. 459 (2007) 251–261.

[103] C. Huang, X. Peng, B. Yang, Y. Zhao, S. Weng, T. Fu, Investigation of interaction between dislocation loop and coherent twin boundary in BCC Ta film during nanoindentation, Nanomaterials. 7 (2017).

[104] M.D. Sangid, T. Ezaz, H. Sehitoglu, I.M. Robertson, Energy of slip transmission and nucleation at grain boundaries, Acta Materialia. 59 (2011) 283–296.

[105] P. Chen, F. Wang, B. Li, Dislocation absorption and transmutation at $\{101\bar{2}\}$ twin boundaries in deformation of magnesium, Acta Materialia. 164 (2019) 440–453.

[106] M.F.A. Ulrich Fred Kocks, Ali Suphi Argon, Thermodynamics and kinetics of slip, Oxford : Pergamon press, 1975.

[107] S. Glasstone, M. Glasstone, K.J. Laidler, N. Eyring, H. Eyring, ith J. Laidler, The Theory of Rate Processes: The Kinetics of Chemical Reactions, Viscosity, Diffusion and Electrochemical Phenomena, McGraw-Hill Book Company, 1941.

[108] G. Esteban-Manzanares, E. Martínez, J. Segurado, L. Capolungo, J. LLorca, An atomistic investigation of the interaction of dislocations with Guinier-Preston

zones in Al-Cu alloys, Acta Materialia. 162 (2019) 189–201.

[109] D. Chen, L.L. Costello, C.B. Geller, T. Zhu, D.L. McDowell, Atomistic modeling of dislocation cross-slip in nickel using free-end nudged elastic band method, Acta Materialia. 168 (2019) 436–447.

[110] P.A. Geslin, R. Gatti, B. Devincre, D. Rodney, Implementation of the nudged elastic band method in a dislocation dynamics formalism: Application to dislocation nucleation, Journal of the Mechanics and Physics of Solids. 108 (2017) 49–67.

[111] T. Zhu, J. Li, A. Samanta, A. Leach, K. Gall, Temperature and strain-rate dependence of surface dislocation nucleation, Physical Review Letters. 100 (2008) 1–4.

2. Fundamental theories and methods

Although a wealth of advanced experimental methods is increasingly applied in nano-scale experimental observations, the high price and the inability to directly observe the dynamic development details of the defect response still have many limitations in experimental observation, including the preparation of samples that meet the requirements and harsh test conditions. On the contrary, the application of computer simulation in materials science allows us to comprehend the nature of materials from the atomic and even electronic levels. The detailed interaction mechanisms can further be adopted in the FEM or 3d-DDD to extend the space and time scale.

In this chapter, the fundamental concepts of MD simulation will be introduced at the beginning. Then the transition state theory will be addressed, with the help of which we can directly and quantitatively compare the simulation to the realistic experimental data. The nudged elastic band (NEB) method and its developed versions will be used to identify the transition state. The methods for identifying and visualizing defects are also discussed briefly.

2.1. Molecular dynamics method

The MD method is an effective tool for investigating condensed matter features such as solid/liquid structure and surface interface energy. It is a deterministic method used to calculate the balance and transfer properties of a multi-body system. Since Alder and Wainwright proposed the hard spheres model to investigate the solid-liquid phase transition in 1957 [1,2], MD methods are gradually expanded and applied to different fields such as materials [3], physics [4], chemistry [5], biology, etc. With the significant advancements in computer technology, the time step of molecular dynamics simulation can now reach the femtosecond level, and the simulation system can be as small as a few

particles, as large as one million or even hundreds of millions of particles. Commercial software that realizes molecular dynamics calculations is also constantly developed and improved, such as LAMMPS [6], MS, NAMD, and AMBER.

2.1.1. Fundamental

The basic hypothesis of MD is that all the particles in the system obey the Newton's second law, namely,

$$F_i = m_i a_i \tag{2-1}$$

Where, F_i is the atomic force of the particle i, m_i is the mass and a_i is the acceleration defined by

$$a_i = \frac{d^2 r_i}{dt^2} \tag{2-2}$$

In Eq. (2-2), r_i represents the location of the particle and t represents time.

The interaction between particles is essentially given by the classical potential function, which satisfies the superposition principle. In this way, the force can be derived from the gradient of the interacting potential U, which is a function of atomic positions r_i of all the atoms in the system,

$$F_i = -\nabla U(r_1, r_2, r_3 \cdots, r_N) = -\frac{\partial U}{\partial r_i} \tag{2-3}$$

The above-mentioned fomulars can also be derived from the Lagrange motion equation. In Cartesian coordinates, we can get

$$\frac{d^2 r_i}{dt^2} = -\frac{1}{m_i}\frac{\partial U}{\partial r_i} \tag{2-4}$$

Because Eq. (2-4) describes the relationship between atomic trajectories and potential energy, the accuracy of the simulation is highly dependent on the interacting potential

files. To obtain the position and velocity of the atom at any moment, one just need to time-integrate Eq. (2-1) and Eq. (2-4) with a given initial position and velocity, as

$$\begin{aligned} v_i &= v_i^0 + a_i t \\ r_i &= r_i^0 + v_i^0 t + \frac{1}{2} a_i t^2 \end{aligned} \tag{2-5}$$

2.1.2. Integration algorithms

When considering the couple nature of the atomic motions in the polyatomic system, it is hard or impossible to find an analytical solution to the equation of motion, such as Eq. (2-4). MD methods usually use the finite difference method to solve the equations of motion. Time is discretized so that the trajectory of the particles can be approximated gradually. Following this idea, several representative integration algorithms have been proposed, such as Verlet algorithm [7–9], Beeman algorithm, Gear algorithm, etc.

Taking Verlet algorithm as a reference, this method was first used in MD by Verlet, and its basic ideas are that the locations are represented by two third-order Taylor expansions. One part is a forward time-step $t - \Delta t$ and another is a backward time-step $t + \Delta t$,

$$r(t+\Delta t) = r(t) + v(t)\Delta t + \frac{1}{2!}\frac{dv(t)}{dt}(\Delta t)^2 + \frac{1}{3!}\frac{d^2v(t)}{dt^2}(\Delta t)^3 + O[(\Delta t)^4] \tag{2-6}$$

$$r(t-\Delta t) = r(t) - v(t)\Delta t + \frac{1}{2!}\frac{dv(t)}{dt}(\Delta t)^2 - \frac{1}{3!}\frac{d^2v(t)}{dt^2}(\Delta t)^3 + O[(\Delta t)^4] \tag{2-7}$$

Combining Eq. (2-1), (2-6) and (2-7), the formula can be reduced to,

$$r(t+\Delta t) = 2r(t) - r(t-\Delta t) + \frac{F(t)}{m}(\Delta t)^2 + O[(\Delta t)^4] \tag{2-8}$$

Additionally, the velocities can be evaluated from the positions by using,

$$v(t) = \frac{r(t+\Delta t) - r(t-\Delta t)}{2\Delta t} \tag{2-9}$$

Verlet algorithm is simple to execute and can retrieve particle coordinates, velocity, and force in a synchronous manner. The truncate error in calculated positions is of the

order of $(\Delta t)^4$ and the corresponding error related to velocity is of the order of $(\Delta t)^2$. In the integrating process, the positions and velocities of the particles at current and previous step should be given first, and then the force is calculated at the current step. The new position in the next time-step can be derived from Eq. (2-8). Repeat the above steps until the preset integration time is reached.

Similarly, the Leap-frog Verlet algorithm [10] calculates the velocities and positions at time $t+\Delta t/2$, resulting in

$$\begin{aligned} r(t+\Delta t) &= r(t)+v(t+\Delta t/2)\Delta t \\ v(t+\Delta t/2) &= v(t-\Delta t/2)+a(t)\Delta t \\ v(t) &= \frac{1}{2}\left[v(t-\Delta t/2)+v(t+\Delta t/2)\right] \end{aligned} \tag{2-10}$$

The advantage of this algorithm is that we do not need to take the difference of two large values to get a small one (therefore no loss of precision), and the velocities are explicitly calculated. The downside is that they are not calculated at the same time as the positions.

To avoid position and velocity being out of sync without compromising accuracy,, Velocity Verlet algorithm [7] was proposed and it utilizes position, velocity and acceleration simultaneously, as Eq. (2-11). The velocity Verlet algorithm inherits the advantages of previous methods with reasonable accuracy. However, it still shows high fluctuations in total energy.

$$\begin{aligned} r(t+\Delta t) &= r(t)+v(t)\Delta t+\frac{1}{2}\Delta t^2 a(t) \\ v(t+\Delta t) &= v(t)+\frac{1}{2}\Delta t\left[a(t)+a(t+\Delta t)\right] \end{aligned} \tag{2-11}$$

2.1.3. Interatomic potentials

As mentioned above, the key of MD simulation is to solve the motion trajectory of atoms through the interaction among atoms. The potential function determines the mutual

responses and thus fundamentally determines all the properties of materials. Therefore, potential function is very important for MD simulation, the workload of calculation and the reliability of simulation results are highly dependent on the selection of potential function. Potential functions can be empirical, semi-empirical, or calculated using quantum mechanics. With the development of recent decades, some potential functions that can simulate specific materials in a more realistic way have been developed.

In the early stage of MD simulations, Lennard-Jones (LJ) potential was extensively used to mimic the atomic behaviors of noble gases and liquids [11,12]. The pairwise interaction between two particles separated by distance *r* is described as,

$$U_{LJ}(r) = \varepsilon_0 \left[\left(\frac{r_0}{r} \right)^m - \frac{m}{n} \left(\frac{r_0}{r} \right)^n \right] \tag{2-12}$$

where m and n are dependent on the elements. ε_0 can be treated as the chemical bond strength and r_0 is defined as the equilibrium bond distance. These parameters can be fitted to reproduce experimental data or first principles calculations.

Although the pair potential may accurately imitate the features of noble gases, the electron cloud distribution in metals can be considerably influenced by the surrounding atoms and the interaction force between the atoms is accordingly changed. Pair potential is no longer applicable to the metal materials. This challenge was successfully handled by the emergence of many-body potential.

Common choices for the semi-empirical many body potentials are those based on the embedded atom method (EAM) which is first proposed by Daw in 1984 [13]. For the EAM, the metal is treated as positively charged ions “embedded” in a local electron density. The energy of the system therefore derives from an embedding energy as well as the ion core repulsion. This potential is basically based on the concept of local density which allows one to account for the dependence of the individual bond strength on the local environment. The total energy, therefore, is given by

$$E = \frac{1}{2}\sum_{i \neq j} \varphi_{ij}(r_{ij}) + \sum_{i} F(\bar{\rho}_i)$$
$$\bar{\rho}_i = \sum_{i \neq i} \rho_j(r_{ij}) \tag{2-13}$$

Here, $\varphi_{ij}(r_{ij})$ is the core-to-core repulsive energy between atom *i* and *j* separated by distance *r*. The second term $F(\bar{\rho}_i)$ is the energy for embedding atom *i* into the electron density $\bar{\rho}_i$. The electron density follows a linear superposition rule to account for the surrounding atoms. The embedding energies and pair interactions are usually determined empirically by fitting to various bulk properties or density functional theory (DFT) calculations. The EAM potential has been widely used and gives a good description of many bulk effects, such as phonon spectra, thermal expansion, and elastic constants, and a fair description of many surface effects. Therefore, in this dissertation, EAM potential is used to simulate behaviors of Cu, Al, and other FCC metals. It is also worth noting that the modified embedded atom method (MEAM) [14], embedded-defect method (EDM) [15], Angular-Dependent Potential (ADP) [16], and Tersoff potential [17] are also widely used in metal simulations.

2.1.4. Ensemble, temperature and pressure control

The positions, velocities and atomic force of the particles can be directly produced in the MD simulations. However, macroscopic quantities like as temperature, pressure, and so on cannot be directly approximated. Fortunately, statistical mechanics provides the mathematical expressions that connect macroscopic phenomena to the motion and distribution of individual particles in the system. A collection of points in phase space satisfying the conditions of a particular thermodynamic state is called an ensemble. In statistical mechanics, common ensembles are: the microcanonical ensemble, the canonical ensemble and the grand canonical ensemble.

(1) *NVE Ensemble (microcanonical ensemble).*

NVE ensemble is used to study the properties of isolated, conservative systems, which have no exchange of energy with the outside world and conserve the number of particles (N), volume (V), and total energy (E). The particles in the NEV ensemble only contain the exchange of potential and kinetic energies and follow the Newton's second law without any temperature and pressure control.

(2) *NVT Ensemble (canonical ensemble)*

In this ensemble, the temperature, volume and number of particles are assumed to be constant. The temperature of the system is controlled through a heat bath and energy is exchanged between the particles in system and the virtual particles in the heat bath. Generally, temperature control algorithms include Velocity Rescaling, Berendsen Thermostat [18], Andersen Thermostat [19] and Nosé-Hoover Thermostat [20]. The detailed information about Nosé-Hoover thermostat will be given later.

(3) *NPT Ensemble (isothermal-isobaric)*

The isothermal-isobaric ensemble allows temperature and pressure to be controlled simultaneously. A 'pressure bath' is required in addition to a 'heat bath'. It corresponds most closely to experimental conditions where the temperature and pressure are typically kept fixed. Since the pressure P of the system is conjugated to its volume V, the pressure value can be adjusted by adjusting the volume or shape of the original cell.

(4) μVT *Ensemble (grand canonical)*

The grand canonical ensemble is a generalization of the canonical ensemble where the restriction to a definite number of particles in the system is removed. It describes systems in contact with a 'heat bath' at temperature T and a particle reservoir that maintains the chemical potential μ. The system not only exchanges heat with the 'heat bath' but also exchanges particles with the reservoir. The volume keeps constant, but the number of particles and energy fluctuate around thermal equilibrium.

(5) *Temperature and thermostat method*

In the MD simulation, the temperature is related to the movement of the particles. For an equilibrium system with a constant temperature T, the kinetic energy obeys,

$$\left\langle \frac{1}{2}mv^2 \right\rangle = \frac{3}{2}k_B T \tag{2-14}$$

k_B is the Boltzmann constant. Additionally, if the momentum of system is set as zero or constant, the DoF of the N-particle system is $N_{DoF} = 3N - 3$, and hence, the temperature is deduced from Eq. (2-14) as,

$$T = \frac{1}{(3N-3)k_B}\sum_i m_i v_i^2 \tag{2-15}$$

Temperature can be controlled through several algorithms, and the Velocity Rescaling method is the most straightforward and simplest way among them. In this method, the velocity of each particle is directly rescaled through the pre-factor λ, as

$$\begin{aligned} v_i^0(t) &= \lambda v_i(t) \\ \lambda &= \sqrt{\frac{T_0}{T}} \end{aligned} \tag{2-16}$$

Through this way, the temperature can be arbitrarily and rudely rescaled from current T to desired T_0. But it does not follow the NVE ensemble and may not provide the correct statistical measures.

Aside from Velocity Rescaling, there is a deterministic and sophisticated method, Nosé-Hoover Thermostat [20]. In this scheme, the physical system is brought in contact with an imaginary external heat bath and exchanges energy with it, as shown in Fig. 2-1.

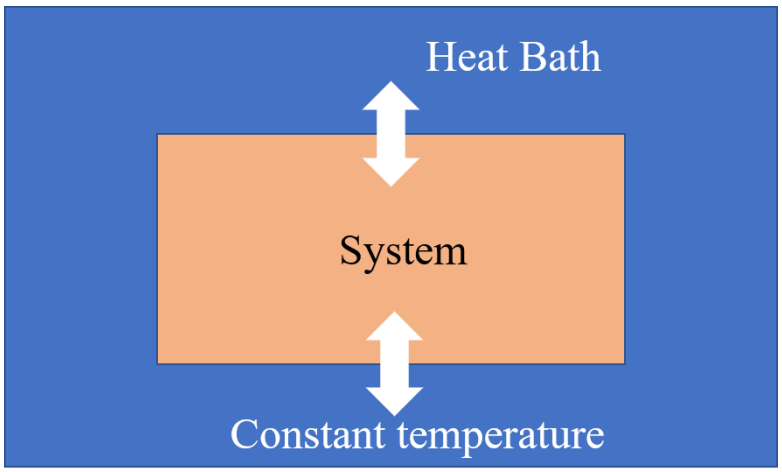

Fig. 2-1 Nosé-Hoover Thermostat. Heat exchanges between the system and imaginary external heat bath

The energy of the physical system fluctuates in a Nosé-Hoover thermostat, but the energy of the system plus the energy of the thermal bath is conserved. The Hamiltonian is written as

$$H_{N-H} = \sum_{i=1}^{N} \frac{1}{2} m_i v_i^2 + E(tot) + \frac{Q}{2} \xi^2 + N_f k_B T_0 \ln s \tag{2-17}$$

Here, $E(tot)$ is the total energy of the system, N_f is the number of degrees of freedom in the physical system, s is the additional DoF introduced by the heat bath, k_B is the Boltzmann constant, Q is the effective Mass and ξ is a time dependent friction coefficient. When the system temperature is greater than the target temperature, ξ increases, thus reducing the atomic velocity and the system temperature. Conversely, when the system temperature is lower than the target temperature, ξ decreases, thereby increasing the atomic velocity and the system temperature. The nose-Hoover method can produce a more realistic NVT ensemble, so that it is widely used in simulation systems.

(6) Pressure and barostat

Similarly, the pressure P of the system can be defined as

$$PV = Nk_BT + \frac{1}{3}\left\langle \sum_i r_i \cdot F_i \right\rangle \tag{2-18}$$

Here, V is the volume of the system and F is the atomic force, r is the position.

The existing barostat techniques mainly include three methods: Berendsen[18], Anderson [19] and Parrinello-Rahman[21]. Among them, Andersen method assumes that the system is connected to the outside world through a piston, as shown in Fig. 2-2.

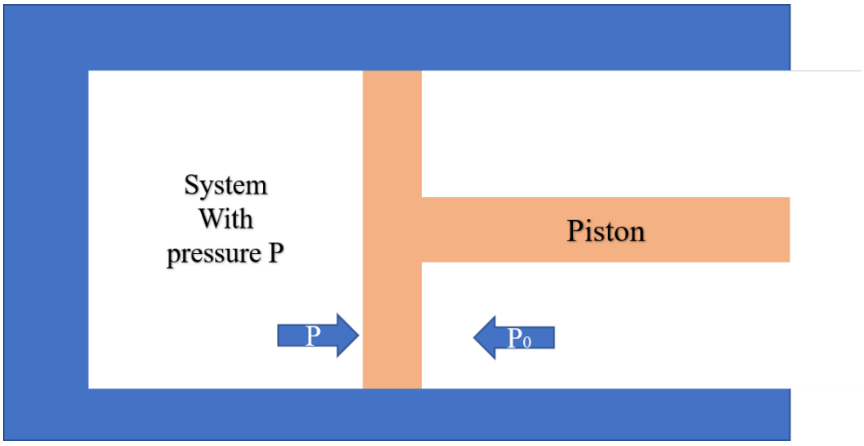

Fig. 2-2 Schematic of the Molecular Dynamics simulation at constant pressure

When the external pressure is unbalanced with the pressure generated inside the simulated system, the piston makes the system expand or contract uniformly, and finally, the internal and external pressures of the system are equal. The Hamiltonian of the composite system composed of the simulated system and the piston is

$$H = \sum_{i=1}^{N} \frac{P_i^2}{2m_iL^2} + E(tot) + \frac{p_{vpiston}^{\ 2}}{2Q} + P_0V \tag{2-19}$$

here, L is the length of the original system, $p_{vpiston}$ and Q are the momentum and mass of the piston, P_0 is the desired pressure and V is the volume.

2.1.5. Time step and boundary condition

As described in Section 1.2.2, the timestep Δt significantly influences the results and accuracy of the simulation. A larger timestep will, of course, expand the time scale simulated for the system, but it will also reduce the accuracy, which may result in some unreasonable phenomena. Worse, the computation will not converge, reducing computational efficiency. A small timestep will reflect a more accurate results, however it may consume too many computational resources to get a desired time scale. Therefore, an appropriate timestep of 1fs are used in this work.

In most cases, the target of molecular dynamics simulation is to examine the properties of an infinite molecular system under certain structural conditions, such as the concentration of particular species in a bulk compound. Simulation of that infinite system is impossible without any confinement to the size of the system. In order to overcome such length scale problem, it is essential to choose boundary conditions that mimic the presence of an infinite bulk surrounding the *N*-particle system. To solve this problem, the periodic boundary condition (PBC) is proposed. As a consequence, an atom leaving the box to the right via one boundary can be identified with an atom entering the box from the left at the opposite boundary. There is a problem that needs to be paid attention to in the actual calculation. Due to the consideration of the cut-off radius of the potential energy and the interaction of the particles, the size of the primitive cell must be greater than twice the cut-off radius of the potential function, so that the particle *i* cannot interact with the *j* particle and its mirror image at the same time.

2.2. Transition state theory and NEB method

Although MD simulation can provide a wealth of important information about defect interactions, one major drawback is that the extremely high strain rate applied to the system makes the results hard to compare with the realistic experimental data. Hence, a

very narrow time scale, of picosecond to nanosecond at most, limits the application scope of the MD method. On the contrary, many defect interactions or evolutions, such as the dislocation slip, dislocation-precipitate interaction, GB migration and dislocation-GB interaction, are treated as thermally activated and can be precisely described by the transition state theory (TST). In TST, the energy barrier is more important than the CRSS, and it can be determined by sampling the minimum energy path (MEP). This path is the way most likely to occur. Actually, there are many alternative paths in the state transition process and, correspondingly, different energy barriers need to be overcome. MEP is, thus, the one with the lowest energy barrier.

Therefore, in the TST, the most important issue is to find the MEP, in which the peak is defined as the saddle point. The MEP further provides information on energy barrier and the atomic configurations of the saddle point as well as the configurations along the evolution path.

2.2.1. Transition state theory

As the physical meaning of the atomic simulations is difficult to quantitatively compare with the experiments, TST provide another way to estimate the unit interaction process [22–24]. For the thermally activated process such as the dislocation slip and defects interaction, TST establishes the corresponding transition rate Γ at the constant stress state by [25]

$$\Gamma = \nu \exp(\frac{\Delta G(\tau)}{k_B T}) \tag{2-20}$$

where, k_B is the Boltzmann constant, T is the absolute temperature, ν is the fundamental attempt frequency usually at the order of $10^{11} \sim 10^{12} / s$, ΔG is the activation Gibbs free energy which depend on the shear stress τ, temperature and system size. Obviously, the determination of ΔG is the fundamental task for estimating the

transition rate in TST and is depends on the specific activation processes of the defect interaction. Qualitatively, the higher the temperature, the greater the stress, and the lower the energy required, and vice versa [4].

2.2.2. NEB method

(1) NEB and CINEB method

To find the transition state of the unit interaction process, many chain-of-states methods have been proposed to search the MEP by inserting a serial of internal images, called replica, between the initial state and final state. Many methods, such as the drag method, plane elastic band, Elber-Karplus method, and self-penalty walk, have been utilized [26–28]. However, Nudged Elastic Band (NEB) and its metamorphoses, such as Climbing image NEB (CI-NEB) [29] and Free end NEB (FENEB) [23], are currently the most efficient and program-friendly methods.

In the standard NEB estimation, several intermediate states are created by a linear interpolation process between the initial and final state. Meanwhile, the initial state R_0 and final state R_N should be given first and they should be at their own equilibrium state. The *N*-1 intermediate images, namely $[R_1, R_2, \cdots, R_{N-1}]$, are connected by the elastic bands. The whole system will be treated as the first guess of MEP and will be subsequently adjusted by the dynamic minimized algorithm, like quick-min and FIRE method.

As shown in Fig. 2-3, because the replicas are connected by the elastic band and affected by the potential force from the surrounding atoms, the total force $\mathbf{F}_i^{NEB}$ acting on an image is the sum of the spring force along the local tangent $\mathbf{F}_i^{s||}$ and the true force perpendicular to the local tangent $\mathbf{F}_i^{\perp}$, as

$$\mathbf{F}_i^{NEB} = \mathbf{F}_i^{s||} + \mathbf{F}_i^{\perp} = \mathbf{F}_i^{s||} - \nabla U(R_i)\big|_{\perp} \tag{2-21}$$

where, the true force is controlled by the potential function U, as

$$-\mathbf{F}_i^{\perp} = \nabla U(R_i)\big|_{\perp} = \nabla U(R_i) - \nabla U(R_i)\cdot\hat{\boldsymbol{\tau}}_i \tag{2-22}$$

$\hat{\boldsymbol{\tau}}_i$ is the normalized local tangent at replica i. Correspondingly, the spring force is

$$\mathbf{F}_i^{s||} = k(\left|R_{i+1} - R_i\right| - \left|R_i - R_{i-1}\right|)\hat{\boldsymbol{\tau}}_i \tag{2-23}$$

k is the spring constant. Conventionally, the whole replicas will converge to the MEP with proper minimization. However, the saddle point may need estimated by interpolate the current MEP if none of the replicas represents the saddle point in the standard NEB method. Henkelman proposed the CI-NEB method to predict a more accurate MEP based on the results of standard NEB method [29]. The replica with the highest energy obtained from standard NEB is reapplied by a new climbing force

$$\mathbf{F}_{i\max} = -\nabla U(R_{i\max}) + 2U(R_{i\max})\cdot\hat{\boldsymbol{\tau}}_{i\max}\hat{\boldsymbol{\tau}}_{i\max} \tag{2-24}$$

Obviously, the maximum energy replica is not affected by the spring force but the other replicas follow the way depicted in Eq. (2-21). Qualitatively, the highest energy replica climbs up along the potential surface along the elastic band and once the results converge, the highest energy replica will station near the saddle point in which way the CINEB estimate a more precise MEP without adding any significant computational effort.

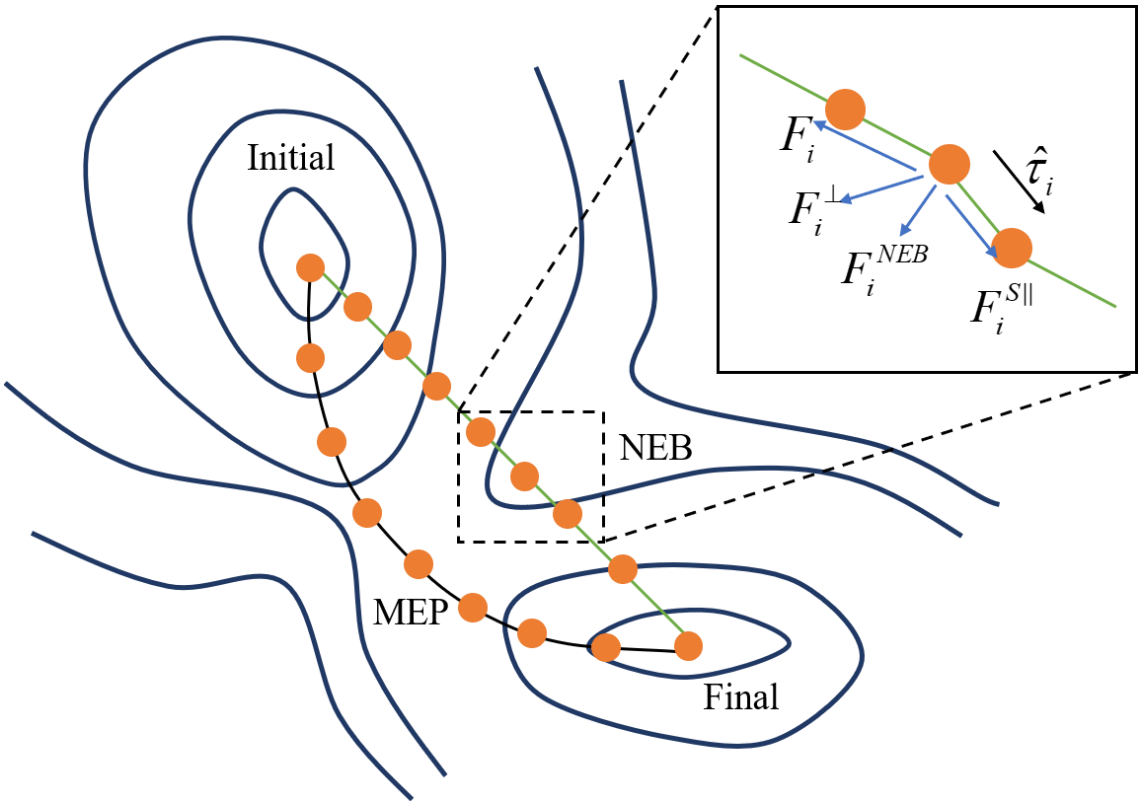

Fig. 2-3 Two components make up the nudged elastic band force: the spring force $\mathbf{F}_i^{s\|}$, along the tangent $\hat{\boldsymbol{\tau}}_i$, and the perpendicular force due to the potential $\mathbf{F}_i^{\perp}$.

Additionally, the normalized local tangent $\hat{\boldsymbol{\tau}}_i$ can be obtained as,

$$\hat{\boldsymbol{\tau}}_i = \begin{cases} \hat{\boldsymbol{\tau}}_i^{+} = R_{i+1} - R_i & \text{if } U_{i+1} > U_i > U_{i-1} \\ \hat{\boldsymbol{\tau}}_i^{-} = R_i - R_{i-1} & \text{if } U_{i+1} < U_i > U_{i-1} \end{cases}$$

$$\textit{else} \tag{2-25}$$

$$\hat{\boldsymbol{\tau}}_i = \begin{cases} \hat{\boldsymbol{\tau}}_i^{+} \Delta U_i^{\max} + \hat{\boldsymbol{\tau}}_i^{-} \Delta U_i^{\min} & \text{if } U_{i+1} > U_{i-1} \\ \hat{\boldsymbol{\tau}}_i^{+} \Delta U_i^{\min} + \hat{\boldsymbol{\tau}}_i^{-} \Delta U_i^{\max} & \text{if } U_{i+1} < U_{i-1} \end{cases}$$

Where,

$$\begin{aligned} \Delta U_i^{\max} &= \max(|U_{i+1} - U_i|, |U_{i-1} - U_i|) \\ \Delta U_i^{\min} &= \min(|U_{i+1} - U_i|, |U_{i-1} - U_i|) \end{aligned} \tag{2-26}$$

The reaction path defined in this way can ensure the equidistant distribution of the image in space.

(2) Free end NEB method

Although it is convenient to find the MEP and saddle point for a system with a small number of atoms, such as lattice diffusion, with the NEB or CINEB method, it is still inefficient or inaccurate to investigate the evolution process under high stress or strain state. Because the potential surface is so severely distorted by the stress that the saddle point comes very close to the initial point. This may cause an inaccurate estimation of the MEP because of the lack of resolution. As illustrated in Fig. 2-4 (a), with the applied load increasing from S_1 to S_{ath}, the energy landscape will be distorted and the saddle point (gray circle) comes closer to the initial state (white circle) which may need a large number of replicas to depict the whole MEP from initial to final state (black circle). To save the computational recourses and increase the efficiency, Zhu proposed the Free end NEB (FENEB). In this method, the whole elastic band is cut short and meanwhile it allows the end of the cut chain to swing along an energy contour to keep the energy constant during the minimization. Therefore, FENEB does not request the final configuration to stay at the equilibrium state but rather converge to the MEP like the other intermediate replica in the chain. Dissimilar to the NEB or CINEB method, the end of the chain still feels a virtual force, as [23]

$$\mathbf{F}_N = \mathbf{k}_N - \frac{((\mathbf{k}_N \cdot \nabla U(R_N))\nabla U(R_N)}{\left|\nabla U(R_N)\right|^2} \tag{2-27}$$

$\mathbf{k}_N$ is the spring force delivered from replica R_{N-1}.

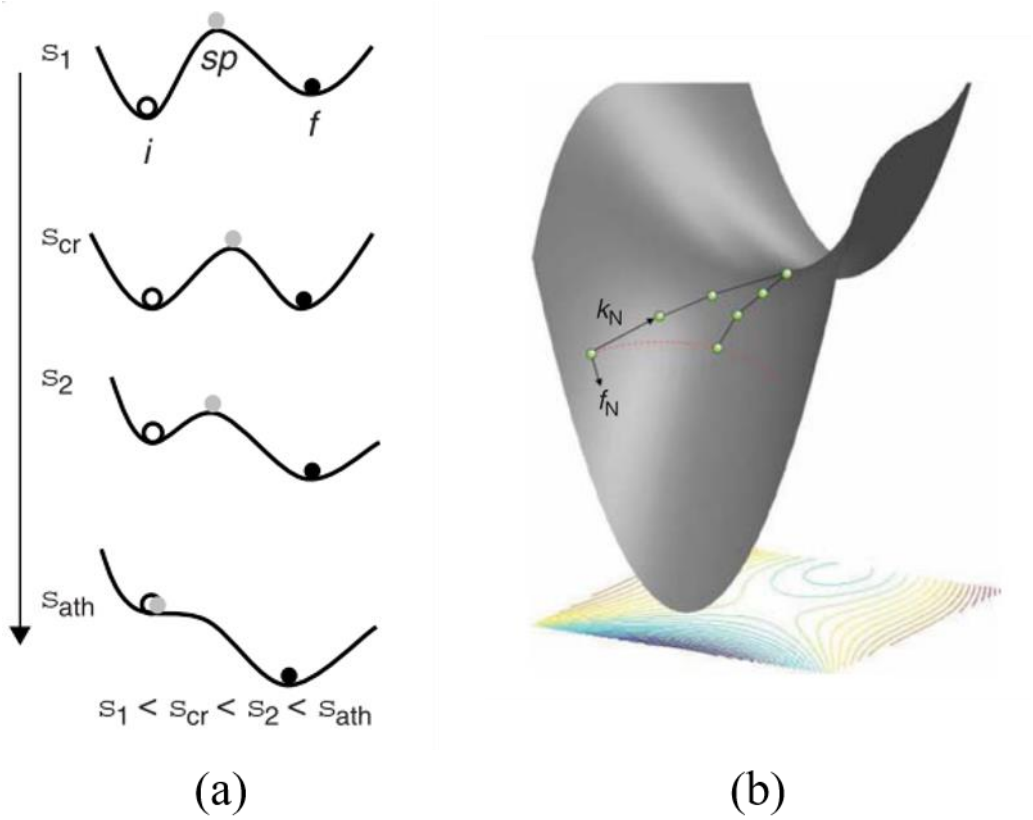

Fig. 2-4 (a) Energy landscape at different applied loads, the white circle represents the initial state *i*, black circle is the final state *f* and gray circle corresponds to the saddle-point. (b) Illustration of the method showing one end of the elastic band is fixed and the other is freely moved along an energy contour [4].

2.2.3. Activation volume and strain rate sensitivity

(1) Activation volume

The activation volume is usually defined as [4,5,30],

$$V_{stress} = -\frac{\partial \Delta G(\sigma)}{\partial \sigma} \tag{2-28}$$

Physically, the activation volume represents the amount of atoms which are related to the thermally activated process. The corresponding atoms should be activated and hence in the high energy state. This parameter fundamentally distinguishes the different

mechanisms of transition process and it will keep constant if the stress does not change too much, as shown in Fig. 2-5. For example, lattice diffusion would give an activation volume of about $0.1b^3$ because only a small group of atoms are involved during the diffusion process. However, for a forest cutting process, such as the Orowan looping of a dislocation line across the pinning points in coarse-grained metal, the activation volume can reach about 1000 b^3 [4]. A normal dislocation-interface mediated process usually has an apparent activation volume of 10-100 b^3.

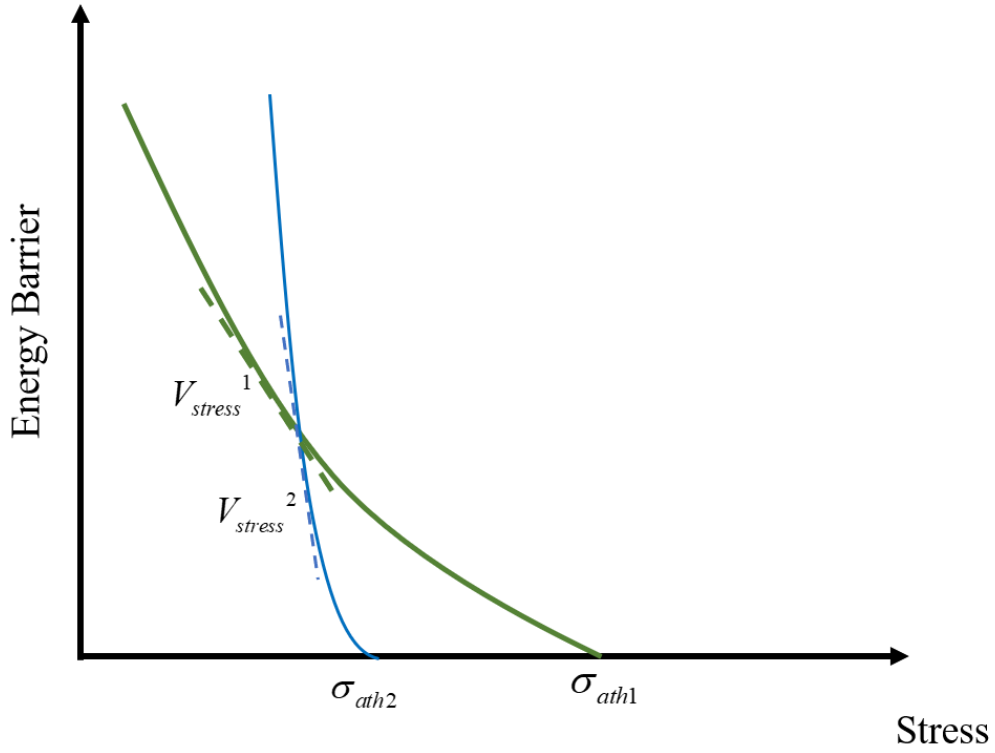

Fig. 2-5 Schematic of the stress-dependent activation energy for two competing thermally activated processes. The activation volumes are significantly different although the activation energy may be the same at the cross point.

(2) Strain rate sensitivity

The strain rate sensitivity (SRS) *m* is usually used to describe the relationship between strain rate and the flow stress in the experiments. Definition of SRS is based on

incremental changes in strain rate during tests performed at a fixed temperature and fixed microstructure, to determine corresponding changes in flow stress. m is defined as,

$$m = \frac{\partial \ln \sigma}{\partial \ln \varepsilon}|_T \tag{2-29}$$

The magnitude of m is in the range of 0~1, where 0 represents rate independent behaviors and 1 represents the linear Newtonian flow. Further analysis will give,

$$m = \frac{\sqrt{3} k_B T}{V_a \sigma} \tag{2-30}$$

Here, V_a is the apparent activation volume and is different from the value obtained from V_{stress}. Because V_{stress} is estimated for the single or bi-crystal model and V_a represents the nature of the polycrystalline bulk materials. To connect these two different activation volumes, the Taylor factor $M = 3.1$ is introduced to transfer the stress for single or bi-crystal to that for the polycrystalline materials, and we can get,

$$V_a = \frac{\sqrt{3}}{M} V_{stress} \tag{2-31}$$

It is worth mentioning that this derivation is based on tensile stress. Things would be a little different if we consider the transformation process from shear stress in simulation to the tensile stress in experiments. We will discuss this part in the later section. Through this way, we can successfully link the MD and NEB simulations to the real experiments and quantitatively estimate the simulation results.

2.3. Crystal defect analysis method

To identify and visualize the defects, such as GBs, dislocations, and stacking fault (SF), several methods can be implemented.

(1) Centrosymmetric parameters (CSP)

CSP was proposed by Kelchner [31], as

$$P_{CSP} = \sum_{i=1}^{N} \left| \mathbf{r}_i + \mathbf{r}_{i+N/2} \right|^2 \tag{2-32}$$

where $\mathbf{r}_i$ and $\mathbf{r}_{i+N/2}$ are two neighbor vectors from the central atom to a pair of opposite neighbor atoms. Generally, N is 12 for the FCC material and N is 8 for body-centered cubic (BCC) material. If the atom is in the perfect FCC lattice and the ideal centrosymmetric crystal will be fulfilled. Therefore, the contribution of all neighbor atoms calculated by Eq. (2-32) will be eliminated by each other. A value larger than zero indicates the existence of the defects.

(2) Common neighbor analysis (CNA)

CNA was proposed by Honeycutt in 1987 [32]. The CAN calculates the fingerprint for pairs of atoms, which is designed to characterize the local structural environment. According to this method, a fourth order parameter (*ijkl*) is used to illustrate the state of the atom. *i* judges whether the two atoms are the nearest neighbor atom pair, *j* determines the number of nearest neighbors shared by an atom pair, *k* represents the number of bonds between the shared nearest neighbors; *l* represents the number of bonds on the longest chain among the bonds of the shared nearest neighbors.

(3) Dislocation analysis (DXA)

DXA was proposed by Stukowski and Albe [33]. The DXA transforms the original atomistic representation of a dislocated crystal into a line-based representation of the dislocation network. It determines the Burgers vector of each dislocation and identifies dislocation junctions. The algorithm can recognize partial dislocations and also certain secondary grain boundary dislocations (e.g. twinning dislocations in FCC) [33]. The defect identification process was realized by Ovito Software [34].

References

[1] B.J. Alder, T.E. Wainwright, Studies in Molecular Dynamics. I. General Method, The Journal of Chemical Physics. 31 (1959) 459–466.

[2] B.J. Alder, T.E. Wainwright, Phase Transition for a Hard Sphere System, The Journal of Chemical Physics. 27 (1957) 1208–1209.

[3] T. Tsuru, Y. Shibutani, Y. Kaji, Fundamental interaction process between pure edge dislocation and energetically stable grain boundary, Physical Review B - Condensed Matter and Materials Physics. 79 (2009) 1–4.

[4] T. Zhu, J. Li, S. Yip, Atomistic Reaction Pathway Sampling: The Nudged Elastic Band Method and Nanomechanics Applications, in: Nano Cell Mech., John Wiley & Sons, Ltd, Chichester, UK, 2012: pp. 311–338.

[5] T. Zhu, J. Li, X. Lin, S. Yip, Stress-dependent molecular pathways of silica-water reaction, Journal of the Mechanics and Physics of Solids. 53 (2005) 1597–1623.

[6] S. Plimpton, Fast parallel algorithms for short-range molecular dynamics, Journal of Computational Physics. 117 (1995) 1–19.

[7] W.C. Swope, H.C. Andersen, P.H. Berens, K.R. Wilson, A computer simulation method for the calculation of equilibrium constants for the formation of physical clusters of molecules: Application to small water clusters, The Journal of Chemical Physics. 76 (1982) 637–649.

[8] L. VERLET, Computer “Experiments” on Classical Fluids. II. Equilibrium Correlation Functions, Physical Review. 165 (1968) 201–214.

[9] L. Verlet, Computer “Experiments” on Classical Fluids. I. Thermodynamical Properties of Lennard-Jones Molecules, Physical Review. 159 (1967) 98–103.

[10] R.W. Hockney, The potential calculation and some applications, Methods in Computational Physics. 9 (1970) 135–211.

[11] A. Rahman, F.H. Stillinger, Molecular Dynamics Study of Liquid Water, The Journal of Chemical Physics. 55 (1971) 3336–3359.

[12] A. Rahman, Correlations in the Motion of Atoms in Liquid Argon, Physical Review. 136 (1964) A405–A411.

[13] M.S. Daw, M.I. Baskes, Semiempirical, Quantum Mechanical Calculation of Hydrogen Embrittlement in Metals, Physical Review Letters. 50 (1983) 1285–1288.

[14] M.I. Baskes, Modified embedded-atom potentials for cubic materials and impurities, Physical Review B. 46 (1992) 2727–2742.

[15] R. Pasianot, D. Farkas, E.J. Savino, Empirical many-body interatomic potential for bcc transition metals, Physical Review B. 43 (1991) 6952–6961.

[16] Y. Mishin, M.J. Mehl, D.A. Papaconstantopoulos, Phase stability in the Fe–Ni system: Investigation by first-principles calculations and atomistic simulations, Acta Materialia. 53 (2005) 4029–4041.

[17] J. Tersoff, Empirical interatomic potential for silicon with improved elastic properties, Physical Review B. 38 (1988) 9902–9905.

[18] H.J.C. Berendsen, J.P.M. Postma, W.F. van Gunsteren, A. DiNola, J.R. Haak, Molecular dynamics with coupling to an external bath, The Journal of Chemical Physics. 81 (1984) 3684–3690.

[19] H.C. Andersen, Molecular dynamics simulations at constant pressure and/or temperature, The Journal of Chemical Physics. 72 (1980) 2384–2393.

[20] W.G. Hoover, Canonical dynamics: Equilibrium phase-space distributions, Physical Review A. 31 (1985) 1695–1697.

[21] M. Parrinello, A. Rahman, Polymorphic transitions in single crystals: A new molecular dynamics method, Journal of Applied Physics. 52 (1981) 7182–7190.

[22] T. Zhu, J. Li, A. Samanta, A. Leach, K. Gall, Temperature and strain-rate dependence of surface dislocation nucleation, Physical Review Letters. 100 (2008) 1–4.

[23] T. Zhu, J. Li, A. Samanta, H.G. Kim, S. Suresh, Interfacial plasticity governs strain

rate sensitivity and ductility in nanostructured metals, Proceedings of the National Academy of Sciences of the United States of America. 104 (2007) 3031–3036.

[24] G. Esteban-Manzanares, E. Martínez, J. Segurado, L. Capolungo, J. LLorca, An atomistic investigation of the interaction of dislocations with Guinier-Preston zones in Al-Cu alloys, Acta Materialia. 162 (2019) 189–201.

[25] M.F.A. Ulrich Fred Kocks, Ali Suphi Argon, Thermodynamics and kinetics of slip, Oxford : Pergamon press, 1975.

[26] T.A. Halgren, W.N. Lipscomb, The synchronous-transit method for determining reaction pathways and locating molecular transition states, Chemical Physics Letters. 49 (1977) 225–232.

[27] R. Elber, M. Karplus, A method for determining reaction paths in large molecules: Application to myoglobin, Chemical Physics Letters. 139 (1987) 375–380.

[28] W. Nowak, R. Czerminski, R. Elber, Reaction path study of ligand diffusion in proteins: application of the self penalty walk (SPW) method to calculate reaction coordinates for the motion of CO through leghemoglobin, Journal of the American Chemical Society. 113 (1991) 5627–5637.

[29] G. Henkelman, B.P. Uberuaga, H. Jónsson, Climbing image nudged elastic band method for finding saddle points and minimum energy paths, Journal of Chemical Physics. 113 (2000) 9901–9904.

[30] L. Li, L. Liu, Y. Shibutani, Defect interaction summary between edge dislocations and <112>-axis symmetric tilt grain boundaries in copper on activation barriers and critical stresses, International Journal of Plasticity. 149 (2022) 103153.

[31] C.L. Kelchner, S.J. Plimpton, J.C. Hamilton, Dislocation nucleation and defect structure during surface indentation, Physical Review B. 58 (1998) 11085–11088.

[32] J.D. Honeycutt, H.C. Andersen, Molecular dynamics study of melting and freezing of small Lennard-Jones clusters, The Journal of Physical Chemistry. 91 (1987) 4950–4963.

[33] A. Stukowski, K. Albe, Extracting dislocations and non-dislocation crystal defects from atomistic simulation data, Modelling and Simulation in Materials Science and Engineering. 18 (2010) 085001.

[34] A. Stukowski, Visualization and analysis of atomistic simulation data with OVITO-the Open Visualization Tool, Modelling and Simulation in Materials Science and Engineering. 18 (2010).

3. GB energy and stacking fault energy

To investigate the interactions between the dislocation and GB, it is necessary to understand the inherent properties of the GB structures. As mentioned in the Section 1, GB structure varies according to the misorientation between the two adjacent grains, which has a substantial influence on plastic behavior. The arrangement of the atoms in the vicinity of the GB region will consequently affect the interaction results. To a certain extent, the GB energy can reflect the regularity of the atom arrangement of the GB region [1]. Therefore, it is necessary to investigate the GB energy first and provide fundamental information for the researches in later sections.

On the other hand, Rice pointed out that the stacking fault energy (SFE) and unstable stacking fault energy (USFE) could serve as the sign to identify the transition point of the brittleness and toughness of materials [2]. This indicates that the SFE and USFE affect the mechanism of the interaction between GB and dislocations. To figure out the intrinsic details, it is also important to estimate the SFE and USFE before we conduct further MD simulations. Additionally, to verify the accuracy of the potential file, it is also necessary to calculation some material properties, such as the elastic constant, SFE, and compare them with the experiments.

In this chapter, the procedure for constructing the GB and SF will be introduced. Then, GB energies for <112>-axis tilt symmetric tilt GB in Cu and <110>/<100>/<111>-axis tilt symmetric tilt GB in Cu, Al and Ni will be estimated. For typical FCC metals including Al, Cu, Ni, Au, Ag, and Pd, SFE and USFE will be calculated.

3.1. GB and GB energy

3.1.1. Fundamental concept of GB

Conventionally, GB can be precisely described by 9 parameters, including 5

macroscopic parameters to define the misorientation of the adjacent grains and 4 microscopic parameters to minimize the energy of the GB structure. The combination of nine criteria ensures the existence of realistic structures in reality. But the GB are commonly defined by the rotation axis $[uvw]$ and GB plane normal $\{hkl\}$. For example, the twin boundary can be described as $\Sigma 3\langle 110\rangle\{111\}$. Here, $\langle 110\rangle$ means the rotation axis is along $\langle 110\rangle$ direction, and $\{111\}$ means the GB plane normal is along $\{111\}$ direction. $\Sigma 3$ is the coincident position lattice (CLS) value which will be discussed later.

GBs can be built by rotating one grain around one specific axis $[uvw]$ for a certain degree θ. The interface between the two grain correspondingly forms a GB. GBs can be categorized to tilt, twist and mixed GB according to the rotation axis and GB plane normal [3]. If the rotation axis is parallel with the GB plane, which also means $[uvw]\perp\{hkl\}$, the GB is tilt. If the rotation axis is perpendicular with the GB plane, which also means $[uvw]\|\{hkl\}$, the GB is twist. Otherwise, we call the rest mixed GB.

As shown in Fig. 3-1 [4], two simple cubic lattice are rotated by 36.9° around <100> axis, and the black circles depict the coincided sites and white circles represent the original atom sites. The black circles form the CSL and the value of CSL is defined as the reciprocal of the ratio of CSL sites to original lattice sites [3]. Therefore, we can get the CSL value of Fig. 3-1 is 5. Generally, the value of CSL can be calculated from the rotation axis $[uvw]$ and rotation angle 2θ, as

$$\begin{aligned}\tan\theta &= \frac{n}{m}\sqrt{\left(u^2+v^2+w^2\right)}\\ \Sigma &= m^2+\left(u^2+v^2+w^2\right)n^2\end{aligned} \tag{3-1}$$

Here, *m* and *n* are integers and relatively prime. Σ should be the odd number, if not, Σ should be divided by 2 until it is odd.

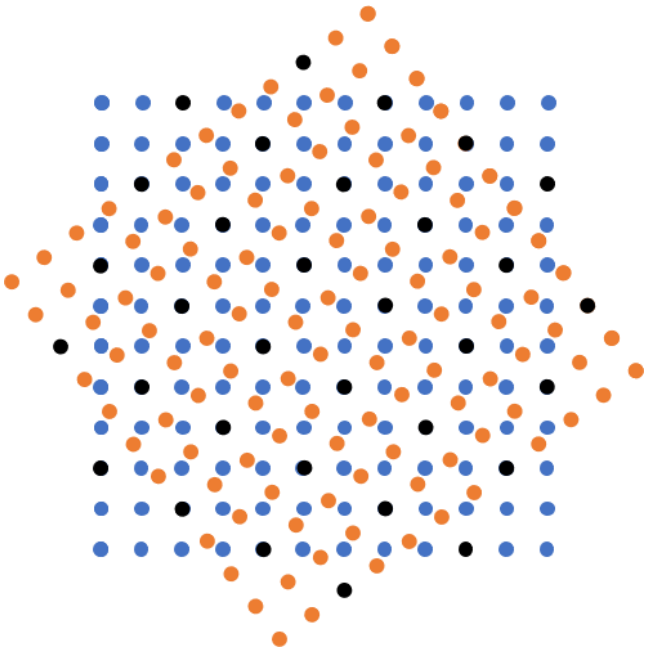

Fig. 3-1 A coincident site lattice ($\Sigma 5$) formed from two simple cubic lattices rotated by 36.9° about <001> axis. Black circles denote sites common to both lattices.

3.1.2. Model of GB and Bi-crystal structure

As mentioned above, we can obtain the GB by rotating one grain and, thus, the interface is the GB. Taking <001> axis tilt symmetric GB as an instance, as shown in Fig. 3-2, the primitive grain cell is divided into two grains. Then, Grain I and Grain II are rotated around the *Z*-axis (<001>) by $\pm\theta$. The re-combined bi-crystal will contain one GB with the CSL value calculated by Eq. (3-1). The rotated orientations can be derived by

$$\begin{bmatrix} x \\ y \\ z \end{bmatrix} = \begin{bmatrix} \frac{u^2+(v^2+w^2)\cos\theta}{u^2+v^2+w^2} & \frac{uv(1-\cos\theta)-w\sqrt{(u^2+v^2+w^2)}\sin\theta}{u^2+v^2+w^2} & \frac{uw(1-\cos\theta)+v\sqrt{(u^2+v^2+w^2)}\sin\theta}{u^2+v^2+w^2} \\ \frac{uv(1-\cos\theta)+w\sqrt{(u^2+v^2+w^2)}\sin\theta}{u^2+v^2+w^2} & \frac{v^2+(u^2+w^2)\cos\theta}{u^2+v^2+w^2} & \frac{vw(1-\cos\theta)-u\sqrt{(u^2+v^2+w^2)}\sin\theta}{u^2+v^2+w^2} \\ \frac{uw(1-\cos\theta)-v\sqrt{(u^2+v^2+w^2)}\sin\theta}{u^2+v^2+w^2} & \frac{vw(1-\cos\theta)+u\sqrt{(u^2+v^2+w^2)}\sin\theta}{u^2+v^2+w^2} & \frac{w^2+(u^2+v^2)\cos\theta}{u^2+v^2+w^2} \end{bmatrix} \begin{bmatrix} x \\ y \\ z \end{bmatrix} \quad (3\text{-}2)$$

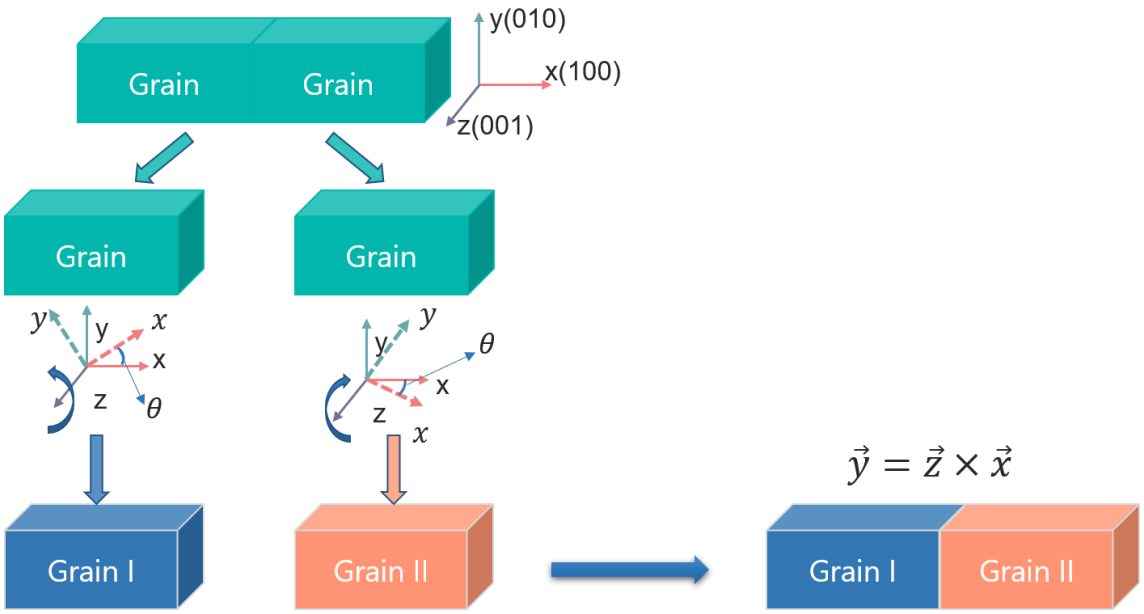

Fig. 3-2 The creation procedures of the bi-crystal structure with one GB.

However, this procedure only contains 5 DoFs of the 9 parameters as mentioned above. Because only the macroscopic parameters are introduced through the rotation. The microscopic parameters which determine the energy state of the GB should be found in another way. To do so, we need to displace the grain along the in-plane direction and find the equilibrium structure with the lowest GB energy. The detailed steps can follow:

1) Create the bi-crystal structure according to the orientations calculated by Eq. (3-2);
2) Measure the periodic length of the lateral edge which is perpendicular to the GB plane normal (the Y and Z in Fig. 3-2);
3) Divide the lateral edge into 10 equal parts and form a 10*10 grid.
4) Displace one grain for about $(n\Delta y, m\Delta z)$ in (Y, Z) direction, where, $n, m \in [0, 50]$ and $\Delta y, \Delta z$ are the unit length divided in Step 3.
5) Calculate the GB energy for all the displaced models in Step 4. And record the lowest GB energy and structure.

The most stable GB can be obtained in this manner. If more precise results are required, simply increase the number from 10 to 20 or larger and generate more models. This will

take extra time and computational resources as well. In addition, the lattice model used for grain boundary construction may have too small atomic spacing in the region around grain boundary, resulting in serious lattice distortion. The solution is to set a critical distance and delete one of the atomic pairs within the critical distance. This distance was varied from 1.2 Å to 2.4 Å and keep the step size to 0.1 Å.

To calculate the GB energy, periodic boundary conditions Periodic boundary conditions were used in all three directions and thus two GBs will be included in the model. One is located in the middle and the other intersects at the boundary surface. MS simulations with conjugate gradient (CG) method were used to calculate the system energy. The static GB energies E_{static}^{GB} were calculated through the rigid displacement method mentioned above, according to the formula:

$$E_{static}^{GB} = \frac{E_{system} - N \cdot E_{cohesive}}{2A} \tag{3-3}$$

where, A is the area of GB, E_{system} is the whole sandwich-like structure energy that contains two GB planes because of the periodic condition in all three directions, N is the number of atoms and $E_{cohesive}$ is the cohesive energy per atom in the perfect lattice. It is worth noting that EAM potentials were used to calculate the MD and energy measures for Al [5], Cu [6], Ni [5]. Table 3-1 give the mechanical parameter calculated for different materials. μ is isotropic shear modulus for the $\{111\}[1\bar{1}0]$ direction in a single crystal. C11, C12, C44 is the elastic constants.

Table 3-1 Mechanical parameter calculated for different materials.

Material	Lattice constant (Å)	$E_{cohesive}$ (ev)	C11 (GPa)	C12 (GPa)	C44 (GPa)	μ (GPa)
Al	4.05	-3.36	113.74	61.50	31.86	27.95
Cu	3.625	-3.54	169.93	122.65	76.41	41.15
Ni	3.52	-4.45	248.71	148.17	126.16	74.96

3.1.3. GB energy map

Two kinds of GBs were investigated, <110>-axis and <112>-axis tilt GBs. Therefore, two directions, <110> and <112>, are set as Y-axis when we created the bi-crystal. X and Z changed according to the rotation angle.

(1) <112>-axis tilt symmetric GB

The corresponding relationship of <112>-axis GB energy vs. misorientation angle is depicted in Fig. 3-3.

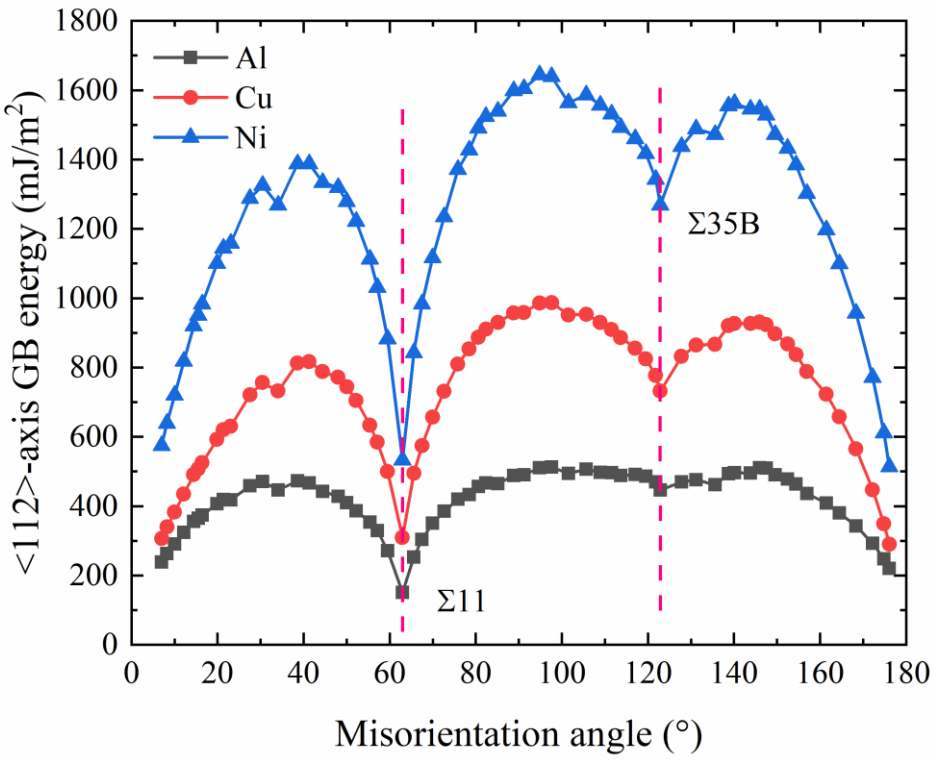

Fig. 3-3 The <112>-axis grain boundary energy as a function of the misorientation angle for Al, Cu, and Ni.

As shown in Fig. 3-3, the map contained two local minima and three cusps. This tendency has been confirmed by Shibuta [7] for γ-iron. Taking Cu as an example, the lowest local minimum corresponds to Σ11A GB with 62.96° misorientation angle and 309 mJ/m^2 GB energy. The second valley is Σ35B GB with 122.88° misorientation angle and GB energy of 731 mJ/m^2. In general, two types of GB structures can be distinguished, the morphologies of which seem to be flat and zigzag. The relatively simple and regularly arranged flat GB structures ensure these local minima, as shown in Fig. 3-4. Comparing the GB structures with the static GB energies, the energy of a zigzag type GB, such as Σ73A, was higher than that of a flat type GB, such as Σ11A.

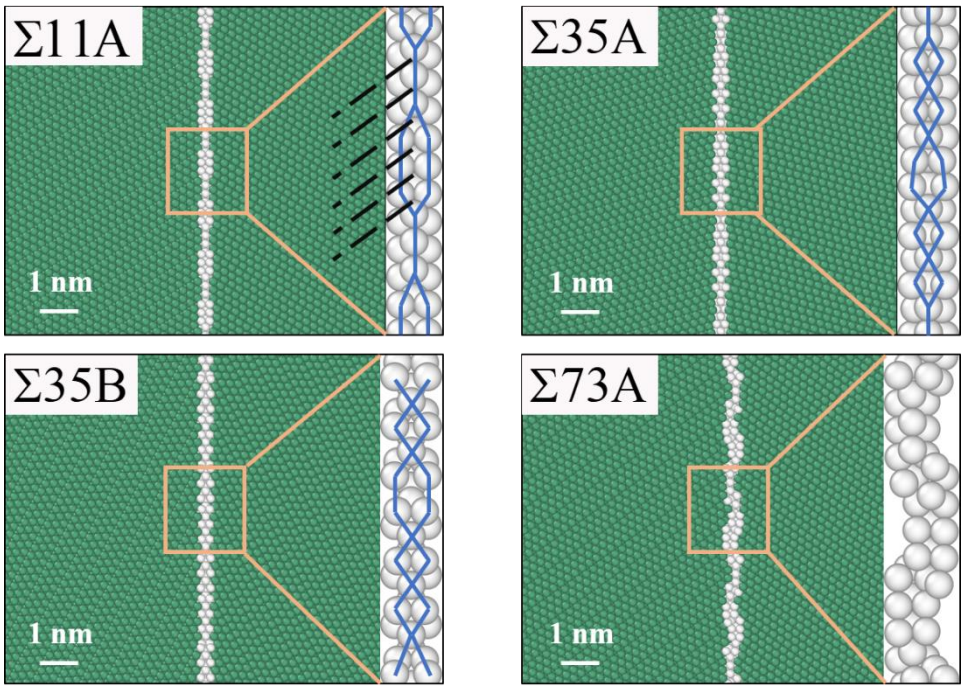

Fig. 3-4 <112>-axis GB structure with flat and zigzag features. The righthand part of each image shows the geometry of the GB. The blue lines show the structural arrangement of the GB atoms. The black dot lines in Σ11A represent the potential slip planes and they are omitted for brevity in other GBs. The white short line represents the scale bar of 1 nm.

(2) <110>-axis tilt symmetric GB

Fig. 3-5 gives the energy map of <110>-axis tilt symmetric GB in Al, Cu, and Ni. Obviously, the map is similar to the <112>-axis tilt symmetric GB, containing two local minima and three cusps. However, the lowest energy shows at Σ3(111) GB, which is also called coherent twin boundary (CTB). The twin boundary is formed by a plane of atoms in (111) direction, this is also the close-packed plane in FCC metals. Therefore, the regular sequence of the atoms guarantees the lowest energy among the GBs. The GB energy of the CTB is 75 mJ/m^2, 15 mJ/m^2, 7 mJ/m^2 for Al, Cu, and Ni, respectively. It is also should be note that different potentials may generate different GB, but the trends are the same and the difference should be small.

Analogously, Σ11B is another minimum of the map. It is worth mentioning that, Σ11B in <110>-axis tilt GB is actually the same GB with Σ11A in <112>-axis tilt GB. The atom arrangements are identical in these two GBs, the only difference lies in the axis and orientations of the grains. For example, in Cu, the GB energy for both Σ11 GB, (<112> Axis and <110> Axis), are 309 mJ/m^2. The GB energies of Σ11 for another two metals are 150 mJ/m^2 (Al) and 450 mJ/m^2 (Ni). Generally, as shown in Fig. 3-5, the energy is larger in Ni and would be smallest in Al except for CTB. The GB energy reflects the nature of materials and can significantly affect the strength of the bulk materials.

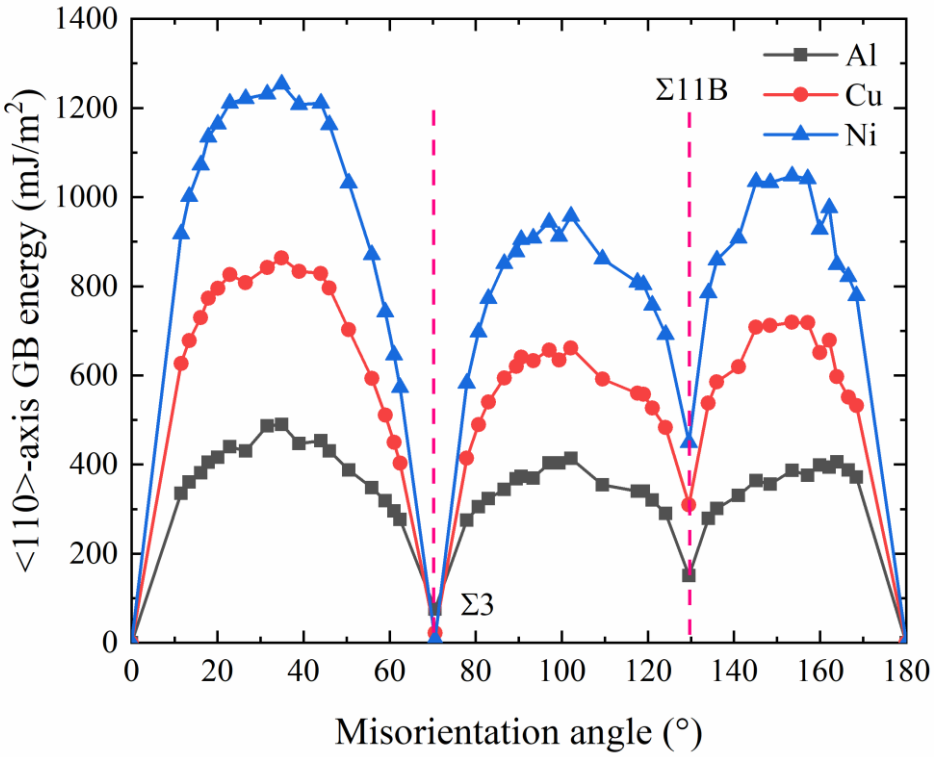

Fig. 3-5 The <110>-axis grain boundary energy as a function of the misorientation angle for Al, Cu, Ni.

(3) <100>-axis tilt symmetric GB

Fig. 3-6 gives the energy map of <100>-axis tilt symmetric GB in Al, Cu, and Ni. Different from the results above, the energy map is periodic and the period is 90°. No obvious global minimum can be found but one peak can be found at around 40°, $\Sigma 73A(08\bar{3})$ GB. The peak energies are 690 mJ/m^2, 1208 mJ/m^2, 1812 mJ/m^2 for Al, Cu, and Ni, respectively.

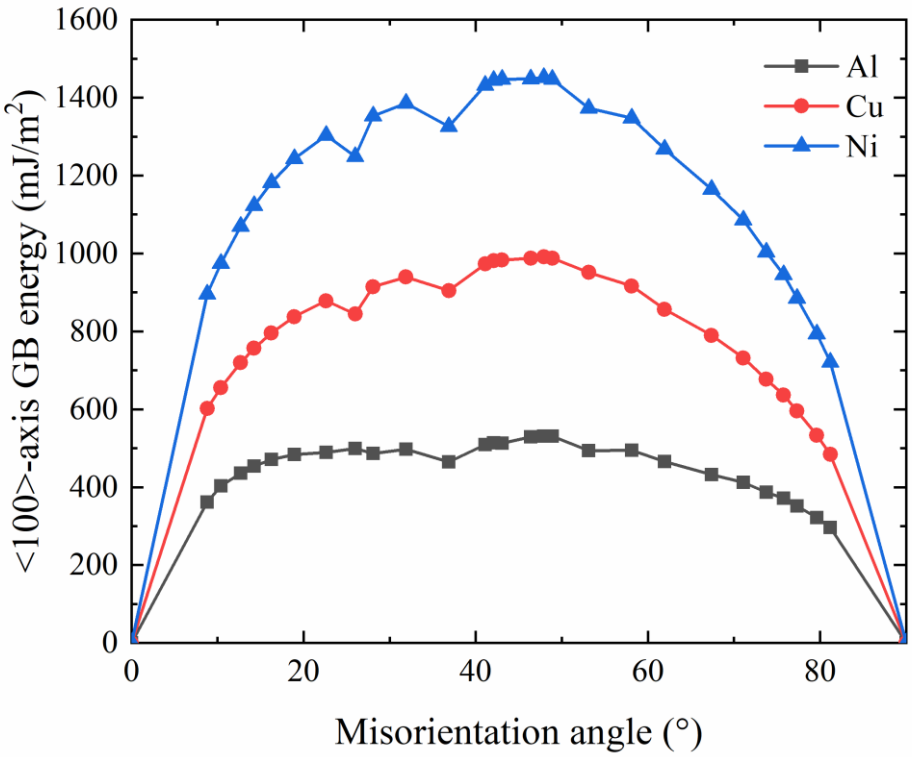

Fig. 3-6 The <100>-axis grain boundary energy as a function of the misorientation angle for Al, Cu, Ni.

(4) <111>-axis tilt symmetric GB

Fig. 3-7 give the the energy map of <100>-axis tilt symmetric GB in Al, Cu, and Ni. One local minimum was found at 60°, the $\Sigma 3(1\bar{2}1)$ GB. The corresponding GB energies are 354 mJ/m^2, 640 mJ/m^2, and 979 mJ/m^2, for Al, Cu, and Ni, respectively. Similar to <100>-axis GB, the energy map is periodic and the period is 120°. One special feature

is that this energy map is also symmetric about 60°, which cannot be observed in the other kinds of GB.

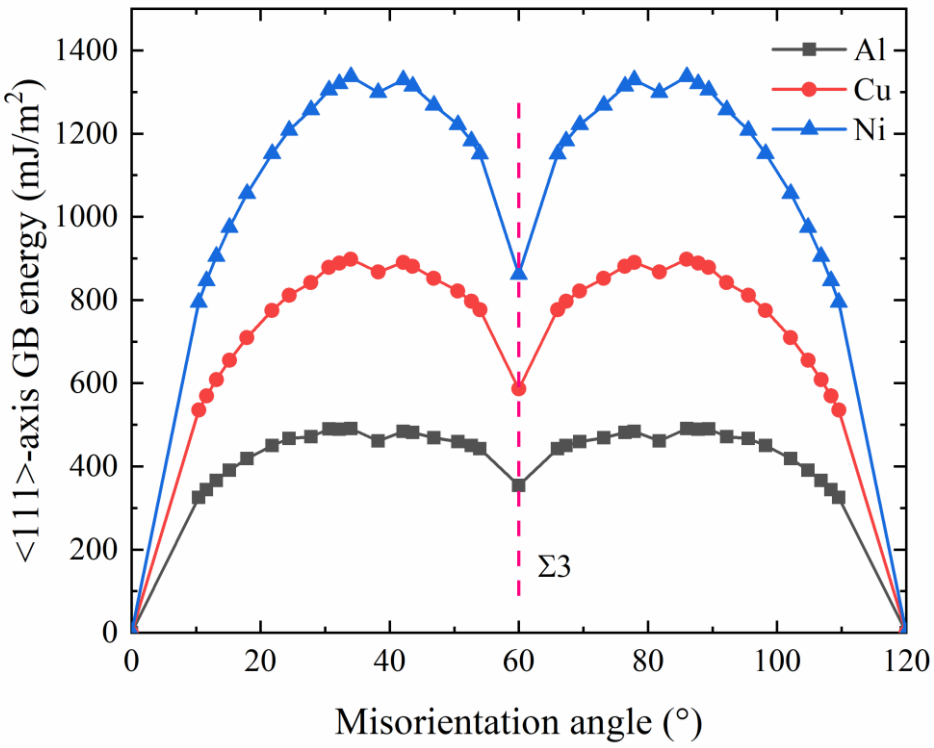

Fig. 3-7 The <111>-axis grain boundary energy as a function of the misorientation angle for Al, Cu, Ni.

3.2. Stacking fault energy and generalized stacking fault curve

As the most common 2D planar defects in the crystalline materials [8], the stacking fault (SF) can be formed during grain growth, partial dislocation moving, or deforming systems containing point defects. Conventional, the close-packed crystalline, like FCC metal, can be treated as many close-packed atom planes stack up in a certain sequence. In FCC, the close-packed plane is $\{111\}$ plane. If we define the stacking sequence as ABCABC as the normal stacking sequence. When the normal stacking sequence is destroyed or dislocated, the SF can be formed as a sequence of $ABC\ldots BCABCABC$. In

this type of SF, one A layer was deleted, therefore, one intrinsic SF can be formed, as shown in Fig. 3-8(a). On the contrary, if one layer, for example B, is inserted. The sequence changes to ABC…B…ABCABC, and one extrinsic SF forms, as shown in Fig. 3-8(b).

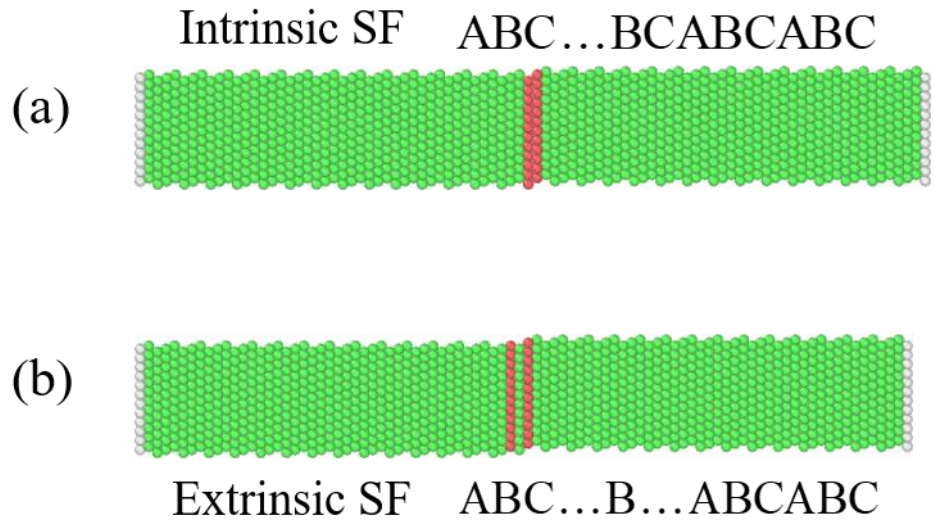

Fig. 3-8 (a) Intrinsic SF. (b) Extrinsic SF.

Although no lattice distortion will be generated during the formation of the SF, it still changes the integrity of the crystal and the periodicity of the normal arrangement. This causes the electrons to diffract abnormally, which increases the energy of the crystal. This energy is called stacking fault energy [8]. From the point of view of energy, the higher the stacking fault energy, the less the occurrence of stacking fault.

It is possible to measure the SF energy through the MS or MD simulations. A traditional way is that one can rigidly displace part of the single grain long the [112] direction. With the displacements increasing, the defect-free single crystal will generate planar defects. When the displacement reaches $\frac{a}{6}[112]$, the intrinsic SF will be formed and

when the When the displacement reaches $\frac{a}{3}[112]$, the extrinsic SF will be formed. One can calculate the energy changes with respect to the displacement and get an energy curve, which is called generalized stacking fault curve (GSFC).

The above-mentioned displacement method is one way to get the GSFC. However, with the help of NEB, it is convenient to get the GSFC. In this method, we only need to construct two configurations, the initial state and final state, to calculate the GSFC. The NEB will find the MEP from single crystal to extrinsic SF which is identical to the displacement method. But the cost is much smaller. To do so, taking Cu as an example, the initial state, namely a single crystal, and the final state, the extrinsic SF, should be constructed first. As shown in Fig. 3-9, the initial state is the single crystal. The orientation of the single crystal is $X=[\bar{1}10], Y=[111], Z=[11\bar{2}]$. The size of the model is about $1.5\text{nm}\times 18\text{nm}\times 2.6\text{nm}$ in $X\times Y\times Z$.

Divide the single crystal into left and right grains in the middle plane. Move the left grain entirely $\frac{a}{6}[112]$ in the positive direction of X axis, and then move the right grain entirely $\frac{a}{6}[112]$ in the negative direction of X-axis. In this way, the final state can be formed. The initial and final configurations should be energy-minimized first with LAMMPS [9]. Periodic boundaries were applied to X and Z direction and free surface was applied to the Y direction to let the structure extend. Once the energy was minimized, the initial and final states were used to find the MEP with the NEB method. Quick-min minimizer was used with 36 replicas. The detailed information of NEB can be found in Section 2.

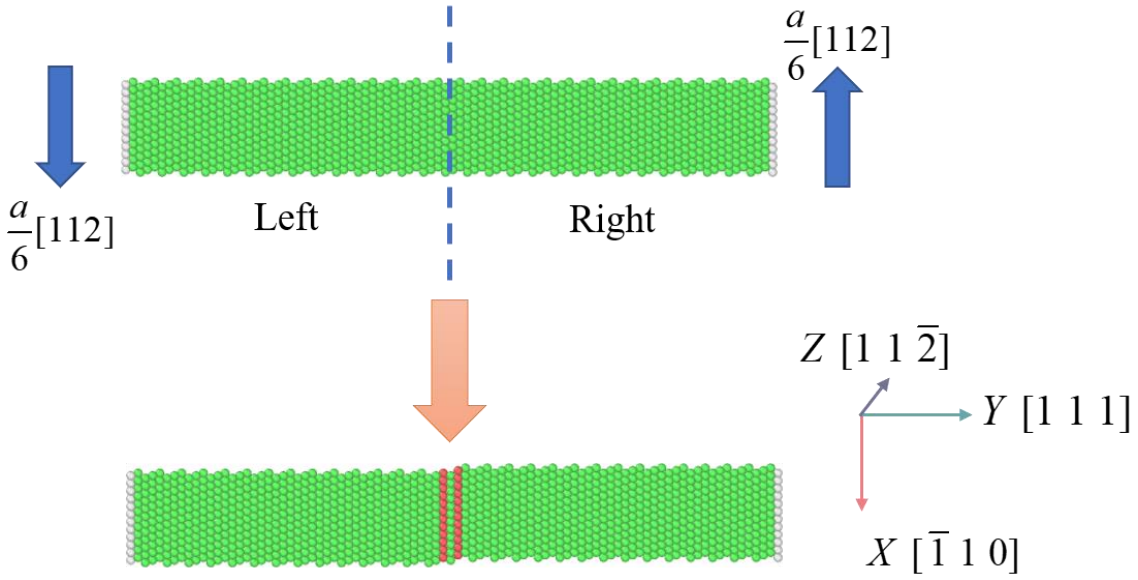

Fig. 3-9 The slab model used for calculating the stacking-fault energy of FCC metals. The initial state is the perfect single crystal and the final state is the extrinsic SF.

After the MEP was found, the GSFC can be calculated by

$$\gamma_i = \frac{E_i - E_{initial}}{A} \tag{3-4}$$

where, E_i is the potential energy of the ith replica. $E_{initial}$ is the energy of the initial state. A is the area of the SF, which equals to $Y \times Z$ in the current model.

Tacking Al for an instance, Fig. 3-10 (a) gives the GSFC of Al and Fig. 3-10 (b) gives the corresponding atomic configurations. The calculated intrinsic SFE is $\gamma_s = 145.47 \text{mJ/m}^2$, the extrinsic SFE is $\gamma_{Es} = 150.39 \text{mJ/m}^2$. The first saddle point, unstable SFE is $\gamma_{us} = 164.30 \text{mJ/m}^2$. The second saddle point, unstable twin fault energy is $\gamma_{uTF} = 218.59 \text{mJ/m}^2$. It should be emphasized that the γ_{us} is the energy that should be overcome to create the SF in the perfect defect-free single crystal. Therefore, it is also used to describe the resistance of the dislocation emitting from a crack tip or from a free surface [2,10]. Similarly, the unstable twin fault energy γ_{uTF} is the energy that should

be overcome to create the extrinsic SF in the perfect defect-free single crystal.

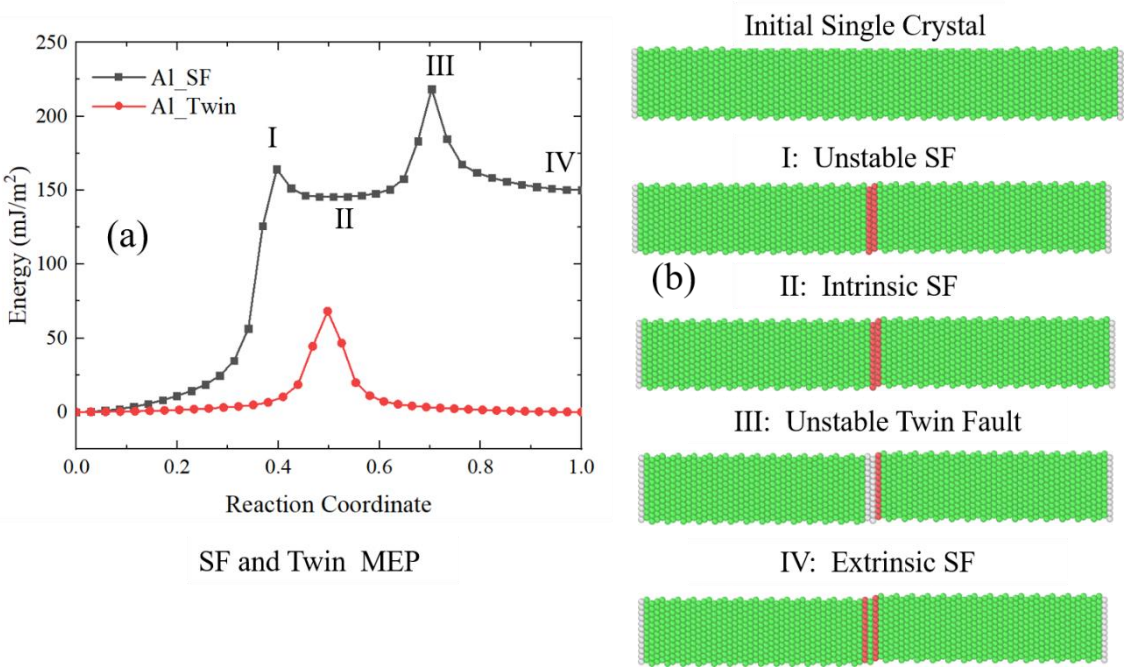

Fig. 3-10 (a) Energy curves along the MEP for Al. (b) atomic configurations as pointed in (a). I: the unstable SF, also the first saddle point; II: the stable SF; III: the unstable twin fault, also the second saddle point; IV: final state, the extrinsic SF.

In addition, the GSFCs of Al [5], Cu [6], Ni [5], Ag [11], Au [12] and Pd [13,14] are plotted in Fig. 3-11 with different potential files and the specific value are listed in Table 3-2. Two different potentials were used for Pd.

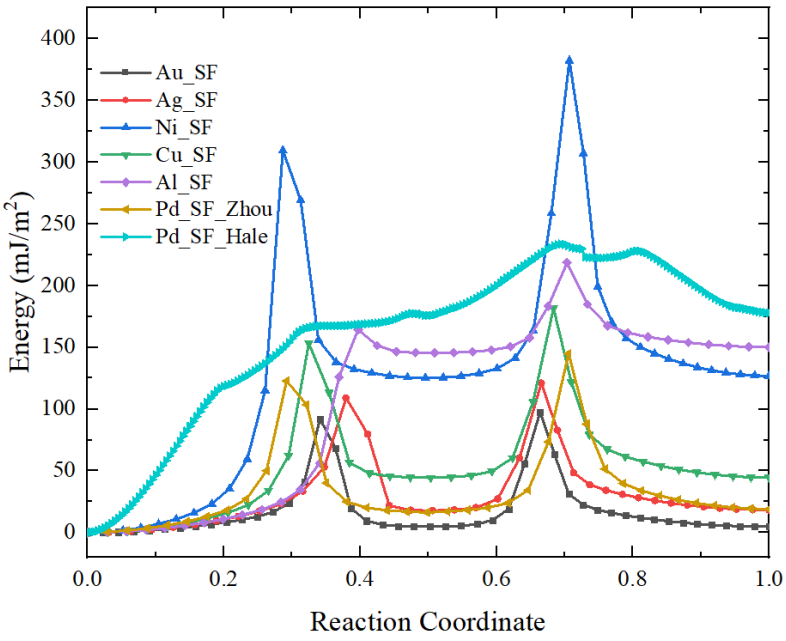

Fig. 3-11 Energy curves along the MEP for Al, Cu, Ni, Ag, Au, and Pd.

Table 3-2 The SF energy of Al, Cu, Ni, Ag, Au, and Pd

Element	γ_s (mJ/m^2)	γ_{us} (mJ/m^2)	γ_{uTF} (mJ/m^2)	γ_{Esf} (mJ/m^2)
Al	145.47	164.30	218.59	150.39
Cu	44.39	153.28	181.68	44.75
Ni	125.25	309.57	382.32	127.24
Ag	17.75	108.90	121.03	18.49
Au	4.72	92.05	97.52	4.85
Pd_Zhou	16.26	122.76	144.91	19.37
Pd_Hale	177.80	40.90	228.12	177.91

It can be seen from Fig. 3-11 that the stacking fault formation energy curves obtained by using different potential functions generally have the same trend except for Pd_Hale. The intrinsic stacking fault energy of the material is approximately equal to the extrinsic

stacking fault energy. However, the unstable SF energy varies greatly among different materials, which may be a potential explanation for the great difference in strength and toughness of materials. We will talk about this problem in the later section.

3.3. Summary

In this chapter, we calculated the elastic constants for Al, Cu, and Ni. The results are in good agreement with the references. The GB energies of <112>/<110>/<100>/<111>-axis were investigated for Al, Cu, and Ni. Furthermore, the stacking fault energies were probed for Al, Cu, Ni, Ag, Au, and Pd. All the information is fundamental to the later researches described in Chapters 4, 5, and 6.

References

[1] B. Kuhr, D. Farkas, I.M. Robertson, D. Johnson, G. Was, Stress Localization Resulting from Grain Boundary Dislocation Interactions in Relaxed and Defective Grain Boundaries, Metallurgical and Materials Transactions A: Physical Metallurgy and Materials Science. 51 (2020) 667–683.

[2] J.R. Rice, Dislocation nucleation from a crack tip: An analysis based on the Peierls concept, Journal of the Mechanics and Physics of Solids. 40 (1992) 239–271.

[3] L. Priester, Grain Boundaries and Crystalline Plasticity, ISTE Ltd and John Wiley & Sons, Inc, Hoboken,USA, 2011.

[4] J. Humphreys, G.S. Rohrer, A. Rollett, The Structure and Energy of Grain Boundaries, in: Recryst. Relat. Annealing Phenom., Elsevier, 2017: pp. 109–143.

[5] Y. Mishin, D. Farkas, M.J. Mehl, D.A. Papaconstantopoulos, Interatomic potentials for monoatomic metals from experimental data and ab initio calculations, Physical Review B - Condensed Matter and Materials Physics. 59 (1999) 3393–3407.

[6] Y. Mishin, M.J. Mehl, D.A. Papaconstantopoulos, A.F. Voter, J.D. Kress, Structural stability and lattice defects in copper: Ab initio, tight-binding, and embedded-atom calculations, Physical Review B - Condensed Matter and Materials Physics. 63 (2001) 2241061–22410616.

[7] Y. Shibuta, S. Takamoto, T. Suzuki, A molecular dynamics study of the energy and structure of the symmetric tilt boundary of iron, ISIJ International. 48 (2008) 1582–1591.

[8] J.P. Hirth, J. Lothe, Theory of dislocation, Krieger Pub. Co, New York, 1982.

[9] S. Plimpton, Fast parallel algorithms for short-range molecular dynamics, Journal of Computational Physics. 117 (1995) 1–19.

[10] C. Deng, F. Sansoz, Fundamental differences in the plasticity of periodically twinned nanowires in Au, Ag, Al, Cu, Pb and Ni, Acta Materialia. 57 (2009) 6090–

6101.

[11] P.L. Williams, Y. Mishin, J.C. Hamilton, An embedded-atom potential for the Cu-Ag system, Modelling and Simulation in Materials Science and Engineering. 14 (2006) 817–833.

[12] S.M. Foiles, M.I. Baskes, M.S. Daw, Embedded-atom-method functions for the fcc metals Cu, Ag, Au, Ni, Pd, Pt, and their alloys, Physical Review B. 33 (1986) 7983–7991.

[13] L.M. Hale, B.M. Wong, J.A. Zimmerman, X.W. Zhou, Atomistic potentials for palladium-silver hydrides, Modelling and Simulation in Materials Science and Engineering. 21 (2013).

[14] X.W. Zhou, R.A. Johnson, H.N.G. Wadley, Misfit-energy-increasing dislocations in vapor-deposited CoFe/NiFe multilayers, Physical Review B - Condensed Matter and Materials Physics. 69 (2004) 1–10.

4. Interactions between edge dislocations and <112>-axis symmetric tilt grain boundaries in Cu

Vacancies, dislocations, and grain boundaries (GBs), as the most common three kinds of defects in crystalline materials, significantly influence plastic deformation behaviors through their mutual interactions [1–3]. Absorption, transmission, pile-up and reflection of dislocations were observed in the previous studies [4,5,14–18,6–13].

it was probed that the nucleation and lateral motion of the GB disconnections or the direct transmission were present in the interaction process of single screw dislocation and more generally morphological GB structure cases [19]. These interaction mechanisms also reflect the influence of the GB morphology, or more specifically the local GB structures. The structure of the GB is usually described by the axis of rotation and the coincidence site lattice (CSL) value[20–22]. The incident dislocation will be absorbed into <112>-axis Σ11 GB but will transmit trough the GB when it impinges on the <111>-axis Σ57 GB [23]. Bachurin et.al [23] also pointed out that different initial slip planes would give different interaction mechanisms and critical stresses for the same CSL GB which further demonstrate the importance of the local GB structure. Nanoindentation experiments [24] and MD simulation [25] also depicted some seductive slip-GB reaction phenomena, although the consequent multi-dislocations mainly get the mixture property and sinuous topological shapes which may cause more complex reaction mechanisms and quantitative analysis difficulty.

The approaches above only provided the qualitative analysis of reaction phenomena and the CRSS at extremely low temperature (<10 K) or finite temperature with a very high strain rate through MD or at 0 K through molecular statics (MS) simulations. Rare of them consider the energy evolution or the energy barrier for the interaction process.

Sangid et al. [26] established the control box method to capture the inversely proportional relationship between the energy barrier and the statics <110> axis GB boundary energy. Following this way, Chen et al. [27] investigated the matrix dislocation interacting with the twin boundary for hexagonal close packed metal Mg. But this method is sensitive to the choice of the box, no matter the size or the location and may also introduce the artificial effects. Nevertheless, the dislocation-GB interaction usually is identified as a thermally activated process [28,29]. This process can be precisely and energetically described by the transition state theory (TST) (Glasstone and Laidler, 1941), by which the consequently calculated energy barriers and activation volumes are of the capability to illustrate the rate and thermal effects on the interaction process and link the MD simulation to the rate-dependent bulk material mechanical experiments. Plenty of investigations have been probed with the help of this approach, such as the dislocation-precipitate interaction process [31], cross-slip mechanism of the screw dislocation which is hindered by the stacking fault tetrahedra [32], dislocation nucleation process [33,34].

Ordinarily, the TST strategy could be implemented by direct MD simulations with an extremely high cost of computational resources to simulate the rate-controlling dislocation mediated process. On the contrary, the multi-replica chains technique including the standard nudged elastic band (NEB) (Henkelman and Jónsson, 2000; Jónsson et al., 1998), climb image nudged elastic band (CINEB) [37], free-end nudged elastic band (FENEB) [12], would occupy much fewer resources to implement TST and calculate the activation enthalpy barriers, minimum energy path (MEP) and activation volumes. For an instance, Zhu et al. [12] evaluated the energy barrier of screw dislocation-CTB interaction. A Friedel-Escaig-type cross slip mechanism was clarified in the dislocation-CTB interaction process using the FENEB method for Cu. The influence of stress state on the screw dislocation cross-slip mechanism in Al was investigated and a quantitative formula was established to link the cross-slip energy barrier with the stress states [38]. More recently, an analogical Friedel-Escaig mechanism was confirmed in the

screw-CTB interaction of Ni-based high entropy alloys [39].

The foregoing researches only qualitatively focus on the interaction processes between dislocations and one or two specific GBs. Some of them generated the dislocations through the void or notch which may nucleate curved and multiple dislocations and further increase the difficulty to quantitively investigate the interaction process [26]. On the one hand, although the GB structures influence the interaction mechanisms and critical stresses, the general tendency has not been resolved because only limited GB structures were generated and adopted to interact with the dislocation. On the other hand, how will these atomic-scale interactions be quantitatively reflected in the macroscopic bulk material, especially in the plastic behaviors and how to link the MD results to the experiments? To handle these two parts, we first generated a large number of GBs with different CSL values. We plan to establish a relationship between the critical interaction shear stress and the static GB energy. Furthermore, activation energy barriers were got from the NEB method. The corresponding activation volumes and strain rate sensitivities were deduced by the TST and hence the link between the unit dislocation-GB interaction process and the experimental plastic features can be established [40].

In this Chapter, to answer above questions, we first generated a large number of GBs with different CSL values with the aim of establishing a relationship between the critical interaction shear stress and the static GB energy. In addition, the activation energy barriers were obtained by the NEB method. The corresponding activation volumes and strain rate sensitivities were deduced by the TST and hence the link between the unit dislocation-GB interaction process and experimental plastic features was established. It is worth mentioning that we used a sandwich-like model where one dislocation and one GB are introduced and two rigid slabs are used to apply the external load at the upper and lower regions. This is a very straightforward model and is widely used [8,39]. Yu et.al also used the QCM model to investigate the interactions [16,22]. In this method, Yu calculate the far-field stress by the finite element method and estimate the local region by MD method.

The model, hence, is too large to implement the NEB simulation and not suitable for our aim.

4.1. Atomic model and calculation condition

In order to inhibit the curvature effect which generally arises for the notch or voids induced mixed dislocation-GBs interaction process, after the most stable bi-crystal structure was created, the equilibrium bi-crystals were rotated and reshaped to a regular hexahedral model as illustrated by Fig. 4-1 [11]. The *X*, *Y* and *Z* axes of the left parent grain were parallel to $[1\ \bar{1}\ 0]$ (dislocation slip direction), $[\bar{1}\ \bar{1}\ 1]$ (slip plane normal) and $[1\ 1\ 2]$ (edge dislocation line) orientations, respectively. The whole system was divided into three part, the upper rigid region, the lower rigid region and the middle interatomic region. The thickness of the rigid regions is about 10 Å.

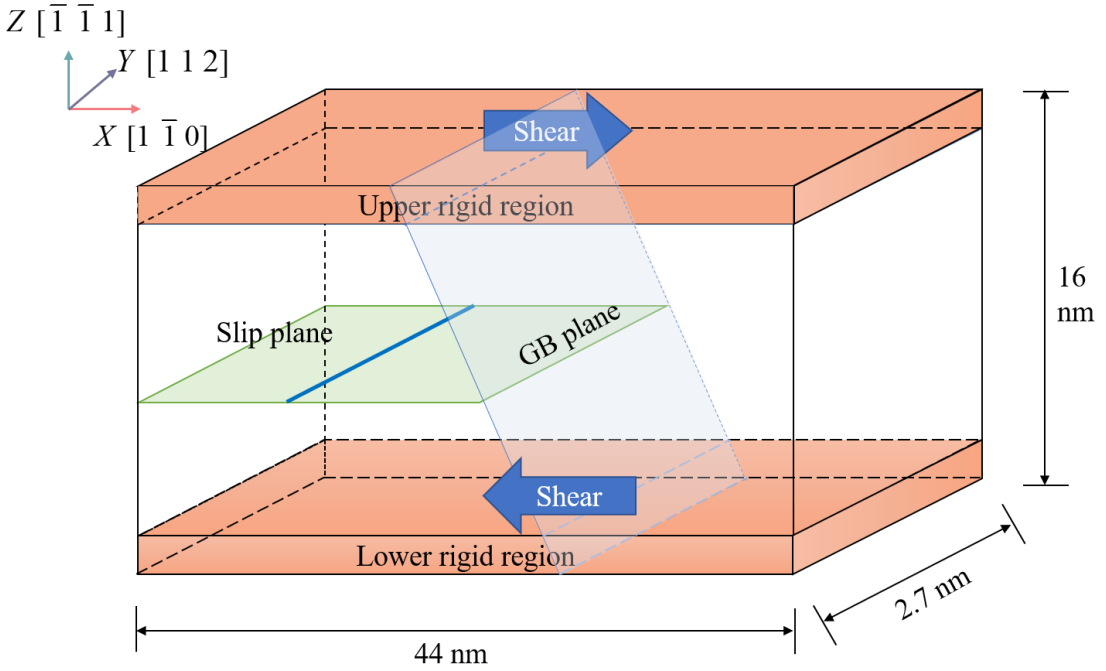

Fig. 4-1 Schematic representation of the interaction model. The domain contains one edge dislocation depicted by blue line on the green slip plane. The upper and lower atomistic plates with 10 Å thickness were set as rigid regions to apply displacement.

The Volterra's displacement field facilitated inserting the edge dislocation into the middle of the left parent grain for the isotropic elastic medium [41]. For an edge dislocation lying along Z axis, if the dislocation core is located at origin of the coordinate, then the displacement produced by the dislocation stress filed can be derived as,

$$\begin{aligned} u_x &= \frac{b}{2\pi}\left[\tan^{-1}\frac{y}{x}+\frac{xy}{2(1-v)(x^2+y^2)}\right] \\ u_y &= -\frac{b}{2\pi}\left[\frac{1-2v}{4(1-v)}\ln(x^2+y^2)+\frac{x^2-y^2}{4(1-v)(x^2+y^2)}\right] \end{aligned} \tag{4-1}$$

where x and y are the atoms coordinate, v is the poison ratio. b is the Burgers vector. The edge dislocation can be introduced to the left grain according to Eq. (4-1). The dislocation maintains the Burgers vector of $[1\ \bar{1}\ 0]$, same as the X-axis and, hence, is parallel with the GB plane. Periodic boundary condition was applied to Y direction to mimic an infinite dislocation line and the two lateral sides preserved free surface condition since the reshape approach already destroyed the intrinsic crystallographic periodicity. The initial dislocation position should be carefully chosen so that the dislocation would not be repelled by the GB or not be attracted to the left free surface and thus not be annihilated. To this end, the dimensions of the domain were about $44\times2.7\times16$ nm^3 in $X\times Y\times Z$ direction, respectively. After and before the system being dislocated, the system was energy-minimized by CG algorithm. However, considering the local GB morphological property, several different slip planes were selected for each GB by changing the Z coordinate of the initial position of dislocations. For example, we recall the GB morphology of $\Sigma11\mathrm{A}$ as depicted in Chapter 2, also as shown in Fig. 4-2. Because of the periodic structure of the GB, there are 6 independent slip planes for the dislocation. Different slip plane may cause different interacting scenarios. Therefore, different initial inserting locations were chosen for different potential slip plane.

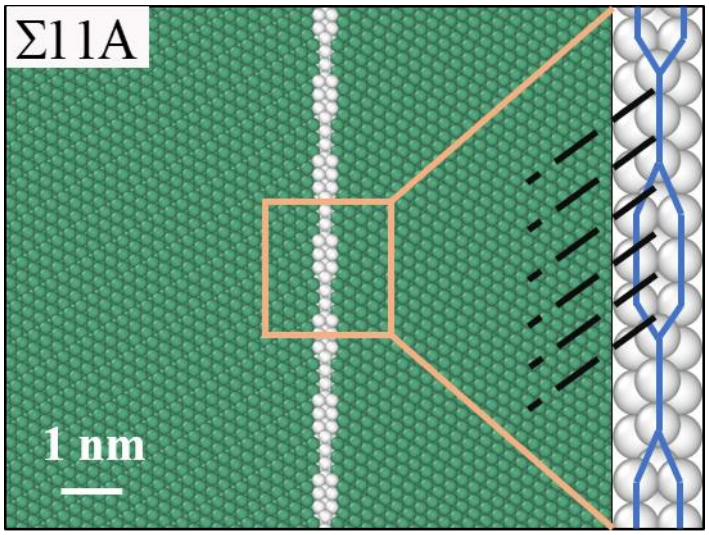

Fig. 4-2 The <112>-axis Σ11A GB Structure. The righthand part of each image shows the geometry of the GB. The blue lines show the structural arrangement of the GB atoms. The black dot lines in Σ11A represent the potential slip planes and they are omitted for brevity in other GBs. The white short line represents the scale bar of 1 nm.

After the minimization, the inserted perfect edge dislocation would dissociate into two partial Shockley dislocations following the Eq. (4-2),

$1/2[1\bar{1}0] \rightarrow 1/6[2\bar{1}1] + 1/6[1\bar{2}\bar{1}]$ or $BC \rightarrow B\alpha + \alpha C$ in Thompson Tetrahedron (4-2)

In order to achieve the edge dislocation movement toward the GB plane, a shear deformation was applied to the system by setting upper and lower rigid region to move in the opposite direction with a velocity of 0.03 Å/ps along the *X*-axis. This may result in a strain rate of about 10^8/s when considering the present model size. The canonical ensemble (NVT) was implemented to update atomic positions and to time-integrate certain physical quantities. The time step was set as 1 fs and system temperature was maintained at 0.1 K to suppress any thermally activated process of the dislocation itself [8,19]. Atomic configurations were recorded every 2 ps for further analysis or TST evaluation.

With regard to NEB method, a main advantage is the capability to straightforwardly

calculate the activation energy as the function of applied stress or strain. A series of replicas were applied to capture the atomic configurations and MEP of the interaction process. These replicas were generated by interpolating the atom coordinate from the initial replica (R_0) to the final replica (R_N). Altogether, N replicas would be connected by the virtual harmonic elastic springs. The configuration of current replica R_j was somewhat mediated by the previous replica R_{j-1} and the following one R_{j+1}. With proper relaxation, the replicas will eventually converge to the MEP. The saddle point of this path is identified and used to calculate the energy barrier at desired strain or stress state. It is noteworthy that both the initial state R_0 and final state R_N must be at the same external applied load (stress state) or deformation (strain state) because the external work during the whole process has to be excluded. Therefore, the most crucial issue is how to construct the initial and final replicas.

In this work, the same strain state setup was labeled for the MEP traversal. Specifically, the initial state for the desired applied strain was constructed by minimizing the configuration of the same strain obtained by loading process described above. The final state could be constructed by following refs. [29,40,42]. Briefly, once the dislocation reacted with the GB, the whole system would encounter the unloading process to the desired strain, and, the energy minimization was utilized again to get the equilibrium configuration of the final state. Furthermore, high stress and strain state will obviously distort the potential energy surface of the system, making the saddle point very close to the initial state. The standard NEB method is difficult to accurately find the position of the saddle point due to limited replicas. To this end, apart from the CINEB method, FENEB algorithm was also applied to find the energy barrier for the high strain cases with 18 or 24 replicas. The Quick-min method was used for the damped dynamics minimizer with a spring constant of 1 eV/Å.

All MD and NEB simulations were conducted by the large atomic/molecular massively parallel simulator (LAMMPS) code [43] and modeled by an embedded atom method

(EAM) potential for Cu by Mishin et al. [44], which elaborates a stacking fault energy of 44.7 mJ/m^2 against that of 45 mJ/m^2 by the experiment data [12]. Other fundamental properties using the current potential are cohesive energy of 3.54 eV/atom, lattice constant of 3.62 Å, Burgers vector of 2.56 Å. The anisotropic elastic constants calculated by this potential are $C_{11} = 169$ GPa , $C_{12} = 123$ GPa and $C_{44} = 76.2$ GPa and the isotropic shear modulus is derived to be 42.0 GPa for the $\{111\}[1\bar{1}0]$ direction in single crystal. This potential has been substantiated by the ab initio calculation and utilized in many other MD simulations [8,17]. The atomic structure and defects were identified and characterized by OVITO [45] with the Dislocation extraction algorithm (DXA) [46].

4.2. Edge dislocation-GB interactions

Several <112>-axis symmetric tilt GBs were selected to react with the edge dislocation after rotation and reshaping. Before discussing the details of the interaction, we recalled the corresponding relationship of GB energy vs. misorientation angle in Chapter 3, as depicted in Fig. 4-3 or Fig. 3-3.

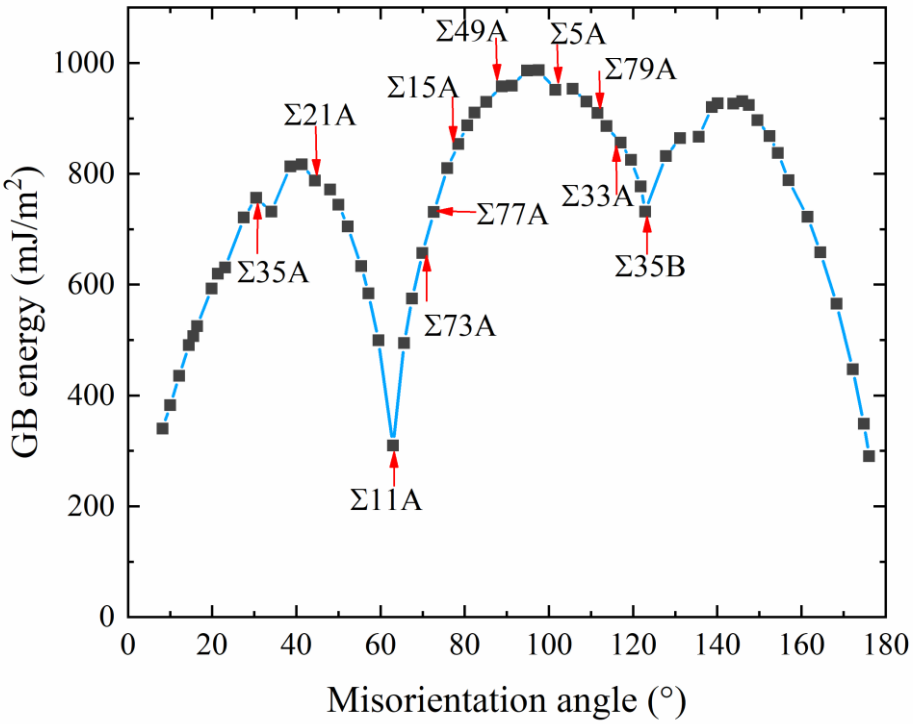

Fig. 4-3 <112>-axis GB energy of Cu as a function of the misorientation angle.

It should be noted that different slip planes may cause different interaction mechanisms and different critical shear stresses because of the local GB property, as shown in Fig. 3-3 for Σ11. Therefore, for each GB, various slip planes were selected and corresponding results are given in the later parts. The number of potential slip planes varies according to the type of the GB. Six independent slip planes were found for Σ11 GB, however, but there were 12 for Σ49A GB. The minimum of the critical shear stress for each GB is given in Table 4-1, because we are interested in the weakest point for the defect interactions. The absorption (denoted A), transmission (denoted T) and pile-up phenomena (denoted P) were all observed in the simulations for different GB structures (see Table 4-1).

Table 4-1 Crystallographic and mechanical details of the edge dislocation-GB interactions. For the interaction events, A stands for absorption, T stands for transmission and P stands for pile-up.

CSL	**Rotation angel** (^{o})	**GB Plane**	**GB Energy** (mJ/m^2)	**Leading partial absorbed stress** (MPa)	**Trailing partial absorbed stress** (MPa)	**Events**	**Events stress** (MPa)
35A	34.05	$(\bar{3}\,5\,\bar{1})$	732	162	670	A	670
21A	44.42	$(\bar{2}\,4\,\bar{1})$	788	/	/	P	/
21A	44.42	$(\bar{2}\,4\,\bar{1})$	788	130	370	A	370
11A	62.96	$(\bar{1}\,3\,\bar{1})$	309	58	1330	A	1330
73A	69.97	$(\bar{3}\,11\,\bar{4})$	657	89	1220	T	1700
73A	69.97	$(\bar{3}\,11\,\bar{4})$	657	87	600	A	600
77A	72.62	$(\bar{2}\,8\,\bar{3})$	731	60	740	T	1730
15A	78.46	$(\bar{1}\,5\,\bar{2})$	854	76	280	A	280
49A	88.83	$(\bar{1}\,9\,\bar{4})$	958	60	240	A	240
5A	101.54	$(0\,2\,\bar{1})$	951	64	310	A	310
79A	111.54	$(1\,11\,\bar{6})$	909	80	230	A	230
33A	117.01	$(1\,7\,\bar{4})$	856	95	510	A	510
35B	122.88	$(\bar{1}\,\bar{5}\,3)$	731	99	380	A	380

4.2.1. Case of absorption

For most of the situations, the absorptions were observed as shown in Table 4-1. Taking $\Sigma 11A(1\ \bar{3}\ \bar{1})$ as a reference, the perfect edge dislocation with the Burgers vector of $1/2[1\ \bar{1}0]$ was dissociated to the leading and trailing partials which were linked by a stacking fault (SF). The corresponding dissociation can be described by Eq. (4-2).

With increasing shear deformation, the two partial dislocations with a SF of about 37 Å wide moved to and impacted the GB. The mechanical behavior during this process is represented by the shear stress/potential energy of the whole system versus shear strain curve (Fig. 4-4). The shear stress for the whole system was calculated by the virial theorem. The loading process showed that in the initial deformation stage, the stress increased with the applied strain when the edge dislocation moved toward the GB. Once a leading partial impinged on the GB (indicated by I in Fig. 4-4 and plotted in Fig. 4-5(b)), the leading partial was immediately absorbed. The subtle reduction of the stress and potential energy illustrated an attractive effect of the GB on the leading partial. Nevertheless, no significant GB structure change was observed. The repulsive effect of the GB on the trailing partial then forced the stress to steadily increase because the applied strain continuously increased. Subsequently, a misfit step and a displacement shift coincidence (DSC) dislocation appeared at the upper half GB, as shown in Fig. 4-4 II and Fig. 4-5(c). Eventually, thoroughgoing absorption events emerged at the critical shear stress τ and shear strain γ of 1330 MPa and 3.79%, respectively. It should be noted that both the stress and energy sustained modest reductions, which was moderated by the GB-structure rearrangement. Several misfit steps on the GB plane and one tumor like mass appeared at the impinging points as indicated by III in Fig. 4-4 and two dashed circles in Fig. 5(d). The interaction mechanism and obtained CRSS agreed well with the results of Yu et al. [29]. Additionally, 6 potential slip planes all showed the absorption events and the critical shear stresses were in the range 1300-1320MPa.

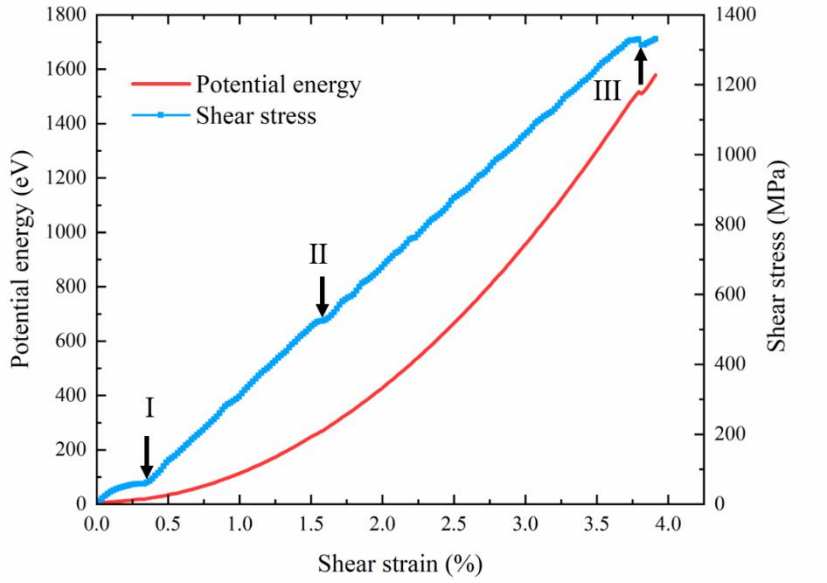

Fig. 4-4 Shear stress and potential energy evolution with respect to the shear strain for the $\Sigma 11A(1\ \bar{3}\ \bar{1})$ case. The roman number in Fig. 4-4 correspond to the state in Fig. 4-5 with the same symbol. I: the leading partial was absorbed into the GB; II: a misfit step appeared on the GB; III: trailing partial was absorbed into the GB.

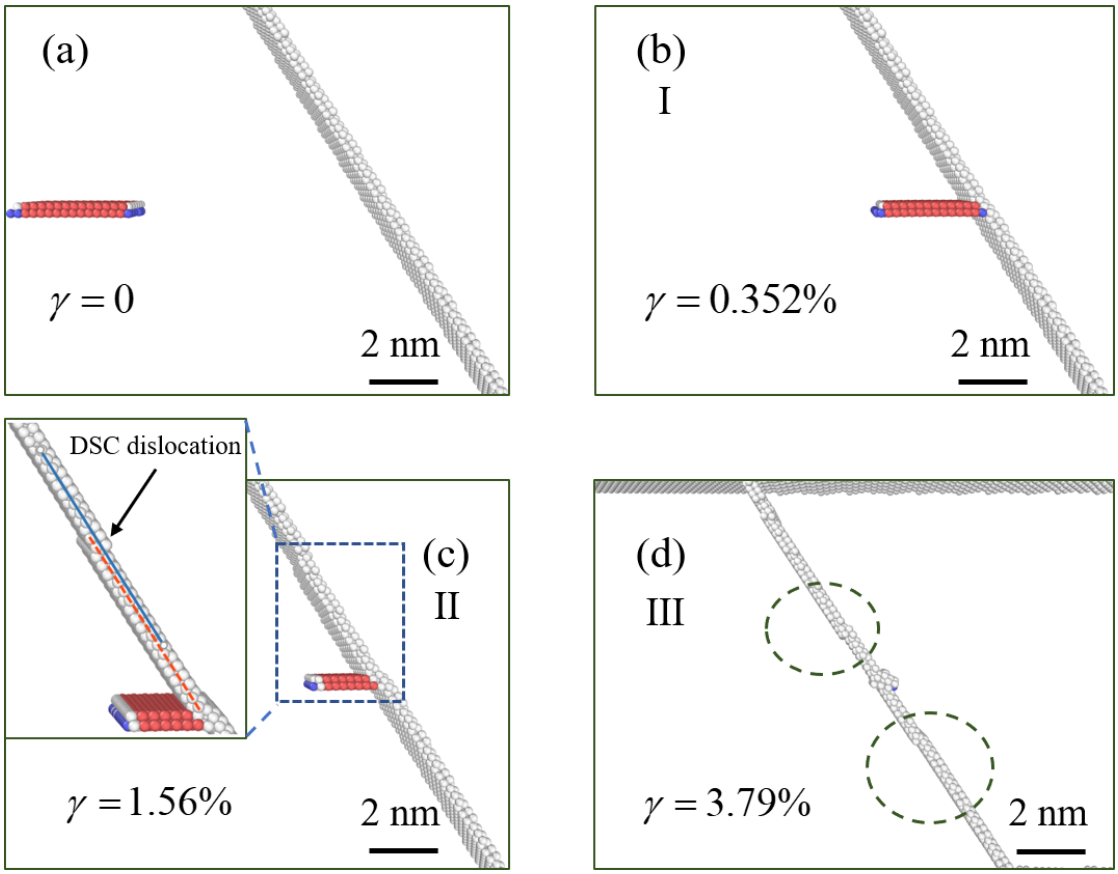

Fig. 4-5 Edge dislocation- Σ11A($1\ \bar{3}\ \bar{1}$) interaction process: (a) Initial state; (b) Absorption of the leading partial dislocation; (c) Occurrence of the misfit step and DSC dislocation; (d) Absorption of the trailing partial dislocation of the final state. Roman numbers in (b) - (d) correspond to the state in Fig. 4-4 with the same symbol. The atoms within perfect FCC structure are invisible for brevity. The scale bar is 2 nm.

4.2.2. Case of pile-up

For the Σ21A($\bar{2}\ 4\ \bar{1}$) GB, three of the five potential slip planes showed the pile-up phenomena as described in Appendix Table.S2. When the edge dislocation moved to the GB, in contrast to spontaneous absorption of the leading partial dislocation in Σ11A($1\ \bar{3}\ \bar{1}$), the leading partial dislocation was initially repelled by GB, as illustrated in Fig. 4-6. Higher stress, even up to 1050 MPa, did not alleviate this situation, which

merely shrank the width of the stacking fault. The high stress or strain state triggered the GB dislocation source and subsequently partial dislocations were generated and emitted from multiple points on the GB (Fig. 4-6(d)). However, the incident leading partial dislocation was still repelled by the GB. For this situation, we did not obtain a clear event stress because the dislocation never touched the GB plane.

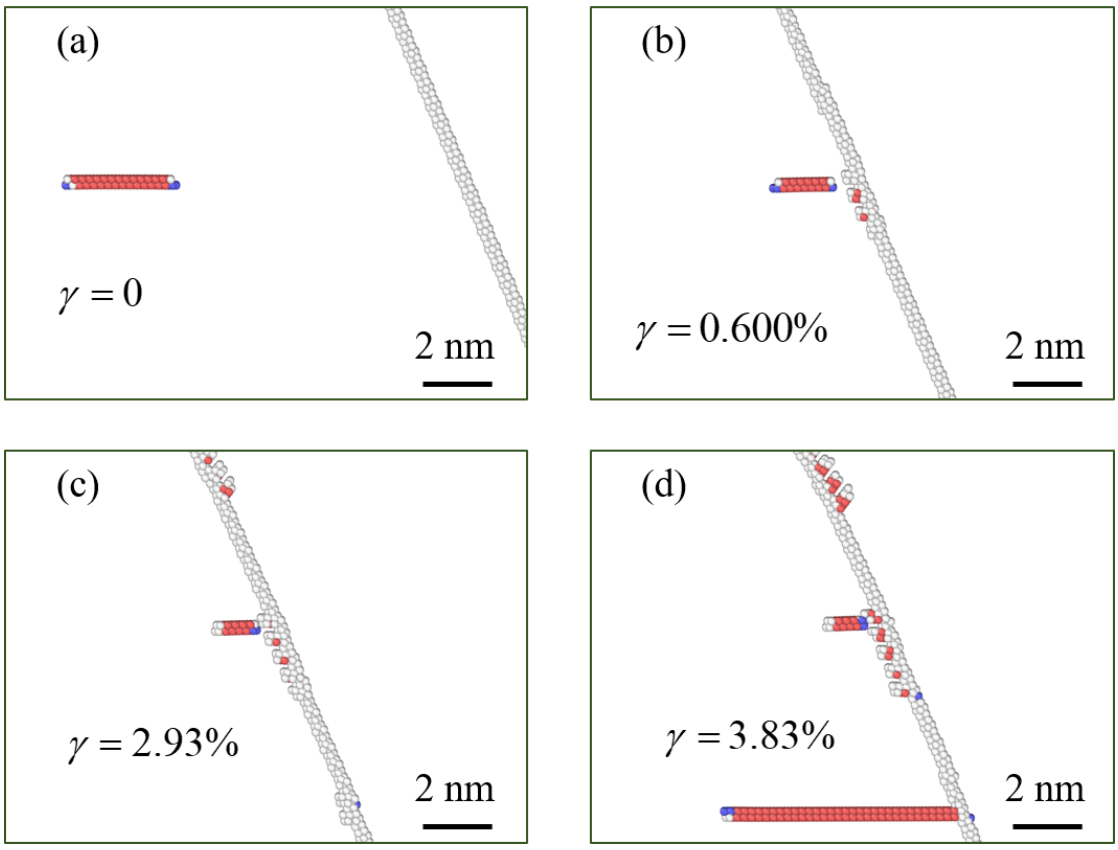

Fig. 4-6 Edge dislocation-$\Sigma 21A(\bar{2}\ 4\ \bar{1})$ interaction process: (a) Initial state. (b) Edge dislocation hindered by the GB. (c) Edge dislocation piled up before the GB and dislocation sources activated on the GB. (d) Partial dislocation released from GB in the high strain state. The edge dislocation still piled up before the GB. The scale bar is 2nm.

4.2.3. Case of transmission

The zigzag type $\Sigma 73A(\bar{3}\ 11\ \bar{4})$ GB is a reference case for the dislocation penetration

and transmission into the adjacent grain (Fig. 4-7 and Fig. 4-8). Analogous to the Σ11A GB, the leading partial dislocation was assimilated once it touched the GB plane. The stacking fault further shrank until trailing partial dislocation absorption occurred at about 1200 MPa stress, indicated by II in Fig. 4-7. One should notice that dislocation transmission did not occur at the same time as absorption. The local GB structure reorganized to serve as the easy release position and emitted one full edge dislocation with the perfect Burgers vector of $1/2[10\bar{1}]_{adjacent}$ at about 1704 MPa. A residual dislocation was found on the GB with the Burgers vector of $\frac{1}{146}[28\ 20\ 13]$. Correspondingly, the stress and potential energy decreased once the transmission finished, as indicated by III in Fig. 4-7. Eventually, the perfect edge dislocation escaped from the right free surface to release the redundant energy and stress. However, absorption cases were also found for some slip planes and lower critical absorption stresses were found at around 600-650 MPa.

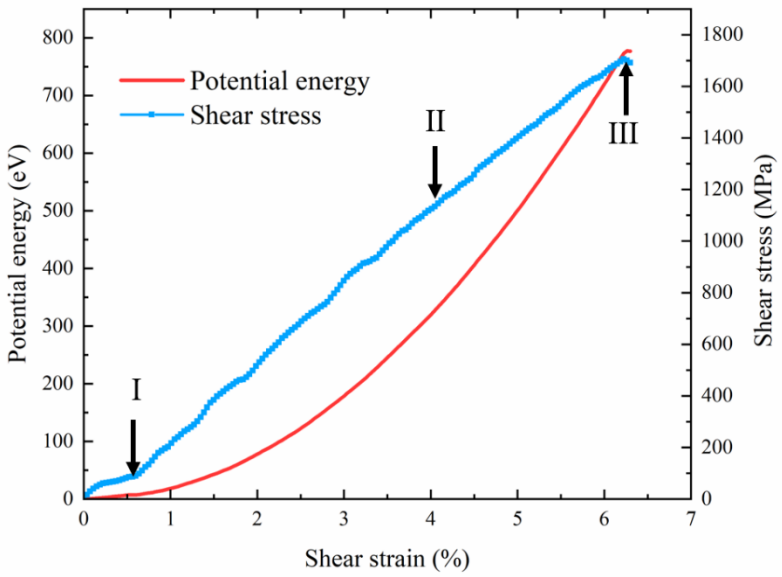

Fig. 4-7 Shear stress and potential energy evolution with respect to the shear strain for $\Sigma 73A(\bar{3}\ 11\ \bar{4})$. Roman numbers in Fig. 4-7 correspond to the states in Fig. 4-8 with the

same symbol. I: The leading partial was absorbed into the GB; II: The trailing partial was absorbed into the GB; III: The penetrating dislocation started to germinate.

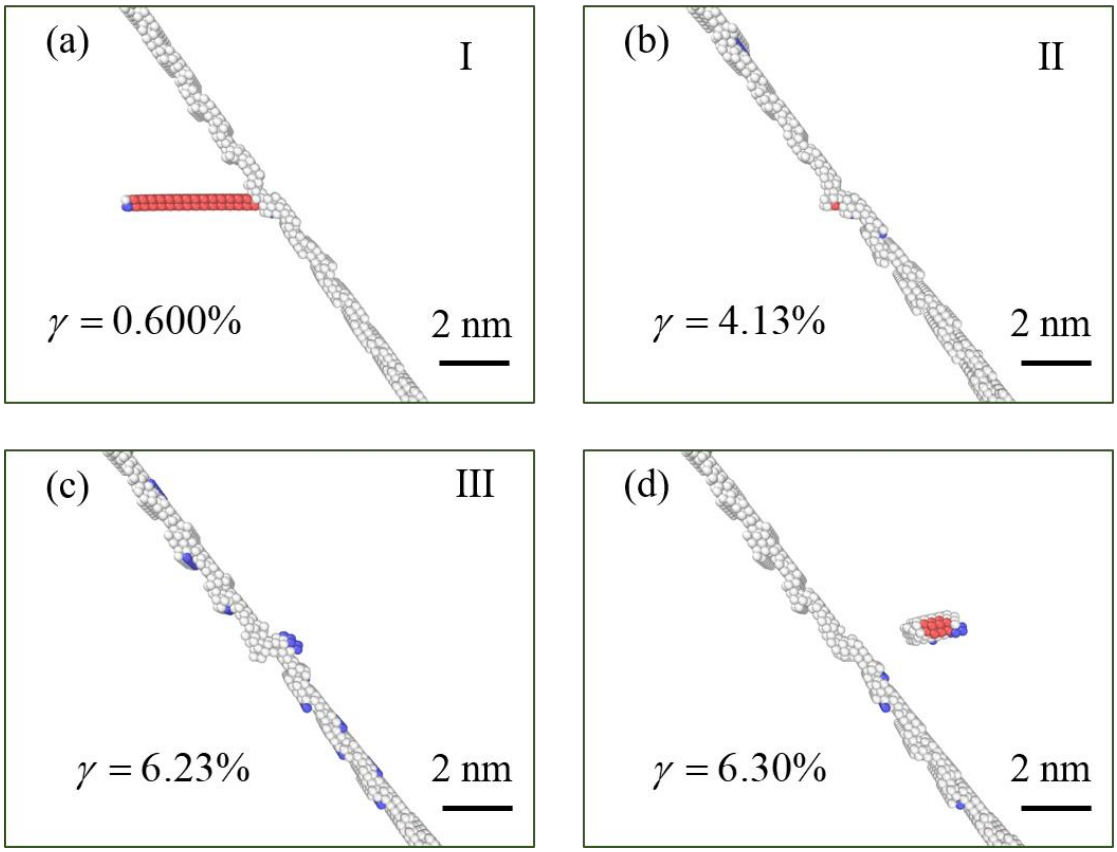

Fig. 4-8 Edge dislocation- Σ73A interaction process: (a) Absorption of the leading partial dislocation; (b) Absorption of trailing partial dislocation; (c) Initiation of the penetrating dislocation; (d) Full edge dislocation movement to the free surface. The roman numbers help to identify the stress state and are the same as those in Fig. 4-7. The scale bar is 2nm.

4.2.4. Relationship between critical stress and GB energy

All the simulations verified that the leading partial dislocations would be incorporated first followed by the trailing partial absorptions except for the pile-up case. The dislocations might be emitted from the interaction points if further loading was supported.

The critical absorbed stress for leading partial and trailing partial with respect to the GB energy are shown in Fig. 4-9. But it is worth mentioning that different potential slip planes estimated different critical shear stresses. Results of different slip planes of all the modelled GBs can be found in the Appendix. We selected and plotted the minimum for each GB in Fig. 4-9 and Table. 4-1, because we are interested in the weakest point of the GB during defect interactions. This is also in line with the engineering application viewpoint because the weakest point determines the threshold of the defect interactions.

The critical shear stress for trailing partial absorption decreased as the static GB energy increased, as shown in Fig. 4-9(a). This agrees well with the consensus that the GB with higher energy may be more unstable and much more easily react with the other defects [26]. Hence, the high-energy structures should be less able to hinder the dislocation sliding and more easily absorb the trailing partial dislocation. Nevertheless, the critical absorption stresses for the leading partial dislocations were severely scatter, and no obvious tendency was detected (Fig. 4-9 (b)). This can be explained by the attractive effect of the GB for the leading partial dislocations. Actually, all of the absorption processes immediately occurred once the leading partial dislocations attached to the GB. By more meticulous MS simulations, when we inserted the dislocation much closer to the GB, the perfect edge dislocations first dissociated into partial dislocations and then the leading partial dislocations were spontaneously absorbed into the GB during the energy minimization process under no external applied stress. Thereafter, the trailing partials were consistently repelled by the GB unless sufficiently high stress was applied for absorption. This spontaneous absorption indicates that the threshold for the edge dislocation-GB interaction may be controlled by the trailing partials rather than the leading partials. However, even the general trend supports that a GB with higher GB energy may need lower stress to absorb the trailing partial dislocation if we consider the weakest point of the GB, there are still some exceptions. For example, even though $\Sigma 35$ A, $\Sigma 35$B and $\Sigma 77$ A all had the same GB energy of about 731 mJ/m^2, the critical shear

stresses for absorption were different. This difference is caused by the local GB structures which are also important to determine the interaction behaviors. However, the tendency still holds: the critical shear stress is lower for the defect interaction with higher GB energy.

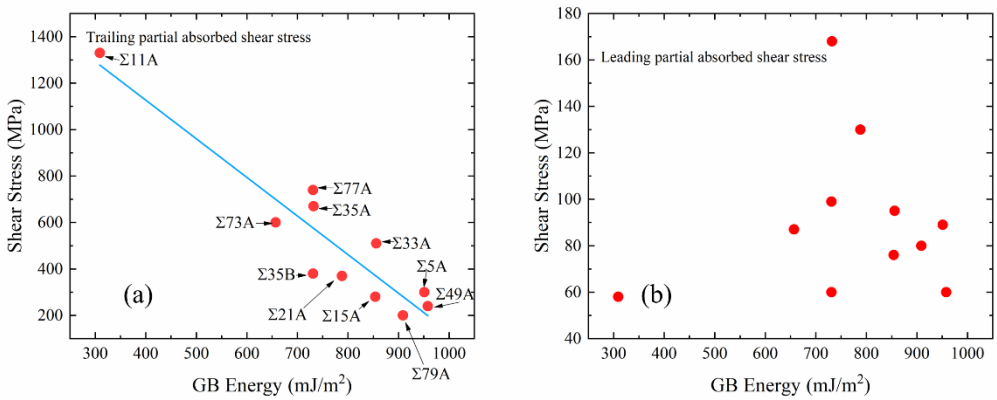

Fig. 4-9 (a) Critical absorbed stress for trailing partial dislocation versus GB energy. (b) Critical absorbed stress for leading partial versus GB energy. The red points are the data from MD and the blue line shows the trend.

4.3. Transition state theory parameters of interactions

4.3.1. Activation barriers in various strain or stress states

One implicit drawback of MD simulation is that, because of the restriction of the extremely high strain rate or other external perturbations, the physical meaning of the phenomenon depicted by the atomic simulations could hardly compare with the experimental rate-dependent response [29]. TST provides another way to accurately predict the rate and thermal effects with the accurately determined energy barrier. For a thermally activated process such as a dislocation slip or defect interaction, TST establishes the corresponding rate at the constant stress state by

$$\Gamma = v\exp(\frac{-\Delta G(\tau)}{k_B T}) \tag{4-2}$$

where, k_B is the Boltzmann constant, T is the absolute temperature, v is the fundamental attempt frequency usually on the order of $10^{11} \sim 10^{12} \mathrm{s}^{-1}$, and ΔG is the activation Gibbs free energy which depends on the stress, temperature and system size.

If the system is at a constant strain state, $\Delta G(\tau)$ can be replaced by Helmholtz activation free energy $\Delta F(\gamma)$. This thermodynamic quantity is the energy barrier for defect interaction in the absence of external work [28,31]:

$$\Delta F(\gamma) = \Delta U(\gamma) - T\Delta S_{\gamma}(\gamma, T) \tag{4-3}$$

where $\Delta U(\gamma)$ is the activation energy obtained by the NEB method, and ΔS_{γ} is the activation entropy at constant strain as the function of the strain γ and temperature *T*, which can be estimated by direct MD simulations under finite temperature. The second term of Eq. (4-3) can be ignored when the temperature is close to 0 K, like the present MD simulations. Through rigorous derivation [31,47], it can be proved that $\Delta F(\gamma) \approx \Delta G(\tau)$ only if the volume of the bi-crystal is much larger than the activation volume.

4.3.2. Cases of absorptions

A few representative cases of interaction processes were successfully evaluated by TST in different strain states. Two cases with almost the same CSL values and GB energies were selected as absorption cases.

In the case of $\Sigma 35\mathrm{A}$, the typical absorption mechanism was observed. The MEP estimated by CINEB for different stress state are shown in Fig. 4-10. The manifold MEPs varied according to the stress. It is worth mentioning that the NEB calculations were implemented under the same strain state for the initial and final replica as described in Section 4.2. Therefore, the corresponding activation energy ΔU shown in Fig. 4-10 is

actually under the framework of the Helmholtz activation free energy. Although Fig. 4-10 shows the relationships between ΔU and various stresses, the relationships are actually equivalent to that between the ΔU and strains because the shear stress τ and strain γ are conjugate variables with a linear relationship [170]. More specifically, from the MD results in Section 4.3, only elastic contributions were included during the defect interaction process since no significant dislocation slip or generation was detected. This elastic deformation guarantees a constant slope of the strain-stress curve of the interaction stage, which is equal to the local shear modulus of the system.

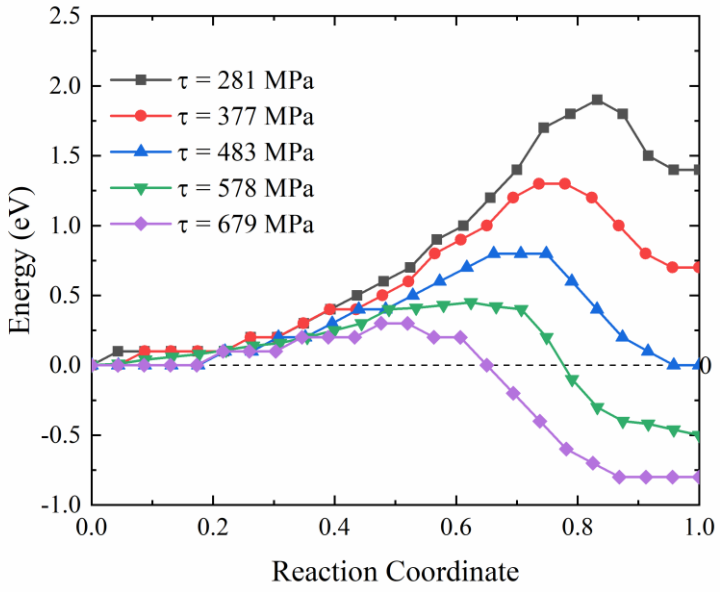

Fig. 4-10 Reaction path as a function of applied stress for Σ35A defect interaction. The dashed line represents the zero-reference line.

Taking the MEP for 377 MPa as an instance (the red curve in Fig. 4-10), the MEP is shown in Fig. 4-11 (a) and corresponding atomic configurations of Point I, II and III are shown in Fig. 4-11(c)–(e). In this case, the CINEB method determined an activation barrier of 1.27 eV for the saddle point shown in Fig. 4-11 (d) (Point II in Fig. 4-11 (a)). The potential energy continuously increased to the saddle point, where the trailing partial

was almost completely absorbed by the GB. Once the absorption process was completed, energy would relax to the final replica (Point III in Fig. 4-11(a)). This interaction mechanism is almost the same as the MD simulation results, which verified the accuracy of the NEB relaxation process.

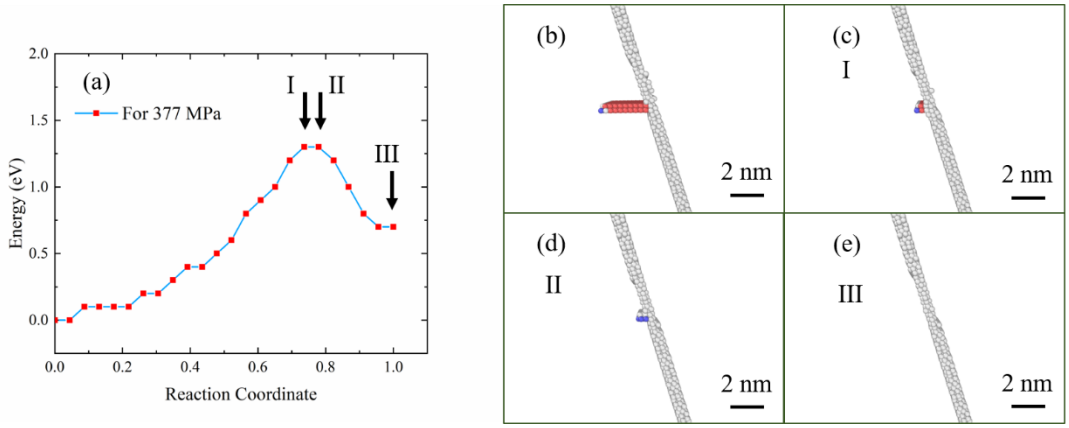

Fig. 4-11 MEP and atomic configurations of the Σ35A defects interaction. (a) MEP under 377 MPa. (b) Initial replica for the NEB calculation. (c)–(e) The NEB–predicted atomic configuration corresponding to Roman numbers in (a). The scale bar is 2nm.

The same CSL value does not guarantee the same defects interaction results from an energy aspect. The MEP of Σ35B is shown in Fig. 4-12. Although the CSL value, or even the GB energy and interaction event type, was almost the same, the stress for a trailing dislocation to be absorbed into Σ35B was 380 MPa which was smaller than that of Σ35A, as referred in Table 4-1. The local GB structure difference caused a sharper MEP for Σ35B in Fig. 4-12. This also provides direct evidence for the suggestion of Bayerschen [48] that the specific mechanism of the defect interaction is significantly influenced by the local GB structure. Moreover, it suggests that the CSL value or static GB energy itself is not sufficient to predict the interaction behavior.

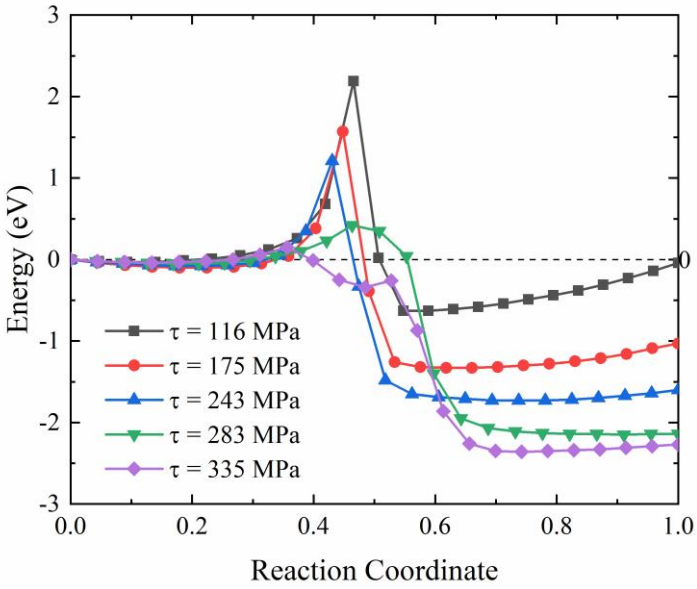

Fig. 4-12 Reaction path as a function of the applied stress for the Σ35B defects interaction. The dashed line is the zero-reference line.

4.3.3. Case of the transmission

The dislocation transmission event was estimated by TST for the Σ73A case, which is mentioned in Section 4.3.3. The stresses for the trailing partial dislocation to be absorbed and transmitted were 1220 MPa and 1700 MPa, respectively. Because the potential energy surface is severely distorted under the high-stress or high-strain state [31], the standard NEB or CINEB method may lead to an inaccurate MEP because the saddle point moves close to the initial state. The FENEB method was used to mitigate this problem [12]. The MEP in the range from 455 MPa to 1435 MPa is shown in Fig. 4-13. Analogous to the absorption case, the energy barrier showed an inversely proportional relationship with the stress, and the higher stress state required lower energy to activate the event. Fig. 4-14 provides the detailed atomistic information for the MEP under 455 MPa as shown by the black curve in Fig. 4-13. The FENEB predicted an activation energy of about 6.11 eV. The mechanism given by FENEB is identical to the MD simulation. When the leading

partial dislocation started to germinate in the adjacent grain, the system climbed over the peak of the MEP, as shown by the saddle point in Fig. 4-14(c). The perfect edge dislocation was then emitted into the adjacent grain and moved out of the model to form a misfit step on the free surface. In the later dislocation slip process, the energy landscape continually decreased to relax the system.

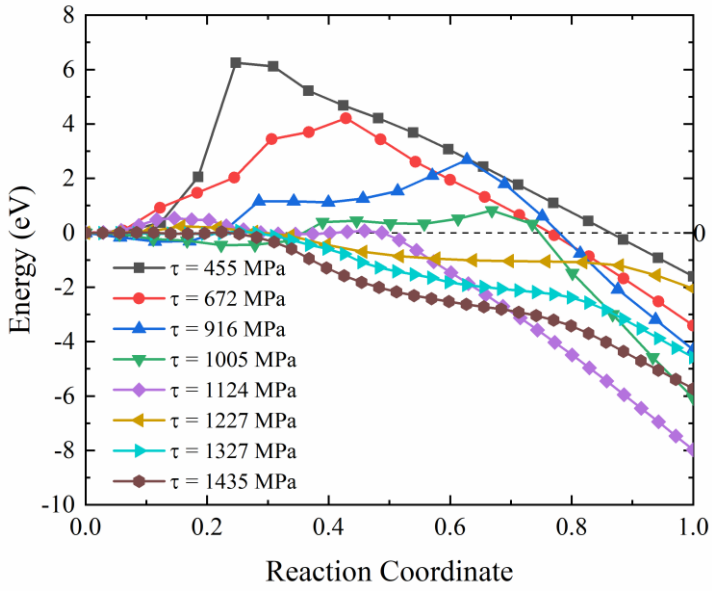

Fig. 4-13 Reaction path as a function of the applied stress for the Σ73A defect interaction.

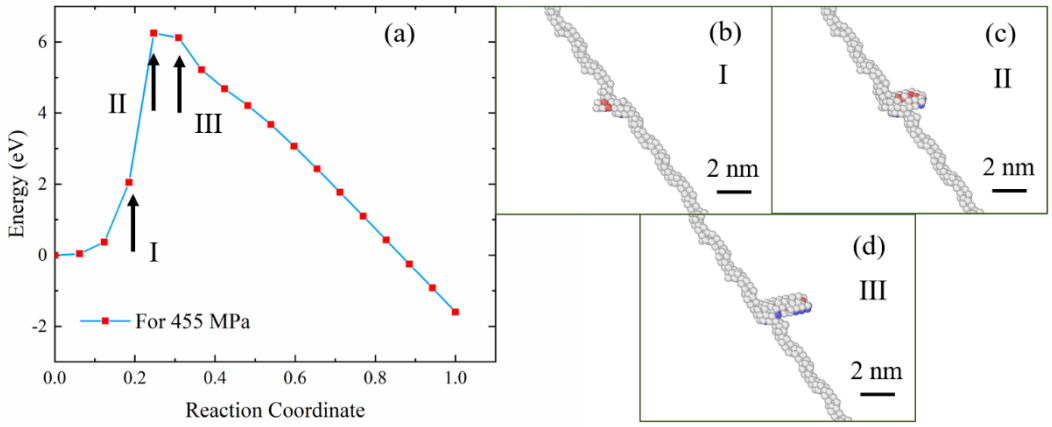

Fig. 4-14 MEP and atomic configurations of the Σ73A defect interaction. (a) MEP under 455MPa. (b)–(d) The NEB predicted atomic configurations corresponding to Roman numbers in (a). The scale bar is 2nm.

4.3.4. Activation volume and strain-rate sensitivity

In this part, we will quantitatively estimate the interaction processes and link the results to the experimental data by TST.

Based on the Gibbs free energy ΔG, the true activation volume V_{stress} assumed under constant stress τ by atomic simulation is expressed as

$$V_{stress} = -\frac{\partial \Delta G(\tau)}{\partial \tau} \tag{4-4}$$

The NEB results reported in Section 3.3.1 were based on a constant strain state. Similarly, the true activation volume V_{strain} as a function of the Helmholtz free energy ΔF can be calculated by

$$V_{strain} = -\frac{\partial \Delta F(\gamma)}{\mu \partial \gamma} = -\frac{\partial \Delta F(\gamma)}{\partial \tau} \tag{4-5}$$

where μ is the local shear modulus of the system and γ is the constant strain. The prerequisites for establishment of the above equation are that the volume of the system should be much larger than the activation volume and the mechanical response of the whole system should be almost linear [31].

Different interaction mechanisms or different rate processes dramatically produce different activation volumes. For example, lattice diffusion would give an activation volume of about $0.1b^3$ because only a small group of atoms are involved during the diffusion process. However, for a forest cutting process, such as the Orowan looping of a dislocation line across the pinning points in coarse-grained metal, the activation volume can reach about 1000 b^3 [29]. A normal dislocation-interface mediated process usually has an apparent activation volume of 10-100 b^3. Therefore, the activation volume has

the capability of characterizing the kinematic signature of the deformation mechanism. Conventionally, the apparent activation volume V_A can be estimated by the experimental strain-rate sensitivity m [12,29,49]:

$$V_A = \frac{\sqrt{3}k_B T}{\sigma m} = \sqrt{3}k_B T \frac{\partial \ln \dot{\varepsilon}}{\partial \sigma} \tag{4-6}$$

where $\dot{\varepsilon}$ is the strain rate and $\sigma = M * \tau_{CRSS}$ is the critical normal stress for the polycrystalline material, in which $M = 3.1$ represents the Taylor factor for FCC materials and τ_{CRSS} is the critical resolved shear stress for the bi-crystal model. Furthermore, because all MD or MS simulations only contain one single dislocation-GB interaction process, the true activation volume can be converted to the polycrystalline materials [12,29], by

$$V_A = \frac{1}{M} V_{strain} \tag{4-7}$$

The strain-rate sensitivity m can be conveniently derived from the true activation volume predicted by the TST which also successfully links the results of the atomic simulation with the actual experiments. Specifically, the true activation volume can be determined through NEB calculations by a method described later. Eq. (4-7) then gives apparent activation volume. Following this, the strain-rate sensitivity *m* can be calculated from Eq. (4-6), by

$$m = \frac{\sqrt{3}k_B T}{\sigma V_A} = \frac{\sqrt{3}Mk_B T}{\sigma V_{strain}} \tag{4-8}$$

The relationships between the activation energies and stresses for $\Sigma 35\,\mathrm{A}$, $\Sigma 35\mathrm{B}$ and $\Sigma 73\,\mathrm{A}$ are given in Fig. 4-15(a)–(c), respectively. A phenomenological equation to describe the dependency of ΔG on the stress was provided by Kocks et al [28]:

$$\Delta G(\tau) = \Delta G_0 \left[1 - \left(\frac{\tau}{\tau_0} \right)^p \right]^q \tag{4-9}$$

where ΔG_0 is the activation energy at zero load and 0 K, τ_0 is the athermal stress when the thermally activated process switches to the athermally mechanical process and dislocation immediately interacts with GB without any thermal perturbation. p and q are the fitting parameters. Considering the conjugate pair of τ and γ in the constant strain state at close to 0 K, Eq. (4-9) can be converted to

$$\Delta F(\gamma) = \Delta U(\gamma) = \Delta U_0(1-\frac{\gamma}{\gamma_0}) = \Delta U_0(1-\frac{\mu\gamma}{\mu\gamma_0}) = \Delta U_0(1-\frac{\tau}{\tau_{TST}}) \quad (4\text{-}10)$$

where ΔU_0 is the activation energy at zero load. γ_0 and τ_{TST} are the critical athermal strain and stress for the interaction at 0 K under the framework of Helmholtz activation free energy, respectively. p and q in Eq. (4-9) are simplified as 1 when considering the linear property shown in Fig. 4-15. Following this assumption, Fig. 4-15 also shows the fitting curves for $\Sigma 35A$, $\Sigma 35B$ and $\Sigma 73A$ using Eqs. (4-5) and (4-10).

Combining Eqs. (6) and (11) is a convenient way to calculate the critical interaction stress τ_{TST} or critical interaction strain γ_0. The intercept of the fitting lines on the Energy barrier axis can be regarded as ΔU_0. The corresponding slopes of fitting curves in Fig. 4-15(a)–(c) can be regarded as the true activation volumes, as described by Eq. (4-5). The critical athermal shear stress or shear strain can be determined by the intercept on the shear-stress axis or combining the slope and ΔU_0 following Eq. (4-10). The activation energies linearly decrease with the stress for all three cases. When the system is under a higher strain/stress state, lower activation energy is needed for the thermally activated process. And hence, larger Γ will be generated according to Eq. (2-1). Since the dimension of Γ is the frequency, i.e. /s, we can easily conclude that a defect interaction under a high-stress state interacts faster than that under the low-stress state. The slopes are -0.00398, -0.00947 and -0.00926 for $\Sigma 35A$, $\Sigma 35B$ and $\Sigma 73A$, respectively. More detailed information of fitting curves and TST-based parameters are

given in Fig. 4-15(a)–(c) and Table 2.

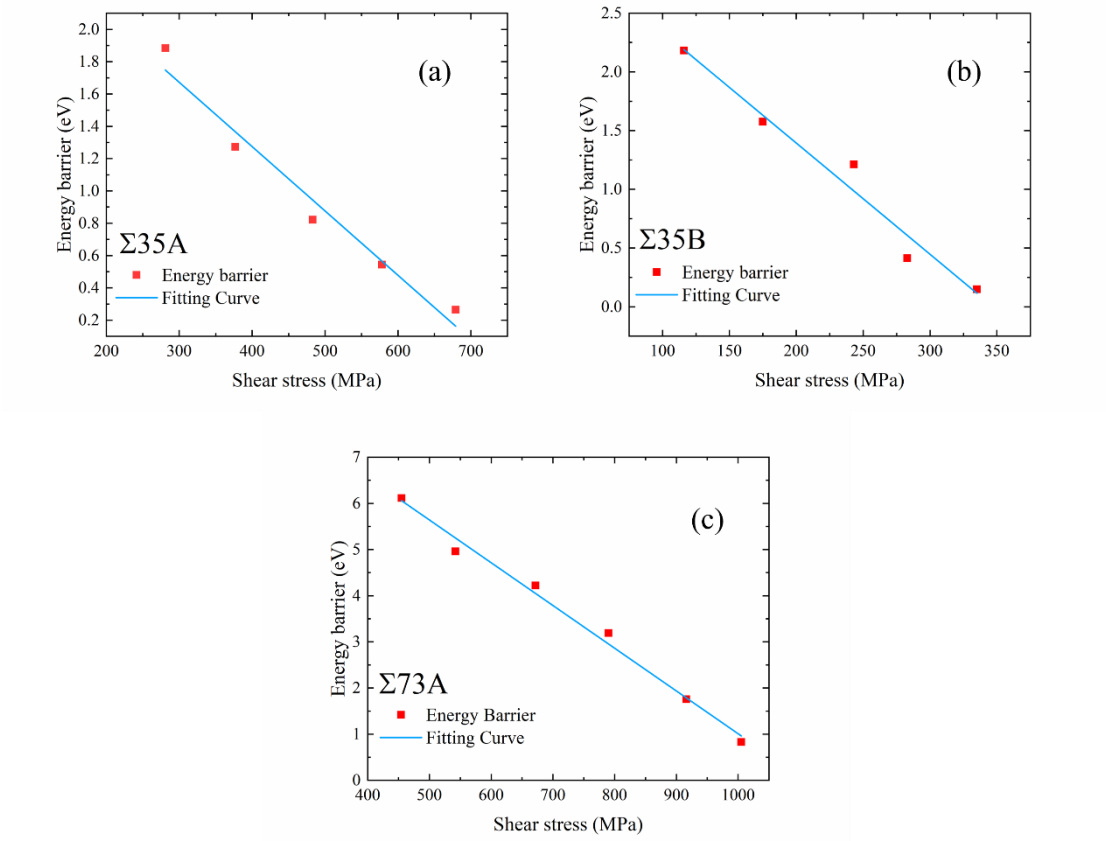

Fig. 4-15 Variation of the activation energy as a function of applied stress for (a) Σ35A, (b) Σ35B and (c) For Σ73A. The red points are the NEB data and blue lines are the fitting curves.

As a summary, the TST parameters, including V_A, V_{strain}, TST predicted critical interaction shear stress from Eq. (4-10) τ_{TST}, and the TST predicted strain-rate sensitivity m are given in Table 4-2. It is worth mentioning that the strain-rate sensitivities were derived at 300 K to agree with the experimental conditions and τ_{TST} served as τ_{CRSS} when considering the orientations of the models.

Table 4-2 TST predicted rate-dependent parameters. τ_{TST} is the TST predicted critical shear stress, ΔU_0 is the activation energy at zero load, V_{strain} is the true activation volume, V_A is the apparent activation volume, and m is the strain rate sensitivity predicted by TST.

GB	**Event**	**GB energy** (mJ/m^2)	**Absorption shear stress by MD (MPa)**	τ_{TST} **(MPa)**	ΔU_0 **(eV)**	V_{strain} (b^3)	V_A (b^3)	m
Σ35A	A	732	693	720	2.87	40	13	0.016
Σ35B	A	731	380	374	3.53	95	30	0.012
Σ73A	T	657	1220	1109	10.27	96	31	0.004

From the experiments of ultrafine-crystal (UFC) Cu and microcrystalline (MC) Cu [49], the apparent activation volumes are in the range 12~48 b^3, where b is the Burgers vector of 2.56 Å. The TST predicted the apparent activation volumes to be in the range 13~31 b^3 depending on the GB type. For the strain-rate sensitivity, experiments provided the values of 0.006, 0.007, and 0.019 for 40 μm MC-Cu [50], 12-90 μm MC-Cu [51], and 300 nm cold-rolled UFC-Cu [52], respectively. The strain rate sensitivities of our simulations are in range of 0.004 to 0.016 which are almost the same with laboratory experiments.

Although the types of GBs we simulated were not strictly consistent with the GBs in the experiment, polycrystalline is an average manifestation of multiple GBs. Therefore, we think that our calculation results are reasonable and can reflect the average characteristic. The activation volumes that are almost consistent with the experiments

further reveal the essence of the dislocation-mediated interaction mechanism and it is indeed a rate-controlling step of plastic flow. The good agreement also verified that the difference between the Gibbs and Helmholtz activation free energies are negligible when the system volume is much larger than the activation volume.

Furthermore, TST predicted that the event stresses are very closed to the MD results especially for the absorption case. However, for $\Sigma 73A$, the rate-dependent parameters were estimated by the data below 1000 MPa. This caused slight deviation in the prediction of the critical shear stress because high stress or strain distorts the energy landscape of the system and the tendency of the energy barrier-stress curve slightly flattens in such a high-stress state. In addition, the activation energy for the transmission event was much higher than that for the absorption event. This is similar for the screw-twin boundary interactions [12], where the activation energy has been reported to be 0.49 eV for absorption but more than 5 eV for transmission into the adjacent grain. The NEB method was applied for another transmission event and gave the energy barrier of 5.4 eV under 440 MPa in $\Sigma 77A$. This barrier is larger than the critical activation energy under zero load for the absorption cases in this study (Table 4-2), which supports that transmission need more energy to be activated than absorption. The NEB calculations of $\Sigma 49A$ under 83 MPa, $\Sigma 5A$ under 85 MPa, $\Sigma 79A$ under 142 MPa estimated the energy barriers for absorption of 0.3, 0.06 and 0.47 eV, respectively. By extrapolating Eq. (4-10), the energy barriers of $\Sigma 35A$, $\Sigma 35B$ and $\Sigma 73A$ (group A) are all larger than that of $\Sigma 49A$, $\Sigma 5A$ and $\Sigma 79A$ (group B) under the corresponding stress or strain state. It was qualitatively predicted that group A had a lower GB energy than group B so higher critical energy is needed for certain interactions.

4.4. Summary

The GB energies of <112>-axis symmetric tilt GBs and their interactions with single edge dislocation have been investigated by MD simulations and TST. The CRSS for

leading and trailing partial dislocations to be absorbed into the GB were determined by MD simulations. The NEB method was performed to estimate the energy barriers for various strain or stress states. The data obtained by the atomic simulations were compared with the experimental data, especially the activation volumes of the interaction events.

It was found that the interaction phenomena depended on the GB type when an edge dislocation impinged upon the interface. Possible phenomena include absorption, transmission and pile-up. A leading partial dislocation was attracted and spontaneously absorbed once it touched the GB regardless of the magnitude of the shear stress. This means that only the trailing partial dislocation determines the critical interaction shear stress, not the whole partial dislocation pair. The highest absorption stress for the trailing partial is up to 1330 MPa for $\Sigma 11A$. In contrast, the lowest one is about 230 MPa for $\Sigma 79A$. If we consider the weakest point of the GB structure, a GB with a higher GB energy requires a lower critical interaction stress. This agrees well with the hypothesis that a lower energy GB has a more stable structure. TST estimation provided the rate-dependent parameters for a series of GBs. In general, the activation barrier decreased as the applied load increased, and the activation energy for transmission was normally higher than that for absorption. The apparent activation volumes of the interactions between edge dislocations and <112>-axis symmetric tilt GB were in the range 13~31b^3 which are reasonable values compared with experiments. The strain-rate sensitivities derived from the framework of Helmholtz free energy were 0.004~0.016, which are also in good agreement with experimental data.

References

[1] N.C. Admal, G. Po, J. Marian, A unified framework for polycrystal plasticity with grain boundary evolution, International Journal of Plasticity. 106 (2018) 1–30.

[2] S. Haouala, R. Alizadeh, T.R. Bieler, J. Segurado, J. Llorca, Effect of slip transmission at grain boundaries in Al bicrystals, International Journal of Plasticity. 126 (2020).

[3] D. Chen, S. Xu, Y. Kulkarni, Atomistic mechanism for vacancy-enhanced grain boundary migration, Physical Review Materials. 4 (2020) 1–9.

[4] D.W. Adams, D.T. Fullwood, R.H. Wagoner, E.R. Homer, Atomistic survey of grain boundary-dislocation interactions in FCC nickel, Computational Materials Science. 164 (2019) 171–185.

[5] T.R. Bieler, P. Eisenlohr, C. Zhang, H.J. Phukan, M.A. Crimp, Grain boundaries and interfaces in slip transfer, Current Opinion in Solid State and Materials Science. 18 (2014) 212–226.

[6] J.P. Couzinié, B. Décamps, L. Priester, Interaction of dissociated lattice dislocations with a $\sum = 3$ grain boundary in copper, International Journal of Plasticity. 21 (2005) 759–775.

[7] Z.H. Jin, P. Gumbsch, K. Albe, E. Ma, K. Lu, H. Gleiter, H. Hahn, Interactions between non-screw lattice dislocations and coherent twin boundaries in face-centered cubic metals, Acta Materialia. 56 (2008) 1126–1135.

[8] Z.H. Jin, P. Gumbsch, E. Ma, K. Albe, K. Lu, H. Hahn, H. Gleiter, The interaction mechanism of screw dislocations with coherent twin boundaries in different face-centred cubic metals, Scripta Materialia. 54 (2006) 1163–1168.

[9] M. Schneider, E.P. George, T.J. Manescau, T. Záležák, J. Hunfeld, A. Dlouhý, G. Eggeler, G. Laplanche, Analysis of strengthening due to grain boundaries and annealing twin boundaries in the CrCoNi medium-entropy alloy, International Journal of Plasticity. 124 (2020) 155–169.

[10] M.A. Tschopp, D.L. McDowell, Dislocation nucleation in Σ3 asymmetric tilt grain boundaries, International Journal of Plasticity. 24 (2008) 191–217.

[11] T. Tsuru, Y. Shibutani, Y. Kaji, Fundamental interaction process between pure edge dislocation and energetically stable grain boundary, Physical Review B - Condensed Matter and Materials Physics. 79 (2009) 1–4.

[12] T. Zhu, J. Li, A. Samanta, H.G. Kim, S. Suresh, Interfacial plasticity governs strain rate sensitivity and ductility in nanostructured metals, Proceedings of the National Academy of Sciences of the United States of America. 104 (2007) 3031–3036.

[13] L. Rémy, INTERACTION BETWEEN SLIP AND TWINNING SYSTEMS AND THE INFLUENCE OF TWINNING ON THE MECHANICAL BEHAVIOR OF fcc METALS AND ALLOYS., Metallurgical Transactions. A, Physical Metallurgy and Materials Science. 12 A (1981) 387–408.

[14] M.D. Sangid, T. Ezaz, H. Sehitoglu, Energetics of residual dislocations associated with slip-twin and slip-GBs interactions, Materials Science and Engineering A. 542 (2012) 21–30.

[15] M. Bönisch, Y. Wu, H. Sehitoglu, Hardening by slip-twin and twin-twin interactions in FeMnNiCoCr, Acta Materialia. 153 (2018) 391–403.

[16] W. Yu, Z. Wang, Interactions between edge lattice dislocations and Σ11 symmetrical tilt grain boundaries in copper: A quasi-continuum method study, Acta Materialia. 60 (2012) 5010–5021.

[17] M. Chassagne, M. Legros, D. Rodney, Atomic-scale simulation of screw dislocation/coherent twin boundary interaction in Al, Au, Cu and Ni, Acta Materialia. 59 (2011) 1456–1463.

[18] E. Bayerschen, A.T. McBride, B.D. Reddy, T. Böhlke, Review on slip transmission criteria in experiments and crystal plasticity models, Journal of Materials Science. 51 (2016) 2243–2258.

[19] J. Li, C. Lu, L. Pei, C. Zhang, R. Wang, Hydrogen-modified interaction between

lattice dislocations and grain boundaries by atomistic modelling, International Journal of Hydrogen Energy. 45 (2020) 9174–9187.

[20] T. Shimokawa, T. Kinari, S. Shintaku, Interaction mechanism between edge dislocations and asymmetrical tilt grain boundaries investigated via quasicontinuum simulations, Physical Review B - Condensed Matter and Materials Physics. 75 (2007) 1–11.

[21] J. Wang, I.J. Beyerlein, C.N. Tomé, Reactions of lattice dislocations with grain boundaries in Mg: Implications on the micro scale from atomic-scale calculations, International Journal of Plasticity. 56 (2014) 156–172.

[22] W. Yu, Z. Wang, Interactions between edge lattice dislocations and Σ11 symmetrical tilt grain boundary: Comparisons among several FCC metals and interatomic potentials, Philosophical Magazine. 94 (2014) 2224–2246.

[23] D. V. Bachurin, D. Weygand, P. Gumbsch, Dislocation-grain boundary interaction in ⟨1 1 1⟩ textured thin metal films, Acta Materialia. 58 (2010) 5232–5241.

[24] G. Dehm, B.N. Jaya, R. Raghavan, C. Kirchlechner, Overview on micro- and nanomechanical testing: New insights in interface plasticity and fracture at small length scales, Acta Materialia. 142 (2018) 248–282.

[25] C. Huang, X. Peng, B. Yang, Y. Zhao, S. Weng, T. Fu, Investigation of interaction between dislocation loop and coherent twin boundary in BCC Ta film during nanoindentation, Nanomaterials. 7 (2017).

[26] M.D. Sangid, T. Ezaz, H. Sehitoglu, I.M. Robertson, Energy of slip transmission and nucleation at grain boundaries, Acta Materialia. 59 (2011) 283–296.

[27] P. Chen, F. Wang, B. Li, Dislocation absorption and transmutation at {101¯2} twin boundaries in deformation of magnesium, Acta Materialia. 164 (2019) 440–453.

[28] M.F.A. Ulrich Fred Kocks, Ali Suphi Argon, Thermodynamics and kinetics of slip, Oxford : Pergamon press, 1975.

[29] T. Zhu, J. Li, S. Yip, Atomistic Reaction Pathway Sampling: The Nudged Elastic

Band Method and Nanomechanics Applications, in: Nano Cell Mech., John Wiley & Sons, Ltd, Chichester, UK, 2012: pp. 311–338.

[30] H.E. S Glasstone, KJ Laidler, The theory of rate processes; the kinetics of chemical reactions, viscosity, diffusion and electrochemical phenomena, McGraw-Hill Book Company, 1941.

[31] G. Esteban-Manzanares, E. Martínez, J. Segurado, L. Capolungo, J. LLorca, An atomistic investigation of the interaction of dislocations with Guinier-Preston zones in Al-Cu alloys, Acta Materialia. 162 (2019) 189–201.

[32] D. Chen, L.L. Costello, C.B. Geller, T. Zhu, D.L. McDowell, Atomistic modeling of dislocation cross-slip in nickel using free-end nudged elastic band method, Acta Materialia. 168 (2019) 436–447.

[33] P.A. Geslin, R. Gatti, B. Devincre, D. Rodney, Implementation of the nudged elastic band method in a dislocation dynamics formalism: Application to dislocation nucleation, Journal of the Mechanics and Physics of Solids. 108 (2017) 49–67.

[34] T. Zhu, J. Li, A. Samanta, A. Leach, K. Gall, Temperature and strain-rate dependence of surface dislocation nucleation, Physical Review Letters. 100 (2008) 1–4.

[35] G. Henkelman, H. Jónsson, Improved tangent estimate in the nudged elastic band method for finding minimum energy paths and saddle points, Journal of Chemical Physics. 113 (2000) 9978–9985.

[36] H. JÓNSSON, G. MILLS, K.W. JACOBSEN, Nudged elastic band method for finding minimum energy paths of transitions, in: Class. Quantum Dyn. Condens. Phase Simulations, WORLD SCIENTIFIC, 1998: pp. 385–404.

[37] G. Henkelman, B.P. Uberuaga, H. Jónsson, Climbing image nudged elastic band method for finding saddle points and minimum energy paths, Journal of Chemical Physics. 113 (2000) 9901–9904.

[38] G. Esteban-Manzanares, R. Santos-Güemes, I. Papadimitriou, E. Martínez, J. LLorca, Influence of the stress state on the cross-slip free energy barrier in Al: An atomistic investigation, Acta Materialia. 184 (2020) 109–119.

[39] S. Hayakawa, H. Xu, Temperature-dependent mechanisms of dislocation–twin boundary interactions in Ni-based equiatomic alloys, Acta Materialia. 211 (2021) 116886.

[40] L. Li, L. Liu, Y. Shibutani, Defect interaction summary between edge dislocations and <112>-axis symmetric tilt grain boundaries in copper on activation barriers and critical stresses, International Journal of Plasticity. 149 (2022) 103153.

[41] P. Hirel, Atomsk: A tool for manipulating and converting atomic data files, Computer Physics Communications. 197 (2015) 212–219.

[42] T. Zhu, J. Li, S. Yip, Atomistic study of dislocation loop emission from a crack tip, Physical Review Letters. 93 (2004) 9–12.

[43] S. Plimpton, Fast parallel algorithms for short-range molecular dynamics, Journal of Computational Physics. 117 (1995) 1–19.

[44] Y. Mishin, M.J. Mehl, D.A. Papaconstantopoulos, A.F. Voter, J.D. Kress, Structural stability and lattice defects in copper: Ab initio, tight-binding, and embedded-atom calculations, Physical Review B - Condensed Matter and Materials Physics. 63 (2001) 2241061–22410616.

[45] A. Stukowski, Visualization and analysis of atomistic simulation data with OVITO-the Open Visualization Tool, Modelling and Simulation in Materials Science and Engineering. 18 (2010).

[46] A. Stukowski, K. Albe, Extracting dislocations and non-dislocation crystal defects from atomistic simulation data, Modelling and Simulation in Materials Science and Engineering. 18 (2010).

[47] S. Ryu, K. Kang, W. Cai, Predicting the dislocation nucleation rate as a function of temperature and stress, Journal of Materials Research. 26 (2011) 2335–2354.

[48] E. Bayerschen, A.T. McBride, B.D. Reddy, T. Böhlke, Review on slip transmission criteria in experiments and crystal plasticity models, Journal of Materials Science. 51 (2016) 2243–2258.

[49] L. Lu, R. Schwaiger, Z.W. Shan, M. Dao, K. Lu, S. Suresh, Nano-sized twins induce high rate sensitivity of flow stress in pure copper, Acta Materialia. 53 (2005) 2169–2179.

[50] R.P. Carreker, W.R. Hibbard, Tensile deformation of high-purity copper as a function of temperature, strain rate, and grain size, Acta Metallurgica. 1 (1953) 654–663.

[51] P.S. Follansbee, U.F. Kocks, A constitutive description of the deformation of copper based on the use of the mechanical threshold stress as an internal state variable, Acta Metallurgica. 36 (1988) 81–93.

[52] Q. Wei, S. Cheng, K.. Ramesh, E. Ma, Effect of nanocrystalline and ultrafine grain sizes on the strain rate sensitivity and activation volume: fcc versus bcc metals, Materials Science and Engineering: A. 381 (2004) 71–79.

5. Interaction between screw dislocations and coherent twin boundaries in fcc metals

In the last chapter, we investigated the interactions between edge dislocation and GBs. Obviously, the type of GBs will have a considerable influence on the behaviors of the materials. However, it has been illustrated that both the strength and ductility can be remarkably increased when the CTB density rises as already developed as TWIP (Twinning induced plasticity) steel [1]. This suggests that the CTB can hinder the dislocation slip, while, under certain conditions, dislocations still interact with the CTB to furnish the ductility of the Nano-twinned metals [2–5]. Therefore, it is important to fundamentally understand the interactions between the CTB and dislocations.

The Σ3 coherent twin boundary (CTB) and screw dislocation interactions have been thoroughly investigated from experimental and computational aspects [3,6–12]. Meanwhile, atomic simulations, such as molecular dynamics (MD) and molecular static simulations, can provide more detailed information to uncover the interaction mechanisms [3,4,6,13–17]. Absorption, transmission, and pile-up are all alternatives to the interactions which may be determined by the type of dislocations, kinds of GBs, material elements, temperature, and any combination of previous factors [3,6,17,18]. For example, a screw dislocation will be spontaneously absorbed by the CTB when the incident dislocation touches the CTB plane in Al. While further loading is necessary to realize the subsequent absorption or transmission in other face-centered metals (FCC), such as Ni and Cu [3,4,6]. To explain the spontaneous absorption in Al and the difference in the other FCC metals, Jin et al. proposed to consider the sign of the ratio between $R=(\gamma_{us}-\gamma_s)/\mu b_p$ and $R'=(\gamma_{ut}-\gamma_s)/\mu b_p$, where γ_s is the intrinsic stacking fault

energy (SFE), γ_{us} is the unstable stacking fault energy (USFE), γ_{ut} is the energy barrier to create a twin fault along a pre-existing twin plane, μ is the shear modulus in $\{111\}\langle 110\rangle$ shear plane and b_p is the Burgers vector of the partial dislocation. It is suggested that R represented the resistance of the transmission event because one new dislocation was nucleated at the twined grain if the incident screw dislocation penetrated through the CTB. This parameter emphasizes the importance of γ_{us} which is also used to demonstrate the resistance of the dislocation emission from a crack tip or free surface [19,20]. Analogously, R' was used to describe the resistance of the screw dislocation being absorbed into the CTB because the absorption process was like the Friedel-Escaig (FE) cross-slip [21]. Therefore, a negative value of R' means that it is energetically favored for absorption without any resistance [6]. Nevertheless, Jin did not link the SFE to the thresholds of the interactions in various metals. By accounting for SFE and the potential effects of the MD simulations on the critical interaction shear stresses of the bi-crystal system (CISSes), Chassagne showed a linear correlation between the CISS and $\mu b_p / \gamma_s$. However, there were still some data points that did not follow this rule [3]. On the other hand, Deng tried to use γ_{us} to determine the CISS for a defect-free twin nanowire which is failed to explain the result of Chassagne [3,20]. Apparently, new explanations need to be proposed to describe the influence of materials on CISS, which is the objective of the present research. In this paper, the relationship among SFE, USFE and CISS was determined by MD simulations.

Furthermore, few MD simulations considered the energy barriers, activation volumes, and strain rate sensitivities of the interactions which are the measures based on the transition state theory and could be directly compared with the experimental data. Lacking these quantitative measures, the MD simulations are limited to the extremely high strain rate and can hardly address the finite temperature and quasi-static strain rate regime. In

this chapter, we will focus on the interactions between CTB and screw dislocations in typical FCC metals, such as Al, Cu, Ni, Ag, Au, and Pd based on the transition state theory and MD simulations.

5.1. Atomic models and simulation condition

To investigate the screw dislocation-CTB interaction by MD simulations for different materials, a sandwich-like model was constructed where upper and lower 10 Å atoms were used to apply external load and served as the rigid region, and the internal region contained one CTB, as shown in Fig. 5-1 [3,6,15–17,22]. The *X*, *Y* and *Z* axes of the left parent grain were parallel to $[1\ 1\ \bar{2}]$ (dislocation slip direction), $[1\ \bar{1}\ 0]$ (screw dislocation line) and $[1\ 1\ 1]$ (slip plane normal) orientations, respectively. The Volterra displacement field facilitated insertion of the screw dislocation into the middle of the left grain of the isotropic elastic medium with a Burgers vector of $\frac{a}{2}[1\ \bar{1}\ 0]$, where a is the lattice parameter. The specific displacement filed can be described by

$$u_z = \frac{b}{2\pi}\tan^{-1}\frac{y}{x} \tag{5-1}$$

The periodic boundary condition was applied in the Y direction to mimic an infinite dislocation line and the two lateral sides preserved the free surface condition. The dimensions of the domain were about 35×16 nm^2 in the $X\times Z$ directions. *Y* direction is about $16\sqrt{2}a$ which should be large enough to mimic the quasi-3D simulations [20]. The total number of atoms involved in the model ranges from 310,000 to 380,000. However, a larger model (50×20 nm^2 in the $X\times Z$ directions) would not significantly change the CISS and the obtained conclusions. After and before the system was dislocated, the system was energy-minimized by the CG algorithm.

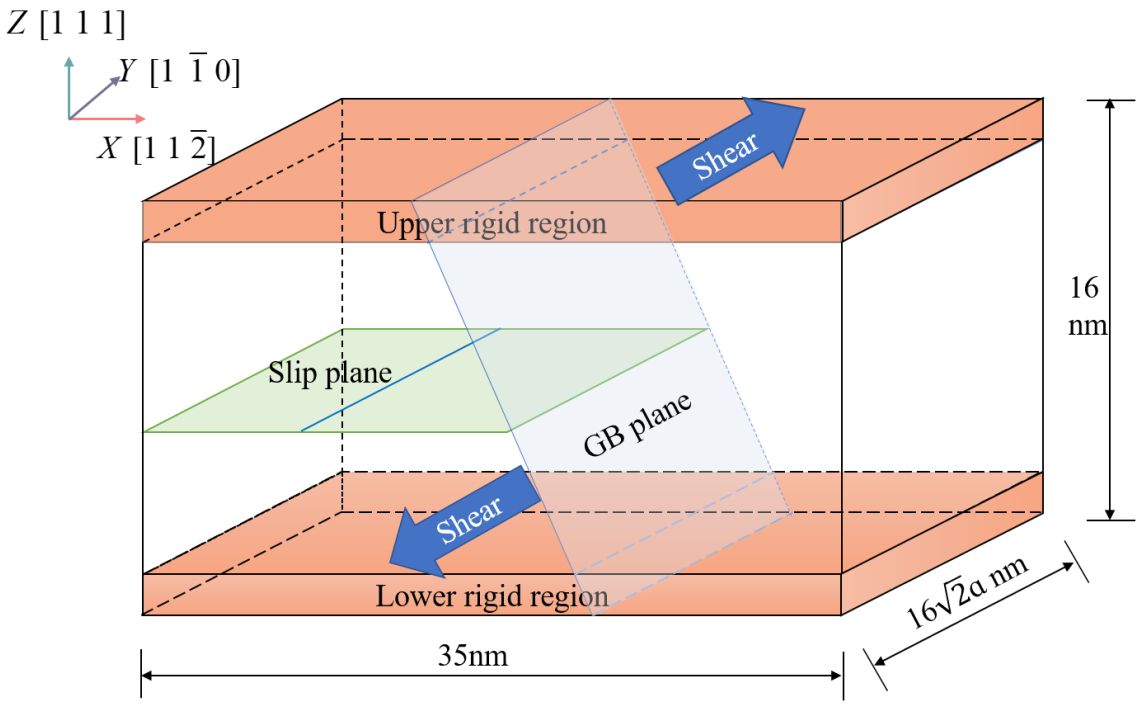

Fig. 5-1 Schematic representation of the interaction model. The domain contains one screw dislocation indicated by the blue line on the green slip plane. The upper and lower atomistic plates with thicknesses of 10 Å were set as rigid regions to apply displacement.

To realize the screw dislocation movement toward the GB plane, a shear deformation was applied to the system by setting the upper and lower rigid regions to move in opposite directions with a velocity of 0.015 Å/ps along the *Y*-axis. Considering the size of the present model, this may result in a strain rate of about 10^8 /s. The canonical ensemble (NVT) was used to update and track atomic positions. The time step was set to 1 fs and the system temperature was maintained at 0.1 K to suppress any thermally activated processes of the dislocation itself [6]. Atomic configurations were recorded every 2 ps for further analysis. The energy barrier under a certain deformation state was calculated using the free-end NEB method [16]. The initial and final states which are necessary to implement the NEB were constructed by the loading and unloading process as mentioned in Chapter 4 [17,22–24]. NEB method was also used to calculate γ_s, γ_{us} and γ_{ut}. The

quick-min method was used for the damped dynamics minimizer with a spring constant of 1 eV/Å and 18 replicas. EAM potentials were used to calculate the MD and energy measures for Al [25], Cu [26], Ni [25], Ag [27], Au [28] and Pd [29,30]. Two different potentials were used for Pd and two different mechanisms were subsequently observed. To distinguish the difference, we use Pd_Hale and Pd_Zhou to describe the results with different potentials. Additionally, the method to calculate the CTB energy and stacking fault energy can be referred to Chapter 3.

5.2. Screw dislocation-CTB interactions

5.2.1. Energy of CTBs and the generalized stacking fault curves

The fundamental parameters, including the magnitude of the Burgers vector of the partial dislocation b_p, the shear modulus of the $\{111\}\langle 110\rangle$ plane, the SFE γ_s, and USEF γ_{us}, are listed in Table 5-1 for different materials. The method to estimate the Energy of the CTB, defined as E_{CTB}, and the unstable twin fault energy to create the extrinsic SF from a pristine crystal, γ_{uTF}, are depicted in Chapter 3. Recall the map of generalized stacking fault curves (GSFCs) in Chapter 3 and rename it as Fig. 5-2.

Table 5-1 Properties of different materials.

Element	b_p (nm)	μ (GPa)	γ_s (mJ/m^2)	γ_{us} (mJ/m^2)	γ_{ut} (mJ/m^2)	E_{CTB} (mJ/m^2)	γ_{uTF} (mJ/m^2)
Al	0.165	27.9	145.5	164.3	68.1	75.18	218.59
Cu	0.148	41.2	44.4	153.3	138.9	22.24	181.68
Ni	0.144	75.0	125.3	309.6	257.9	63.46	382.32
Ag	0.167	25.6	17.8	108.9	105.4	9.16	121.03
Au	0.166	24.2	4.72	92.1	93.4	2.37	97.52

Pd_Zhou	0.159	43.2	16.3	122.8	128.7	3.67	144.91
Pd_Hale	0.159	34.0	175.8	177.8	40.9	118.22	228.12

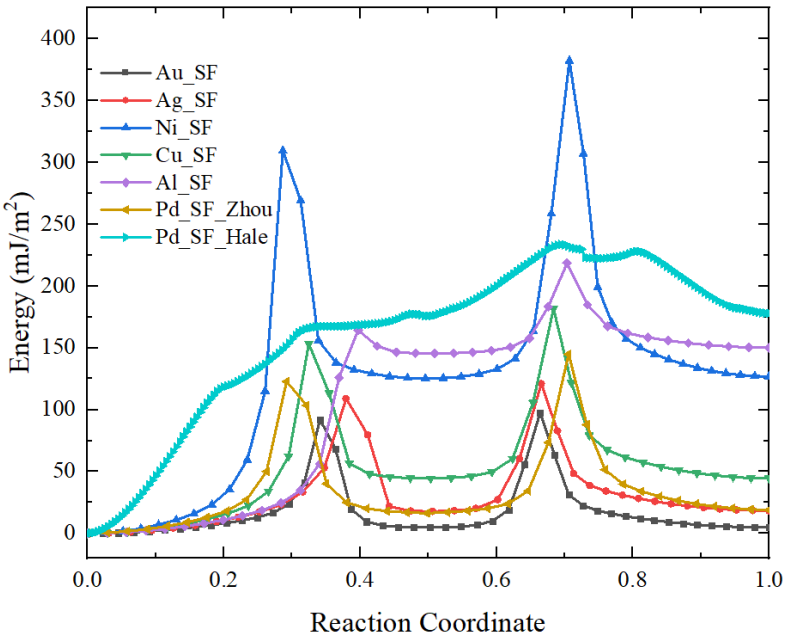

Fig. 5-2 Energy curves along the MEP for Al, Cu, Ni, Ag, Au, and Pd.

It could be seen that, for most of the GSFCs, there exits two peaks that represent the γ_{us} and γ_{uTF}. However, no obvious peaks could be found in the Fig. 5-2 for Pd_Hale. The SFE obtained from experiments for Pd is about 180 mJ/m^2 [31], which is very close to the prediction of Pd_Hale. Although Pd_Zhou gave a coincident tendency of the GSFC as the other FCC metals, the SFE γ_s is about 16.3 mJ/m^2 which is much lower than the experimental result. This is the reason we selected two different potentials for Pd.

Another important parameter proposed by Jin is γ_{ut} which represent the energy barrier to create a twin fault along a pre-existing twin plane. Actually, the process to create a new twin fault from as pre-existing twin plane is more or less similar to the twin plane migration process, as shown in Fig. 5-3.

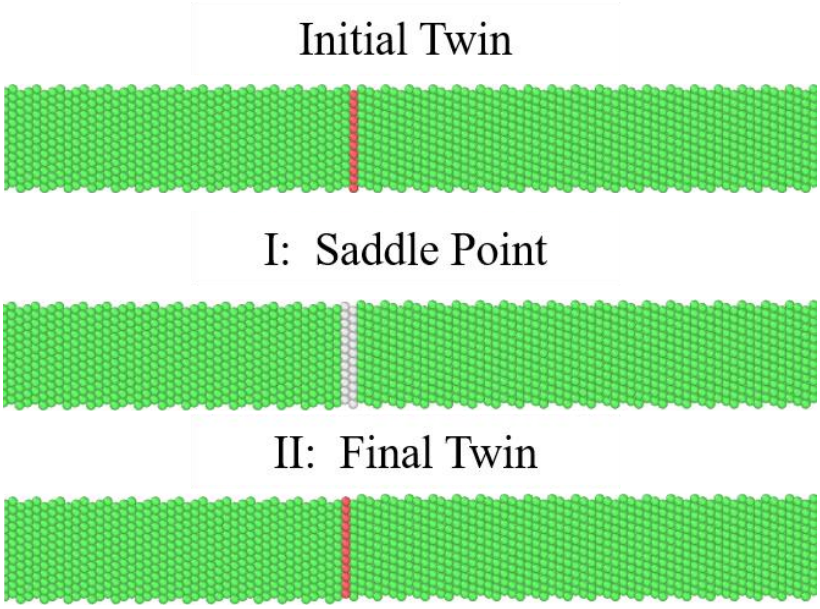

Fig. 5-3 The twin plane migration process. The final twin migrates one atom layer to the left direction when comparing to the initial twin. The NEB method gives the saddle point which represent the energy barriers that should be overcame to achieve the final goal.

The corresponding MEP of the γ_{ut}-formation is shown as Fig. 5-4. And the magnitudes are given in Table 5-1

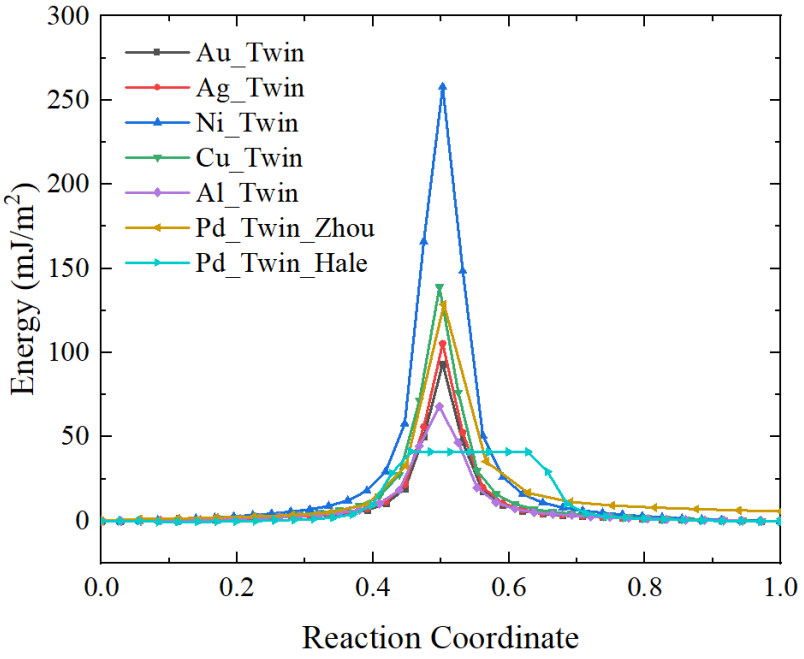

Fig. 5-4 The MEPs of twin migration process for FCC metals.

5.2.2. Interactions between CTB and screw dislocation

The inserted perfect screw dislocation first dissociated into two partial dislocations linked by a SF after the energy minimization [3,6]. When the external load increased, the leading partial dislocation marched toward the CTB and was hindered before the CTB except for Al and Pd_Hale. Two different scenarios were observed when the incident dislocation impinged on the CTB if the external load continued to increase. One is absorption, such as Al, Cu, and Pd_Hale. Another situation is the transmission.

(1) Absorption

Although, Al, PD_Hale and Cu all presented the case of absorption. The internal mechanism is quite different.

In Cu, the corresponding strain-stress curve and corresponding atomic configurations are shown in Fig. 5-5. As we can see, the dissociated dislocation partials were hindered by the CTB. When the leading partial first impacted the CTB at the Point I, the slope of the stress-strain curve slightly increased because there is no dislocation slip. When the stress was increased to 445 MPa, namely Point II, the dislocation penetrated through the CTB and slipped on the CTB plane. Very slight stress drop was found at the moment of penetration. One step was generated on the CTB plane which is identical to the results of Jin [6] and Chassagne [3]. Further load increasing would separate the two partial dislocations and let them slip away from each other until they were stopped by the upper and lower load region.

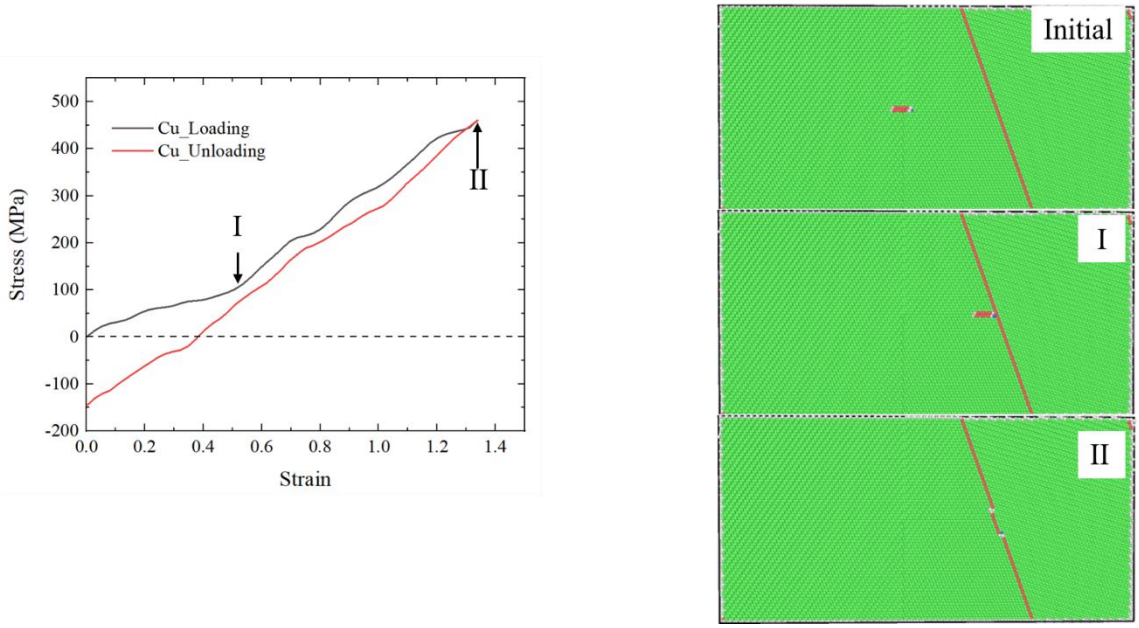

Fig. 5-5 The strain-stress curve of the Cu, the black line represents the loading process and the red curve represents the unloading process. Point I: the leading partial dislocation impacted the CTB. Point II: the CTB absorbed the screw dislocation and one misfit step was formed on the CTB.

In Al, as depicted in Fig. 5-6, the perfect screw dislocation dissociated into two partial dislocations first as depicted in the Initial state. when the external load increased, the partial dislocations moved toward the CTB. And a slight stress drop could be found before the partials reached the CTB plane. Different from the scenario in Cu, the leading partial dislocation was not hindered by the CTB but was immediately absorbed by the CTB at Point II. So did the trailing partial. One misfit step was observed on the CTB. The trajectory of the misfit step thereafter was similar to that of Cu when the external load increased.

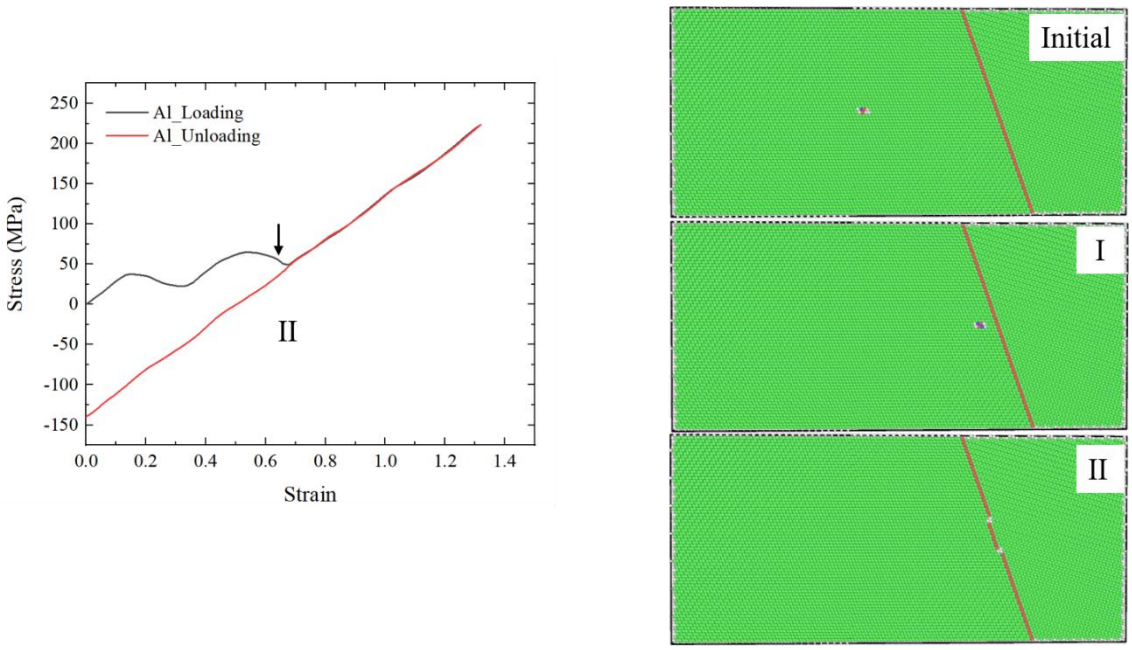

Fig. 5-6 The strain-stress curve of the Al, the black line represents the loading process and red curve represents the unloading process. Point I: the leading partial dislocation moved close to the CTB. Point II: the CTB spontaneously absorbed the screw dislocation and one misfit step was formed on the CTB.

As for Pd, both the absorption and transmission were observed because two different potentials were implemented. We introduce the results of absorption first.

Similar to the Al, in Pd_Hale, the dissociated partial dislocations were not hindered by the CTB. The spontaneous absorption was observed once the leading partial dislocation touched the CTB plane as shown in Fig. 5-7. The perfect screw dislocation was not dissociated when the energy was minimized as shown in the Initial state. The further load would dissociate the perfect dislocation and drive the partial dislocations to move close to the CTB. At Point two, the screw dislocation was spontaneously absorbed by the CTB. At this moment, a significant drop can be observed in the Energy-Strain curve as depicted

by the black line in Fig. 5-7. To a certain extent, this significant energy drop indicates that this absorption is energy favorable.

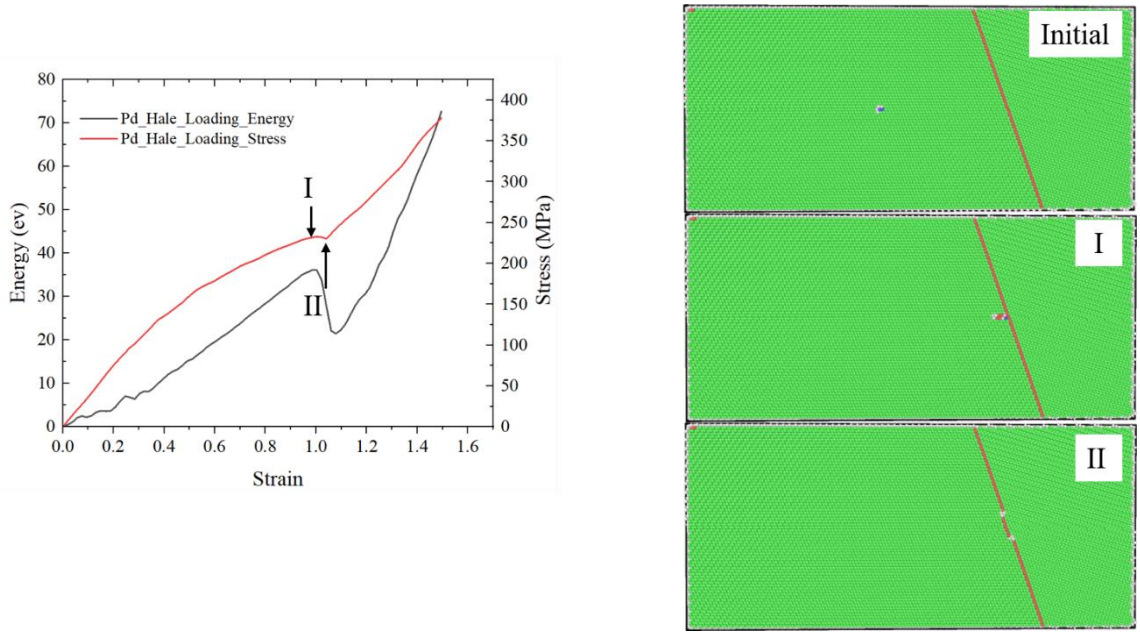

Fig. 5-7 The strain-stress curve of the Pd_Hale, the black line represents stress evolution during the loading process and the red curve represents the energy evolution during the loading process. Point I: the leading partial dislocation moved close to the CTB. Point II: the CTB spontaneously absorbed the screw dislocation and one misfit step was formed on the CTB.

Actually, in Al and Pd_Hale, if the initial inserted location of the screw dislocation was close enough to the CTB, the dislocation might be absorbed by the CTB even when the system underwent energy minimization without any external load. Clearly, there is a fundamental difference among the Cu, Al, and Pd_Hale, although the interactions are both absorptions. The reason will be discussed later.

(2) Transmission

The transmissions were observed in Ni, Au, Ag, Au, and Pd_Zhou.

In Ni, as shown in Fig. 5-8, the dissociated partial dislocations moved toward the CTB

when the external load increased, a significant slope change was observed in the stress-strain curve at Point I. Before Point I, the dislocation moved in the parent grain and was not hindered or stopped by any obstacle. Therefore, the instant shear modulus is quite small at this stage. However, when the leading partial was stopped by the CTB, no dislocation slip was permitted in the grain and the instant shear modulus raised which cause the change of the slope in Fig. 5-8. Once the dislocation penetrated through the CTB, a significant stress drop was observed at Point II. When the strain was increasing, the transmitted dislocation moved toward the free surface and eventually escaped from the free surface. The CISS of Ni is about 510 MPa.

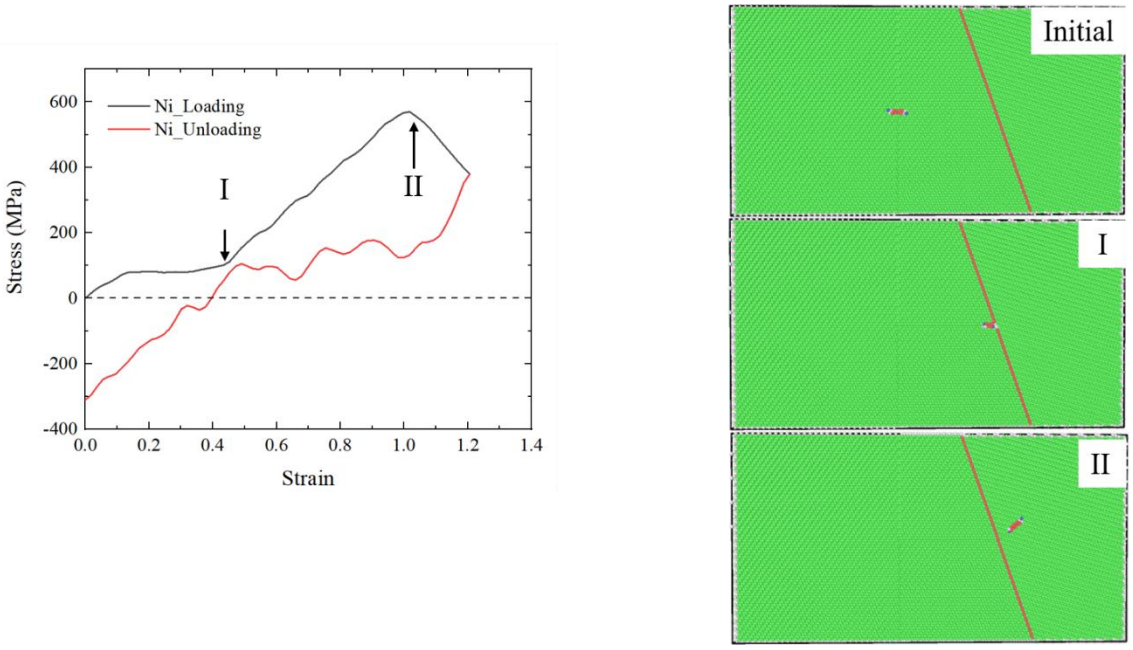

Fig. 5-8 The strain-stress curve of the Ni, the black line represents the loading process and red curve represents the unloading process. Point I: the leading partial dislocation was hindered by the CTB. Point II: the screw dislocation penetrated through the CTB and slipped in the twined grain.

The situations of Ag, Au, and Pd_Zhou are almost the same as Ni. The corresponding stress-strain curves and atomic configurations are shown in Fig. 5-9,10,11 for Ag, Au, and Pd_Zhou, respectively. Obviously, the CTB repelled the screw dislocation and hinder the

leading partial dislocations at Point I in Ag, Au, and Pd_Zhou. The screw dislocation would penetrate through the CTB at about 340 MPa, 324 MPa, and 440 MPa for Ag, Au, and Pd_Zhou, respectively. From Fig. 5-11, the energy and the stress of the system decreased once the dislocation was transmitted through the CTB. Only when the screw dislocation escaped from the free surface, the stress and energy raised again because the system underwent elastic deformations.

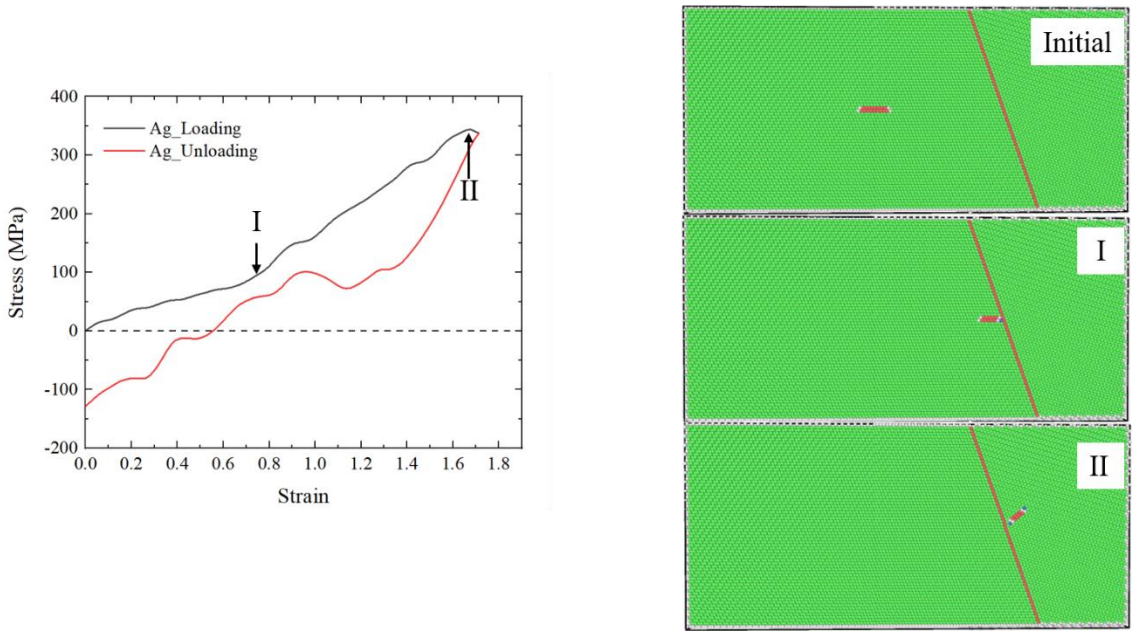

Fig. 5-9 The strain-stress curve of the Ag, the black line represents the loading process and red curve represents the unloading process. Point I: the leading partial dislocation was hindered by the CTB. Point II: the screw dislocation penetrated through the CTB and slipped in the twined grain.

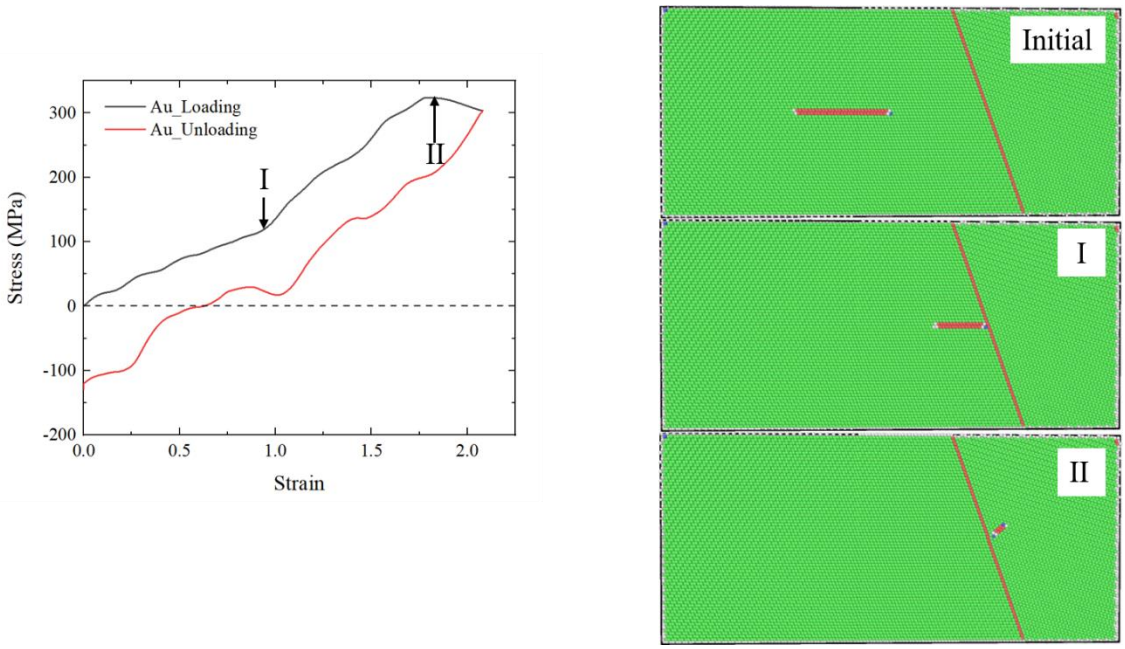

Fig. 5-10 The strain-stress curve of the Au, the black line represents the loading process and red curve represents the unloading process. Point I: the leading partial dislocation was hindered by the CTB. Point II: the screw dislocation penetrated through the CTB and slipped in the twined grain.

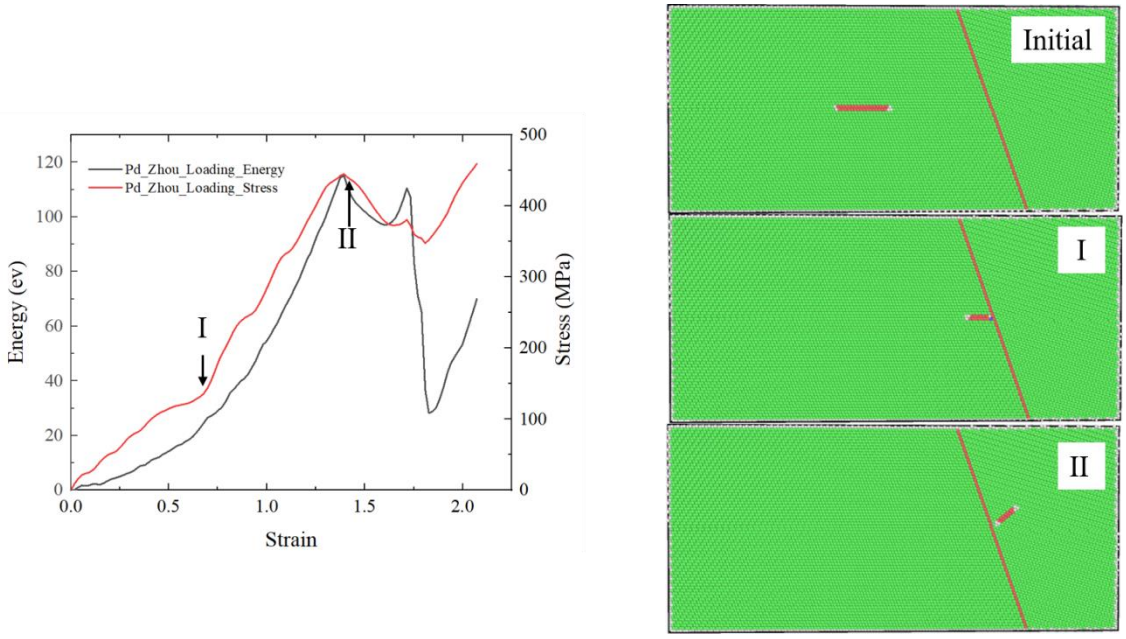

Fig. 5-11 The strain-stress curve of the Pd_Zhou, the black line represents stress evolution during the loading process and red curve represents the energy evolution during the loading process. Point I: the leading partial dislocation moved close to the CTB. Point II:

the CTB spontaneously absorbed the screw dislocation and one misfit step was formed on the CTB.

5.2.3. Relationship between CISS and stacking fault energy.

(1) The spontaneous and nonspontaneous absorption

As we discussed above, although the absorptions were observed in Al, Pd_Hale, and Cu. There are fundamental differences among the internal mechanisms. Why was the screw dislocation spontaneously absorbed by the CTB in Al and Pd_Hale? Why wasn't it absorbed by the CTB unless the CISS was fulfilled in Cu?

One misfit step nucleated when the screw dislocation was absorbed by the CTB. This misfit step is somehow like the results of creating a new twin fault along a pre-existing twin plane as proposed by Jin [6]. Therefore, γ_{ut} naturally plays a very important role on the determination of the interaction mechanisms for different materials. Taking Al and Ni as a comparison, as shown in Fig. 5-12, The generalized stacking fault energy curves and twin fault nucleation curves were obtained by NEB method using the way described in Chapter 3 and Chapter 5. The specific values can also be found in Table 5-1. Obviously, in Al, γ_{ut} is smaller than γ_s which may generate a negative $R' = (\gamma_{ut} - \gamma_s)/\mu b_p$. The same situation can be found in Pd_Hale using the data in Table 5-1. However, γ_{ut} is larger than γ_s in Ni, Cu and other metals. As proposed by Jin, the value of R' represents the resistance of the CTB to the screw dislocation. If R' is positive, the CTB will repel the screw dislocation and further load is necessary to trigger the interaction. However, a negative R' means the energy of current system is large enough to support the spontaneous absorption. Therefore, the screw dislocation was immediately absorbed once it touched the CTB in Al and Pd_Hale. A positive R' in the other situations means the CISS should also be positive rather than zero.

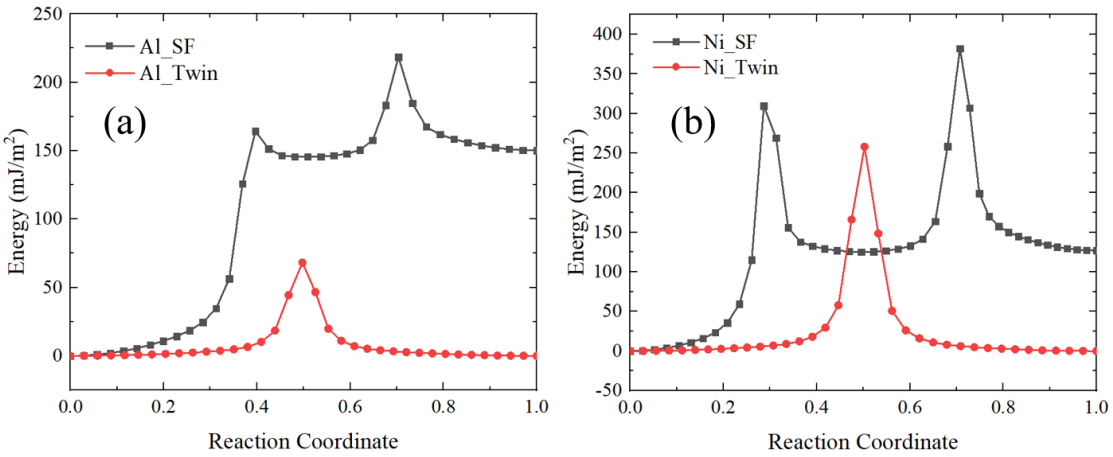

Fig. 5-12 The generalized stacking fault energy curves and twin fault nucleation curves for Al (a) and Ni (b). The black line is the generalized stacking fault energy curve, and the red line is twin fault nucleation curve.

(2) Relationship between CISS and energetic measures

Chassagne tried to describe the dependence of the CISS on the materials. A linear relationship was found between the CISS and $\mu b_p / \gamma_s$ with only one exception for Cu [3]. Table 5-2 gives the information on the CISS and some energetic measures based on the SFE and USFE. Both the present results and the results of Chassagne's work. In addition, we added another potential for Pd_Foiles to furnish the database. However, combined with our results, we found that this linear trend became ambiguous because it did not support the trend for Ag, Au and, Pd, as shown in Fig. 5-13(a). Clearly, Chassagne's model is insufficient to describe the relationship between CISS and energetic measures. Rice proposed that γ_{us} affected the threshold to emit a dislocation from the crack tip and this parameter was further used to explain the dislocation emission from the free surface [19,20]. Considering that the transmission process is similar to emitting a dislocation from the CTB, we think γ_{us} and γ_s both play a crucial role in the

determination of CISS. Following Chassagne, we got a linear relationship between CISS and $1/(\gamma_{us}-\gamma_s)$ as shown in Fig. 5-13 (b). It is clear that not only our results but also Chassagne's results all support this trend for transmission and absorption. The internal partial dislocation pair already provided the energy of SF γ_s in the parent grain (shown in Fig. 5-13(c)). Physically, γ_{us} represents the resistance of the CTB to emit the partial dislocation into the adjacent grain, which may also serve as the necessary condition for the interaction. The constricted perfect dislocation on the CTB served as the dislocation source as shown in Fig. 5-13 (d). Since the CISS was the activated stress necessary to trigger the defect interaction of the whole bi-crystal, it was related to $1/(\gamma_{us}-\gamma_s)$ rather than $\mu b_p/\gamma_s$. Qualitatively, the higher difference between the γ_{us} and γ_s indicates a higher resistance for the interaction. Therefore, a higher CISS should be needed. In another word, the negative slope should be reasonable, as shown in Fig. 5-13(b). This good agreement indicates the significance of $1/(\gamma_{us}-\gamma_s)$ and the accuracy of our model.

Additionally, in the Table 5-2, all the values of $\gamma_{ut}-\gamma_s$ are negative for the cases of spontaneous absorption. This trend is consistent with what we discussed above. It is noted that we got a CISS of about 445 MPa for Cu compared with that of 300 MPa in Chassagne's paper. It was thought that the present result was closer to Jin's results (465 MPa) and then, we omitted Chassagne's result only for Cu in Fig. 5-13.

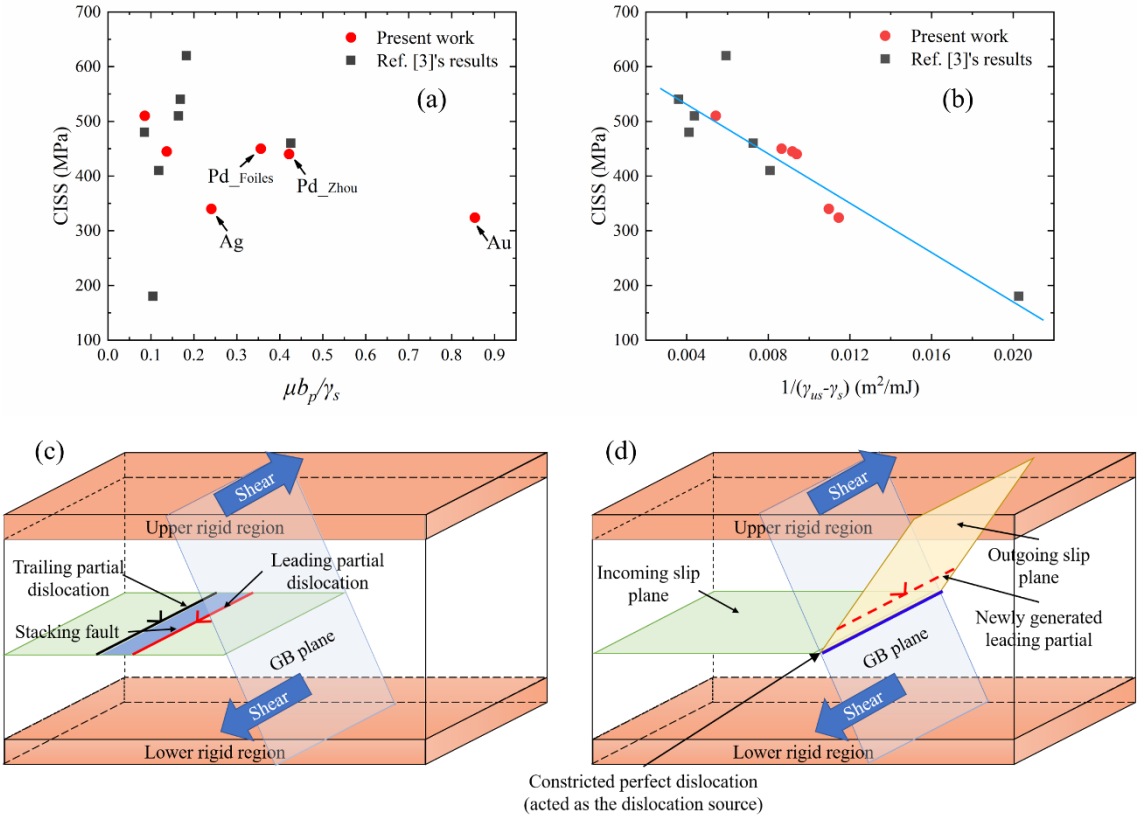

Fig. 5-13 The relationship between CISS and energy measures. (a) CISS versus $\mu b_p / \gamma_s$ used by Chassagne et al. [3]. (b) CISS versus $1/(\gamma_{us} - \gamma_s)$. The line is a visual guide. The red points are the data form ref. [3] and black points are the results of this work. (c) The leading and trailing partial dislocations were connected by the stacking fault which was related to γ_s. (d) The constricted perfect dislocation on the CTB was acted as the dislocation source and the critical energy state was related to γ_{us}. The dash red line indicated the newly generated leading partial once the constricted perfect dislocation started to react with the CTB and penetrated it.

Table 5-2 Material properties for various FCC metals. For the events, “SA” stands for spontaneous absorption, “A” stands for absorption, and “T” stands for transmission.

Element	Event	CISS (MPa)	$\mu b_p / \gamma_s$	$1/(\gamma_{us}-\gamma_s)$ (m^2/mJ)	$\gamma_{ut}-\gamma_s$ (mJ/m^2)
Present results					
Al	SA	0	0.032	0.0531	-77.4
Cu	A	445	0.137	0.0092	94.5
Ni	T	510	0.086	0.0054	132.6
Ag	T	340	0.241	0.0110	87.7
Au	T	324	0.854	0.0115	88.6
Pd_Zhou	T	440	0.422	0.0094	112.4
Pd_Hale	SA	0	0.031	0.4801	-134.8
Pd_Foiles	A	500	0.383	0.0079	110
Chassagne’s results [3]					
Al_Ercolessi	SA	0	0.049	0.0448	-51.6
Al_Mishin	SA	0	0.030	0.0535	-81.7
Au_Grochola	A	180	0.1051	0.0204	15.1
Cu_Mendelev	T	510	0.1641	0.0044	206.9
Cu_Ackland	T	540	0.169	0.0036	257
Cu_Foiles	T	460	0.426	0.0073	130.2
Ni_Mishin	T	480	0.085	0.0041	177
Ni_Angelo	A	410	0.118	0.0081	70.3

5.3. Analysis of interactions based on the transition state theory

5.3.1. Energy barriers, activation volumes and strain rate sensitivities

We further calculated the energy barriers under various stress states for Cu, Ni, Ag, and

Au as shown in Fig. 5-14 [16,32]. And Fig. 5-15(a) and (c) gives the final states of Cu, Ni, Ag, Au that were used for the free-end NEB (FENEB) method. In addition to the energy barriers, the saddle points were also produced by the FENEB as shown in Fig. 5-15(b) and (d).

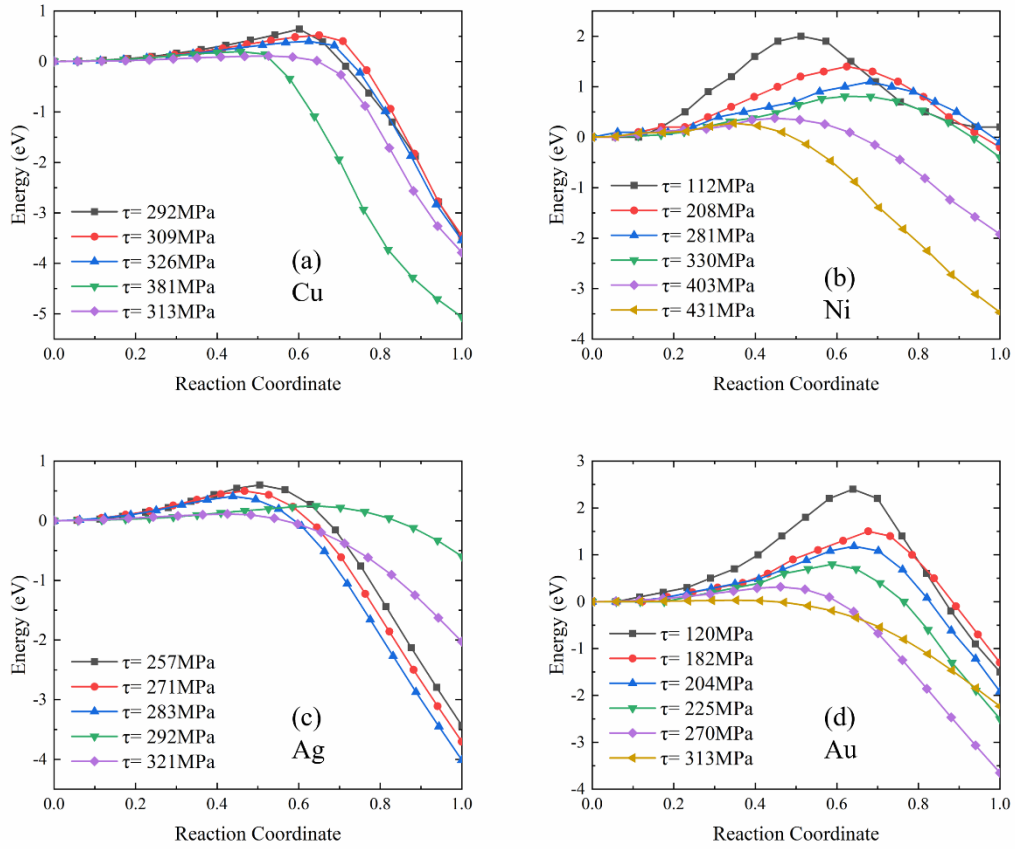

Fig. 5-14 Evolutions of the energy of the system along the reaction path as a function of the applied shear stress using free-end NEB method. (a) MEP of Cu; (b) MEP of Ni; (c) MEP of Ag; (d) MEP of Au.

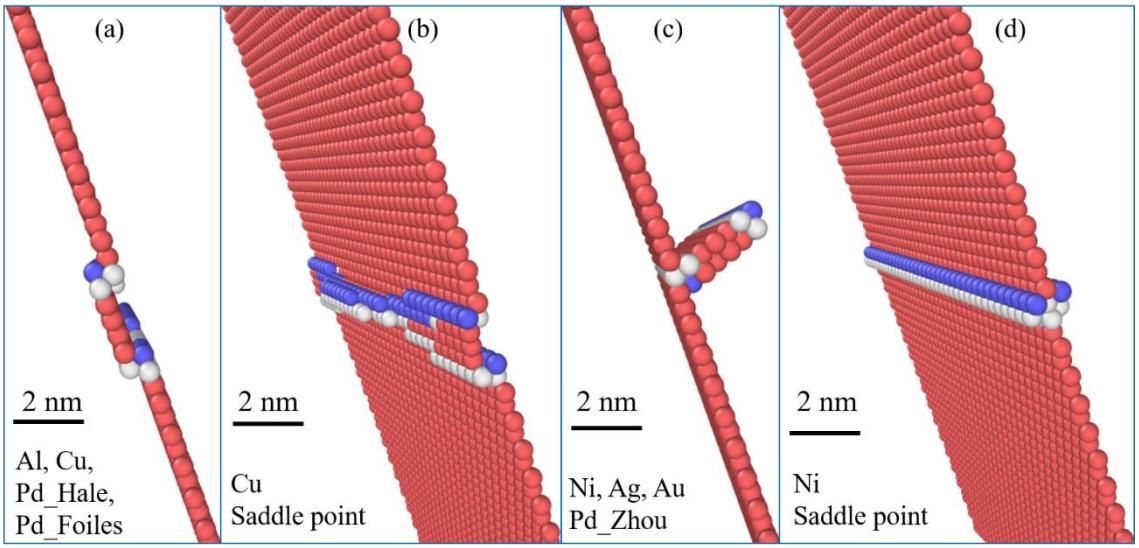

Fig. 5-15 The interaction of different materials. (a) Screw dislocation was absorbed by the CTB and one step was formed in Al, Cu, and Pd_Hale, Pd_Foiles; (b) Saddle point obtained by NEB for Cu which was used to calculate the energy barrier; (c) Screw dislocation transmitted through the CTB in Ni, Ag, Au, and Pd_Zhou; (d) Saddle point obtained by NEB for Ni where a perfect dislocation was constricted on the CTB plane. The scale bar is 2 nm.

As mentioned in Section 5.2.2, the screw dislocation was absorbed by CTB in Cu which are also shown in Fig. 5-15(a), Jin [6] proposed that the dissociated partial dislocations would be fully constricted to one perfect screw dislocation before it was absorbed by the CTB in Cu for the quasi-2D model. However, the saddle point calculated by FENEB suggested another different mechanism as shown in the Fig. 5-15(b). Not all of the dislocation but fractional segments were first constricted to the perfect dislocation. Then the constricted parts followed the Friedel-Escaig (FE) cross-slip process [21] and produced two dissociated partial dislocations on the CTB plane. Further load completed the cross-slip process and finally the newly nucleated partial dislocations on the CTB plane slipped away from each other. On the contrary, the saddle points of Ni, Ag, and Au are shown as Fig. 5-15(d). The whole dislocations were constricted to one perfect screw

dislocation and then crossly slip along the plane in the twined grain.

Fig 5-16 gives the relationship between energy barriers and the various stress states. Obviously, the energy barriers decreased linearly with the stress increasing. This is because external energy was introduced if the stress was increased and hence reduced the energy barrier and promoted the interactions.

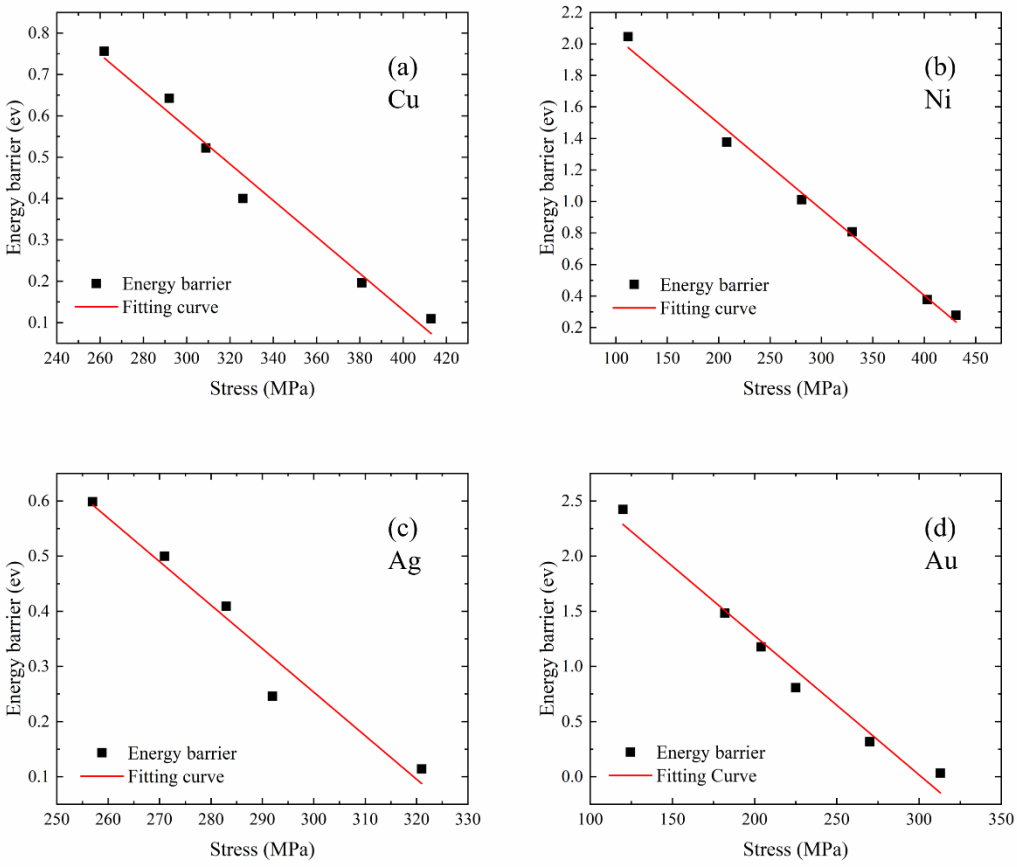

Fig. 5-16 The energy barriers under various stress states for different materials. (a) Cu; (b) Ni; (c) Ag; (d) Au.

The apparent activation volumes can be estimated from the fitting curves in Fig. 5-16 and following the Eqs. (4-4) ~ (4-7). And the strain rate sensitivities can be derived following Eq. (4-8). If we further consider the temperature effects, the corresponding parameter can be revised as,

$$V_{stress} = -\frac{\partial \Delta G(\tau)}{\partial \tau}(1-\frac{T}{T_m}) \tag{5-1}$$

$$V_A = \frac{V_{stress}}{M} \tag{5-2}$$

$$m = \frac{\sqrt{3}k_B T}{\sigma V_A} = \frac{\sqrt{3}Mk_B T}{\sigma V_{stress}} \tag{5-3}$$

where V_{stress} is the activation volume for the current bi-crystal model; V_A is the apparent activation volume corresponding to the tensile experiments for polycrystal bulk materials; $M = 3.1$ represents the Taylor factor for FCC materials with which we can transfer the shear stress τ of the bi-crystal to the tensile or compression stress σ of the polycrystal. k_B is the Boltzmann constant; T is the absolute temperature and equals to 300K when calculating m by Eq. (3) to reflect the experimental temperature. T_m is the surface disordering temperature which can be determined from the melting process, 1300 K for Cu [33], 1700 K for Ni [34], 1110 K for Ag [35], and 1250 K for Au [36]. The corresponding results are summarized in Table 5-3.

Table 5-3 Comparison of activation volume, strain rate sensitivity between experiments and NEB results.

Case	$V_A(b^3)$ MD	m MD	$V_A(b^3)$ Exp.	m Exp.
Cu	11	0.029	12-20 [7]	0.025-0.036 [7]
Ni	19	0.019	10-20 [37]	0.01-0.03 [38,39] 0.016 [37]
Ag	13	0.023	/	/
Au	21	0.015	/	/

Diffusion-controlled Process [16]	/	/	≤ 0.1	≈ 1
Bulk forest hardening [16]	/	/	~1000	0-0.005

Good agreements with the experimental data were found for Cu (absorption) and Ni (transmission). For example, in Cu, the apparent activation volume is about 11 b^3. And the experimental results suggested this value is around 12 b^3 for the Cu with high twin density [7]. Physically, the activation volume represents the amount of materials that are in the high-energy state during the interaction process [24]. This value is regarded as the signature of the dislocation-GB interaction process in contrast to a value of about 1000 b^3 for the bulk forest cutting process[40]. Generally, different mechanisms have dramatically different activation volumes and, hence, this parameter directly links the MD simulation with the experiments and makes the MD simulations more physical and realistic. Moreover, the calculated strain rate sensitivity of 0.023 reflected the relationship between flow stress and the applied strain rate [7], which is also almost the same as the experimental data around 0.025-0.036. The activation volume and strain rate sensitivity of Ni, 15 b^3 and 0.019, are all consistent with the experiments of 10-20 b^3 and 0.016 [37–39]. Additionally, the activation volumes of Ag and Au are 13 b^3 and 21 b^3, respectively. And they are in the reasonable range of the dislocation-interaction mechanism. The activation volumes for different materials are all around 20 b^3 because the internal interaction mechanisms are similar and all belong to the dislocation-interface interactions which usually have the typical activation volumes of 10-100 b^3.

5.3.2. Relationship between energy barriers and stacking fault energy

Additionally, we show the relationship between energy barriers and $1/(\gamma_{us}-\gamma_s)$

under certain stress for different metals in Fig. 5-17. Obviously, the difference between USF and SF energies also affects the energy barriers. Under the same stress state, energy barriers decrease with $1/(\gamma_{us}-\gamma_s)$ increasing. Although it doesn't show the linearity as CISS in Fig. 5-13 (b), it still emphasizes that a larger difference between USF and SF energies indicates a high resistance of the interaction. Therefore, a larger energy barrier exists for this interaction process. This trend is mutually corroborated with the trend between the CISS and $1/(\gamma_{us}-\gamma_s)$.

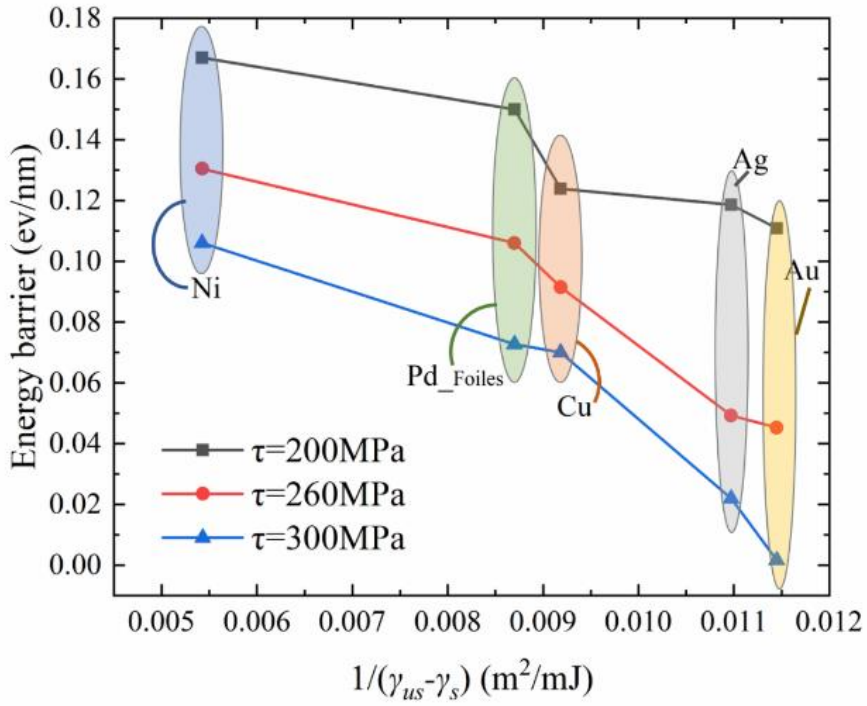

Fig. 5-17 The relationship between $1/(\gamma_{us}-\gamma_s)$ and energy barriers under various stress states for different materials.

5.4. Summary

In this chapter, the interactions between the screw dislocations and CTB were

investigated based on the MD simulations and NEB method. Several conclusions can be made as follows:

(1) The screw dislocation was spontaneously absorbed by the CTB in Al and Pd_Hale;

(2) The screw dislocation was absorbed by the CTB in Cu when the shear stress reached about 445 MPa. The activation volume of the dislocation-CTB interaction in Cu is about 11 b^3. And the strain rate sensitivity is about 0.029. Both the activation volume and strain rate sensitivity correspond well with the experimental data.

(3) Through NEB, in Cu, the interaction process followed the Friedel-Escaig (FE) cross-slip mechanism. The cross-slip process was progressive and only fractional segments were constricted to the perfect dislocation.

(4) In Ni, Ag, Au and Pd_Zhou, the screw dislocations penetrated through the CTB and slipped along the plane in the twined grain. Unlike the progressive FE cross slip process in Cu, the whole partial dislocations were constricted to the perfect screw dislocation and then penetrated through the CTB.

(5) The activation volumes of the dislocation-CTB interaction in Ni, Ag, and Au are about 15 b^3, 13 b^3, and 21 b^3, respectively. And the strain rate sensitivities are about 0.019 for Ni, 0.023 for Ag, and 0.015 for Au.

(6) A linear relationship between CISS and $1/(\gamma_{us}-\gamma_s)$ was found. The CISS would decrease when the value of $1/(\gamma_{us}-\gamma_s)$ increases. Energy barriers under the same stress states for different materials have a similar trend on $1/(\gamma_{us}-\gamma_s)$.

References

[1] B.C. De Cooman, Y. Estrin, S.K. Kim, Twinning-induced plasticity (TWIP) steels, Acta Materialia. 142 (2018) 283–362.

[2] Y.F. Shen, L. Lu, Q.H. Lu, Z.H. Jin, K. Lu, Tensile properties of copper with nano-scale twins, Scripta Materialia. 52 (2005) 989–994.

[3] M. Chassagne, M. Legros, D. Rodney, Atomic-scale simulation of screw dislocation/coherent twin boundary interaction in Al, Au, Cu and Ni, Acta Materialia. 59 (2011) 1456–1463.

[4] M. Dupraz, S.I. Rao, H. Van Swygenhoven, Large scale 3-dimensional atomistic simulations of screw dislocations interacting with coherent twin boundaries in Al, Cu and Ni under uniaxial and multiaxial loading conditions, Acta Materialia. 174 (2019) 16–28.

[5] L. Lu, Y. Shen, X. Chen, L. Qian, K. Lu, Ultrahigh Strength and High Electrical Conductivity in Copper, Science. 304 (2004) 422–426.

[6] Z.H. Jin, P. Gumbsch, E. Ma, K. Albe, K. Lu, H. Hahn, H. Gleiter, The interaction mechanism of screw dislocations with coherent twin boundaries in different face-centred cubic metals, Scripta Materialia. 54 (2006) 1163–1168.

[7] L. Lu, R. Schwaiger, Z.W. Shan, M. Dao, K. Lu, S. Suresh, Nano-sized twins induce high rate sensitivity of flow stress in pure copper, Acta Materialia. 53 (2005) 2169–2179.

[8] V. Samaee, M. Dupraz, T. Pardoen, H. Van Swygenhoven, D. Schryvers, H. Idrissi, Deciphering the interactions between single arm dislocation sources and coherent twin boundary in nickel bi-crystal, Nature Communications. 12 (2021).

[9] P.J. Imrich, C. Kirchlechner, C. Motz, G. Dehm, Differences in deformation behavior of bicrystalline Cu micropillars containing a twin boundary or a large-angle grain boundary, Acta Materialia. 73 (2014) 240–250.

[10] J.P. Couzinié, B. Décamps, L. Priester, Interaction of dissociated lattice

dislocations with a $\sum = 3$ grain boundary in copper, International Journal of Plasticity. 21 (2005) 759–775.

[11] J. Kacher, B.P. Eftink, B. Cui, I.M. Robertson, Dislocation interactions with grain boundaries, Current Opinion in Solid State and Materials Science. 18 (2014) 227–243.

[12] T.R. Bieler, P. Eisenlohr, C. Zhang, H.J. Phukan, M.A. Crimp, Grain boundaries and interfaces in slip transfer, Current Opinion in Solid State and Materials Science. 18 (2014) 212–226.

[13] Z.H. Jin, P. Gumbsch, K. Albe, E. Ma, K. Lu, H. Gleiter, H. Hahn, Interactions between non-screw lattice dislocations and coherent twin boundaries in face-centered cubic metals, Acta Materialia. 56 (2008) 1126–1135.

[14] Z. Chen, Z. Jin, H. Gao, Repulsive force between screw dislocation and coherent twin boundary in aluminum and copper, Physical Review B. 75 (2007) 1–4.

[15] T. Tsuru, Y. Shibutani, Y. Kaji, Fundamental interaction process between pure edge dislocation and energetically stable grain boundary, Physical Review B - Condensed Matter and Materials Physics. 79 (2009) 1–4.

[16] T. Zhu, J. Li, A. Samanta, H.G. Kim, S. Suresh, Interfacial plasticity governs strain rate sensitivity and ductility in nanostructured metals, Proceedings of the National Academy of Sciences of the United States of America. 104 (2007) 3031–3036.

[17] L. Li, L. Liu, Y. Shibutani, Defect interaction summary between edge dislocations and <112>-axis symmetric tilt grain boundaries in copper on activation barriers and critical stresses, International Journal of Plasticity. 149 (2022) 103153.

[18] S. Hayakawa, H. Xu, Temperature-dependent mechanisms of dislocation–twin boundary interactions in Ni-based equiatomic alloys, Acta Materialia. 211 (2021) 116886.

[19] J.R. Rice, Dislocation nucleation from a crack tip: An analysis based on the Peierls concept, Journal of the Mechanics and Physics of Solids. 40 (1992) 239–271.

[20] C. Deng, F. Sansoz, Fundamental differences in the plasticity of periodically twinned nanowires in Au, Ag, Al, Cu, Pb and Ni, Acta Materialia. 57 (2009) 6090–6101.

[21] B. Escaig, Sur le glissement dévié des dislocations dans la structure cubique à faces centrées, Journal de Physique. 29 (1968) 225–239.

[22] G. Esteban-Manzanares, E. Martínez, J. Segurado, L. Capolungo, J. LLorca, An atomistic investigation of the interaction of dislocations with Guinier-Preston zones in Al-Cu alloys, Acta Materialia. 162 (2019) 189–201.

[23] T. Zhu, J. Li, S. Yip, Atomistic study of dislocation loop emission from a crack tip, Physical Review Letters. 93 (2004) 9–12.

[24] T. Zhu, J. Li, S. Yip, Atomistic Reaction Pathway Sampling: The Nudged Elastic Band Method and Nanomechanics Applications, in: Nano Cell Mech., John Wiley & Sons, Ltd, Chichester, UK, 2012: pp. 311–338.

[25] Y. Mishin, D. Farkas, M.J. Mehl, D.A. Papaconstantopoulos, Interatomic potentials for monoatomic metals from experimental data and ab initio calculations, Physical Review B - Condensed Matter and Materials Physics. 59 (1999) 3393–3407.

[26] Y. Mishin, M.J. Mehl, D.A. Papaconstantopoulos, A.F. Voter, J.D. Kress, Structural stability and lattice defects in copper: Ab initio, tight-binding, and embedded-atom calculations, Physical Review B - Condensed Matter and Materials Physics. 63 (2001) 2241061–22410616.

[27] P.L. Williams, Y. Mishin, J.C. Hamilton, An embedded-atom potential for the Cu-Ag system, Modelling and Simulation in Materials Science and Engineering. 14 (2006) 817–833.

[28] S.M. Foiles, M.I. Baskes, M.S. Daw, Embedded-atom-method functions for the fcc metals Cu, Ag, Au, Ni, Pd, Pt, and their alloys, Physical Review B. 33 (1986) 7983–7991.

[29] L.M. Hale, B.M. Wong, J.A. Zimmerman, X.W. Zhou, Atomistic potentials for palladium-silver hydrides, Modelling and Simulation in Materials Science and Engineering. 21 (2013).

[30] X.W. Zhou, R.A. Johnson, H.N.G. Wadley, Misfit-energy-increasing dislocations in vapor-deposited CoFe/NiFe multilayers, Physical Review B - Condensed Matter and Materials Physics. 69 (2004) 1–10.

[31] J. Cai, F. Wang, C. Lu, Y.Y. Wang, Structure and stacking-fault energy in metals Al, Pd, Pt, Ir, and Rh, Physical Review B - Condensed Matter and Materials Physics. 69 (2004) 1–4.

[32] T. Zhu, J. Li, A. Samanta, A. Leach, K. Gall, Temperature and strain-rate dependence of surface dislocation nucleation, Physical Review Letters. 100 (2008) 1–4.

[33] R. Freitas, T. Frolov, M. Asta, Step free energies at faceted solid surfaces: Theory and atomistic calculations for steps on the Cu(111) surface, Physical Review B. 95 (2017) 1–13.

[34] Z.F. Zhou, Y.C. Zhou, Y. Pan, C.F. Xu, Melting of Ni nanowires with and without oxide capping, Acta Materialia. 58 (2010) 3059–3067.

[35] T. Liang, D. Zhou, Z. Wu, P. Shi, Size-dependent melting modes and behaviors of Ag nanoparticles: A molecular dynamics study, Nanotechnology. 28 (2017).

[36] P. Carnevali, F. Ercolessi, E. Tosatti, Melting and nonmelting behavior of the Au(111) surface, Physical Review B. 36 (1987) 6701–6704.

[37] E. Ma, Watching the nanograins roll, Science. 305 (2004) 623–624.

[38] F. Dalla Torre, H. Van Swygenhoven, M. Victoria, Nanocrystalline electrodeposited Ni: Microstructure and tensile properties, Acta Materialia. 50 (2002) 3957–3970.

[39] R. Schwaiger, B. Moser, M. Dao, N. Chollacoop, S. Suresh, Some critical experiments on the strain-rate sensitivity of nanocrystalline nickel, Acta Materialia.

51 (2003) 5159–5172.

[40] T. Zhu, J. Li, Ultra-strength materials, Progress in Materials Science. 55 (2010) 710–757.

6. Reversible plasticity by reversible defect interactions

6.1. Research background

It is well established that the plasticity in the crystalline materials is strongly dependent on the behaviors of the dislocations [1]. The nucleation and movement of dislocations, dislocations escaping from the free surface, twinning, defect interactions are usually characterized as the signs of the occurrences of plasticity. When the system overcomes the yielding point and then executes the unloading procedure, a residual strain would normally remain in the bulk material. The same situations exist in the nanoscale where the emitted dislocation is bounded by the free surface or grain boundaries (GBs) [2,3]. The defect interactions also contribute to the crystal plasticity in the nanostructure metals. In most cases, structures that have undergone a defect reaction remain unchanged or continue to develop during the unloading process and thus generate residual strains. They barely recover to the initial state where the residual strain is zero. However, recent experiments observed some unique dislocation behaviors of the nanocrystal structures during the unloading process which resulted in reversible plasticity or pseudo-elasticity.

6.1.1. Reversible plasticity induced by reversal movement of dislocation

First, the movement of the dislocation in Mg has been reported to be reversible during the cyclic loading as shown in Fig. 6-1 [4]. During the initial loading, the dislocation slid leftwards, retracted during unloading, slid leftwards again during the second loading, and finally retraced back during the second unloading. It's worth noting that the reversal movement was not driven by the reverse loading, i.e. a load greater than zero was applied in the negative direction. Actually, the reversible movement of the dislocations is the fundamental part of the reversible plasticity , which has been expanded to other reversible mechanisms [5,6].

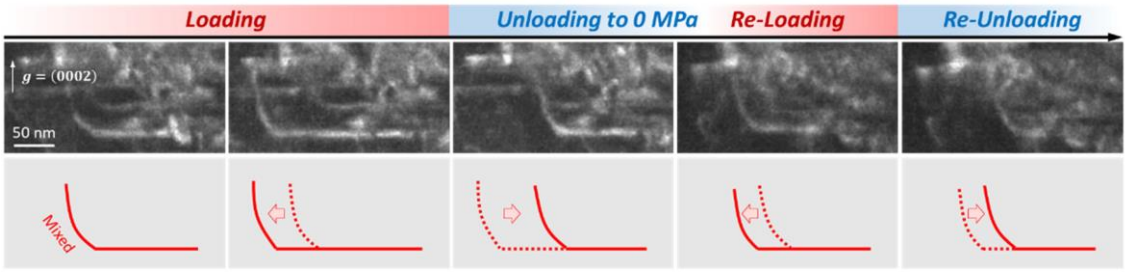

Fig. 6-1 Reversible motion of a $<c+a>$ dislocation under cyclic loading [4].

Barsoum et al. [5] found that the compressive deformations of Ti_3SiC_2 were fully reversible at room temperature as depicted in Fig. 6-2. Even the load reached 1 GPa, such large, repeatable, isothermal, fully reversible, hysteresis loops (both in terms of stress and/or strain) were still achieved. The authors revealed that the reversible plasticity was caused by the formation of the incipient kink band (IKB) in Fig. 6-3. IKBs consisted of two dislocation walls (shown in red) of opposite sign, and a uniform spacing of D as shown in Fig. 6-3a. When the load increased, the IKBs would be generated and dislocations moved to extend the internal areas of the elliptic cylinder with the two ends linked. These processes mediated the plastic deformations. Dashed lines in Fig. 6-3c denote walls that have separated from the source and are moving away from the source. This only happens at higher temperatures and/or stresses. Unless the ends touched the interface and detached to form the kinking band in Fig. 6-3d, the unloading process would reverse the movement of the dislocations to heal the plastic deformation and close the elliptic cylinder. At room temperature, the formations of IKB dominated so that the deformation was fully reversible. On the contrary, at elevated temperature greater than 1300K, the hysteresis loops were open and irreversible.

Although Barsoum identifies the IKB as the key factor, the reversal movement of the dislocations should be the actual key, which realizes and enables the reversible contraction and expansion deformation of the IKB elliptic cylinder during loading and

unloading processes.

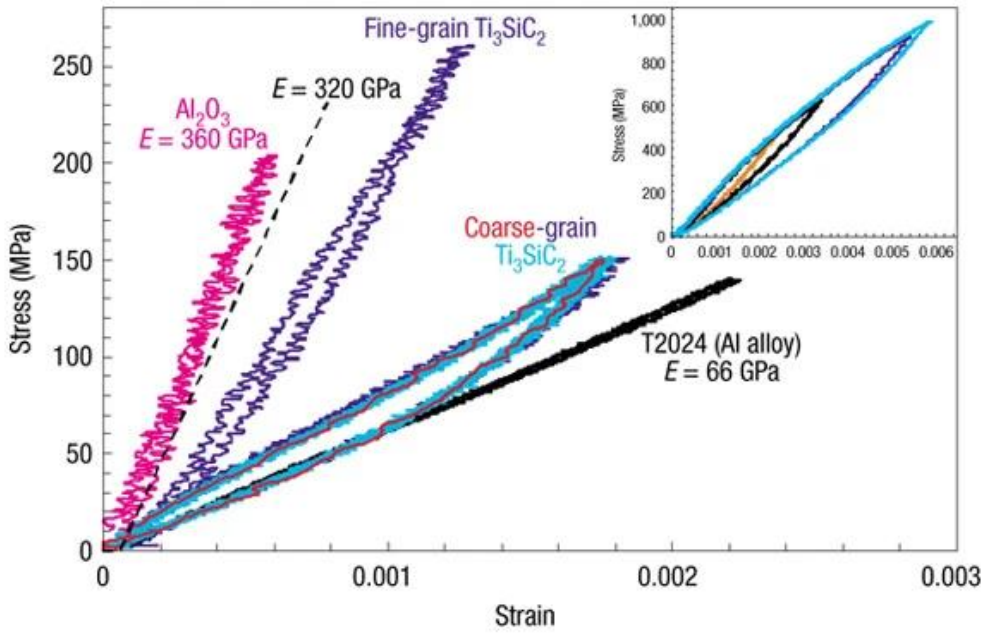

Fig. 6-2 Stress–strain curves at room temperature for fine and coarse-grained Ti_3SiC_2, Al_2O_3 and Al [5]. The inset shows successive loops obtained as the stress was increased up to 1 GPa.

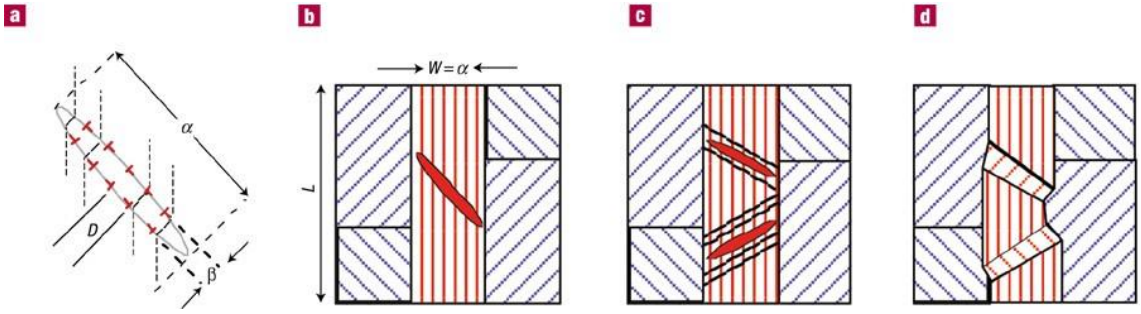

Fig. 6-3 Kink-band formation [5]. (a) Thin elliptic cylinder with axes α and β where $\alpha \gg \beta$. (b) Formation of an IKB in hard (red) grains adjacent to soft (blue) grains. (c) Multiple pile-ups and kink bands in a large grain. (d) Same as (c) after removal of stress, emphasizing formation of grain boundaries (dark lines).

A more obvious example related to the reversibility of dislocation motion was given in the low angle grain boundary (LAGB) migration process under loading-unloading cycle [6], as shown in Fig.6-4. This superior plastic reversibility of metallic bi-crystals mainly originates from conservative motion of the readily dissociated GB dislocations that fundamentally suppress the irreversible damage accumulation arising from the pronounced heterogeneous surface nucleation and annihilation of partials or twins. The LAGB was consist of a column of dislocations and it moved downward under the leftward shear loading as shown in Fig. 6-4(a)-(c) and (k). When underwent rightward shear loading, the LAGB migrated upward as shown in Fig. 6-4(b)-(e). 2^{nd}-5^{th} cycle loading maintained this reversible process as shown in Fig. 6-4(f)-(k). The yellow arrows denote the direction of applied shear load.

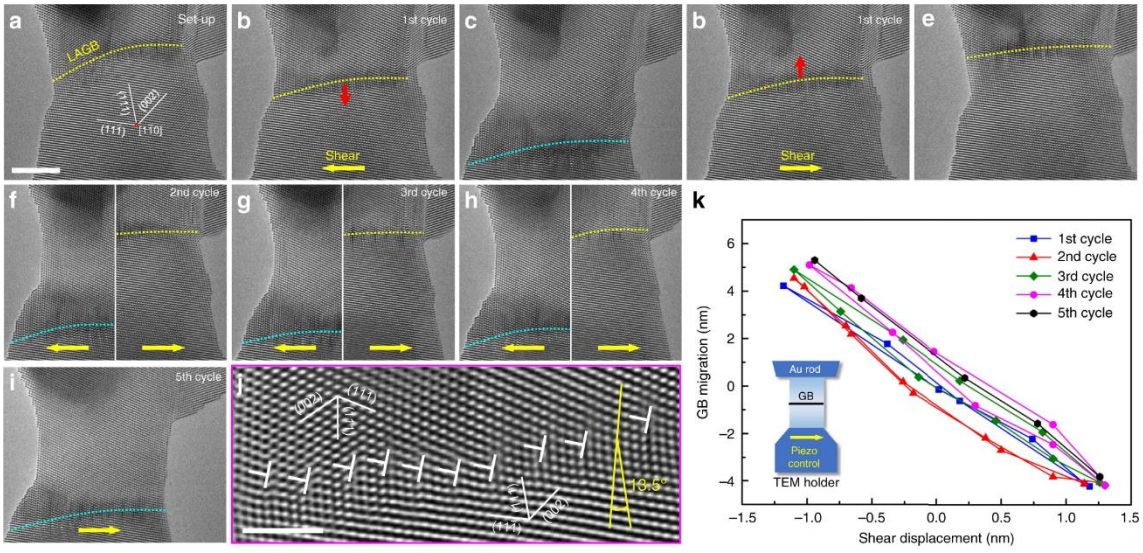

Fig. 6-4 Reversible migration of a 13.5° $[1\bar{1}0]$ low angle grain boundary (LAGB) in shear loading cycles. (a) An as-fabricated gold (Au) bi-crystal with an LAGB. (b), (c) Downward migration of the LAGB under leftward shear loading. (d)-(e) Upward migration of the LAGB under rightward shear loading. (f)-(h) Reversible migration of this LAGB in subsequent shear loading cycles. (i) The LAGB after the left shear in the fifth cycle. (j) Atomistic structure of the 13.5° $[1\bar{1}0]$ LAGB. (k) loading cycles. Scale

bars: (a) 5 nm and (j) 2 nm [6].

Obviously, the reversible plasticity can be realized by the reversal motion of dislocations in forms of IKB or LAGB migrations.

6.1.2. Reversible plasticity induced by twinning and detwinning

The second way to achieve the reversible plasticity has been confirm to be the twinning and detwinning process [7,8]. This mechanism was verified by MD simulations in Cu/Ni/Au/Ag nanowires as depicted by Fig. 6-5. The twinning and detwinning process mediated the reversible transformation from {111} facets to {100} facets. In Fig. 6-5, cross-section 1-1 shows the elongated hexagonal lattice in the unrotated domain with the $<110>/\{111\}$ configuration, and cross-section 2-2 is in the transition region containing both the $<100>/\{100\}$ and the $<110>/\{111\}$ configurations, and cross-section 3-3 shows the square lattice in the reoriented domain with the $<100>/\{100\}$ configuration. In experiment. as shown in Fig. 6-6 [8], the original {111}-dominant facets were oriented to the {100}-dominant configurations by twinning when the probe compressed gold nanowire. However, this process was reversible when the probe detached the Au nanowire and the plastic deformations were recovered by detwinning process.

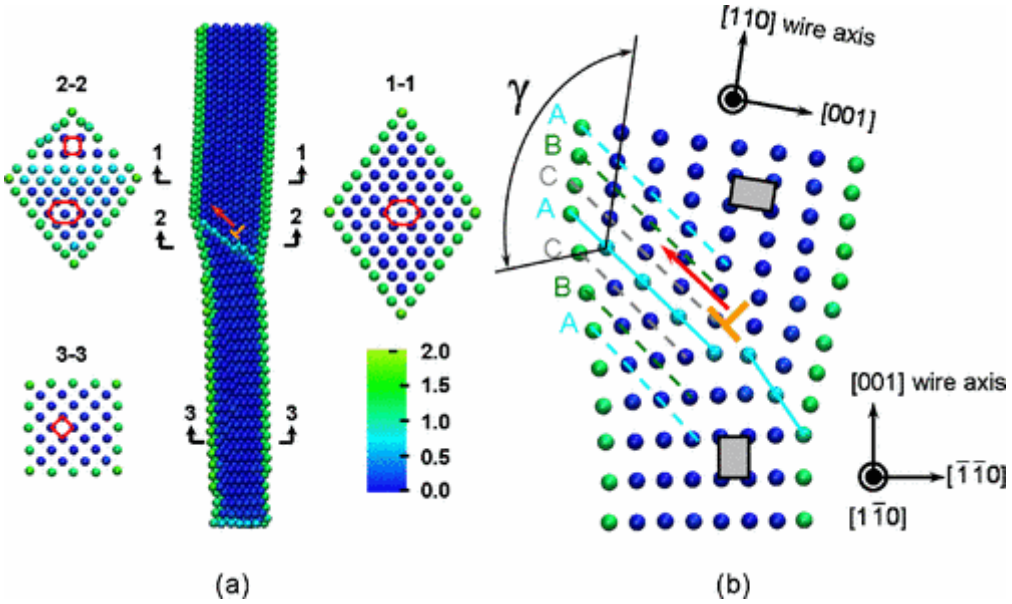

Fig. 6-5 Lattice orientations on the cross sections of a 1.8*1.8 nm Cu nanowire at a strain of 0.24. The misorientation angle in (b) $\gamma = 109.5^{\circ}$ [7].

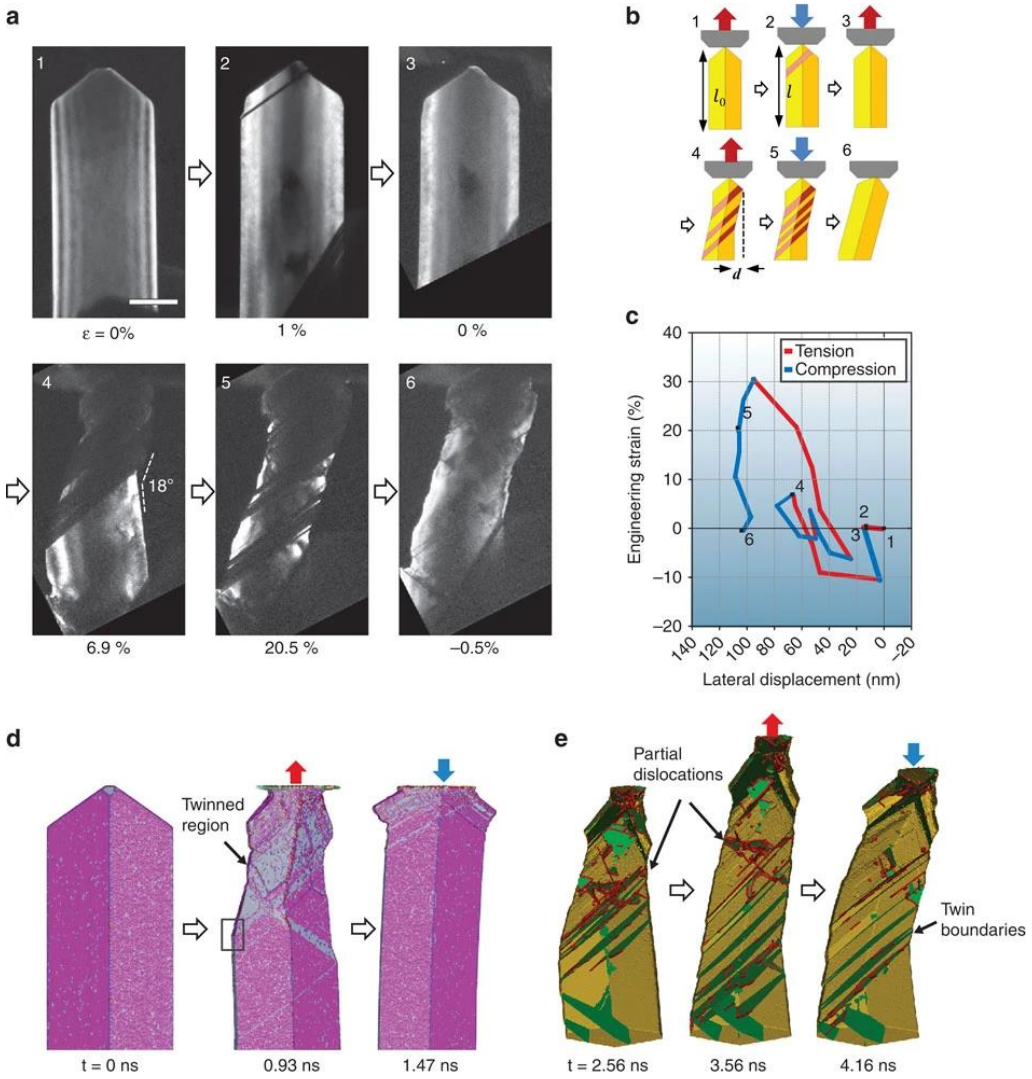

Fig. 6-6 Reversible plastic deformation through twinning and detwinning transition [8].

The reversible plasticity can also been found through the stress-strain curve as depicted as shwon in Fig. 6-7 [7]. The residual strain was almost zero after the unloading and detwinning in MD simulations, even though the unloading point exceeded the yielding points A.

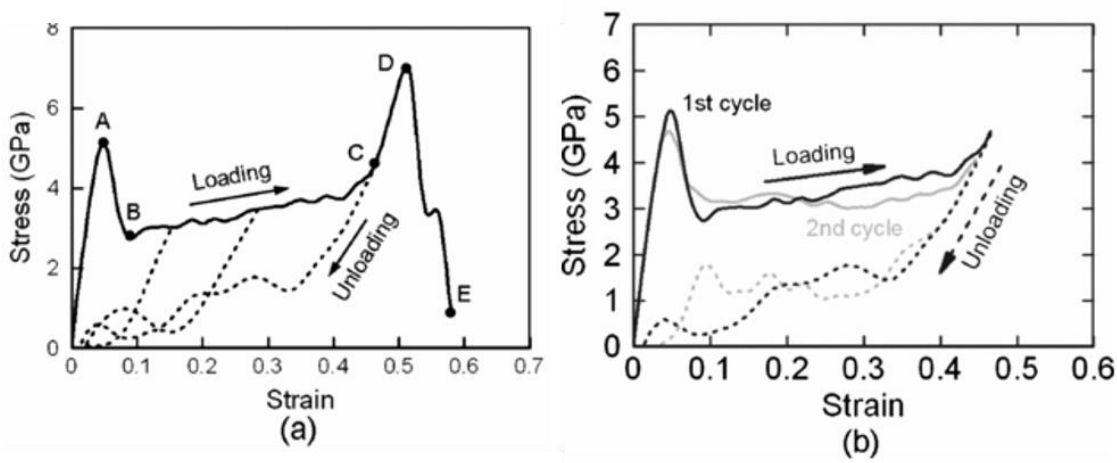

Fig. 6-7 (a) The stress-strain curves of Cu nanowire at 200 K during loading and unloading. (b) the same wire under cyclic loading and unloading [7].

6.1.3. Reversible plasticity induced by twin boundary

Cheng, Qin and Gao et al. [9,10] found that leading partial dislocations nucleated from the free surface of a bi-twinned Ag nanowire can be obstructed by the single TB, and the blocked partials can be retracted under the repulsive force from the TB during unloading, leading to plastic strain recovery or Bauschinger effect as shown in Fig. 6-8. Furthermore, as demonstrated in Fig. 6-9, the penta-twinned Ag nanowire enhanced this recovery process and enabled entirely reversible plasticity.

Although the phenomena are quite clear and straightforward, the detailed mechanism of the interactions between the dislocation and coherent twin boundary (CTB) are yet unrevealed in the perspective of anomalously reversible plasticity.

The questions naturally arise as to why reversible plasticity has not been observed in previous simulations? Can this reversibility be extended to other structures or other metals? In this chapter, we investigated the reversible plasticity which is induced by the reversible interactions between the edge dislocation and grain boundaries (GBs).

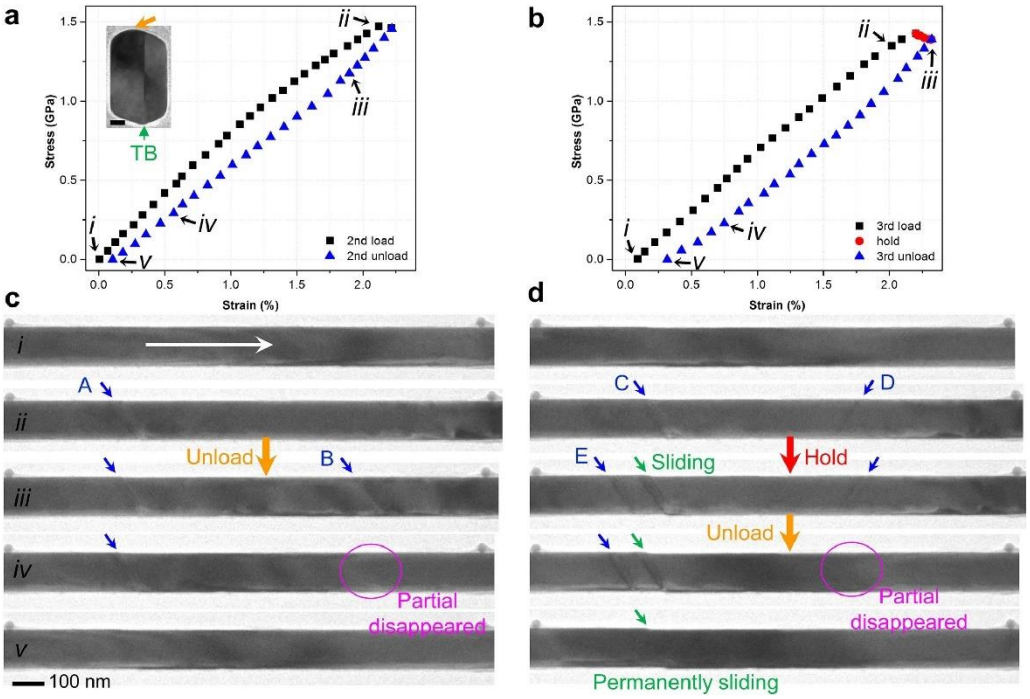

Fig. 6-8 Mechanical responses and microstructure evolution of a bi-twinned Ag NW under in-situ TEM tensile testing [10]. (a-b) Stress–strain curves for the bi-twinned NW without or with a holding step, respectively. (c-d) Snapshots of microstructure evolution during loading–unloading and loading-holding-unloading processes, respectively.

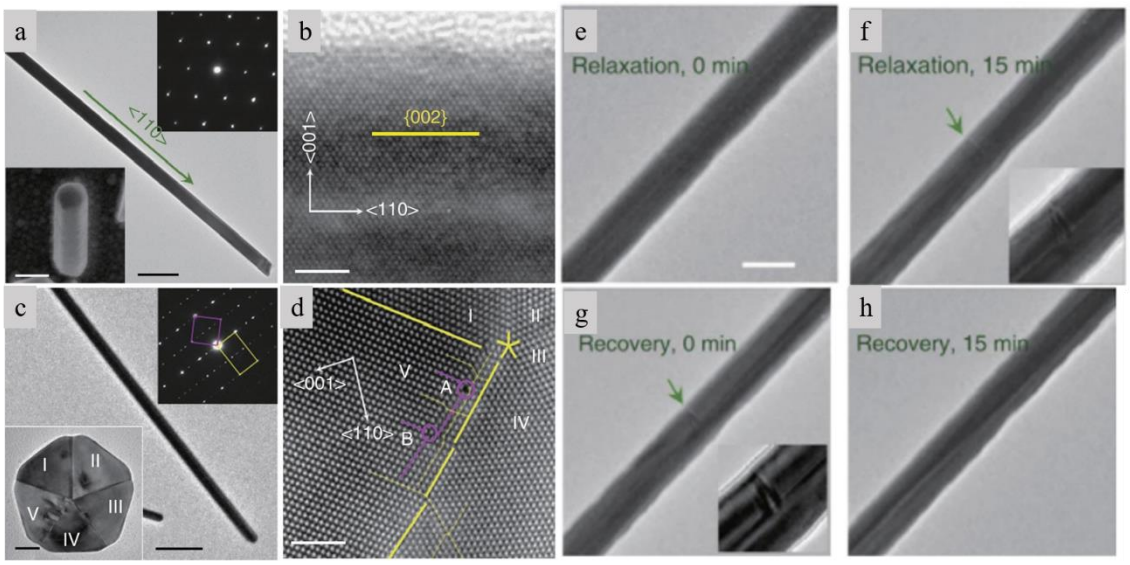

Fig. 6-9 (a-d) Structural characterization of single-crystal and penta-twinned Ag NWs. (e-f) Dislocation was nucleated during loading. (g-h) Dislocation disappeared during

unloading [9].

6.2. Atomic models and simulation condition

Two kinds of GBs are included in this chapter, the <110>-axis $\Sigma3(1\bar{1}\bar{1})$ CTB and <110>-axis tilt symmetric $\Sigma11(\bar{1}13)$ GB. These two GBs are the local minima of the <110>-axis family as mentioned in Chapter 3. The main setups for the MD simulations are identical with those in Chapter 4. The only difference is that the GBs have been chosen differently. In Chapter 4, the <112>-axis tilt GBs guarantee that the edge dislocation is parallel with the GBs. Therefore, the entire dislocation line collided with the GB plane at the same time. However, the CTB belong to the <110>-axis tilt GB. There is an angle θ of about 35.27° between the straight dislocation line and CTB or 62.76° between the straight dislocation line and $\Sigma11(\bar{1}13)$ as shown in Fig. 6-10. EAM potentials were used to model Al [11], Cu [12], Ni [11], and Ag [13]. The sizes of the simulation box were all about $40\text{nm}\times15\text{nm}\times15\text{nm}$ in $X\times Y\times Z$ directions for CTB models and about $70\text{nm}\times20\text{nm}\times8\text{nm}$ for $\Sigma11(\bar{1}13)$ GB models. About 700,000-800,000 atoms were included in the simulations. After the dislocation was introduced, the system was energy-minimized through CG algorithm. It is worth noting that two kinds of dislocations were introduced. One is with the Burgers vector of $\frac{a}{2}[\bar{1}10]$ and is defined as positive dislocation. Another is with the Burgers vector of $\frac{a}{2}[1\bar{1}0]$ and is defined as negative dislocation, where a is the lattice parameter. Displacements were applied to the upper and lower rigid region to drive the edge dislocation to move toward the GB. Certainly, the direction of the applied displacement should also change according to the direction of the Burgers vector to ensure that the dislocation move to the GB region.

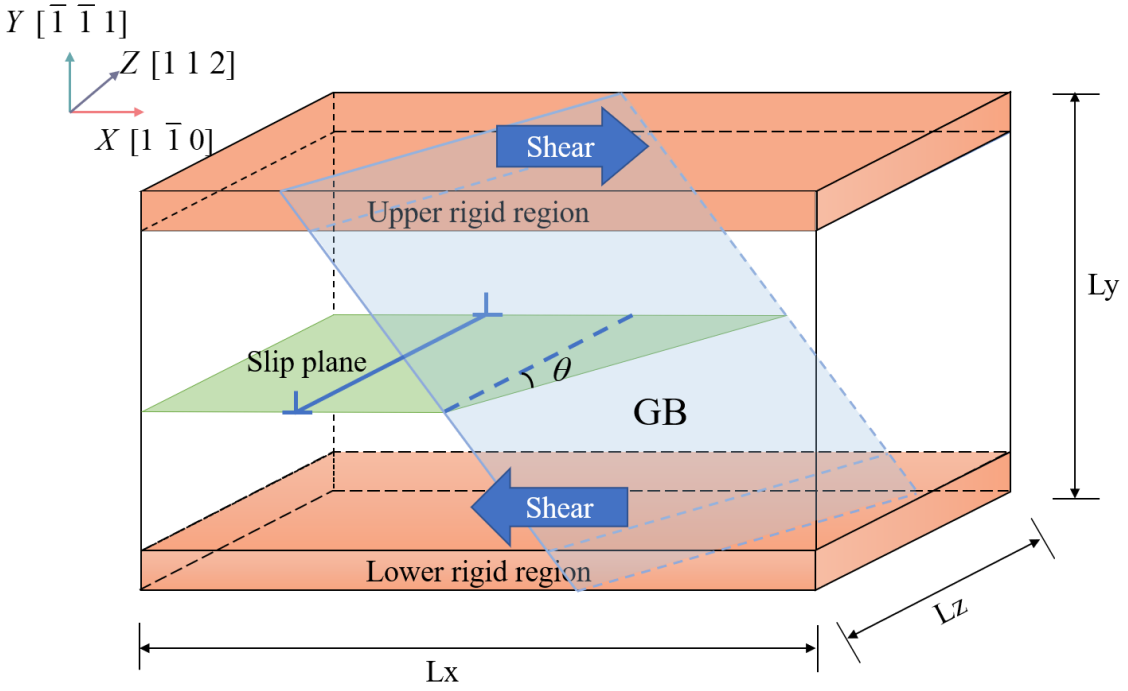

Fig. 6-10 Schematic representation of the interaction model. The domain contains one edge dislocation depicted by blue line on the green slip plane. The upper and lower atomistic plates with 10 Å thickness were set as rigid regions to apply displacement.

6.3. Edge dislocation-CTB interactions

6.3.1. Material: Aluminum (Al)

a) Irreversible interaction of positive dislocation

The shear stress-strain and system energy-strain curves during the loading and unloading process are given in Fig. 6-11(a) and (b), respectively. Obviously, there remained a residual strain of roughly 0.42 % when the stress reached 0 MPa during the unloading process, as illustrated by the red curve in Fig. 6-11(a).

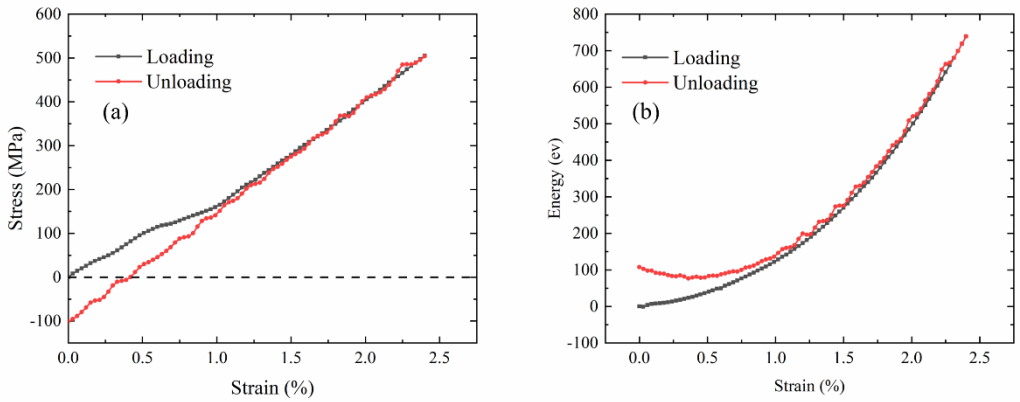

Fig. 6-11 (a) The stress-strain curves of positive edge dislocation-CTB interaction during loading and unloading process. (b) The energy-strain curves of positive edge dislocation-CTB interaction during loading and unloading process.

Referring to the atomic morphologies as shown in Fig. 6-12(a), the perfect dislocation would dissociate into two partial dislocations after the energy minimization. As the displacement increased, the leading partial slid to the CTB and touched the CTB at $\gamma = 0.72\% / \tau = 125$ MPa. The trailing partial was still repelled by the CTB until most part of the dislocation line impacted the CTB plane. At $\gamma = 1.14\% / \tau = 195$ MPa, as shown in Fig. 6-12(c), one end of the edge dislocation was absorbed by the CTB while the main part of the dislocation line still remained in the parent grain. Eventually, all of the dislocation was completely absorbed by the CTB in Fig. 6-12(d). One sessile dislocation and one partial dislocation were generated after the defect interactions, following by,

$$\frac{1}{2}[\bar{1}10] \rightarrow \frac{1}{6}[\bar{1}1\bar{2}] + \frac{1}{3}[\bar{1}11] \tag{6-1}$$

The mobile dislocation with the Burgers vector of $\frac{1}{6}[\bar{1}1\bar{2}]$ slipped on the CTB with the applied load increasing, generating one misfit step on the CTB plane. The sessile dislocation stayed at the impacting point because CTB is not the slip plane for $\frac{1}{3}[\bar{1}11]$

Frank dislocation.

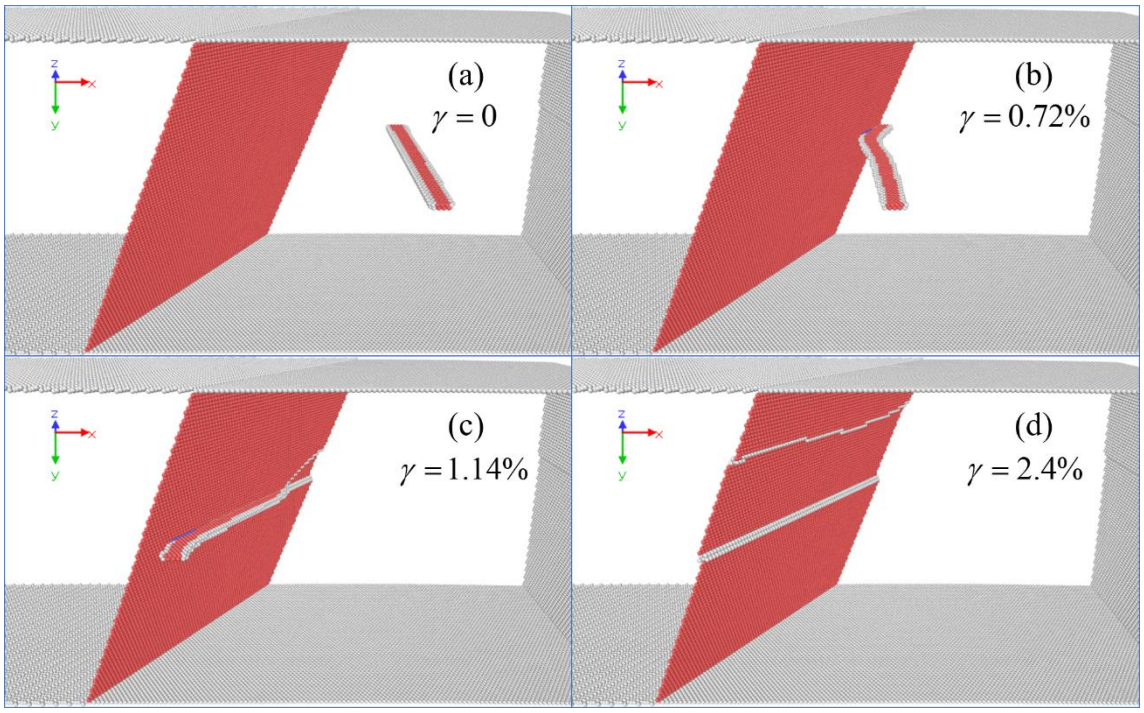

Fig. 6-12. The atomic configurations during the loading process. (a) the initial state. (b) the leading partial dislocations started to touch the CTB. (c) the edge dislocation was absorbed by the CTB at one end while the other end still kept a distance from the CTB. (d) the final state. The edge dislocation was completely absorbed by the CTB leaving one sessile dislocation and one mobile dislocation.

During unloading process, as shown in Fig. 6-13(a), the mobile partial dislocation slipped back toward the impacting point and recombined with the Frank dislocation at one end when $\gamma = 0.6\%$. New perfect dislocation generated at the CTB after the recombination as shown by the dark blue dislocation line in the lower right inset of each subplot in Fig. 6-13. Further decreasing the load, the recombined perfect dislocation dissociated again and the subsequent partial dislocation slipped on the other half of CTB. When the load decreased to 0MPa, as shown in Fig. 6-13(c), most part of the dislocation were combined to perfect dislocation while two ends remained one sessile and one mobile

dislocation. When the deformations were completely removed, namely, $\gamma = 0$, the stress was about -100 MPa and the dislocation line did not recover as shown in Fig. 6-13(d). The energy of the system nearly coincided during the loading and unloading processes, as shown in Fig. 6-11(b). Only after the stress declined below 0 MPa did the overlapping energy lines start to significantly diverge and energy rise, indicating that the system had been reverse loaded. Because the structure of the dislocation has altered, the energy of the final unloading system was higher than that of the initial state.

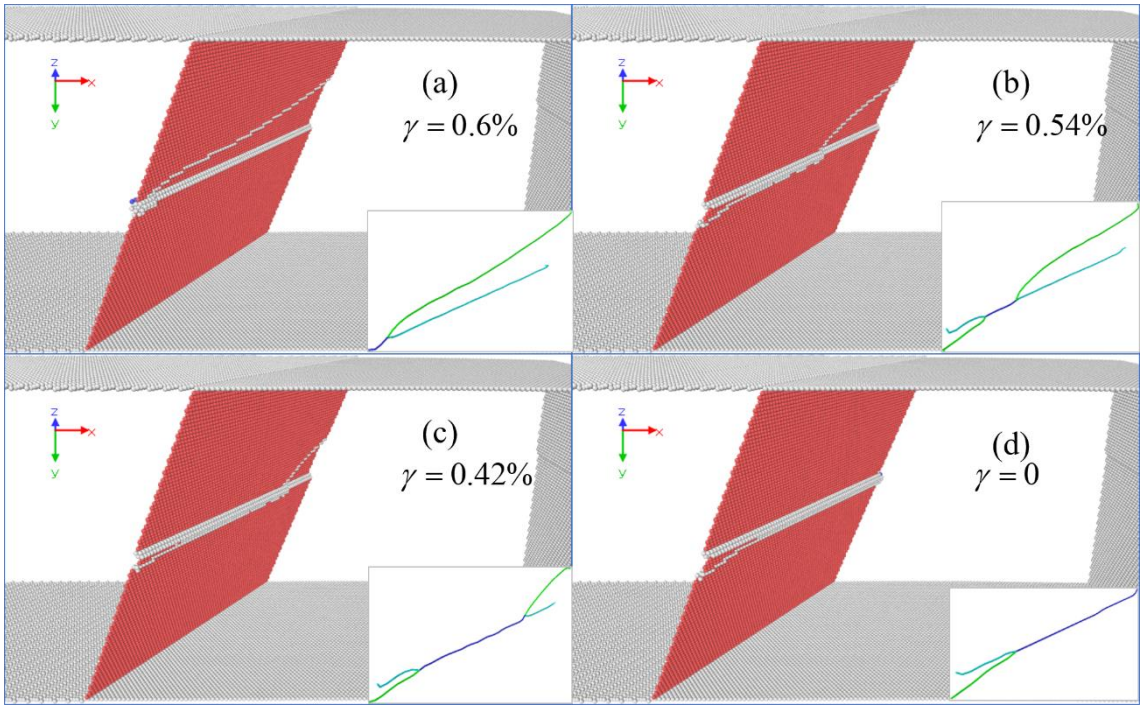

Fig. 6-13 The atomic configurations during the unloading process. (a) Reacted dislocations recombined to the perfect dislocation at one end. (b) The recombined perfect dislocation dissociated into one sessile and one mobile dislocation on the CTB. (c) The atomic configuration at the 0 MPa state. (d) The atomic configuration at the 0-strain state. Each inset at the right corner represents the dislocation line obtained by the DXA algorithm. Dark blue line is the perfect dislocation, green line is the Shockley partial dislocation, light blue line is the Frank sessile dislocation.

b) Reversible interaction of negative dislocation

Fig. 6-14(a) gives the stress-strain curves during the loading and unloading process. Compared with the positive dislocation case, there is no obvious residual strain when the stress decreased to 0 MPa. The energy curves almost overlapped at all stages in Fig. 6-14(b). The overlap of these global-curves implies a reversible defect interaction or reversible plasticity.

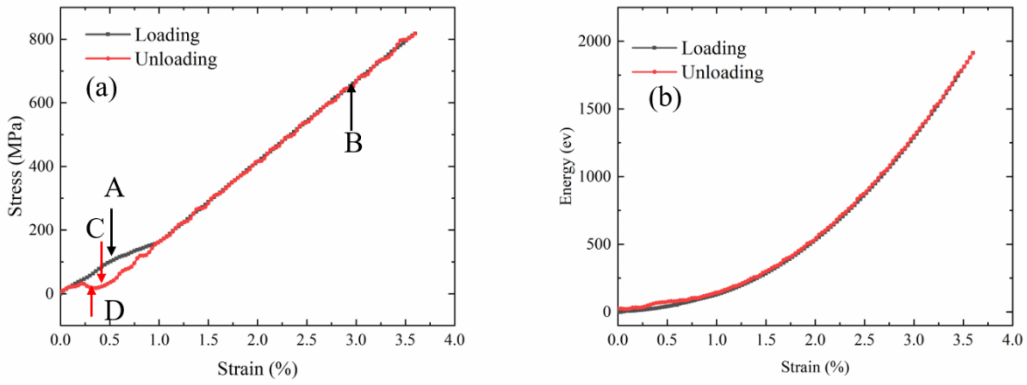

Fig. 6-14. (a) The stress-strain curves of negative edge dislocation-CTB interaction during loading and unloading process. Point A: the dislocation started to impact the CTB. Point B: the dislocation was completely absorbed by the CTB. (b) The Energy-strain curves of negative edge dislocation-CTB interaction during loading and unloading process. Point C: the dislocation started to be peel off from the CTB. Point D: the dislocation was completely peeled off from the CTB.

Taking a closer look at the atomic structure, as shown in Fig. 6-15(a), leading partial dislocation started to impact the CTB at Point A in Fig. 6-14(a). After the entire leading partial dislocation impacted on the CTB, the slope of stress-strain curve slightly raised and at Point B the edge dislocation was completely absorbed by the CTB as shown in Fig. 6-15(b). The interaction can be described as

$$\frac{1}{2}[1\bar{1}0] \rightarrow \frac{1}{6}[1\bar{1}2] + \frac{1}{3}[1\bar{1}\bar{1}] \qquad (6\text{-}2)$$

The negative dislocation was absorbed by the CTB in the same way that the positive dislocation was, and one sessile Frank dislocation and one Shockley partial dislocation were generated. Similarly, the immobile Frank dislocation recorded the impacting point and partial dislocation slipped on the CTB plane. However, the stress responses were a little bit different between these two interactions. Although the stresses are all around 120 MPa when the leading partial dislocation first impacted the CTB, stress would be higher for negative dislocation when it was completely absorbed by CTB (about 670 MPa) than that for positive dislocation (about 450 MPa).

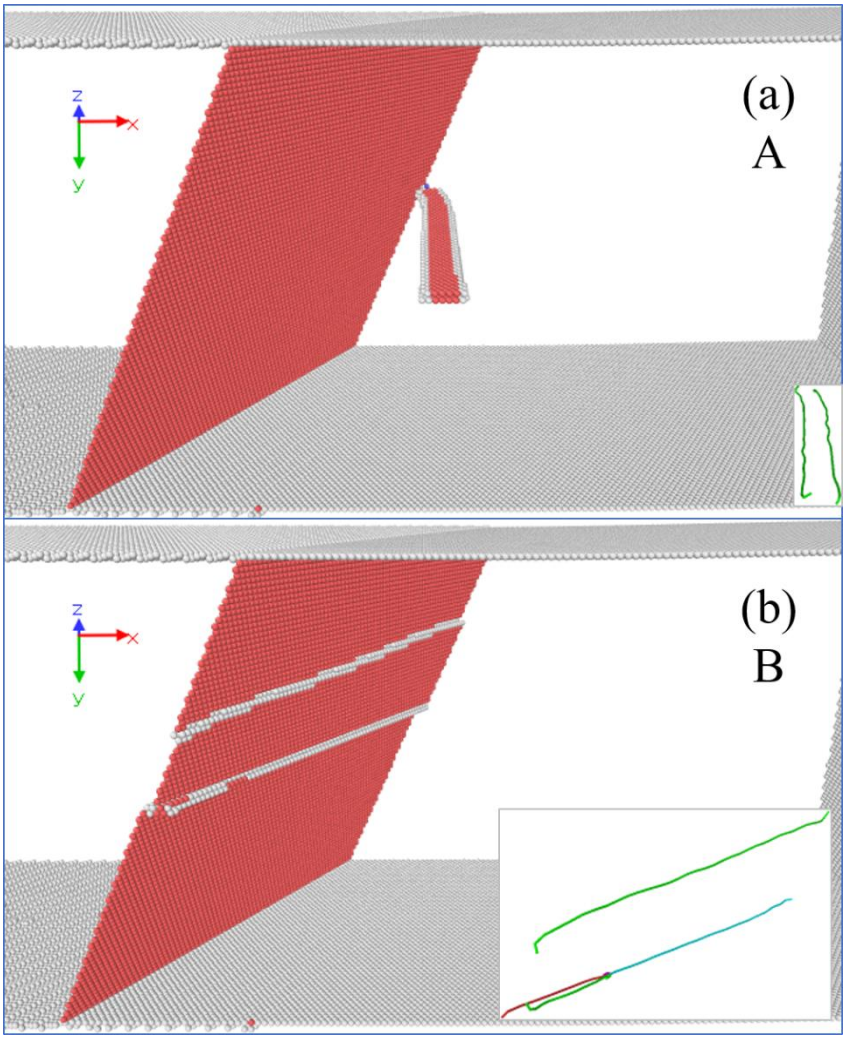

Fig. 6-15 The atomic configurations during the loading process. (a) negative edge dislocation started to impact the CTB at Point A in Fig. 6-14. (b) the negative edge dislocation was absorbed by CTB and one Shockley partial dislocation and one Frank

sessile dislocation were generated at Point B in Fig. 6-14.

During the unloading process, things became considerably different from the positive dislocation, as shown in Fig. 6-16. As seen in Fig. 6-16(b), the nucleated partial dislocation returned to the impacting point, while the original leading partial dislocation peeled off from the CTB and entered the original grain. The peeling off procedure did not arise during the unloading process of the positive dislocation system. Even more surprising is that the edge dislocation started to escape from the CTB at $\gamma = 0.48\% / \tau = 31\text{MPa}$, as shown by the Point C in Fig. 6-14(a) and in Fig. 6-16(c). Further removal of deformation leaded to the continuation of the peeling process (Fig. 6-16(d)). Eventually, the whole part of the negative edge dislocation was completely peeled off from CTB at $\gamma = 0.24\% / \tau = 30\text{MPa}$ as shown in Fig. 6-14 (a) and Fig. 6-16(e). It's worth noting that the stress increased between Point C and Point D, despite the fact that the deformation was being removed continually. The dislocation was peeled off of CTB during this operation, causing the stress to rise. This behavior can be detected due to the displacement-controlled loading of the cell. The negative edge dislocation returned to its original position when the deformation was totally removed, and the stress returned to 0 MPa. The whole process was completely reversible and leaded to a reversible plasticity.

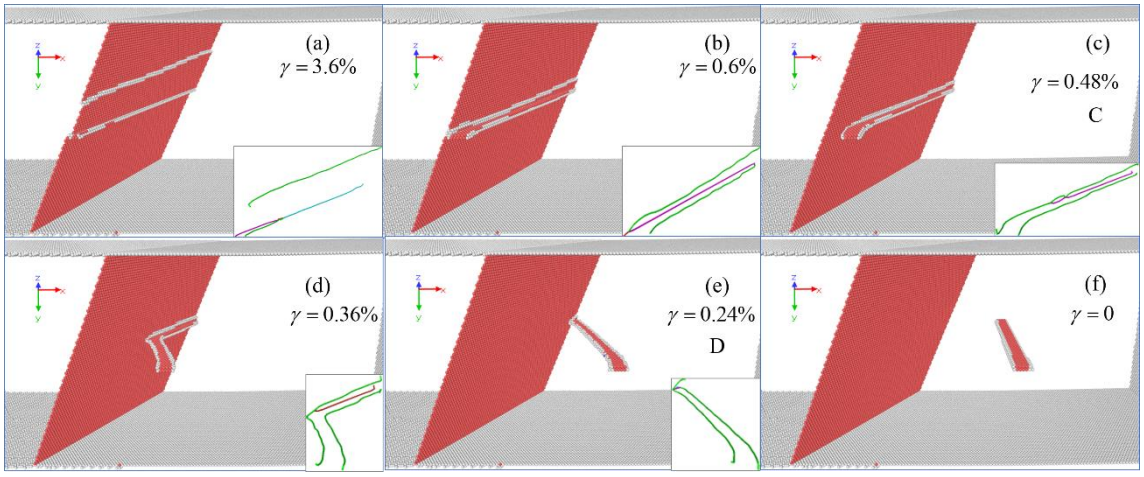

Fig. 6-16. The atomic configurations during the unloading process. (a) the initial state of

the unloading process. (b) the original trailing partial dislocation was peeled off from the CTB and entered the original grain. (c) the original leading partial was peeled off from the CTB. Corresponding to the Point C in Fig.6- 14(a). (d) half of the dislocation was peeled off the CTB. (e) the original dislocation was completely peeled off from the CTB. (e) the dislocation moved back to the original position when the deformation was completely removed.

6.3.2. Material: Copper (Cu)

a) Irreversible interaction in positive edge dislocation

According to the interaction outcome in terms of atomistic phenomenon, the positive dislocation would transmit through the CTB and enter the adjacent grain when the applied deformation was large enough, which is quite different from Al. Fig. 6-17 gives the stress-strain curves and the energy evolution curves during the loading and unloading process. After the unloading process, the residual stress was around 1.04%. The curves of the energy evolutions did not coincide either in Fig. 6-17 (b). Obviously, the strain-stress interaction between positive edge dislocation and CTB is irreversible in Cu, as evidenced by the open hysteresis loop.

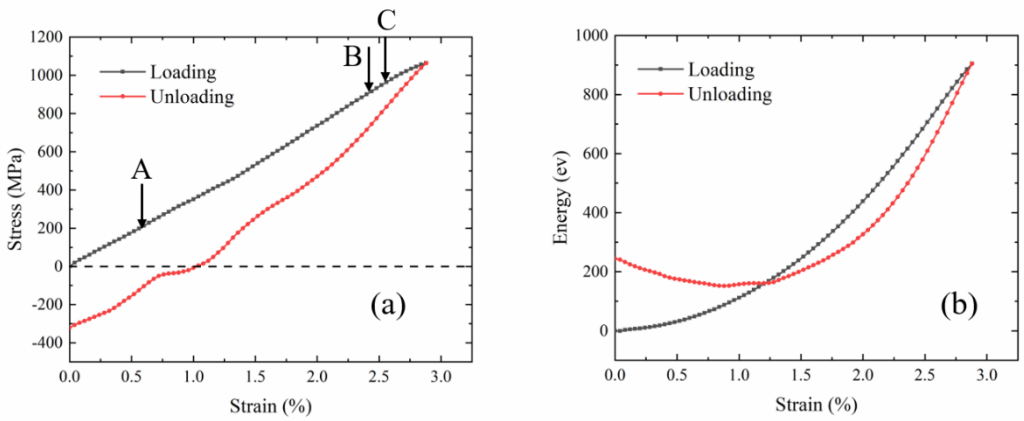

Fig. 6-17 (a) The stress-strain curves of positive edge dislocation-CTB interaction during loading and unloading process. (b) The Energy-strain curves of positive edge dislocation-

CTB interaction during loading and unloading process. Point A: the leading partial touched the CTB. Point B: Entire leading partial dislocation was absorbed by CTB. Point C: dislocation transmitted through the CTB.

The atomic configurations in Fig. 6-18 give distinguishing scenarios from those in Al. First, the width of the stacking fault ribbon of the dissociated dislocation was larger than that of Al as shown in Fig. 6-18(a), which can be elucidated by the difference of the stacking fault energy. The leading partial dislocation impacted the CTB at $\gamma = 0.64\% / \tau = 227\text{MPa}$ (Point A in Fig. 6-17(a)) and was absorbed at $\gamma = 2.32\% / \tau = 868\text{MPa}$ (Point B in Fig. 6-17(a)). Clearly, the stress is larger in Cu than that in Al when the leading partial was absorbed. More importantly, at the early stage, trailing partial dislocation was still repelled by the CTB in Cu, but part of trailing partial already interacted with the CTB before the whole dislocation line impacted the CTB in Al. Increasing the applied deformation would drive the edge dislocation to penetrate through the CTB as shown in Fig. 6-18(d) and Point C in Fig. 6-17(a). The interaction can be described as

$$\frac{1}{2}[\bar{1}10] \rightarrow \frac{1}{6}[\bar{1}1\bar{2}] + \frac{1}{2}[101]^{T} \tag{6-3}$$

One perfect dislocation and one partial dislocation was generated after the interaction. The same as Al, the partial dislocation could slip on the CTB plane when the deformation increased or decreased.

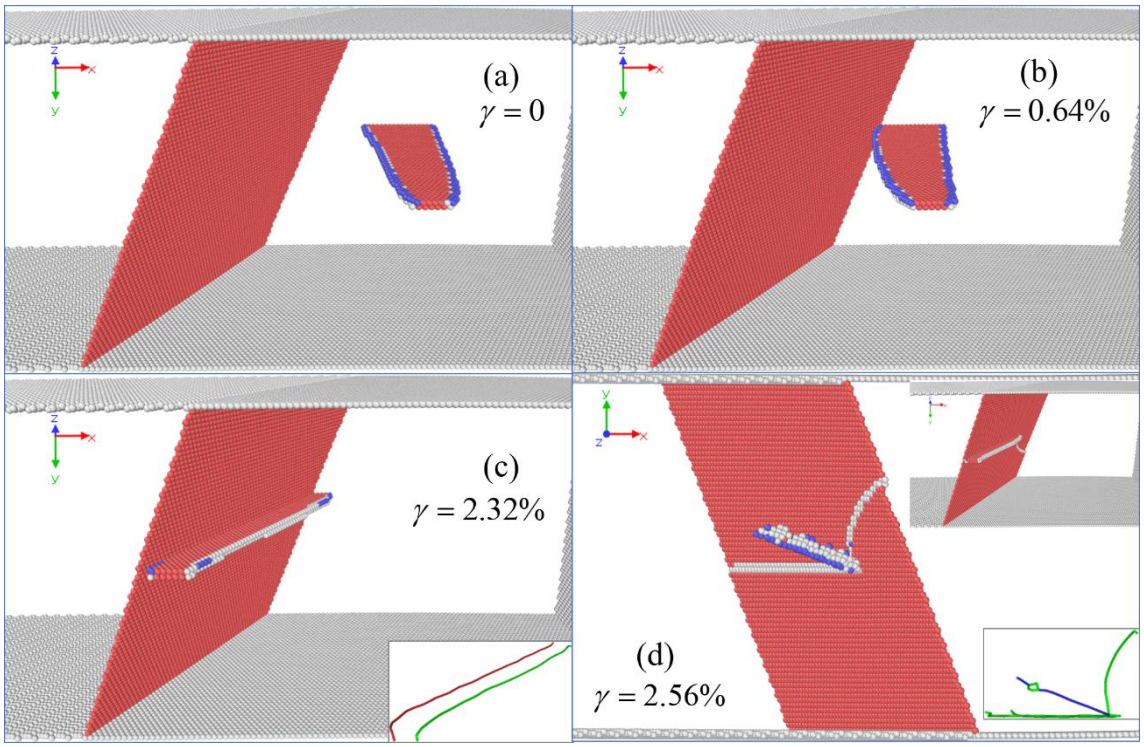

Fig. 6-18 The atomic configurations during the loading process. (a) the initial state. (b) the leading partial dislocations started to touch the CTB at Point A in Fig. 6-17(a). (c) the leading partial dislocation was absorbed by the CTB while the trailing partial dislocation was still repelled by the CTB at Point B in Fig. 6-17(a). The inset represents the dislocation lines. Green line is the Shockley partial dislocation. Red line is the dislocation on the CTB. (d) the final state. Part of the edge dislocation transmitted through the CTB leaving one residual partial dislocation on the CTB and one perfect dislocation in the twinned grain. Green line is the Shockley partial dislocation. Dark blue line is the perfect dislocation in the twinned grain. Note the viewing angle is different from the former three pictures and the inset in the right corner has the same viewing angle.

During the unloading process, as shown in Fig. 6-19, the transmitted perfect dislocation would marched toward the free surface and dissociated in two the partial dislocations, in Fig. 6-19(b) and (c). When the dislocation came in contact with the free surface, a little step appeared. Following the step on the free surface, the slip trajectory can be monitored.

The end of the transmitted dislocation slide to another surface after the deformation was completely removed. The opposite end was blocked at the CTB plane at the same time. The newly nucleated partial dislocation slipped along the CTB plane throughout the unloading process. As can be seen in Fig. 6-17(a) and Fig.6-19(d), the dislocation was unable to recover to its original structure, resulting in irreversible plasticity with a residual strain of roughly 1.04 %.

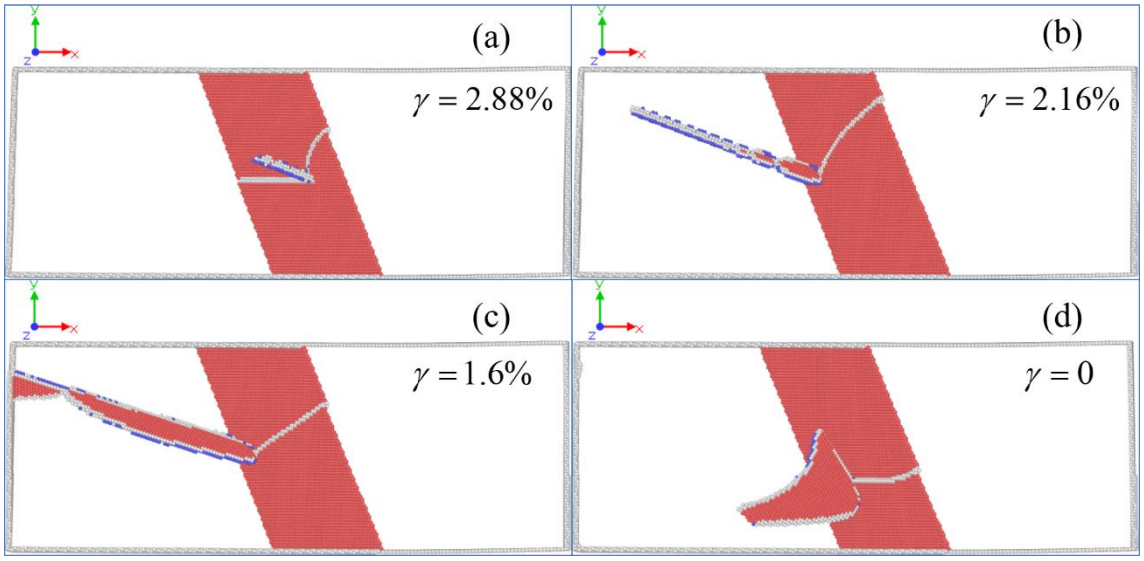

Fig. 6-19. The atomic configurations during the unloading process. (a) the initial state. (b) the dislocation moved toward the free surface. (c) the dislocation impacted the free surface and left one little step on the surface. (d) the final state when the applied displacements were completely removed.

b) Reversible interaction of negative dislocation

The interaction between the negative edge dislocation and CTB, like that of Al, is reversible, resulting in reversible plasticity. As shown in Fig. 6-20, there is no residual strain when the unloading stress came to 0 MPa and the evolutions of system energy almost overlaps for the loading and unloading process. Fig. 6-20 illustrates the reversible plasticity and reversible defect interaction.

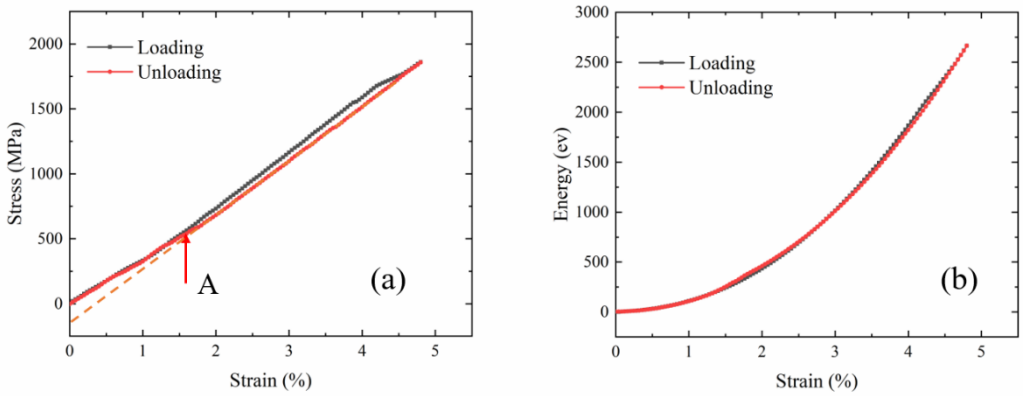

Fig. 6-20 (a) The stress-strain curves of negative edge dislocation-CTB interaction during loading and unloading process. (b) The Energy-strain curves of negative edge dislocation-CTB interaction during loading and unloading process. Point A: dislocation started to move back to the original grain. Dash red line is a visual guide for the extrapolation of the unloading curve if no reversible motion was found.

For the loading process, the entire leading partial dislocation would be absorbed by the CTB at $\gamma = 2.4\% / \tau = 905\text{MPa}$. However, at $\gamma = 4.24\% / \tau = 1687\text{MPa}$, the trailing partial dislocation interacted with the CTB, causing one partial dislocation to be released into the twinned grain. One Shockley partial dislocation was left on the CTB plane. With the deformation increasing, the penetrated trailing partial was released from the interaction region following the leading partial dislocation and eventually, one perfect dislocation was emitted to the twinned grain as shown in Fig. 6-21(c). The interaction can be described as,

$$\frac{1}{2}[1\bar{1}0] \rightarrow \frac{1}{6}[1\bar{1}2] + \frac{1}{2}[\bar{1}\bar{1}0]^T \tag{6-4}$$

It is worth noting that the superscript T in Eq. (6-4) indicates that the Burgers vector was computed using the coordinate of the twinned grain. When the results were compared to the positive dislocation case, it was discovered that, while both situations resulted in dislocation transmission, the outgoing slip planes of the transmitted perfect dislocation

were different. The outgoing dislocation line in the negative dislocation case is parallel with the CTB, which is quite different from that of the positive dislocation case.

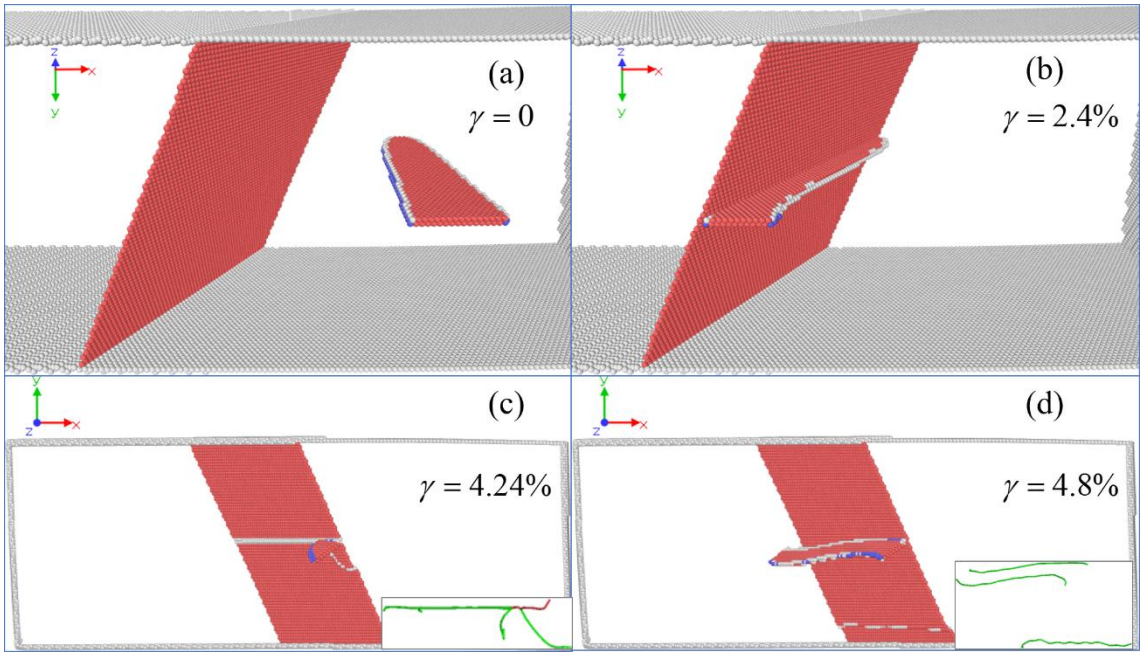

Fig. 6-21 The atomic configurations during the loading process in Cu. (a) the initial state. (b) the leading partial dislocation was absorbed by the CTB while the trailing partial dislocation was still repelled by the CTB. (c) the dislocation started to transmit through the CTB and emit one partial dislocation to the twinned grain and one partial dislocation on the CTB plane. (d) the final state. One perfect dislocation was emitted to the twinned grain and one partial dislocation was left and slipped on the CTB. Green line is the Shockley partial dislocation. Note the viewing angle is different for (c, d) from the former two pictures.

When the system was unloaded, as illustrated in Fig. 6-22, the transmitted perfect dislocation stayed around the vicinity of the GB region rather than moving to the free surface. The partial dislocation on the CTB slipped back to the impacting point and recombined with the transmitted perfect dislocation as the applied strain was gradually reduced. As a result, as illustrated in Fig.6-22(b), the initial incident dislocation was released from the CTB into the original grain at one end of the CTB. Simultaneously, the

slope of the strain stress curve shifted away from the original trend, as indicated by Point A and the dashed red line in Fig. 6-20(a). At $\gamma = 1.12\% / \tau = 379\text{MPa}$, the dislocation was nearly completely detached from the CTB and subsequently returned to its original location. The strain was completely recovered to zero when the applied stress vanished. This reversible process in Cu leaded to the reversible plasticity.

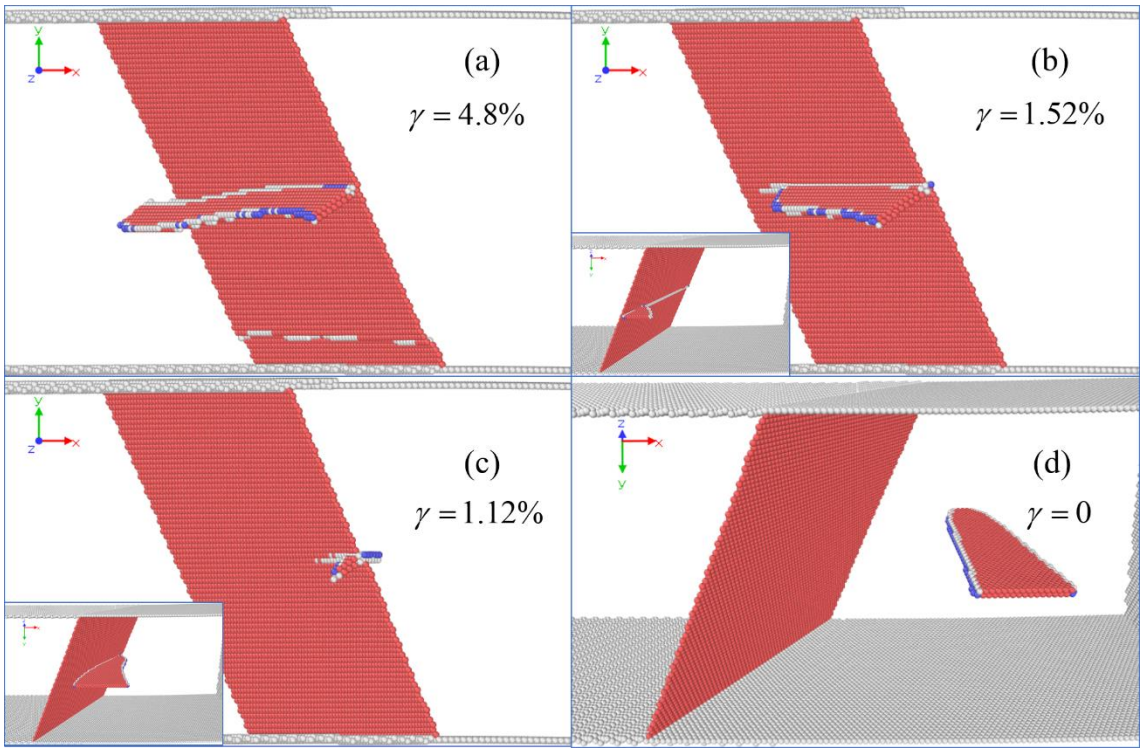

Fig. 6-22 The atomic configurations during the unloading process in Cu. (a) the initial state of unloading process. (b) the original trailing partial dislocation was peeled off the CTB and entered the original grain, corresponding to the Point A in Fig.6- 20(a). (c) the original leading partial was detached from the CTB. (d) edge dislocation moved back to the original location.

6.3.3. Material: Nickle (Ni)

a) Irreversible interaction in positive edge dislocation

It is also irreversible in the interaction between the positive edge dislocation and CTB in Ni. As shown in Fig. 6-23, the residual strain is about 0.36% when the stress decreased

to 0 MPa. In Fig. 6-24, the leading partial dislocation first touched the CTB at $\gamma = 0.64\% / \tau = 388\text{MPa}$ (Point A in Fig. 6-23(a)). Then, it was entirely absorbed as in Fig. 6-24(c), also illustrated by Point B in Fig. 6-23(a). After the transmission, two slipping systems were activated in the twinned grain. In one slip plane, the newly nucleated leading partial dislocation was parallel with the CTB and was emitted to the adjacent grain with the trailing partial dislocation being blocked by the CTB. Another perfect dislocation was emitted on different slip plane at $\gamma = 3.12\% / \tau = 2225\text{MPa}$ (Point C in Fig. 6-23 and Fig. 6-24(d)).

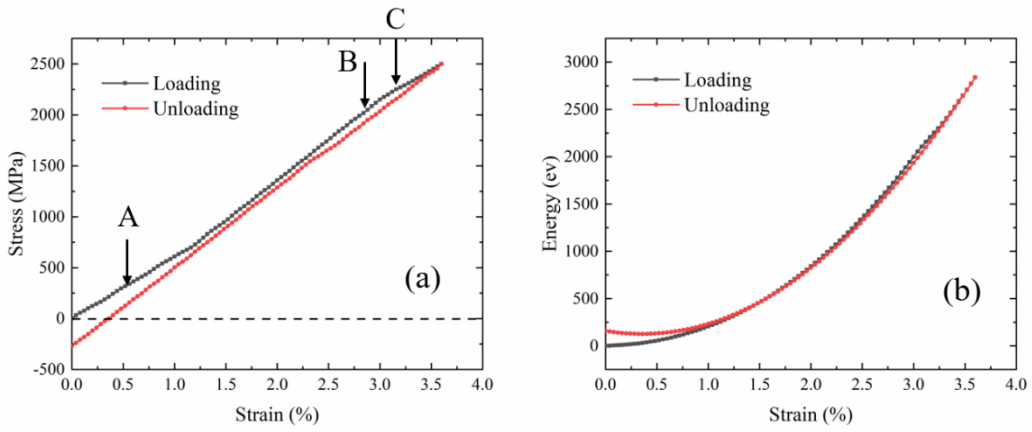

Fig. 6-23 (a) The stress-strain curves of positive edge dislocation-CTB interaction during loading and unloading process in Ni. (b) The Energy-strain curves of positive edge dislocation-CTB interaction during loading and unloading process in Ni. Point A: leading partial dislocation touched the CTB. Point B: entire leading partial dislocation was absorbed by CTB. Point C: Dislocation transmitted through the CTB.

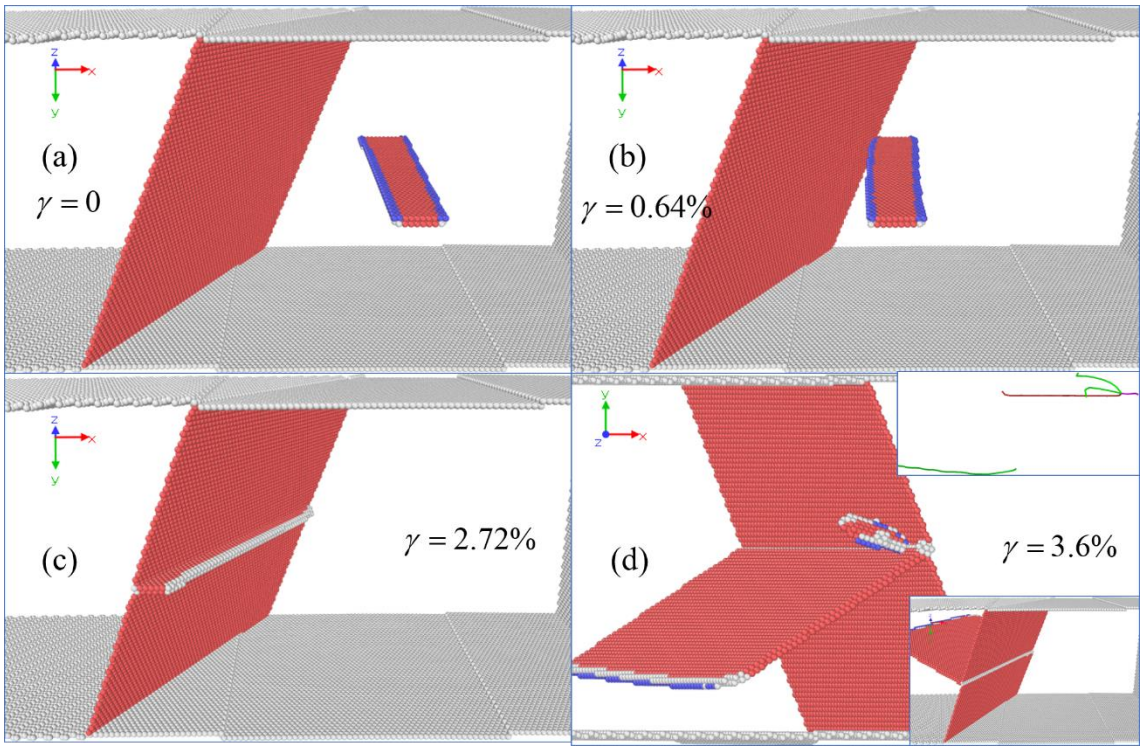

Fig. 6-24 The atomic configurations during the loading process in Ni. (a) the initial state. (b) the leading partial dislocations started to touch the CTB, illustrated by Point A in Fig.6-23(a). (c) the leading partial dislocation was absorbed by the CTB while the trailing partial dislocation was still repelled by the CTB, illustrated by Point B in Fig.6-23(a). (d) the final state: Edge dislocation transmitted through the CTB. Two slip systems were activated. One partial dislocation was first released and the trailing partial was blocked at the CTB. Another perfect dislocation was subsequently emitted at one end of the CTB. The inset represents the dislocation lines. Green line is the Shockley partial dislocation. Note the viewing angle is different from the former three pictures and the inset in the right corner has the same viewing angle.

The final configuration after the applied strain equals 0 is shown in Fig. 6-25. Clearly, the transmitted dislocation did not recover, resulting in a residual strain of roughly 0.36 %. When compared to Cu, this residual strain is considerably lower (1.04 %). However, we noticed that the leading partial returned to the CTB, which is identical to the reversible

dislocation motion discussed in Section 6.1.1. This could explain why the residual strain in Ni is lower than that of Cu, because the penetrating dislocation in Cu moved out of the grain from the free surface rather than partly recovering.

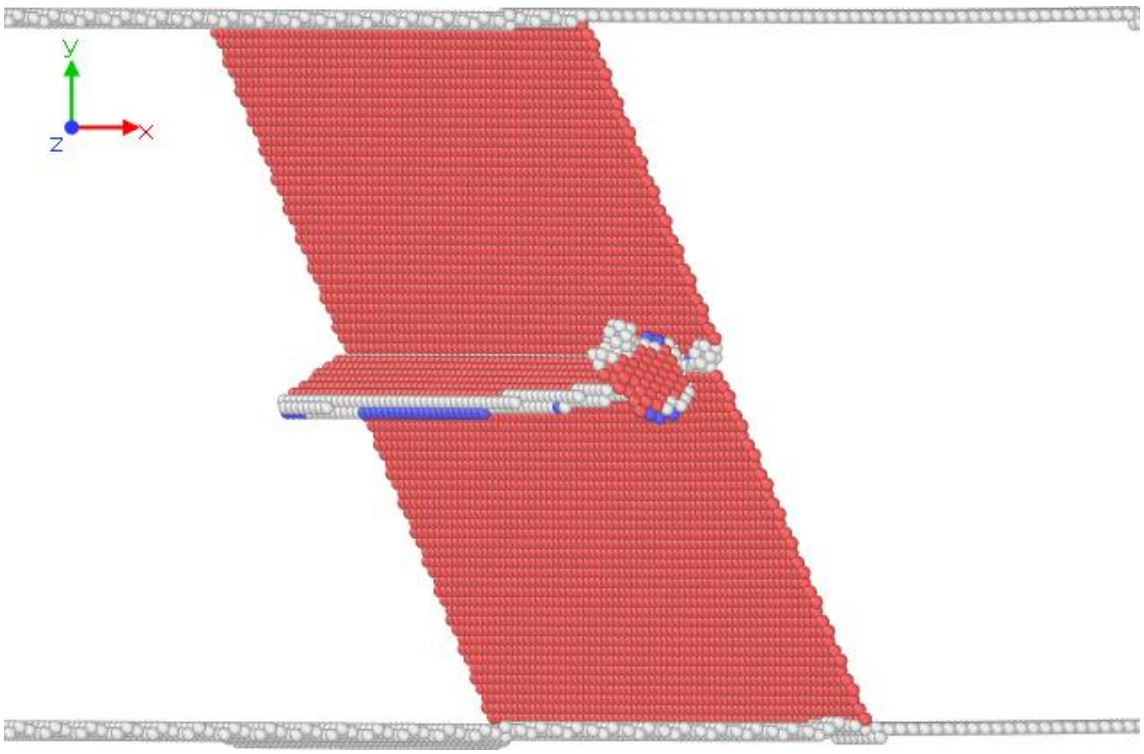

Fig. 6-25. The final configuration in Ni after the applied strain was completely removed.

b) Reversible interaction of negative dislocation

Fig. 6-26 depicts the stress-strain curves and energy evolution curves for negative dislocation-CTB interactions during the loading and unloading process. Obviously, there is no residual strain after unloading. The curves of energy evolution also coincide. As shown by the strain-stress curve in Fig. 6-26(a), two rising step pointed out by Point B and C indicated the abnormal dislocation behaviors that might facilitate the reversible plasticity in Ni, which can be confirmed by the atomic configurations later. Fig. 6-27 gives the atomic configurations after the interaction. At Point A in Fig. 6-26(a), as well as in Fig. 6-27(a, b), the incident dislocation started to interact with the CTB and generate the penetrated dislocation embryo at one end of the adjacent grain near the free surface.

In Fig. 6-27(c, d), the interaction products are quite complicated. Two slip systems were activated. In contrast to the positive dislocation case, two partial dislocations were generated on the CTB and slipped on opposite halves of the CTB. One partial dislocation was released from the impacting point to the twinned grain, leaving a residual stair-rod dislocation at the impacting point. Furthermore, the second slip system was activated, resulting in the emission of another perfect dislocation into the twinned grain. However, a stair-rod dislocation was nucleated after a previously dissociated partial dislocation re-interacted with the CTB. These two slip systems also collided, resulting in a third stair-rod dislocation.

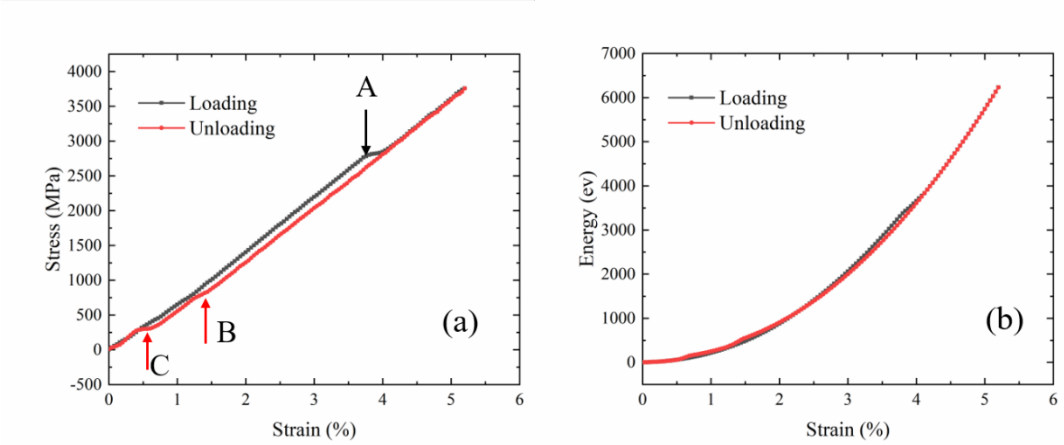

Fig. 6-26. (a) The stress-strain curves of negative edge dislocation-CTB interaction during loading and unloading process in Ni. (b) The Energy-strain curves of negative edge dislocation-CTB interaction during loading and unloading process in Ni. Point A: dislocation started to interact with the CTB. Point B: dislocation started to retract back to the original grain. Point C: dislocation entirely retracted back to the original grain.

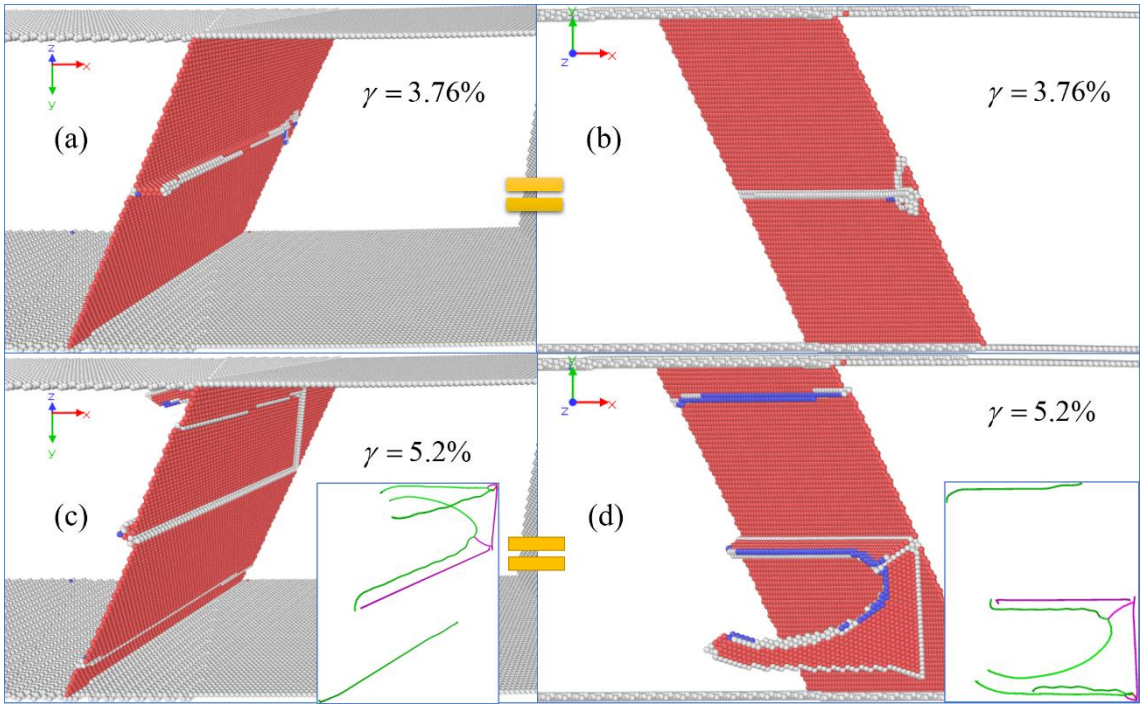

Fig. 6-27. (a, b) Atomic configuration corresponds to Point A in Fig. 6-26. The dislocation started to interact with the CTB. (a) and (b) are from different viewing angle. (c, d) the final state. (c) and (d) are from different viewing angle. The insets represent the dislocation lines. Green line is the Shockley partial dislocation. Purple line is the stair-rod dislocation with Burgers vector of $\frac{1}{6}<110>$.

When system underwent unloading, the stair-rod dislocation, which was generated by the intersection of the two activated slip planes, started to shrink back to the CTB as shown in Fig. 6-28(b). However, Eftink [14,15] proposed that such intersections or stacking fault tetrahedrons were quite stable so that the reversal motion was hard and unlikely to happen. What we have observed refreshes the existing cognition, and reversible motion may likewise occur in the intersection area. The dislocation started to retract back to the original grain at $\gamma = 1.36\% / \tau = 795\text{MPa}$ and completed this retraction at $\gamma = 0.48\% / \tau = 293\text{MPa}$ as illustrated by Point B in Fig. 6-26/Fig. 6-28(c, d) and Point C in Fig. 6-26/Fig. 6-28(e), respectively. Later the dislocation would move

back to the original location when the applied strain equaled to zero, which realized the reversible defect interaction.

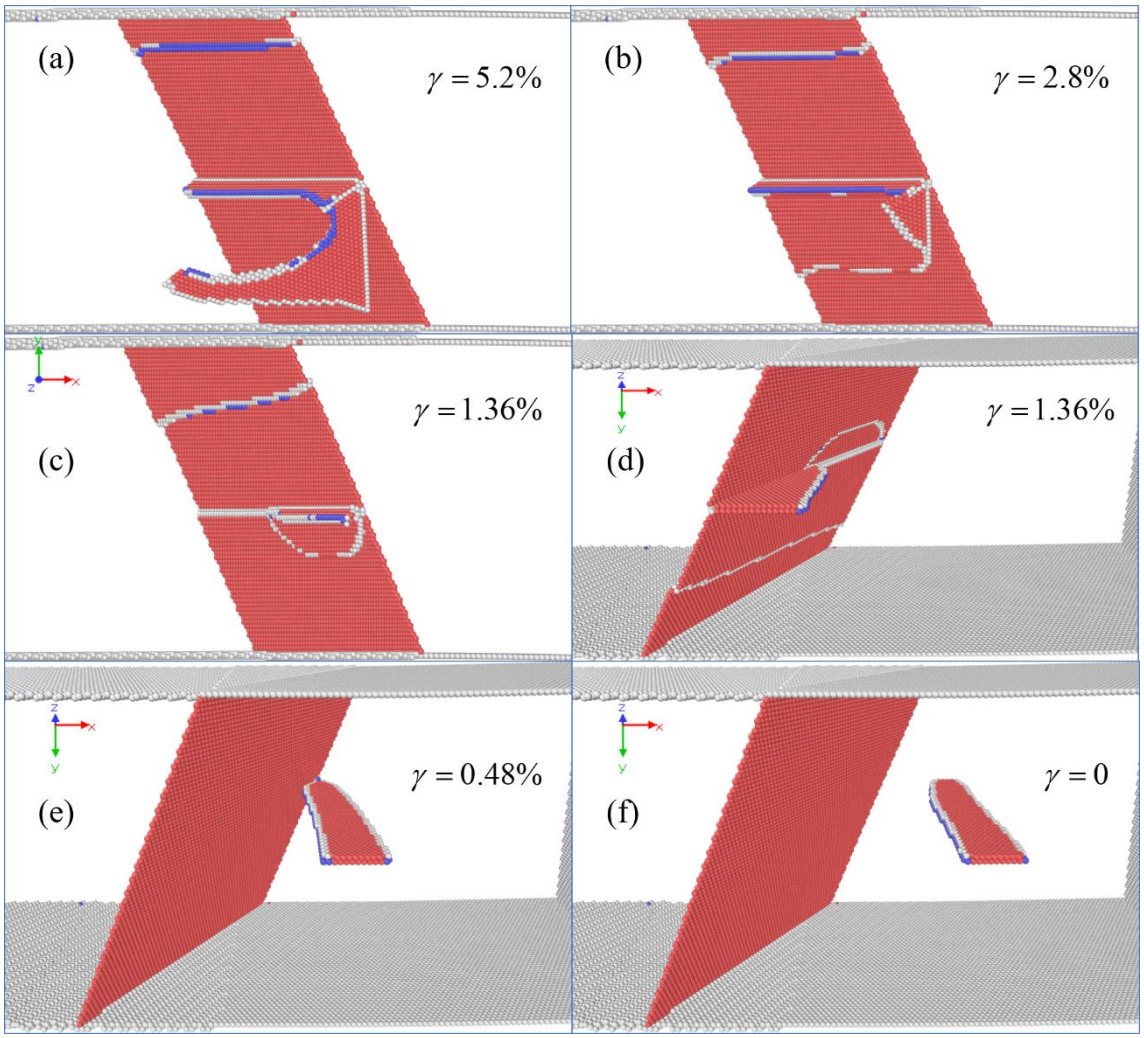

Fig. 6-28 The atomic configurations during the unloading process in Ni. (a) the initial state of unloading process. (b) the stair-rod dislocation shrunk back to the CTB. (c, d) the dislocation started to peel off from the CTB, corresponding to Point B in Fig. 6-26. (c) and (d) are in different viewing angle. (e) the entire dislocation was peeled off from the CTB, corresponding Point C in Fig. 6-26(a). (e) edge dislocation moved back to the original location.

6.3.4. Material: Silver (Ag)

a) Irreversible interaction in positive edge dislocation

Similar to the situations in Al, Cu, Ni, the interaction between positive dislocation and CTB in Ag is also irreversible as shown in Fig. 6-29. The residual strain is about 0.87% when the stress decreased to 0 MPa. At Point A, the dislocation started to transmit through the CTB. One perfect dislocation was released after the interaction just like the situation in Cu, as shown in Fig. 6-30(a), leaving a partial dislocation on the CTB. During unloading, the penetrated perfect dislocation would entirely move out of the model and the residual partial dislocation was left on the CTB as depicted by Point B in Fig. 6-29(a) and Fig. 6-30(b).

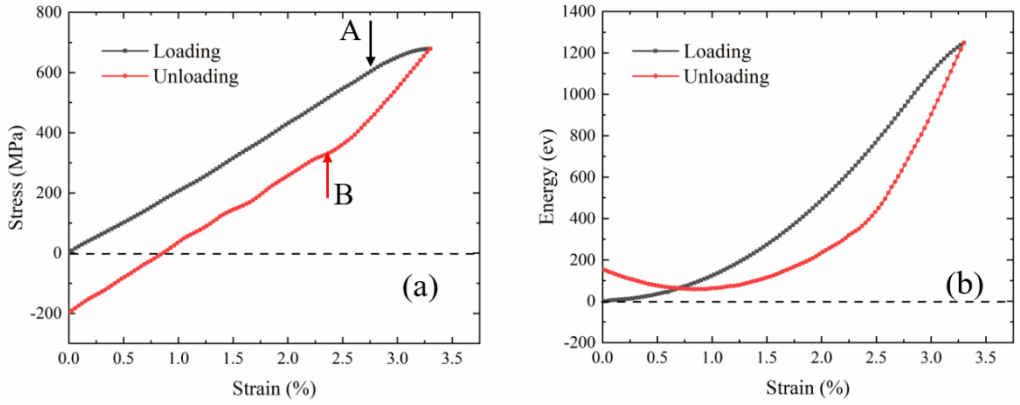

Fig. 6-29 (a) The stress-strain curves of positive edge dislocation-CTB interaction during loading and unloading process in Ag. (b) The Energy-strain curves of positive edge dislocation-CTB interaction during loading and unloading process in Ag. Point A: Dislocation started to transmit through the CTB. Point B: dislocation entirely moved out of the free surface.

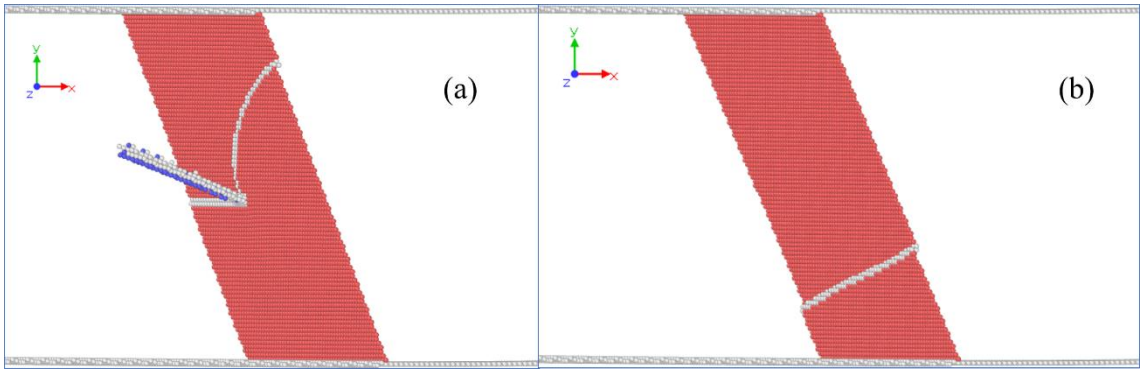

Fig. 6-30 (a) The dislocation transmitted through the CTB in Ag during loading process. (b) final state of the unloading process. The dislocation escaped from the free surface and partial dislocation was left on the CTB.

b) Reversible interaction of negative dislocation

The stress-strain curves and energy evolution curves during the loading and unloading process are listed in Fig. 6-31. When compared to Fig. 6-29, the energy evolution curves of the loading and unloading processes practically coincide, and the changes in stress during the loading and unloading processes are substantially lower for the negative dislocation situation. However, unlike Al, Cu, and Ni, the residual strain was not zero. The residual strain was around 0.12 %, which can be verified from atomic configurations in Fig. 6-32 as well. Two slip systems were activated after the defect interaction. First, one perfect dislocation was emitted into the twinned grain from the center of the model. Second, another partial dislocation was generated and emitted into the twinned grain, leaving one stair-rod dislocation on the CTB. After unloading, all newly generated dislocations automatically moved back to the impacting point and then recombined. Only the original trailing partial dislocation, however, was returned to the original grain. The CTB continued to block the leading partial, resulting in residual strain, as shown by Fig. 6-31(a) and Fig. 6-32(b). Nevertheless, this part-reversible process already decreased the residual strain from 0.87% to 0.12% when it was compared with the positive dislocation.

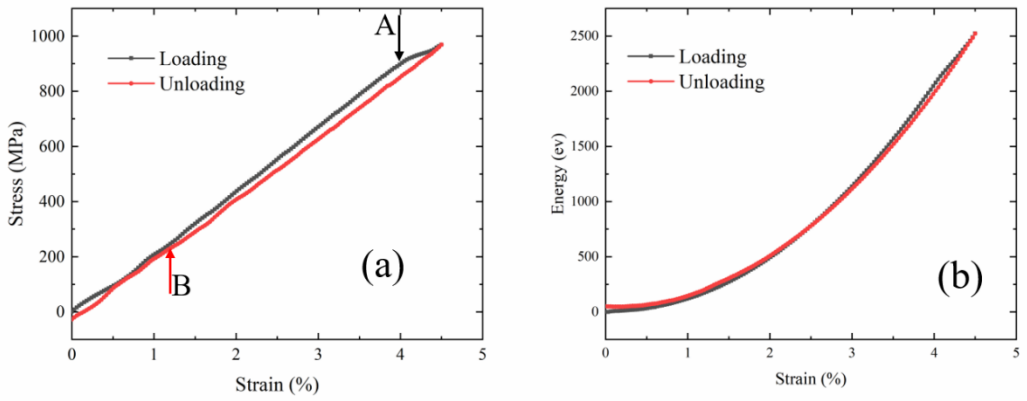

Fig. 6-31 (a) The stress-strain curves of negative edge dislocation-CTB interaction during loading and unloading process in Ag. (b) The Energy-strain curves of negative edge dislocation-CTB interaction during loading and unloading process in Ag. Point A: Dislocation started to transmit through the CTB. Point B: Dislocation started to retract back to the original grain.

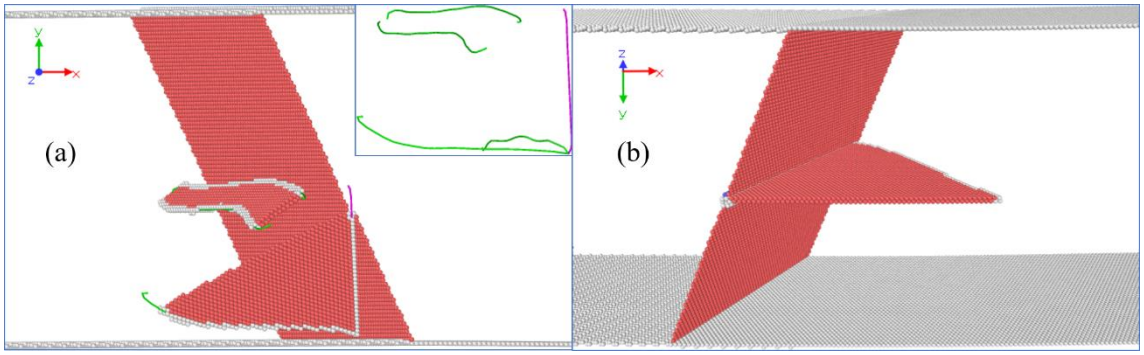

Fig. 6-32 The atomic configurations during the unloading process in Ag. (a) the initial state of unloading process. (b) the final state when the applied strain was removed. Green line is the Shockley partial dislocation. Purple line is the stair-rod dislocation with Burgers vector of $\frac{1}{6}<110>$.

6.4. Edge dislocation-<110>-axis-$\Sigma 11(\bar{1}13)$ GB interaction

The main simulation setups for the defect interaction between edge dislocation and

$\Sigma 11(\bar{1}13)$ GB were identical to the setups in CTB. Al, Cu, Ni, and Ag were considered. It has to be admitted that it is unrealistic to strictly define the positive and negative of a Burgers vector, because this is just a relative concept. If one changes the GB plane based on the symmetry of the geometry, the positive and negative definitions may change accordingly. Therefore, the positive and negative of Burgers vectors discussed in the following text only have a relative meaning, and there is no absolute definition of the positive and negative of Burgers vectors.

6.4.1. Material: Aluminum (Al)

a) Irreversible interaction of positive dislocation

Similar to the situations in CTB, the interaction between positive dislocation and $\Sigma 11(\bar{1}13)$ GB in Al is irreversible as shown in Fig. 6-33. The unclosed hysteresis stress curve gives a residual strain of about 0.56%. When the stress exceeded 0 MPa during the unloading phase, which was similar to reverse loading, the energy increased as well. The atomic configurations during the loading process are depicted in Fig. 6-34. Because the common neighbor analysis method employed in the previous section did not provide a good visual effect for distinguishing the generated complex structure, centrosymmetric parameters were used to identify the GB and dislocations in these figures, as discussed in Chapter 2.4. At Point A (Fig. 6-33), the leading partial dislocation began to impact the GB, and stress started to drop. When the trailing partial was absorbed by the GB, stress, at Point B, increased again, as seen in Figs. 6-33(a) and 6-34(c). Finally, the GB completely absorbed the entire edge dislocation, leaving only one misfit step loop visible on the GB plane in Fig. 6-34(d). Figures 6-34(e) and (f) show the atomic configurations when the stress and strain both achieved zero during the unloading process. Clearly, this is an irreversible interaction because the misfit step loop remained on the GB plane after the deformation was totally eliminated, which is also why the residual strain originated.

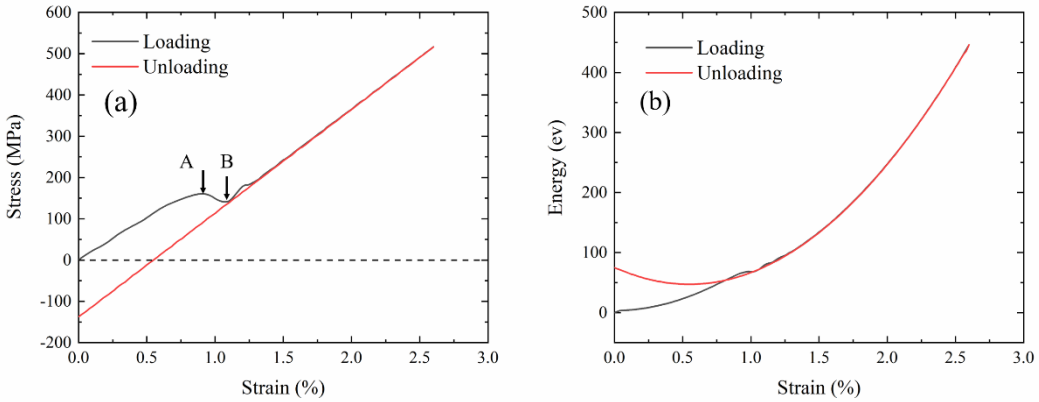

Fig. 6-33 (a) The stress-strain curves of positive edge dislocation-$\Sigma 11(\bar{1}13)$ interaction during loading and unloading process in Al. (b) The Energy-strain curves of positive edge dislocation-$\Sigma 11(\bar{1}13)$ interaction during loading and unloading process in Al. Point A: leading partial dislocation just touched the GB. Point B: trailing partial dislocation was absorbed by the GB.

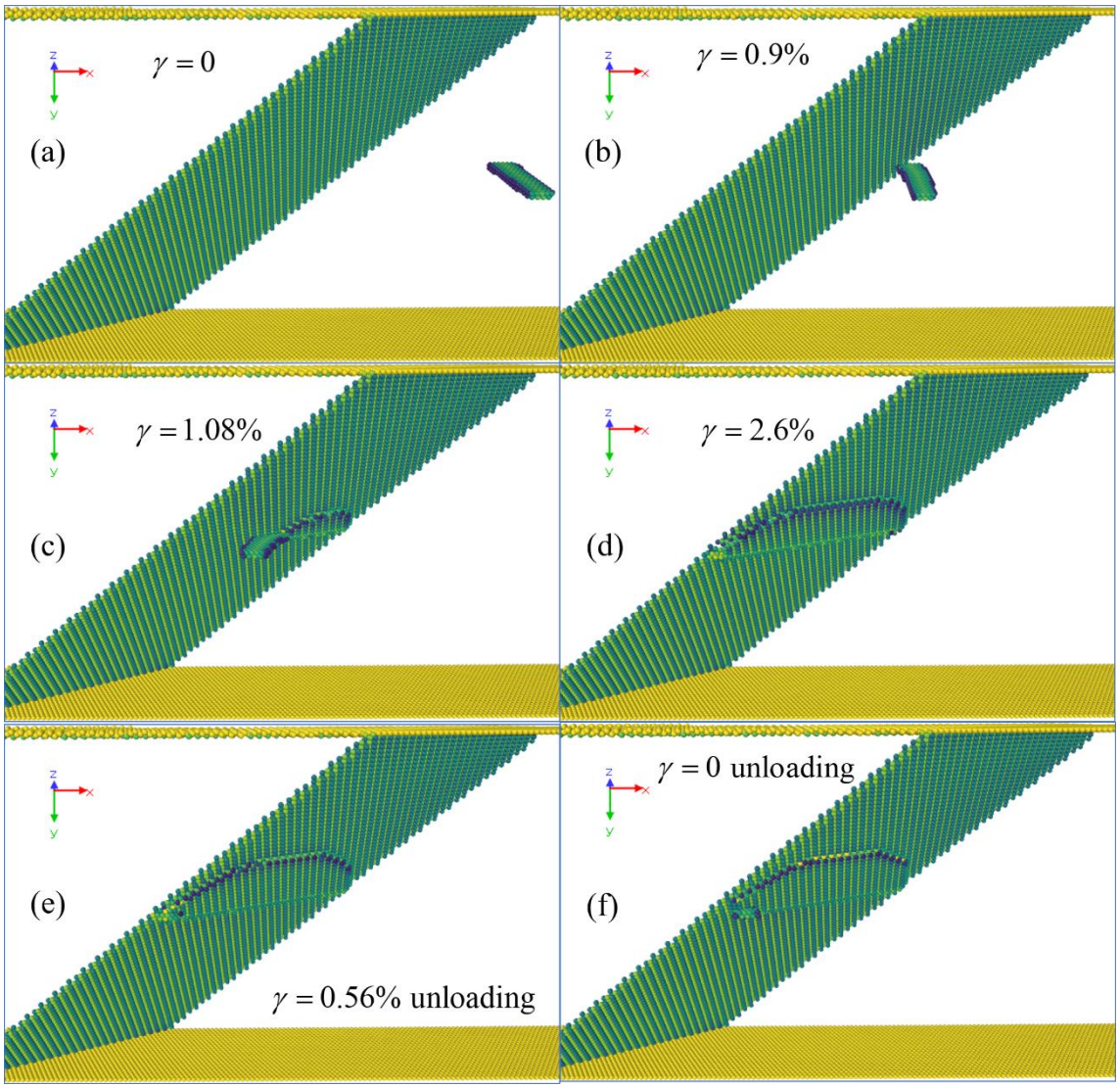

Fig. 6-34 The atomic configurations during the loading and unloading processes in Al. (a) the initial state. (b) the leading partial dislocations started to touch the CTB. Point A in Fig.6-33. (c) the edge dislocation was absorbed by the CTB at one end while the other end still kept a distance from the CTB. Point B in Fig. 6-33. (d) the final state in the loading process. (e) the state in the unloading process when the stress reached 0 MPa. (f) the state in the unloading process when the strain reached 0.

b) Reversible interaction of negative dislocation

c) On the other hand, Fig. 6-35 gives the stress-strain curve and energy-strain curve for

the negative dislocation-$\Sigma 11(\bar{1}13)$ interaction. Although the hysteresis stress curve is closed, the stress reached 0 MPa at $\gamma = 0.44\%$ as shown in Fig. 6-35(a) and Fig. 6-36(e). Hereafter, the stress first decreased to -50 MPa and subsequently increased again to 0 MPa when the deformations were completely removed. From the atomic morphologies, during the loading process, the edge dislocation would progressively transmit through the GB and one partial dislocation was emitted into the adjacent grain as shown in Fig. 6-36(a-c). The trend of strain-stress curve is similar to the irreversible case. However, the interaction mechanism changed to the transmission from absorption. During the unloading process, as shown in Fig. 6-36(e-f), the original dislocation was gradually peeled off from the GB. When $\gamma > 0.44\% / \tau > 0\text{MPa}$, the dislocation had already returned to the original grain and the reversible process was triggered. Although the stress dropped below 0 MPa during this process, however, further removing the applied strain increased the stress again and eventually stress reached 0 MPa again when the dislocation moved back to the original location. The energy evolution of the unloading process also follows a similar trend at $\gamma = 0 \sim 0.44\%$ as shown in Fig. 6-35(b). One should also notice that the trailing partial dislocation was blocked at GB during the loading process, which herein enabled the trailing dislocation to record the information of the impacting point as well.

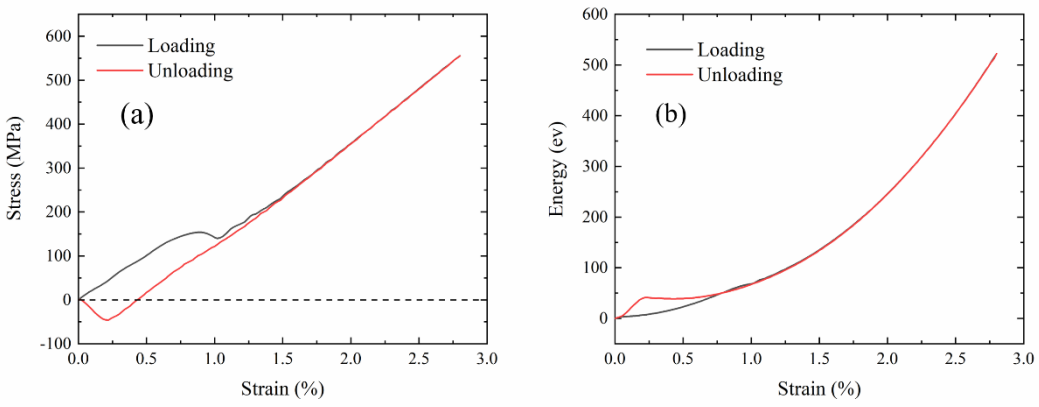

Fig. 6-35 (a) The stress-strain curves of negative edge dislocation-$\Sigma 11(\bar{1}13)$ interaction during loading and unloading process in Al. (b) The Energy-strain curves of negative edge dislocation-$\Sigma 11(\bar{1}13)$ interaction during loading and unloading process in Al.

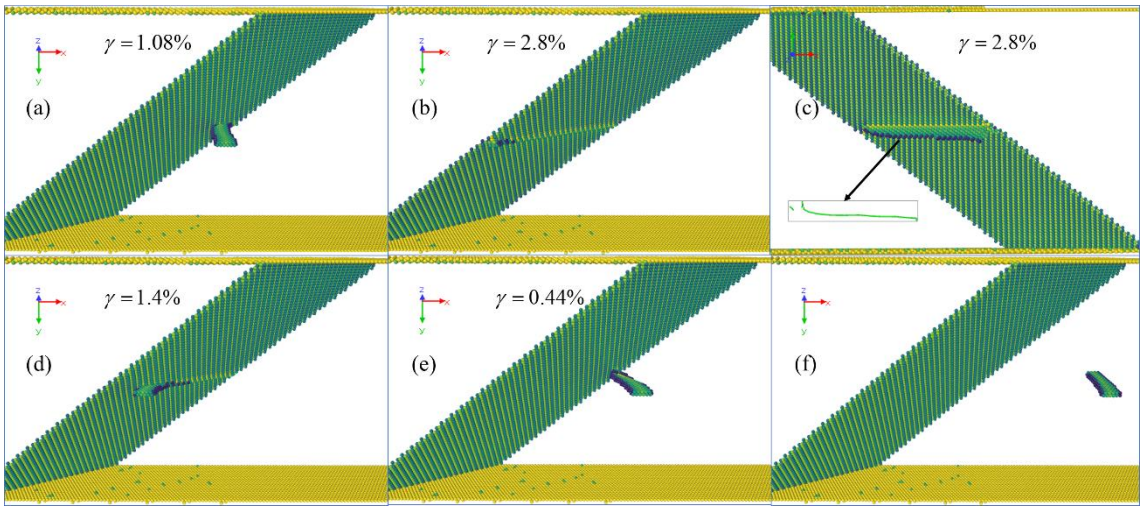

Fig. 6-36 The atomic configurations during the loading and unloading process in Al. (a) the leading partial started to impact the GB in loading process. (b, c) the final state of the loading process in different viewing angles. One partial dislocation was transmitted through the GB and trailing partial was blocked on the GB. (d) the original dislocation started to be peeled off from the GB in the unloading process. (e) one end was blocked at the GB when the stress reached 0 MPa in unloading process. (f) the original dislocation was moving back to the initial location during the unloading process.

6.4.2. Material: Copper (Cu)

a) Irreversible interaction of positive dislocation

Fig. 6-37 gives the stress-strain curves and energy-strain curves in Cu. The corresponding atomic configurations are given in Fig. 6-38. The leading partial dislocation touched the GB at $\gamma = 0.52\% / \tau = 78\text{MPa}$ (Point A/Fig. 6-38(a)). The slope of the stress-strain curve obviously changed at point B/Fig. 6-38(b), when the dislocations

are completely absorbed into the GB. Many misfit steps were intertwined and superimposed on each other, resulting in an extremely complex GB structure after the interaction. As shown in Fig. 6-38(c), the defect interaction was irreversible and left a residual strain of about 0.44% when the stress reached 0 during the unloading process. Although the stress slightly increased when the strain decreased to 0, the dislocation did not recover to its original location.

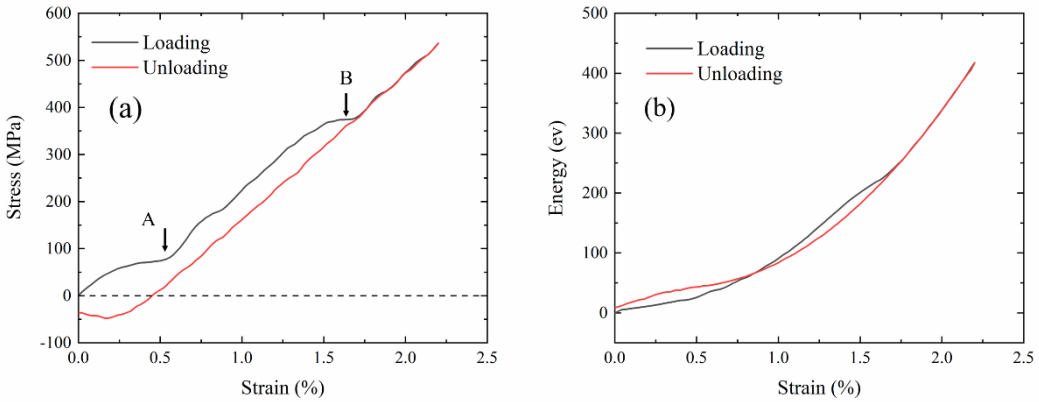

Fig. 6-37 (a) The stress-strain curves of positive edge dislocation-$\Sigma 11(\bar{1}13)$ interaction during loading and unloading process in Cu. (b) The Energy-strain curves of positive edge dislocation-$\Sigma 11(\bar{1}13)$ interaction during loading and unloading process in Cu. Point A: leading partial dislocation just touched the GB. Point B: trailing partial dislocation was absorbed by the GB.

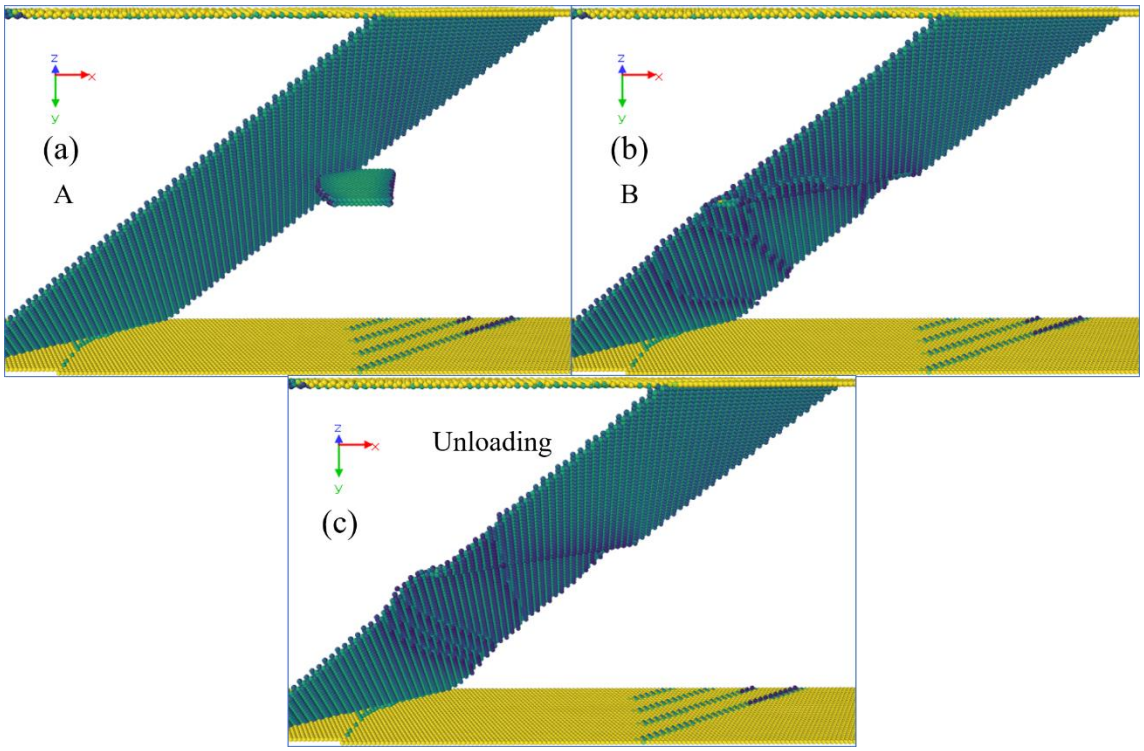

Fig. 6-38 The atomic configurations during the loading and unloading processes in Cu. (a) the leading partial dislocations started to touch the CTB. Point A in Fig.6-37. (b) the edge dislocation was absorbed by the CTB. Point B in Fig. 6-37. (c) the final state of the unloading process.

b) Reversible interaction of negative dislocation

Fig. 6-39 and Fig. 6-40 give the stress-strain curves and corresponding atomic configurations, respectively. As shown in Fig. 6-40(a) and (b), the final state of loading process has a relatively uniform structure than what generated in the positive dislocation case in Fig. 6-38(b). Two misfit steps were generated on the GB plane and another immobile part recorded the impacting region. During the unloading process, newly generated misfit step on the GB returned to the impacting point and recombined to form the original incident dislocation. The original incident dislocation would gradually be retracted back to the original grain when the stress and strain were simultaneously reduced to zero, as shown in Fig. 6-40 (c) and (d). The closed stress hysteresis curve and the almost

completely coincident energy curves showed that this was a completely reversible process.

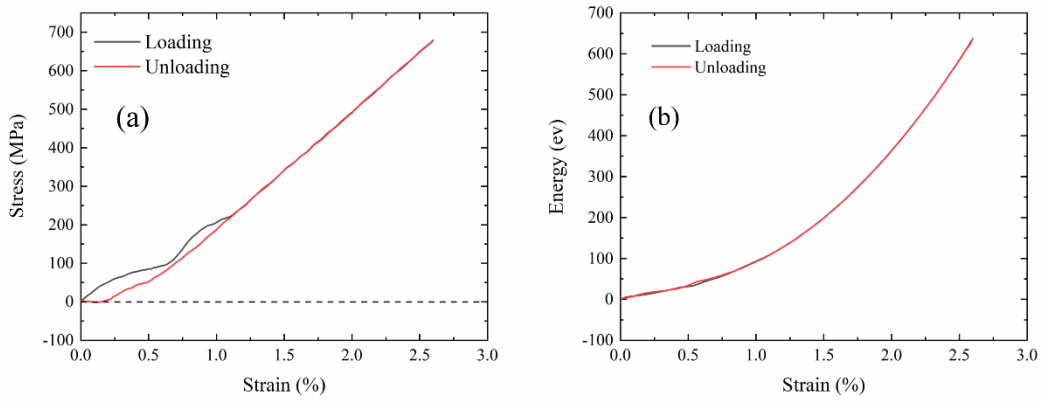

Fig. 6-39 (a) The stress-strain curves of negative edge dislocation-$\Sigma 11(\bar{1}13)$ interaction during loading and unloading process in Cu. (b) The Energy-strain curves of negative edge dislocation-$\Sigma 11(\bar{1}13)$ interaction during loading and unloading process in Cu.

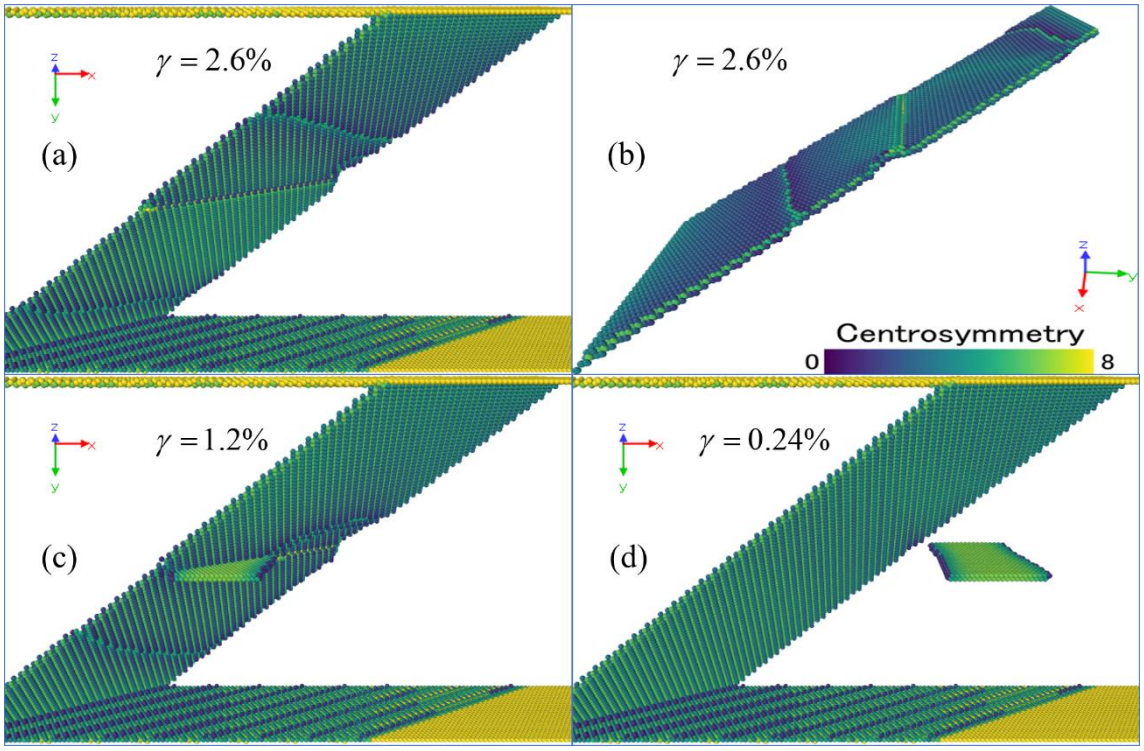

Fig. 6-40 The atomic configurations during the loading and unloading process in Cu. (a,

b) the final state in the loading process. Two misfit steps were generated on the GB and one immobile part located at the impacting point. (c) the dislocation started to retract back to the original grain during the unloading process. (d) the dislocation was completely peeled off from the GB.

6.4.3. Material: Nickle (Ni)

a) Irreversible interaction of positive dislocation

Fig. 6-41 gives the stress-strain curves and energy-strain curves in Ni. The corresponding atomic configurations are given in Fig. 6-42. Obviously, the interaction was irreversible and it left a residual strain of about 0.48% when the stress recovered to 0 MPa. The stress and energy slightly decreased once the leading partial dislocation impacted the GB as shown in Fig. 6-41 Point A and Fig. 6-42(a). Further increasing applied strain made the GB to absorb the dislocation and to generate an immobile defect and two mobile misfit steps on the below half of the GB. However, the unloading process would not recover the structure. It drove the two mobile misfit steps to slip on the GB and to interact with the immobile part in Fig. 6-42(c). Apparently, it is an irreversible interaction between the positive dislocation and $\Sigma 11(\bar{3}3\bar{2})$ GB.

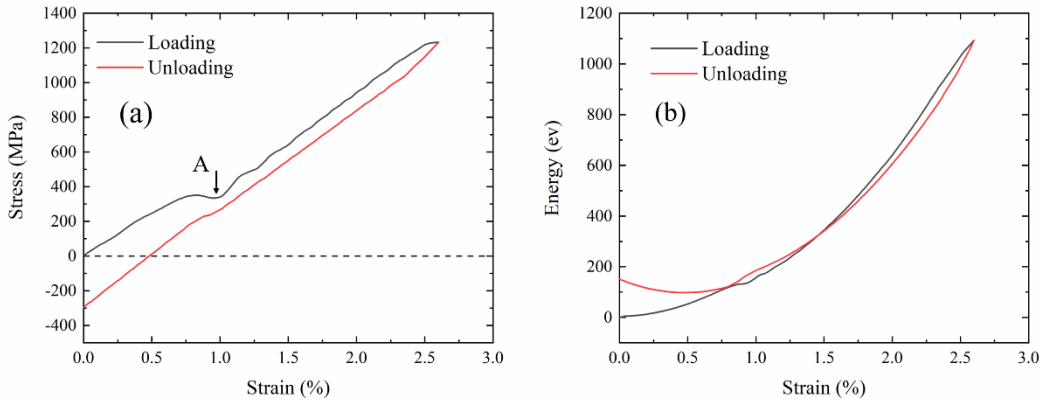

Fig. 6-41 (a) The stress-strain curves of positive edge dislocation-$\Sigma 11(\bar{1}13)$ interaction during loading and unloading process in Ni. (b) The Energy-strain curves of positive edge

dislocation-$\Sigma 11(\bar{1}13)$ interaction during loading and unloading process in Ni. Point A: leading partial dislocation just touched the GB.

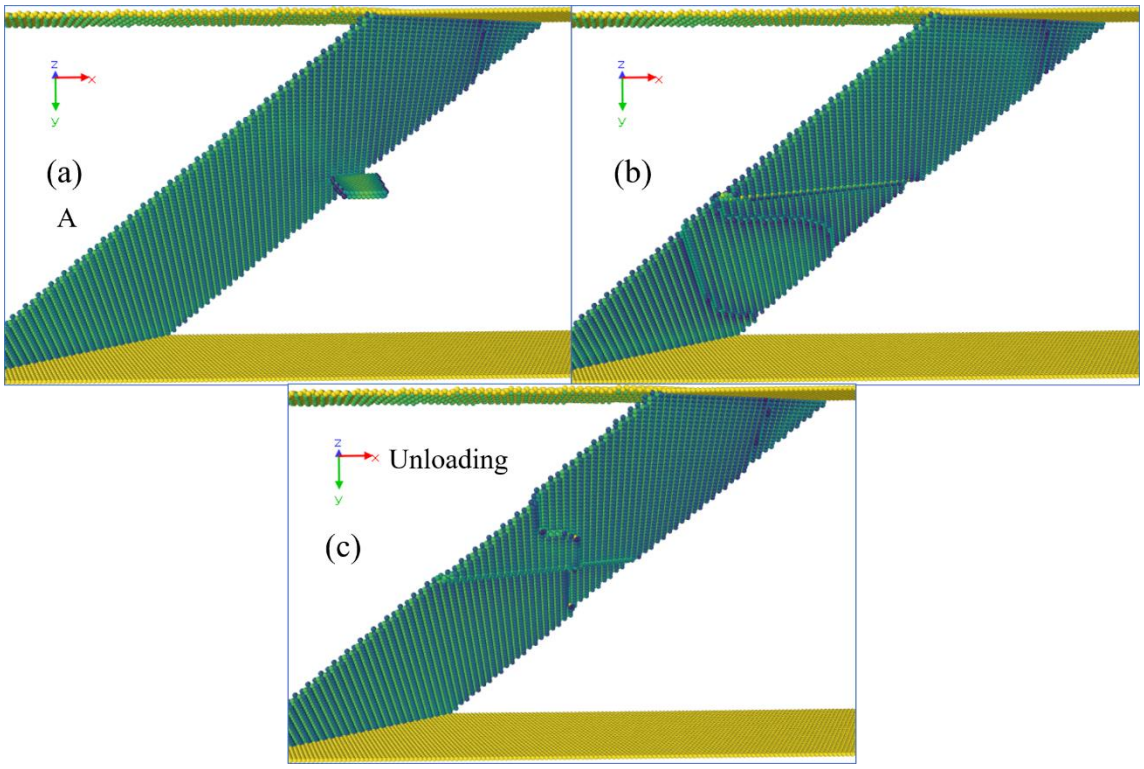

Fig. 6-42 The atomic configurations during the loading and unloading processes in Ni. (a) the leading partial dislocations started to touch the CTB. Point A in Fig.6-41. (b) final state of loading process. The edge dislocation was absorbed by the CTB. (c) the final state of the unloading process.

b) Reversible interaction of negative dislocation

Fig. 6-43 and Fig. 6-44 give the stress-strain curves and corresponding atomic configurations, respectively. If only the stress-strain curve is considered, it does not support reversible plasticity. Because the stress did not return to zero when the strain was zero. However, from the atomic configurations, the defect interaction was reversible as shown in Fig. 6-44 (c-f). The dislocation started to peel off from the GB before the stress

reached 0 MPa as Point A in Fig. 6-43(a) and Fig. 6-44 (c). When $\gamma = 0.44\% / \tau = 0\text{MPa}$ in Point B and Fig. 6-44(d), most of the dislocation peeled off from the GB although the stress equaled to 0. Therefore, the interaction is still defined as the reversible interaction. When the dislocation completely left the GB at $\gamma = 0.1\% / \tau = -127\text{MPa}$, the stress increased again (Point C and Fig. 6-44(e)). Eventually the stress reached -100 MPa when the deformation was removed. It is worth mentioning that if the final state underwent the energy-minimization or relaxation for several picoseconds, the stress would become 0 MPa without any change of the deformation. This is also the reason why the interaction is defined as reversible interaction.

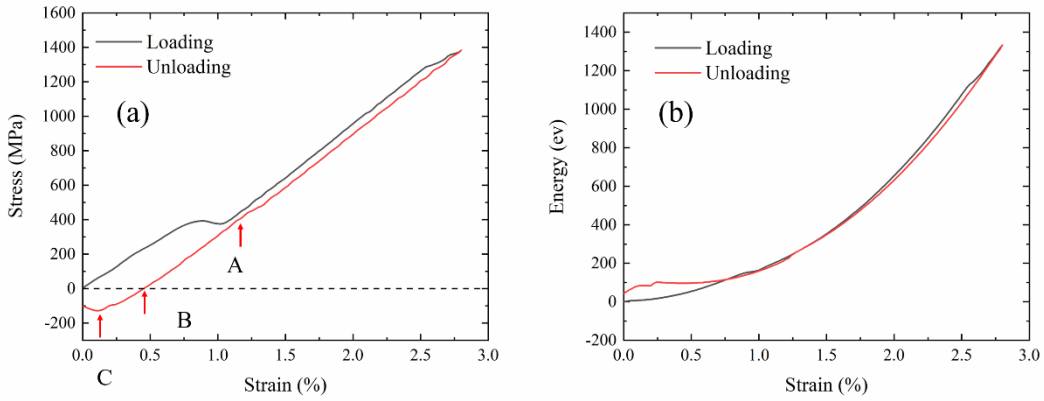

Fig. 6-43 (a) The stress-strain curves of negative edge dislocation-$\Sigma 11(\bar{1}13)$ interaction during loading and unloading process in Ni. (b) The Energy-strain curves of negative edge dislocation-$\Sigma 11(\bar{1}13)$ interaction during loading and unloading process in Ni. Point A: dislocation started to retract back to the original grain. Point B: the stress decreased to 0 MPa with a strain of 0.44%. Point C: dislocation completely left the GB and entirely entered the grain. The stress increased while the strain continuously decreased to 0.

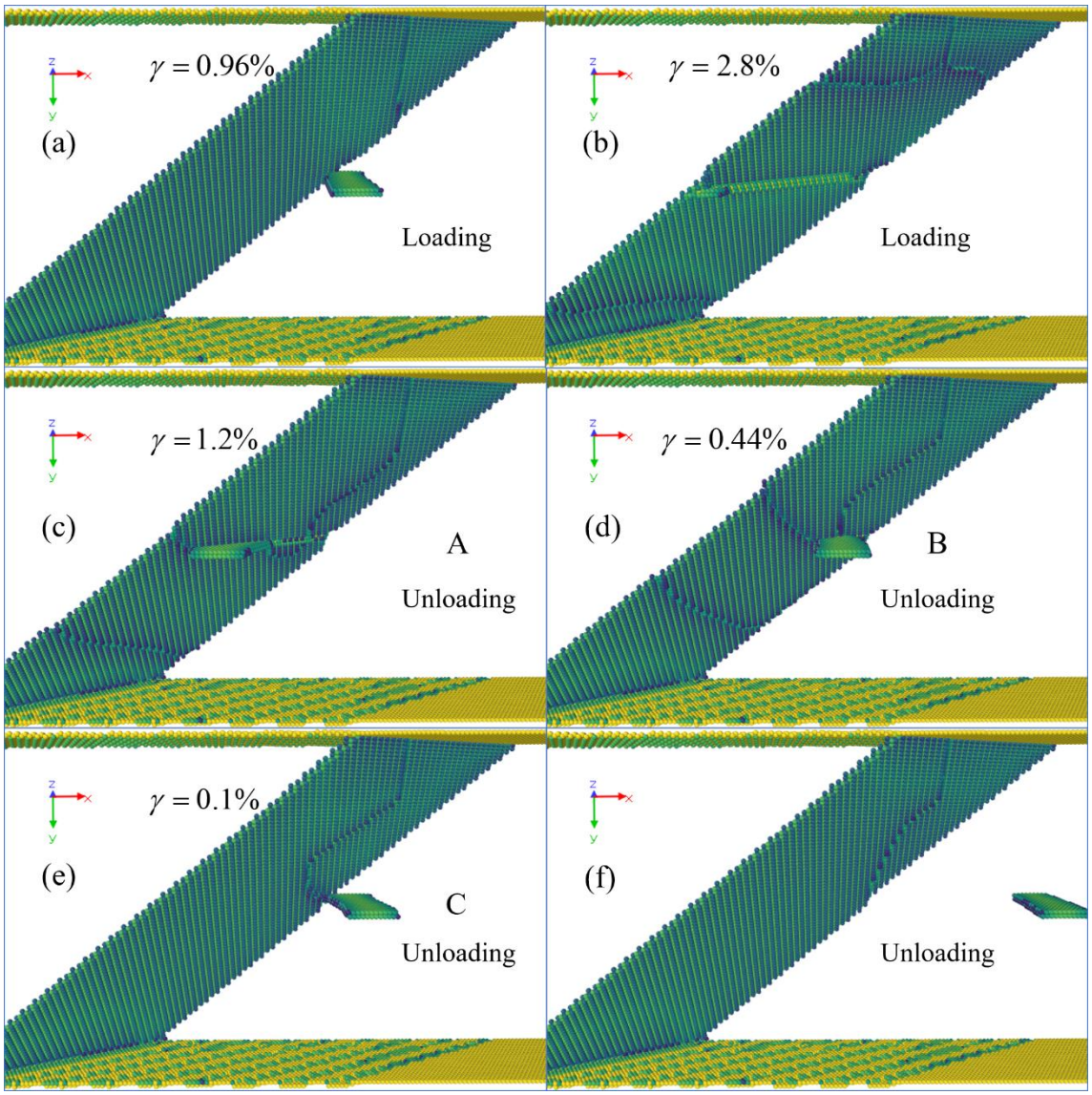

Fig. 6-44 The atomic configurations during the loading and unloading process in Ni. (a) the dislocation started to impact the GB. (b) the final state of the loading process. (c) dislocation started to leave the GB, corresponding to Point A in Fig. 6-44, during the unloading process. (d) the atomic configuration at stress = 0 MPa with residual strain of 0.44%, corresponding to Point B during unloading process. (e) the dislocation entirely entered the original grain and the stress reversely increased. (f) the dislocation moved to the initial position.

6.4.4. Material: Silver (Ag)

Perhaps Ag is the most special case in the considered materials for the interaction between edge dislocation and $\Sigma11(\bar{1}13)$ GB. In Fig. 6-45 (a) and (b), it is clear that the stress curves for both the positive and negative dislocations are not closed. From this perspective, none of them supports fully reversible plasticity. However, the energy evolutions are almost the same and overlapped for both cases, which indicates the special properties for the positive and negative dislocation-$\Sigma11(\bar{1}13)$ interactions.

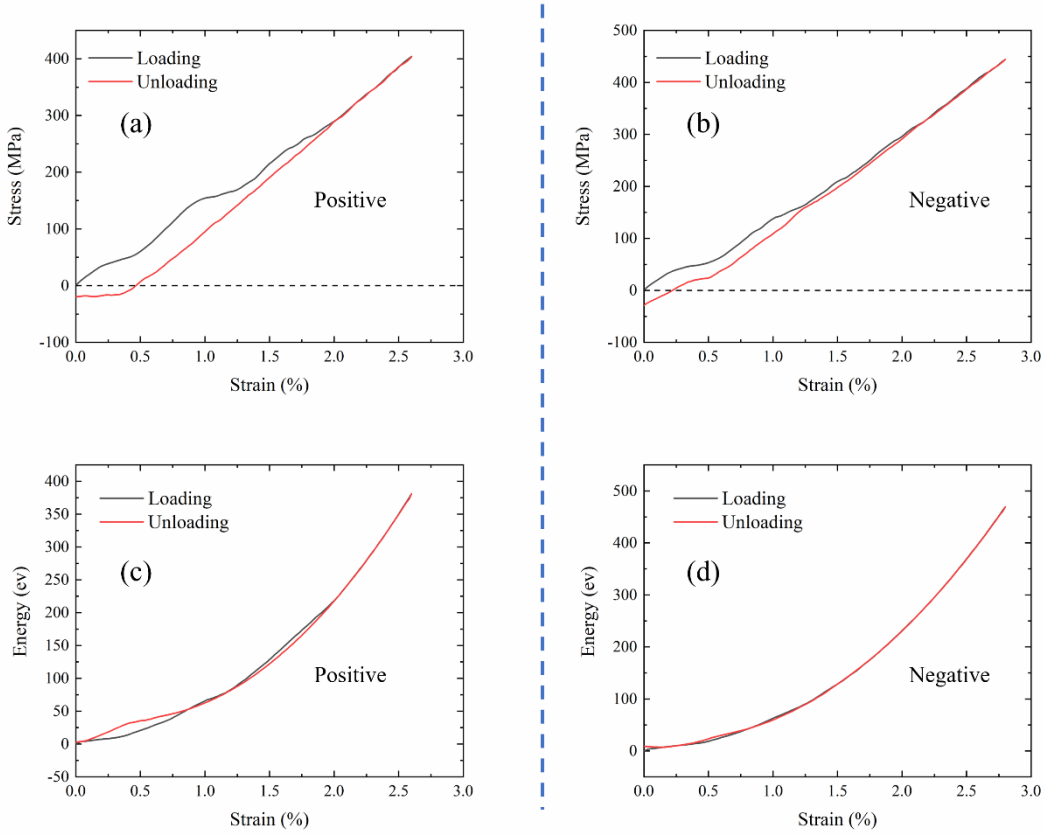

Fig. 6-45 (a) The stress-strain curves of positive edge dislocation-$\Sigma11(\bar{1}13)$ interaction during loading and unloading process in Ag. (b) The stress-strain curves of negative edge dislocation-$\Sigma11(\bar{1}13)$ interaction during loading and unloading process in Ag. (c) The Energy-strain curves of positive edge dislocation-$\Sigma11(\bar{1}13)$ interaction during loading and unloading process in Ag. (d) The Energy-strain curves of negative edge dislocation-

$\Sigma 11(\bar{3}3\bar{2})$ interaction during loading and unloading process in Ag.

Fig. 6-46(Pa)-(Pd) give the atomic configurations of the unloading process for positive dislocation-$\Sigma 11(\bar{1}13)$ GB interaction. Different from the previous material, the positive situation gave a completely reversible interaction in Ag. The original leading partial dislocation started to retract back to the original grain at $\gamma = 0.46\% / \tau = 0$MPa (Fig. 6-46(pb)). Clearly, the reverse loading promoted the reversible process. When the strain was completely removed, the dislocation also returned to its original position (Fig. 6-46(pc)-(pd)). But it should be emphasized that the stress during the reverse loading was maintained around 16 MPa which was very low and the stress was decreased to 0 MPa if the energy-minimization was implemented. Therefore, it could be presumed that the dislocation would be peeled off from the GB even at 0 MPa if the system was fully relaxed.

On the other hand, for the negative dislocation case (Fig. 6-46(Na)-(Nd)), the final unloading provided a partly reversible result like the results in edge-CTB interaction. The leading partial dislocation was retracted back to the original grain, but the trailing partial was blocked on the GB.

For both cases, the slope of the stress-strain curve changed when the leading partial was released to the original grain as shown in Fig. 6-45(a, b). Nevertheless, we have to emphasize that the positive and negative characters are only relative concepts. The results in the simulation only proved that it is possible for the reversible interaction or the reversible plasticity appearing in the Al, Ni, Cu, and Ag.

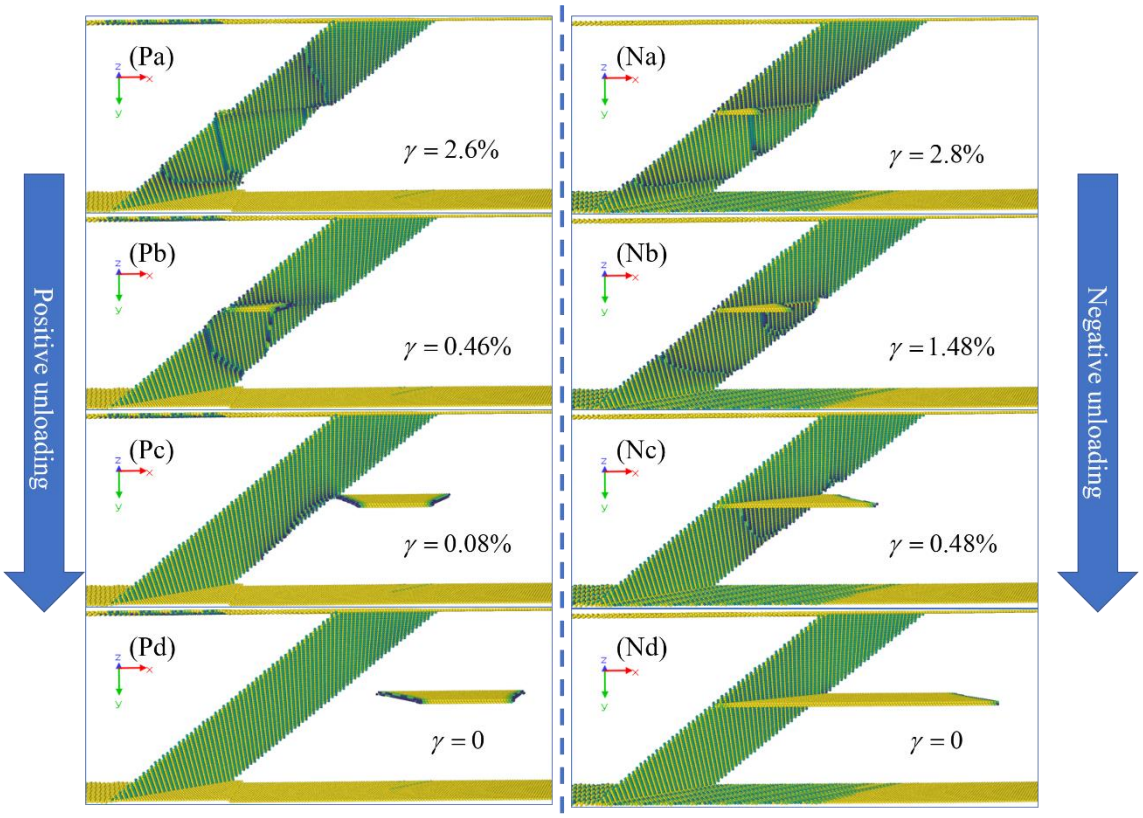

Fig. 6-46 The unloading process of positive and negative dislocation-$\Sigma11(\bar{1}13)$ GB interactions. The left side is positive dislocation-$\Sigma11(\bar{1}13)$ GB interaction and the right half is negative dislocation-$\Sigma11(\bar{1}13)$ GB interaction.

6.5. Edge dislocation-<112>-axis-$\Sigma11(\bar{1}3\bar{1})$ GB interaction

In the previous chapter, we highlighted the decisive influence of the Burgers vector of the dislocation on the reversible plasticity. Two local minima of <110>-axis tilt symmetric GB family, CTB and $\Sigma11(\bar{1}13)$ GB, have demonstrated their ability on the reversible defect interaction and the reversible plasticity. In this section, we would like to show that the other local minimum of the <112>-axis tilt symmetric GB family, $\Sigma11(\bar{1}3\bar{1})$ GB, may also have the same ability in Cu.

The loading process of the interaction between an edge dislocation and $\Sigma11(\bar{1}3\bar{1})$ GB

has been described in Chapter 4.3.1. The leading partial dislocation was spontaneously absorbed by the GB at the beginning and several misfit steps on the GB plane and one tumor like mass appeared at the impinging points as indicated by III in Fig. 4-5(d) or in Fig. 6-47(b). The detailed unloading processes are shown in Fig. 6-47. The two misfit steps on the upper or lower half of the GB moved back to the impacting point when the deformation was gradually removed, referring to the red and blue dash circle in the figure. When $\gamma = 1.72\% / \tau = 547\text{MPa}$, one misfit step reached the impacting point as shown in Fig. 6-47(c) and all the newly generated structures recombined together at $\gamma = 1.64\% / \tau = 531\text{MPa}$, referring to Fig. 6-47(d) and Point A in Fig. 6-47 (a). Also, one subtle platform showed on the stress-strain curve at Point A, which indicated the changes of the atomic structure. Further removing the deformation would release the original trailing partial dislocation into the original grain. When the global stress became 0 MPa, a residual strain of 0.18% could be found. When the deformation was completely removed, the leading partial was still blocked at the GB. Therefore, we called this process as the partly reversible interaction. The reason why the leading partial was not released by the GB was explained in Chapter 4 and here we repeat it again. Even if no external load is applied, it is energetically favored for $\Sigma 11(\bar{1}3\bar{1})$ GB to spontaneously absorb the leading partial dislocation. When the external load was completely removed, it is reasonable that the leading partial would not be released either.

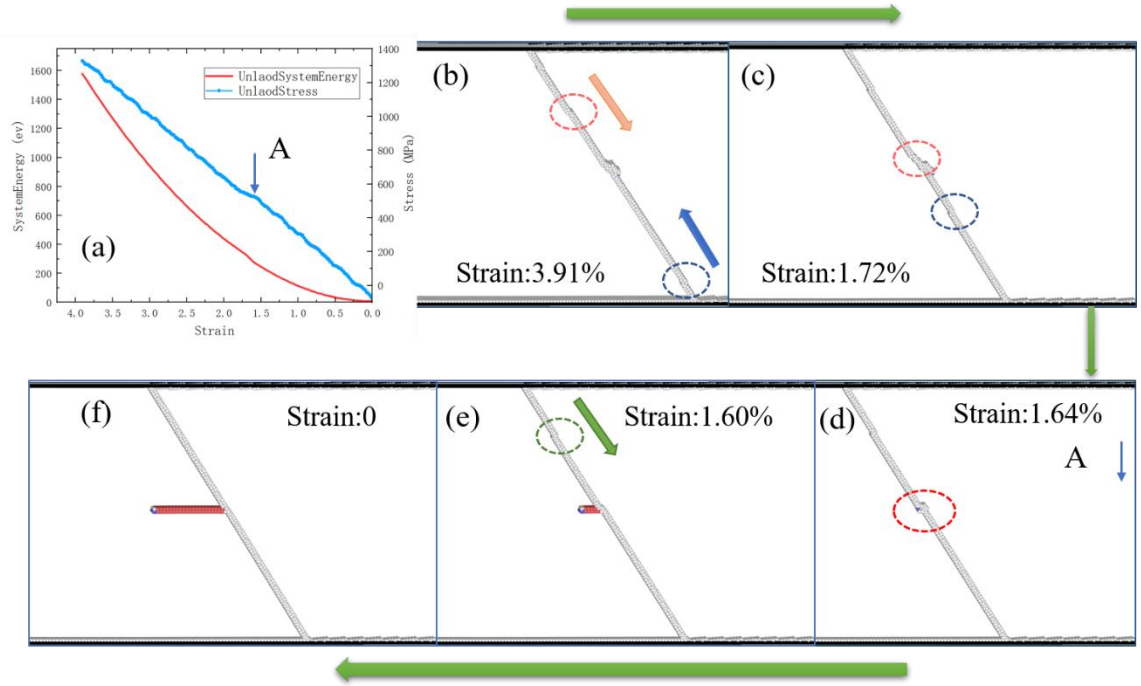

Fig. 6-47 The unloading process of the interaction between an edge dislocation and $\Sigma11(\bar{1}3\bar{1})$ GB. (a) the stress-strain curve and the energy evolution. Red line for energy curve and blue line for stress curve. (c)-(f) the unloading process. Point A: the newly generated products recombined together.

6.6. Discussion

From the foregoing results, it is easy to get one obvious trend that the interactions between negative edge dislocation and <110>-axis $\Sigma3(1\bar{1}\bar{1})$ CTB/<110>-axis $\Sigma11(\bar{1}13)$ GB/<112>-axis $\Sigma11(\bar{1}3\bar{1})$ GB are reversible and thus reversible plasticity can be achieved. For simplicity, we define these three kinds of GBs as reversible GBs (RGBs). On the other hand, the interaction between the positive dislocation and RGBs is irreversible and the residual strains were quite large.

Actually, the reversible process could be divided into several separate parts. First, the initial stage where an incident dislocation moved toward the RGBs during loading process and its counterpart where the peeled off dislocation moved back to the original location

from the RGBs. In these two counterparts, the reversible plasticity followed the mechanism of reversal motion of dislocations mentioned in Chapter 6.1.1. This mechanism has been observed many times in the experiments and it is the fundamental of the reversible plasticity. For convenience, we refer to this mechanism as Reversible Mechanism I (RMI).

Second part is the reversal motion of the penetrated dislocations in the adjacent grain, or reversal motion of the newly nucleated dislocations or misfit steps on the RGBs. According to the conservation of dislocations, the new dislocations created by the reaction must all be re-fused to generate the original dislocation. The reversal motion of the newly nucleated dislocation is a necessary condition for the establishment of the reversible plasticity, without which the residual strain will appear. For example, the transmitted perfect dislocation moved out of the system in the positive-CTB case of Cu as shown in Fig. 6-19. The conservation rule was broken and the process became irreversible. Apart from the dislocation reversely moving in the grain, the reversible motion of the misfit step on the $\sum 11$ GB were also observed in the experiment as shown in Fig. 6-48 [16]. Forward motions of the misfit step would cause the $\sum 11$ GB to migrate, while the reversal motions eliminate the migration and bring the GB to its original location. The reversible motion of the misfit steps on the RGBs is referred to as Reversible Mechanism II (RMII). Actually, RMII is an alternative manifestation of the mechanism of reversal motion of dislocations (RMI).

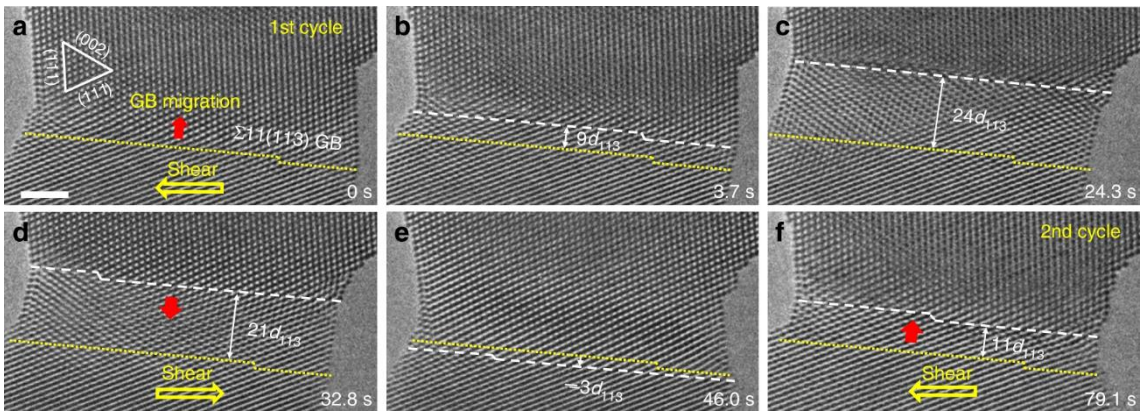

Fig. 6-48 Reversible GB migration in shear loading cycle [16].

Third part is the reversible interaction between dislocation and RGBs. This reversible process is the core of reversible plasticity observed in present study. Although Qin and Gao [9] showed the reversible plasticity of the penta-twinned Ag nanowires in experiments, it is hard to say whether the interaction actually happened. Because what they directly observed is that dislocations were nucleated from the free surface of the nanowire and then dislocations are hindered by the CTB. No penetration was directly observed. If there was no direct interaction between dislocations and CTB, the unloading process would follow RMI, which would lead to the reversible plasticity. However, they implemented the MD simulation to prove that the interaction indeed happened. And compared with penta-twinned structure, the bi-twinned model might lead to less reversible plasticity because tiny residual strain still remained after unloading. This subtle difference corresponds well with our result in Ag because negative dislocation only leads to part-reversible plasticity. But in Cu, Ni, and Al, no residual strain was observed for the CTB cases in the present study.

Apart from the sign of the Burgers vector and the type of the material, the immobile part in the interaction may also play an important role. To a certain extent, the immobile part recorded the information of impacting location. For example, in Cu, there was no immobile part on the CTB after the defect interaction and during the unloading process, the newly nucleated partial dislocation only swung along the CTB plane without any resistance as shown in Fig. 6-18. The same situation can also be observed in Ag in Fig. 6-30. However, for the reversible case, the immobile part stocked at the impacting point and hinder the dislocation to move so that, during the unloading process, the dislocations that arrived at the impact point first can wait for dislocations that arrived later, as shown in Fig. 6-16 and 22.

Moreover, the extremely low energy state of the GBs may also contribute to the

reversible plasticity. CTB is the first local minimum in <110>-axis tilt symmetrical GB family. The local GB rearrangement after the defect interaction can be treated as the nucleation of a new GB with a higher GB energy and higher degree of disorder. It has been proved that the GB with lower GB energy is much stable than the GB with higher GB energy and higher degree of disorder [17,18]. We speculate that the local minimum of the GB energy and lower degree of disorder facilitate the reversible interaction because the disordered structures energetically prefer to form low-energy states. To verify this hypothesis, Chapter 6.4 continued to calculate the interaction between the edge dislocation and $\Sigma 11(\bar{1}13)$ GB which is another local minimum of the <110>-axis tilt symmetrical GB family. Moreover, <112>-axis-$\Sigma 11(\bar{1}3\bar{1})$ GB was also found to have the ability to support partly reversible defect interactions. On the contrary, GBs with high energy and high degrees of disorder do not support the reversible plasticity. For example, Fig. 6-49 gives the final atomic configuration of the unloading process of <110>-axis tilt $\sum 9(1\bar{1}\bar{4})$ GB with a GB energy of 720 mJ/m^2. The dislocation was completely absorbed by the GB and was not released to the original grain when the deformation was removed. Similar situations can be found in Chapter 4 for many <112>-axis GBs, even for the second local minimum $\sum 35B$ GB which has a relatively larger GB energy of about 700 mJ/m^2.

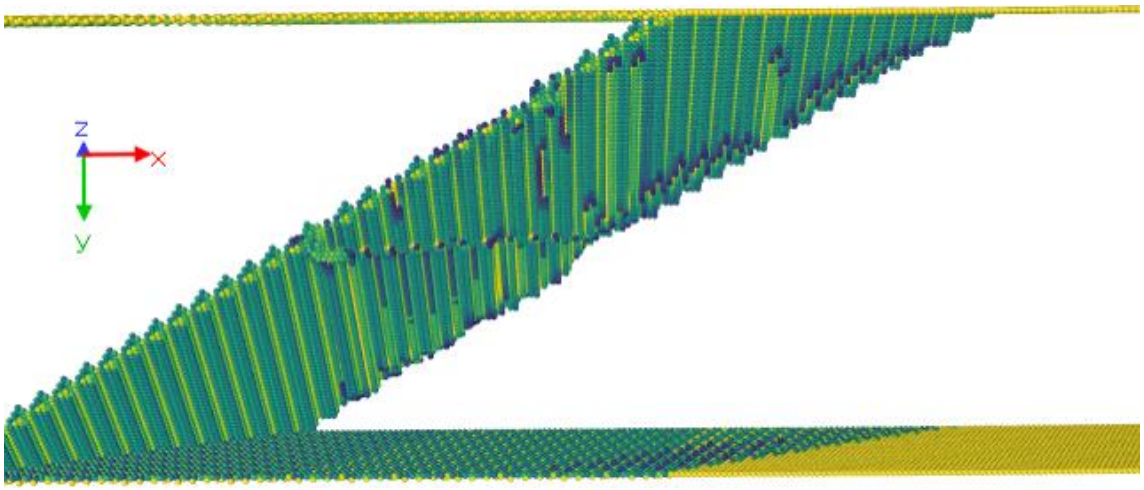

Fig. 6-49 The final atomic configuration of the unloading process for <110>-axis tilt $\Sigma 9(1\bar{1}4)$ GB.

6.7. Summary

The interactions between an edge dislocation and <110>-axis tilt CTB /<110>-axis tilt $\Sigma 11(\bar{1}13)$ GB were investigated in Al, Cu, Ni, and Ag. A similar interaction for <112>-axis-$\Sigma 11(\bar{1}3\bar{1})$ GB was also investigated in Cu. It was found that:

(1) Generally, the interactions between the negative dislocation and CTB were fully reversible and hence led to the reversible plasticity in Cu, Ni, and Al. While partly reversible interaction was found in Ag. The interactions between positive dislocation and CTB were all irreversible in Al, Cu, Ni, and Ag.

(2) The interactions between the negative dislocation and <110>-axis tilt $\Sigma 11(\bar{1}13)$ GB were fully reversible in Al, Cu and Ni. But it is partly reversible in Ag.

(3) The interactions between the positive dislocation and <110>-axis tilt $\Sigma 11(\bar{1}13)$ GB were irreversible in Al, Cu and Ni. But it is fully reversible in Ag.

(4) The interaction between the negative dislocation and <112>-axis-$\Sigma 11(\bar{1}3\bar{1})$ GB was partly reversible in Cu. The trailing partial dislocation would be released to the original grain when the deformation was removed. However, the leading partial dislocation was blocked on the GB.

(5) The reversible plasticity was caused by the reversible defect interactions. It is related to the sign of the Burgers vector of the dislocation. A negative dislocation will facilitate reversible plasticity while a positive dislocation will not. However, the positive or negative dislocation was only a relative concept without rigorous definition.

(6) The reversible plasticity only exists in the local minima of the <110>-axis or <112>-

axis tilt GB family. The extremely low GB energy and low degree of disorder contribute to this special phenomenon.

(7) The reversible process can be divided into three stages. First stage: the reversible motion of dislocation when it moves toward the GB or it moves back to the original location from the GB. Second stage: the reversible motion of the newly generated dislocations or misfit steps on the GB plane. Third stage: the reversible interactions between the dislocation and GB. The first stage and second stage have been confirmed by the experiments. And the third stage is a new finding but we can still find a similar phenomenon in the penta-twinned Ag nanowire.

References

[1] J.P. Hirth, J. Lothe, Theory of dislocation, Krieger Pub. Co, New York, 1982.

[2] C. Deng, F. Sansoz, Fundamental differences in the plasticity of periodically twinned nanowires in Au, Ag, Al, Cu, Pb and Ni, Acta Materialia. 57 (2009) 6090–6101.

[3] T. Zhu, J. Li, A. Samanta, A. Leach, K. Gall, Temperature and strain-rate dependence of surface dislocation nucleation, Physical Review Letters. 100 (2008) 1–4.

[4] B.-Y. Liu, F. Liu, N. Yang, X.-B. Zhai, L. Zhang, Y. Yang, B. Li, J. Li, E. Ma, J.-F. Nie, Z.-W. Shan, Large plasticity in magnesium mediated by pyramidal dislocations, Science. 365 (2019) 73–75.

[5] M.W. Barsoum, T. Zhen, S.R. Kalidindi, M. Radovic, A. Murugaiah, Fully reversible, dislocation-based compressive deformation of Ti 3SiC2 to 1 GPa, Nature Materials. 2 (2003) 107–111.

[6] Q. Zhu, Q. Huang, C. Guang, X. An, S.X. Mao, W. Yang, Z. Zhang, H. Gao, H. Zhou, J. Wang, Metallic nanocrystals with low angle grain boundary for controllable plastic reversibility, Nature Communications. 11 (2020) 3100.

[7] W. Liang, M. Zhou, Atomistic simulations reveal shape memory of fcc metal nanowires, Physical Review B - Condensed Matter and Materials Physics. 73 (2006) 1–11.

[8] S. Lee, J. Im, Y. Yoo, E. Bitzek, D. Kiener, G. Richter, B. Kim, S.H. Oh, Reversible cyclic deformation mechanism of gold nanowires by twinning-detwinning transition evidenced from in situ TEM, Nature Communications. 5 (2014) 1–10.

[9] Q. Qin, S. Yin, G. Cheng, X. Li, T.H. Chang, G. Richter, Y. Zhu, H. Gao, Recoverable plasticity in penta-twinned metallic nanowires governed by dislocation nucleation and retraction, Nature Communications. 6 (2015).

[10] G. Cheng, S. Yin, C. Li, T. Chang, G. Richter, H. Gao, Y. Zhu, In-situ TEM study of dislocation interaction with twin boundary and retraction in twinned metallic nanowires, Acta Materialia. 196 (2020) 304–312.

[11] Y. Mishin, D. Farkas, M.J. Mehl, D.A. Papaconstantopoulos, Interatomic potentials for monoatomic metals from experimental data and ab initio calculations, Physical Review B - Condensed Matter and Materials Physics. 59 (1999) 3393–3407.

[12] Y. Mishin, M.J. Mehl, D.A. Papaconstantopoulos, A.F. Voter, J.D. Kress, Structural stability and lattice defects in copper: Ab initio, tight-binding, and embedded-atom calculations, Physical Review B - Condensed Matter and Materials Physics. 63 (2001) 2241061–22410616.

[13] P.L. Williams, Y. Mishin, J.C. Hamilton, An embedded-atom potential for the Cu-Ag system, Modelling and Simulation in Materials Science and Engineering. 14 (2006) 817–833.

[14] B.P. Eftink, A. Li, I. Szlufarska, I.M. Robertson, Acta Materialia Interface mediated mechanisms of plastic strain recovery in a AgCu alloy, 117 (2016) 111–121.

[15] J. Kacher, B.P. Eftink, B. Cui, I.M. Robertson, Dislocation interactions with grain boundaries, Current Opinion in Solid State and Materials Science. 18 (2014) 227–243.

[16] Q. Zhu, G. Cao, J. Wang, C. Deng, J. Li, Z. Zhang, S.X. Mao, In situ atomistic observation of disconnection-mediated grain boundary migration, Nature Communications. 10 (2019) 1–8.

[17] L. Li, L. Liu, Y. Shibutani, Defect interaction summary between edge dislocations and <112>-axis symmetric tilt grain boundaries in copper on activation barriers and critical stresses, International Journal of Plasticity. 149 (2022) 103153.

[18] M.D. Sangid, T. Ezaz, H. Sehitoglu, Energetics of residual dislocations associated

with slip-twin and slip-GBs interactions, Materials Science and Engineering A. 542 (2012) 21–30.

7. Conclusion remarks

This thesis focused on the interactions between the dislocation and grain boundaries (GBs). We investigated the effects of dislocation types and GB types on the interaction mechanisms and critical interaction shear stress (CISS).

In chapter 1, plenty of literature related to the dislocation-GB interactions are reviewed from the perspectives of the experiments or simulations. Various factors will influence the interaction mechanisms. Absorption, transmission, and pile-up are all possible for the interactions. However, it is hard to get a clear trend of the influence of the GB structure on the interaction mechanisms and CISS. Neither have the energy barriers, activation volumes, and strain rate sensitivities (SRS) of the interactions been systematically investigated. Based on this shortage of the current researches, the influence of the GB energy and GB structures, the effect of the materials on the CISS, and reversible plasticity were investigated in Chapters 4-6, respectively.

In Chapter 2, some fundamental theories and concepts were introduced including the theories and methods related to Molecular dynamics (MD), the concepts and application method of the transition state theory (TST) and nudged elastic band method (NEB). Combing the results of MD with the TST, it is easy to calculate the activation volumes and SRS which can be directly compared with the experiments. This process circumvents the shortcomings of the extremely unrealistic high loading rate of MD so that the results can be directly compared with realistic experiments, and the physical significance of molecular dynamics is enhanced.

In Chapter 3, basic concepts of GB and stacking fault (SF) were first described. Then the GB energy maps of different rotation axes were given. There are two local minima in the <112>-axis tilt symmetric GB family. They are $\Sigma 11A$ (309 mJ/m^2) and $\Sigma 35B$ GB (731 mJ/m^2) in Cu. Similarly, two local minima also appeared in <110>-axis tilt

symmetric GB family in Cu, Al and Ni. $\Sigma3(111)$ is the GB with the lowest GB energy. $\Sigma11B(113)$ is another local minimum. The energy map for <100>-axis tilt symmetric GB family has a period of 90° and exists one peak at $\Sigma73A(08\bar{3})$. The period of <111>-axis tilt symmetric GB family is 120°, and one local minimum is located at $\Sigma3(1\bar{2}1)$ GB with 60° misorientation angle. At last, the generalized stacking fault energy curves (GSFC) were given for Al, Cu, Ni, Ag, Au, and Pd. Although for most of the cases, the intrinsic stacking fault energy (ISFE) are almost the same as the extrinsic stacking fault energy (ESFE), the unstable extrinsic stacking fault energy is much higher than the unstable intrinsic stacking fault energy.

In Chapter 4, interactions between edge dislocations and <112>-axis symmetric tilt grain boundaries in Cu were investigated. It was found that the interaction phenomena depended on the GB type when an edge dislocation impinged upon the interface. Possible phenomena include absorption, transmission and pile-up. The leading partial dislocation was usually attracted and spontaneously absorbed once it touched the GB regardless of the magnitude of the shear stress. If we consider the weakest point of the GB structure, a GB with a higher GB energy requires a lower CISS. This trend described the effects of GB energy on defect interactions. Furthermore, we used the TST and NEB to calculate the activation volumes and SRS for $\Sigma35A$, $\Sigma35B$, $\Sigma73A$. The corresponding values were in the range 13~31b^3 for activation volumes and 0.004~0.016 for SRS. The calculated parameters agreed well with the experimental data.

In Chapter 5, interactions between screw dislocations and coherent twin boundaries (CTBs) were investigated in Al, Cu, Ni, Ag, Au, Pd_Hale, and Pd_Zhou. The screw dislocation was spontaneously absorbed by the CTB in Al and Pd_Hale because the SFE γ_s is larger than the energy to create a new twin fault γ_{ut}. The screw dislocation was absorbed by the CTB in Cu and it would transmit through the CTB in Ni, Ag, Au, and Pd_Zhou. The interaction process followed the Friedel-Escaig (FE) cross-slip mechanism.

A linear relationship between CISS and $1/(\gamma_{us}-\gamma_s)$ was found. The CISS would decrease when the value of $1/(\gamma_{us}-\gamma_s)$ increases. Through TST and NEB method, the activation volumes were 11 b^3, 15 b^3, 13 b^3, and 21 b^3 for Cu, Ni, Ag, and Au, respectively. The corresponding SRS are 0.029 for Cu, 0.019 for Ni, 0.023 for Ag, and 0.015 for Au. The good agreements between the simulation results and experiments could be found in these two parameters. Energy barriers under the same stress states for different materials have a similar trend on $1/(\gamma_{us}-\gamma_s)$.

In Chapter 6, the abnormal reversible plasticity was found. The interactions between an edge dislocation and <110>-axis tilt CTB /<110>-axis tilt $\Sigma11(\bar{1}13)$ GB were investigated in Al, Cu, Ni, and Ag. A similar interaction for <112>-axis-$\Sigma11(\bar{1}3\bar{1})$ GB was also investigated in Cu. The fully reversible interaction processes were observed in Cu, Ni, Al for interactions between negative dislocation and CTB/<110>-axis-$\Sigma11(\bar{1}13)$ GB. The edge dislocation will first be absorbed or transmit through the GB. New reacted products would be generated after the interactions. However, these processes were completely reversible after the deformations were removed. The negative edge dislocation was released from the GB and moved back to the original position. No structural changes would be left on the GB. The positive edge dislocation did not show the reversible feature in Cu, Ni, and Al. The interaction between positive edge dislocation and CTB was irreversible in Ag. But it is fully reversible for <110>-axis-$\Sigma11(\bar{1}13)$ GB. The negative dislocation showed part reversibility in the interactions with both two GBs in Ag. Only the trailing partial dislocation was released back to the grain but the trailing partial dislocation was still absorbed by the GB. The interaction between negative edge dislocation and <112>-axis-$\Sigma11(\bar{1}3\bar{1})$ GB was only considered for Cu and it was partly reversible. The trailing partial dislocation was released to the original grain but the

leading partial was blocked on the GB plane. This special reversibility consists of three stages. Stage one: reversal motion of dislocation which exists during dislocation moving to the GB and released dislocation moving back to the original position. Stage two: reversal motion of newly generated misfit steps or partial dislocations on the GB during loading and unloading processes. Stage three: the reversal defect interaction processes. Stage one and two were directly observed in the previous experiments and stage three is a new finding phenomenon. The extremely low GB energy and low degrees of disorder were believed to contribute to this special feature. Also, the sign of the Burgers vector of the dislocation also mattered.

In summary, the simulations mentioned above provide a deeper understanding of the dislocation-GB interactions. The systematic work revealed the relationship between CISS and GB energy when materials are specified. Moreover, the interactions between a screw dislocation and CTB in various materials were linked to the stacking fault energy. The special reversible plasticity was also found in the dislocation-GB interactions. However, since the interactions between dislocation and GBs are still affected by many other factors, more investigations and theories need to be further proposed and developed.

Appendix

This appendix contains eleven additional tables. Each table records the calculation information of different initial slip planes for different grain boundary structures in Chapter 4. The number of initial slip surfaces varies with the grain boundary structure.

Table S1. Case of Sigma 35A. For interaction events: A stands for absorption, T stands for transmission, and P stands for pile-up.

Slip Plane	Event	Leading partial absorption stress (MPa)	Trailing partial absorption stress (MPa)	Event stress (MPa)
1	A	168	693	693
2	P	/	/	/
3	A	162	670	670
4	P	/	/	/
5	A	161	667	667
6	P	/	/	/
7	A	167	674	674
8	P	/	/	/
9	A	165	690	690
10	P	/	/	/
11	A	170	780	780
12	P	/	/	/

Six of twelve slip planes resulted in absorption. And the other six were pile-up even when the shear stress reached 1.5GPa (the leading partial dislocation was not absorbed into the GB either).

Table S2. Sigma 21A. For interaction events: A stands for absorption, T stands for transmission, and P stands for pile-up.

Slip Plane	Event	Leading partial absorption stress (MPa)	Trailing partial absorption stress (MPa)	Event stress (MPa)
1	P	/	/	/
2	P	/	/	/
3	A	123	400	400
4	P	/	/	/
5	A	130	370	370

Three of five slip planes resulted in absorption. And the other two were pile-up even when the shear stress reached 1.05GPa (the leading partial dislocation was not absorbed into the GB either).

Table S3. Sigma 11A. For interaction events: A stands for absorption, T stands for transmission, and P stands for pile-up.

Slip Plane	Event	Leading partial absorption stress (MPa)	Trailing partial absorption stress (MPa)	Event stress (MPa)
1	A	58	1330	1330
2	A	62	1328	1328
3	A	62	1327	1327
4	A	60	1335	1335
5	A	60	1334	1334
6	A	60	1334	1334

Table S4. Sigma 73A. For interaction events: A stands for absorption, T stands for transmission, and P stands for pile-up.

Slip Plane	Event	Leading partial absorption stress (MPa)	Trailing partial absorption stress (MPa)	Event stress (MPa)
1	A	87	690	690
2	A	87	600	600
3	T	89	1220	1700
4	A	87	620	620
5	T	86	1420	1700
6	T	98	1280	1740
7	A	87	600	600
8	A	87	1330	1330
9	T	90	1280	1700
10	A	97	650	650
11	T	89	1230	1760
12	A	85	622	622

Table S5. Sigma77A. For interaction events: A stands for absorption, T stands for transmission, and P stands for pile-up.

Slip Plane	Event	Leading partial absorption stress (MPa)	Trailing partial absorption stress (MPa)	Event stress (MPa)
1	T	60	740	1730
2	A	69	680	680
3	A	70	/	/
4	A	74	745	745
5	T	70	1250	1522
6	A	73	/	/

Two special cases appeared in this GB. The leading partial dislocations were first absorbed into the GB for Slip plane 3 and 6. Bu the trailing partial dislocations were still repelled by the GB even the stress came to 1700 MPa (Slip plane 3) and 1950 MPa (Slip plane 6). We did not increase the load because the dislocation would be emitted from the constraint part due to the severe deformations.

Table S6. Sigma 15A. For interaction events: A stands for absorption, T stands for transmission, and P stands for pile-up.

Slip Plane	Event	Leading partial absorption stress (MPa)	Trailing partial absorption stress (MPa)	Event stress (MPa)
1	A	75	1030	1030
2	A	76	280	280
3	A	77	296	296
4	A	74	1038	1038

Table S7. Sigma49A. For interaction events: A stands for absorption, T stands for transmission, and P stands for pile-up.

Slip Plane	Event	Leading partial absorption stress (MPa)	Trailing partial absorption stress (MPa)	Event stress (MPa)
1	A	60	240	240
2	A	57	645	645
3	A	56	540	540
4	A	56	390	390
5	A	60	890	890
6	A	62	250	250
7	A	64	510	510
8	A	63	820	820
9	A	63	550	550
10	A	60	620	620
11	A	68	560	560
12	A	68	240	240

Table S8. Sigma79A. For interaction events: A stands for absorption, T stands for transmission, and P stands for pile-up.

Slip Plane	Event	Leading partial absorption stress (MPa)	Trailing partial absorption stress (MPa)	Event stress (MPa)
1	A	80	230	230
2	A	93	200	200
3	A	90	680	680
4	A	91	196	196

Table S9 Sigma 5A. For interaction events: A stands for absorption, T stands for transmission, and P stands for pile-up.

Slip Plane	Event	Leading partial absorption stress (MPa)	Trailing partial absorption stress (MPa)	Event stress (MPa)
1	A	64	310	310
2	A	85	350	350
3	A	89	300	300
4	A	80	320	320

Table S10 Sigma33A. For interaction events: A stands for absorption, T stands for transmission, and P stands for pile-up.

Slip Plane	Event	Leading partial absorption stress (MPa)	Trailing partial absorption stress (MPa)	Event stress (MPa)
1	A	95	510	510
2	A	84	600	600
3	A	89	700	700
4	A	80	645	645

Table S11. sigma 35B. For interaction events: A stands for absorption, T stands for transmission, and P stands for pile-up.

Slip Plane	Event	Leading partial absorption stress (MPa)	Trailing partial absorption stress (MPa)	Event stress (MPa)
1	A	99	380	380
2	A	90	404	404
3	A	90	400	400
4	A	90	390	390
5	A	90	391	391
6	A	89	385	385
7	A	89	383	383

List of contributions

(1) **Li Li**, Lijun Liu, Yoji Shibutani, Defect interaction summary between edge dislocations and <112>-axis symmetric tilt grain boundaries in copper on activation barriers and critical stresses, ***International Journal of Plasticity***, Vol. 149 (2022) 103153

(2) **Li Li**, Lijun Liu, Yoji Shibutani, Defect interactions between screw dislocations and coherent twin boundaries in several fcc materials, ***Materials Transactions***, accepted.

Acknowledgments

I sincerely thank my supervisor, Professor Dr. Yoji Shibutani, for training and teaching me over the three years. It is Prof. Dr. Yoji Shibutani who brought me into the frontier field of micro-nano-scale material mechanics. This will be the most precious treasure in my life. Looking back on the past, I have a lot of emotion. I was really nervous when I first met Prof. Yoji Shibutani. After our first conversation, I clearly felt the kindness and grace of Prof. Yoji Shibutani. For the first time, I clearly felt that even serious scientific researchers can be so humorous and kind. For these, I had a more profound experience in future scientific research and life. In every group discussion and every research report, the kindness of Prof. Yoji Shibutani would calm my nerves first. However, he is also very rigorous in academic research and has a strong academic insight. In every presentation, he would sharply and accurately point out the shortcomings of my researches. Therefore, I greatly admire his academic insight and profound knowledge. This thesis is accomplished under the guidance of Prof. Dr. Yoji Shibutani, I would like to express my greatest gratitude to him. Thank him for this careful guidance on the topic selection and writing scheme of this thesis, as well as his great efforts in the process of revising and completing the thesis.

I want to express my gratefulness to Dr. Lijun Liu in our lab, the Shibutani & Tanaka Laboratory. Dr. Liu has patiently taught me how to operate the molecular dynamics software LAMMPS. I thank her for her help in my daily life and for the valuable and constructive supervise in academic researches. I also want to thank Prof. Hiro Tanaka for his valuable suggestions and advice on the study. Also thank the members of our lab, I hope they all get good futures.

I also want to thank Ms. Yamaguchi Atsuko. Thank for her selfless help during my studies and my Ph.D. application.

Appreciation are given to Dr. Qiyuan He and Mr. Tianhao Zhang in the Department of

Applied Chemistry of Osaka university, Mr. Xingyu Zhang in the Department of Mechanical Engineering of Osaka university, for their help in the daily life.

I want to express my gratefulness to Prof. Shigenobu Ogata, Prof. Katsuyoshi Kondoh and Prof. Akihiro Nakatani for their time and efforts during the reviewing process and defense. Thank for the dissertation committee for the valuable and constructive comments on this dissertation.

I acknowledge the China Scholarship Council (No.201806280033) for the financial support to my studies as a Ph. D student.

Finally, I would like to express my greatest thanks to my parents Mr. Li Weidong and Ms. Huang Ronglian. Thank them for their encouragement during these years I have been aboard. At last, I really want to thank my girlfriend, Miss Yan Yeyun. Long-distance relationship is a very difficult thing, and I am very thankful that we persevered.

April 2022, Osaka

Li Li